UNIVERSITÀ DEGLI STUDI DI CAGLIARI
Facoltà di Scienze Matematiche, Fisiche e Naturali

Applications of perturbation theory in black hole physics

Paolo Pani

A thesis submitted for the degree of Doctor of Philosophy

Supervisor: **Prof. Mariano Cadoni**

January 2010

Abstract

Black holes have many faces. Arguably, they are the most interesting objects in theoretical physics, revealing the elusive connection between gravity and quantum mechanics. Within the gauge/string duality they provide useful insights on strongly coupled quantum field theories and on quantum gravity. Furthermore, probing the strong curvature regime of any gravity theory, black holes carry the imprint of possible strong curvature corrections to General Relativity. Finally, beside their unique theoretical properties, several experimental evidences suggest that astrophysical black holes exist in nature and they are believed to be very common objects in the universe. In this dissertation we discuss several applications of linear perturbation theory in black hole physics. As applications in theoretical physics, we study perturbations of dilatonic black holes in Einstein-Maxwell theory and the holographic properties of the dual field theory via the Anti de Sitter/Condensed Matter duality. Furthermore we discuss a method to compute long-lived quasinormal modes of Schwarzschild-Anti de Sitter black holes and we study vortex black hole solutions in three dimensional Anti de Sitter gravity. As applications in astrophysics, we discuss how the characteristic oscillations of black holes in string-inspired theories of gravity can provide observable signatures of deviations from General Relativity. We study two well-motivated effective theories: Dynamical Chern-Simons gravity and Einstein-Dilatonic-Gauss-Bonnet gravity. We conclude by discussing the black hole paradigm. Motivated by the lacking of a definitive answer on the existence of astrophysical black holes, we study some viable alternatives, generally called "black hole mimickers". We focus on two representative cases: static thin-shell gravastars and superspinars. We discuss their stability, gravitational-wave signature and viability as astrophysical objects.

KEY-WORDS:
Black holes; Perturbation theory; AdS/CFT correspondence; Holography; Modified gravity; Effective theories; Gravitational waves; Quasinormal modes; Black hole mimickers.

a Giu
è qualche cosa che hai fatto,
suppongo.

Acknowledgements

I wish to thank the University of Cagliari and the Italian National Institute of Nuclear Physics (INFN) for financial and logistical support and the Master and Back foundation programme of Regione Sardegna for a grant. This work has been also partially founded by FCT - Portugal through project PTDC/FIS/098032/2008.

I warmly thank my supervisor, Mariano Cadoni, for his guidance, for all the physics he taught me and for the possibility he gave me to find my way in gravitational physics.

I am also extremely grateful to Vitor Cardoso. It is a pleasure and an honor to work with him, being always conscious that I will have something important to learn.

A special thanks goes to Emanuele Berti. Although we have not met (yet!), the useful discussions we had, and his irreplaceable contributions to our works, certainly made me a better physicist.

During these years, I had the pleasure to work with Enrico Barausse, Yanbei Chen, Giuseppe D'Appollonio, Leonardo Gualtieri, Carlos Molina, Richard Norte and Matteo Serra. Many parts of this work are the outcome of various fruitful collaborations with them.

I would like to thank my gravity-group mates in Cagliari: Maurizio Melis and Cristina Monni, and those I met in Lisbon: Mariam Bouhmadi, Jordi Casanellas, Magdalena Lemos, Andrea Nerozzi, Jorge Rocha and Helvi Witek. I hope we will have many other interesting discussions in future.

I cannot express my gratitude enough to my parents Francesco and Rosanna and to my sister Carly, for their constant support, to the rest of my family, especially to my grandmothers and to my aunt Lella, who helped me in correcting this thesis, and to my family-in-law: Albi, Dianella, Fra and Gino.

To my long, long-dated friends, Ale, Alessandra, Beccio, Fede, Giorgio, Marzia, Matte, Pierma, Ricca, Save, Valeria(s). They share the misfortune to be the people who know me better and, in spite of this, they will always support me with their love. *Se' bon a' sutt!*

I would like to thank all the members of the Physics Department in Cagliari, who contribute to make it a wonderful place to work in. In particular my physics-class mates and friends, Francesco, Giamba, Nicola, Scrilly and Gary, the No-Trash Cougar. Although we took different paths and we are now spread around the world, we keep constantly nonsensing about physics and white weapons.

In this difficult period, during which Italian Governments are degrading Public Education and Academic Research year by year, I cannot forget to express my gratitude to my high school Science professors: Maria Tonina Fancello, Guido Orrù, Maria Clorinda Todde and Luigi Uras. If now I am physicist, this is also due to their early guidance.

Last, as usual, comes Giu. Sharing the life with you, with your unconditional love, energy, peace of mind and happiness, makes me a better person. I love you.

Contents

Preface

The work presented in this dissertation was mainly carried out at the Physics Department, University of Cagliari in the period between January 2008 and December 2010. Part of this work has been also done at Centro Multidisciplinar de Astrofísica (CENTRA), Instituto Superior Técnico - Lisbon and at the Physics Department, University of Rome - La Sapienza. I thank these institutions for their kind hospitality.

List of papers included in this dissertation

Most of the work presented in this thesis has been done within different scientific collaborations, whose members I kindly acknowledge for giving me the possibility and the honor to work with them.

Chapter 2 is the outcome of a collaboration with Mariano Cadoni and Giuseppe D'Appollonio. It is based on the following paper :
Phase transitions between Reissner-Nordstrom and dilatonic black holes in 4D AdS spacetime. Mariano Cadoni, Giuseppe D'Appollonio, Paolo Pani. Published in JHEP 1003:100,2010.

Chapter 4 is the outcome of a collaboration with Emanuele Berti and Vitor Cardoso. It is based on the following paper :
Breit-Wigner resonances and the quasinormal modes of anti-de Sitter black holes. Emanuele Berti, Vitor Cardoso, Paolo Pani. Published in Phys.Rev.D79:101501,2009.

Chapter 5 is the outcome of a collaboration with Mariano Cadoni and Matteo Serra. It is based on the following paper :
Scalar hairs and exact vortex solutions in 3D AdS gravity. Mariano Cadoni, Paolo Pani, Matteo Serra. Published in JHEP 1001:091,2010.

Chapter 7 is the outcome of a collaboration with C. Molina, Vitor Cardoso and Leonardo Gualtieri, mostly done at Physics Department of the University of Rome, La Sapienza. It is based on the following paper :
Gravitational signature of Schwarzschild black holes in dynamical Chern-Simons gravity. Carlos Molina, Paolo Pani, Vitor Cardoso, Leonardo Gualtieri. Published in Phys.Rev.D81:124021,2010.

Chapter 8 is the outcome of a collaboration with Vitor Cardoso, mostly done at Centro Multidisciplinar de Astrofísica (CENTRA) in the Physics Department of Instituto Superior Técnico in Lisbon. It is based on the following paper :
Are black holes in alternative theories serious astrophysical candidates? The case for Einstein-Dilaton- Gauss-Bonnet black holes. Paolo Pani and Vitor Cardoso. Published in Phys. Rev. D79:084031,2009

Chapter 10 is the outcome of a collaboration with Emanuele Berti, Vitor Cardoso, Yanbei Chen and Richard Norte. It is based on the following papers :
Gravitational wave signatures of the absence of an event horizon. I. Nonradial oscillations

of a thin-shell gravastar. Paolo Pani, Emanuele Berti, Vitor Cardoso, Yanbei Chen, Richard Norte. Published in Phys.Rev.D80:124047,2009.
and
Gravitational-wave signatures of the absence of an event horizon. II. Extreme mass ratio inspirals in the spacetime of a thin-shell gravastar. Paolo Pani, Emanuele Berti, Vitor Cardoso, Yanbei Chen, Richard Norte. Published in Phys.Rev.D81:084011,2010.

Chapter 11 is the outcome of a collaboration with Enrico Barausse, Emanuele Berti and Vitor Cardoso. It is based on the following paper :
Gravitational instabilities of superspinars. Paolo Pani, Enrico Barausse, Emanuele Berti, Vitor Cardoso. Published in Phys.Rev.D82:044009,2010.

Note for the reader

For the sake of readability, this dissertation is divided into three independent parts, preceeded by a general introduction. We shall keep each part as much self-contained as possible, sometimes at cost of some repetitions. Chapters 1, 6 and 9 are introductory to Part I, II and III respectively, while the remaining chapters are self-contained.

Unless otherwise stated, in this work we mainly use geometrized units $c = G = 1$, except in Chapters 2 and 3, where we use Planck units $c = G = \hbar = k_b = 1$. Furthermore we mainly adopt $(-,+,+,+)$ convention for the signature of the metric, except in Chapter 8 where the opposite signature is used. At the beginning of each chapter we shall usually remind the adopted conventions and define abbreviations. A list of most commonly used abbreviations is given below.

AdS:	Anti de Sitter
BF:	Breitenlohner-Freedman
BH:	Black Hole
CFT:	Conformal Field Theory
CS:	Chern-Simons
DCS:	Dynamical Chern-Simons
EDGB:	Einstein-Dilatonic-Gauss-Bonnet
EMRIs:	Extreme Mass Ratio Inspirals
GR:	General Relativity
LIGO:	Large Interferomenter Gravitational-wave Observatory
LISA:	Laser Interferometer Space Antenna
PPN:	Parametrized Post Newtonian
QFT:	Quantum Field Theory
QNM:	QuasiNormal Mode
RN:	Reissner-Nordström

I declare that none of the original work contained in this disseration is not substantially the same as any that I have submitted for any other degree, diploma or similar qualification and that no part of it has already been or is being concurrently submitted for any such degree or diploma or any other qualification.

Introduction

Physics is like sex. Sure, it may give some practical results, but that's not why we do it.
Richard Feynman

Once considered just as bizarre solutions of Einstein's equations, nowadays black holes have acquired a fundamental place in astrophysics, theoretical physics and gravity in general, in such a way that it makes sense to define *black hole physics* as a wide set of different topics generically related to black holes. Accordingly, black holes have many faces and spread their influence in several areas of physics.

On the mathematical side, black holes emerge as solutions of field equations in General Relativity, as well as in several extensions of it, such as low energy effective theories arising from String Theory. They are almost unavoidably present in any relativistic theory of gravity and they probe the high energy/strong curvature regime. On the astrophysical side, black holes are the most compact celestial objects and they are believed to be very common in the universe. Stellar-mass black holes are widely accepted as final stage of the evolution of sufficiently massive stars. Supermassive black holes seem to populate the center of many galaxies at low redshift, and could have played an important role in the Universe structure formation. However, while electromagnetic observations have already provided us with strong evidences for the astrophysical reality of black holes, a definitive answer on their existence is still lacking and it will hopefully come from gravitational-wave detectors. Finally, black holes may not only exist as astrophysical objects but, accordingly to some recent theories of gravity at the TeV scale, higher dimensional microscopic black holes could be produced by ultra-high energy cosmic rays in the atmosphere and might also be created in high-energy particle collisions at the Large Hadron Collider, which has recently started collecting data.

However, the question whether black holes exist in nature, and the corresponding wealth of information that their existence would provide, is only a partial – although of fundamental relevance – motivation to study these objects. In fact, beside the interest in their very existence, recently black holes have been investigated as *theoretical tools*, which can provide useful insights on the quantum properties of gravity, and can reveal unexpected connections between gravity and quantum field theories. Recent theoretical developments, started with the Anti de Sitter/Conformal Field Theory (AdS/CFT) correspondence [1], have revealed a deep and

intimate connection between gravity in Anti de Sitter spacetime and some non-perturbative strongly coupled regime of certain gauge theories. In this *gauge/string* duality, black holes in Anti de Sitter play a fundamental role, being related to quantum field theories at finite temperature living on the boundary of the Anti de Sitter space [2]. Within this framework one is more interested in a phenomenological description of elusive strongly coupled field theories via holography, rather than in developing realistic black hole models. Hence black holes in Anti de Sitter space, with uncommon topologies or non-conventional couplings to matter fields, are now considered common *theoretical laboratories*, where fundamental issues on our present knowledge of gravity can be investigated [3].

Accordingly to the numerous areas of interest of black hole physics, the arguments presented in this thesis cover a wide range of different, and apparently disconnected, topics. The *trait d'union* between these different topics is our approach of investigation. We discuss several applications of *black hole perturbation theory* in theoretical physics and astrophysics.

Perturbation theory plays a prominent role in physics, describing the linear response of a system to small solicitations. Arguably almost any transport phenomena in nature can be described as a small deviation from an unperturbed system. The harmonic vibrations of a guitar string, or a sound wave travelling into a medium, or the light wave propagation, are all common examples which can be modeled by perturbation theory. Historically, perturbation theory had its roots in the Ptolemaic astronomic system, where *epicycles* were used to compute small corrections to the unperturbed motion of planets. In modern times, during the 20th century perturbation theory had been largely developed in the context of quantum mechanics. The Stark effect and the Zeeman effect are two of the most celebrated applications of perturbation theory to quantum systems. However, the most astonishing outcome was developed in the context of quantum field theory, where the perturbative approach to scattering problems is based on the celebrated Feynman diagrams.

In the context of black hole physics, the study of linear perturbations dates back to the pioneeristic works by Regge and Wheeler [4], followed by fundamental developments by Zerilli [5] and Vishveshwara [6]. Black hole perturbation theory is a well-established and active area and we cannot make justice of the huge amount of literature here, but we refer to some excellent reviews [7, 8, 9] and to references therein.

Black hole perturbations are of fundamental relevance in several contexts. First, they allow us to discuss the linear stability issue for black holes in General Relativity, as well as in modified theories of gravity. Stability of gravitational systems is of great importance, as unstable objects either do not exist in nature or indicate some drastic dynamical evolution or phase transition. Within General Relativity in four dimensions, asymptotically flat and static (Schwarzschild and Reissner-Nordström) or rotating (Kerr) black holes all passed this stability test and they had been found to be stable against gravitational, electromagnetic, scalar and fermionic perturbations. However the situation changes in higher dimensions or in asymptotically curved spacetimes.

Furthermore, characteristic frequencies of black holes, the so-called quasinormal modes (QNMs), play such a crucial role that they would deserve an independent discussion [9]. From the physical standpoint, black hole QNMs are complex frequencies that satisfy causally-motivated boundary conditions: namely they describe purely ingoing waves at the event horizon and purely outgoing waves at infinity. The real part of the frequency corresponds to the oscillation frequency, whereas the imaginary part corresponds to the damping rate. From the astrophysical standpoint QNMs dominate an exponentially decaying "ringdown" phase at

intermediate times in the gravitational wave signal from a perturbed black hole [8]. They also play an important role in the ringdown phase of gravitational systems produced by the merger of a pair of black holes [10, 11]. Moreover QNMs can be used to infer the black hole mass and angular momentum [12], in order to test the no-hair theorems of General Relativity [13, 14].

From a more theoretical standpoint, black hole QNMs (and black hole perturbations in general) are holographically related to equilibrium properties, as well as transport phenomena, of strongly coupled thermal gauge theories via the AdS/CFT correspondence or via some more phenomenological extension of it [15]. In fact QNMs are related to poles of the retarded correlators in the dual gauge theory, providing useful insights on the transport coefficients and on the quasiparticle spectrum. For instance, the universality of the viscosity to entropy ratio in strongly coupled field theories has been recently revealed within the AdS/CFT duality [16]. This result is related to the universality of black branes QNMs in the hydrodynamic limit and it roughly agrees with experimental observations [17]. Furthermore, black holes non-trivially coupled to scalar and electromagnetic fields have been recently studied as holographic duals to superfluids and superconductors [18, 3]. For example, they are currently investigated as gravitational duals to real high-temperature superconductors [19, 20], which are not adequately explained by the standard theory of superconductivity. Further attempts of using holographic models of perturbed black holes to approach condensed matter systems include the Fermi gas at unitarity [21], non-Fermi liquids [22], strange metal regions of the cuprate superconductors and the quantum Hall effect.

Finally, perturbation theory allows us to compute the signal emitted in gravitational waves from astrophysical processes involving black holes. For instance, sun-like stars or stellar black holes infalling into, merging, or orbiting supermassive black holes emit a characteristic gravitational-wave signature, which will hopefully be detected by Ground-based gravitational-wave interferometers and by future planned space-based interferometers. Thus gravitational wave observations will incontrovertibly confirm or disprove our belief that ultracompact astrophysical objects possess an event horizon and are rotating black holes indeed [23]. A few years ago, the achievement of design sensitivity of the Large Interferomenter Gravitational-wave Observatory (LIGO) [24] marked the beginning of a new era in gravitational physics, as the advent of high-precision spectroscopy marked a new era in atomic physics during the 20th century. In spectroscopy a precise detection of the atomic radiation had provided us with spectacular confirmations of quantum mechanics and had drastically improved our present knowledge of quantum mechanical systems. Likewise, black holes are the most fundamental gravitational systems and can be regarded as "gravitational atoms", encoding the intimate origin of *geometrodynamics*. Therefore the detection of gravitational waves from black holes and other compact objects will push forward our present knowledge of gravitational phenomena to unprecedented levels. Furthermore, if the black hole picture turns out to be correct, future gravitational wave interferometers will allow to discriminate between black holes in different theories of gravity, thus confirming General Relativity or signaling possible high-energy completions of it. In fact the characteristic perturbations spectrum of an astrophysical object can be used to discriminate between black holes in different theories, but also to discern black holes from other ultra-compact objects [25]. This is a common approach in astrophysics: for example properties of matter inside neutron stars can be related to the specific gravitational signature associated to different equations of state [8].

All these applications constitute individual and active areas of research by themselves. Accordingly, we found it useful to divide the present work into three independent parts, which

are glued together by our common approach of investigation.

Part I is devoted to black holes in Anti de Sitter space and, in particular, to some applications related to black holes within the so called Anti de Sitter/Condensed Matter duality, a phenomenological extension of the AdS/CFT correspondence. In this framework we study phase transitions between different black hole solutions in Einstein-Maxwell dilaton gravity, and relate these to phase transitions in a strongly coupled quantum field theory, in which a scalar operator acquires a nonvanishing expectation value. The phase transition is related to the inset of an instability of Reissner-Nordström black holes towards scalar perturbations. We construct new numerical solutions describing dilatonic black branes with electric and magnetic charge and we describe their holographic properties using the Anti de Sitter/Condensed Matter duality. Electromagnetic perturbations of these solutions are holographically dual to the electrical and thermal conductivity in the boundary field theory and we find transport phenomena reminiscent of electron motion in real materials. Next we discuss characteristic oscillation frequencies of Schwarzschild black holes in Anti de Sitter. We develop a method to compute these complex frequencies numerically when their characteristic timescale is large. These long-lived modes presumably dominate the black hole response to perturbations, hence the thermalization timescale in the dual field theory. We conclude Part I by describing exact vortex solutions coupled to scalar fields in three-dimensional Anti de Sitter gravity.

Part II and III are devoted to more astrophysical – though purely theoretical – applications of black hole physics. Part II deals with the study of black holes in gravity theories beyond General Relativity and their astrophysical imprints. We focus on two of the most viable theories which correct the Einstein-Hilbert action by adding squared curvature terms: namely Dynamical Chern-Simons gravity [26] and Einstein-Dilatonic-Gauss-Bonnet gravity [27]. Both these theories arise as consistent truncations of string theory at low energies and introduce some scalar field, whose dynamics encodes modifications beyond General Relativity. We shall discuss black holes in these alternative theories as viable astrophysical candidates. Again our main approach is to compute the black hole response to gravitational perturbations and study its characteristic spectrum. We also discuss the signature emitted in gravitational waves from these objects. Such a signature can be a smoking-gun for strong curvature corrections beyond General Relativity and gives a characteristic imprint hopefully detectable by next gravitational wave interferometers.

In Part III we adopt a different point of view and we critically discuss the *black hole paradigm* with an open-minded approach. Motivated by the lacking of a definitive answer on the existence of astrophysical black holes, we shall discuss some other astrophysical objects, usually called *black hole mimickers*. These objects can truly mimick many properties of a black hole spacetime and they are indeed almost indistinguishable from a real black hole by means of electromagnetic measurements. Unlike black holes, these objects do not possess an event horizon. Thus their causal structure is intimately different from that of a black hole and this leaves a characteristic imprints in their gravitational perturbations spectrum, eventually having also an impact on their linear stability. We mainly focus on two representative candidates of black hole mimickers: static thin-shell gravastars [28] and superspinars [29]. For the first model we numerically prove linear stability against gravitational perturbations in a wide range of the parameter space. Then we discuss these objects as viable astrophysical candidates, showing that their quasinormal modes spectrum is completely different from that of a black hole. This also leaves a characteristic imprint in the gravitational waves emitted by a point-like particle orbiting the gravastar. This configuration is a good approximation of

a very common situation in astrophysics: a small star ($M \sim M_\odot$) orbiting a supermassive ($M \sim 10^6 M_\odot$) object [30]. We analyze this situation and contrast it with the analogous case with a black hole as supermassive central object. The power radiated in gravitational waves during the inspiral shows distinctive peaks corresponding to the excitation of the polar oscillation modes and providing a very specific signature of the horizonless nature of the central object. Finally, as for superspinars, we investigate their stability against gravitational perturbations and prove that they suffer from several instabilities. We discuss the implications of these instabilities for the Cosmic Censorship and conclude that superspinars cannot be viable astrophysical alternatives to black holes.

Generally speaking, this dissertation gives further confirmations of the prominent role played by black holes in modern physics. In particular, the investigation of black hole perturbations provides us with fundamental insights both in theoretical physics and in astrophysics. These modern applications were perhaps anticipated in John Archibald Wheeler's autobiography in 1998:

> *Black holes teach us that space can be crumpled like a piece of paper into an infinitesimal dot, that time can be extinguished like a blown-out flame, and that the laws of physics that we regard as 'sacred', as immutable, are anything but.*

Sitting on the shoulders of giants, we still have much to learn from this lesson.

Part I

Black holes in Anti de Sitter space

Chapter 1

Black holes and Anti de Sitter/Condensed Matter duality

1.1 A new approach to strongly coupled field theories

Unification plays a central role in physics. Newton's Law of Universal Gravitation, and modern astrophysics in turn, originated from the discovery that celestial and terrestrial objects are governed by the same dynamics. More recently, Maxwell equations provided a unified description of both electrical and magnetic phenomena. The concept of *spacetime* itself, *i.e.* the unification of two previously unrelated concepts such as the space and the time, was one of the major breakthroughs in Einstein's relativity. Historically unification processes in physics have never been mere superpositions of two previously disconnected phenomena. Indeed new and unexpected consequences emerge from the unified description. This is the case for electromagnetic waves in Maxwell theory, for General Relativity as relativistic theory of spacetime dynamics, or for the $W^{\pm}$ and Z^0 bosons as natural outcomes of the electroweak theory by Glashow, Weinberg and Salam.

So far, in this spasmodic search for unification principia, gravity has resisted all the attempts to include it in a unified theory of fundamental interactions. Although a definitive quantum theory of gravity is one of the most urgent goals in theoretical physics, nevertheless the very idea of unification has been revisited after one of the most important conceptual breakthroughs in theoretical physics of the late 1990s, the Anti de Sitter/Conformal Field Theory (AdS/CFT) correspondence [1]. Loosely speaking the AdS/CFT correspondence (also known as Maldacena conjecture) is a duality between a string theory defined in some Anti de Sitter space and a quantum field theory *without* gravity defined on the conformal boundary of this space. We will give a precise definition of the AdS/CFT correspondence in the next section, now focusing on some of its conceptual implications.

The AdS/CFT correspondence initiated several new lines of research both into quantum gravity and quantum field theories and nowadays it is one of the most active research areas in theoretical physics. Remarkably the AdS/CFT correspondence is a strong/weak coupling duality. In fact, as we briefly review in the next section, it maps the strong coupling regime of the gauge theory into the weak coupling (small curvature) regime of the string theory and viceversa. The duality also provides us with a new interpretation of energy scales in physics, suggesting a complementary approach to the quest for a "theory of everything", which should

possibly describe physics at any energy scale. In fact, the AdS/CFT duality establishes an equivalence between different regimes of two completely unrelated theories (even living in different number of dimensions!) which, in this approach, are actually regarded as the same theory as seen at different values of the coupling. Furthermore, if a quantum gravity theory is dual to a quantum field theory – wherein no notion of gravity exists – then the question of which is "more fundamental" is meaningless. Thus the AdS/CFT correspondence provides a revolutionary view of the fundamental laws of nature, in which the traditional classification of fundamental forces – hence their unification – is possibly an ill-posed question.

Despite its technicalities and its limited range of applications, the AdS/CFT correspondence is often regarded as the "tip of the iceberg": a new paradigm within which new hidden connections between gravity and quantum field theories can be investigated. In fact Maldacena duality was the first and more rigorous realization of a more general *holographic principle* for gravity, *i.e.* the idea that the number of local degrees of freedom in a gravity theory scales with the area enclosing a volume, and not with the volume itself [31, 32]. Remarkably, this idea originated from the black hole entropy formula [33], which is indeed proportional to the event horizon area, rather than to the black hole volume. Maldacena's conjecture motivates the intriguing expectation that the relation between string theory and quantum field theories or, more generically, the *gauge/gravity* duality [2] holds also when the (somehow restrictive) hypothesis of AdS/CFT correspondence are not fulfilled. In fact, following the original example of the AdS/CFT correspondence, many other dual theories have been discovered, including non-supersymmetric and non-conformal theories. With the same spirit more phenomenological realizations of the AdS/CFT correspondence are pursued vigorously. This is the case for the so-called Anti de Sitter/Condensed Matter (AdS/CM) duality. The AdS/CM program aims to develop effective and phenomenological models of AdS gravity, *i.e.* models not necessarily arising from consistent string theories, and to give a dual description of real condensed matter systems at strong coupling.

In fact, beside more fundamental and epistemological implications, condensed matter physics provides practical motivations to investigate the gauge/string duality. First, the traditional condensed matter paradigms are based on perturbative techniques and on a description in terms of weakly interacting quasiparticles. Nevertheless there are many strongly coupled systems, *e.g.* unconventional materials with strongly correlated electrons, that challenge usual perturbative approaches. In the AdS/CFT approach strongly coupled systems can be holographically related to classical gravity at relatively small curvatures, which is computationally much more tractable via standard methods. In this framework the AdS/CFT correspondence provides a unique approach to strong interactions and it will hopefully offer new insights into some aspects of strongly coupled condensed matter. Secondly, condensed matter systems can be engineered and investigated in detail in laboratories. Thus the AdS/CFT correspondence offers the fascinating perspective of feasible experimental tests of gravitational theories via their condensed matter duals. Theoretical concepts such as supersymmetries, conformal symmetries, couplings with scalar and non-abelian fields and so on, may have a precise description in terms of dual field theory and their imprints will eventually be tested in condensed matter experiments.

Finally, the correspondence also works in the opposite direction, *i.e.* it maps weakly coupled quantum field theories without gravity into quantum gravity theories in their full-fledged strong curvature regime. Although this topic is far to be well understood and is not covered in the present dissertation, it is nevertheless intriguing that new insights on quantum

gravity may eventually come from conventional condensed matter physics.

In the next section we shall give a concise definition of the AdS/CFT correspondence, whereas in Section 1.3 we shall discuss the prominent role of black holes and black hole perturbations within this holographic framework. For comprehensive discussions on the AdS/CFT correspondence and on holographic methods in condensed matter physics, we refer to some excellent reviews [2, 3, 34].

1.2 AdS/CFT correspondence in a nutshell

It is due to give a somehow more precise formulation of the ideas discussed in the previous section. For this purpose, here we briefly review the first and most studied example of gauge/string duality, involving $D = 4$, $\mathcal{N} = 4$ Yang-Mills theory and string theory in $AdS_5 \times S^5$.

The $\mathcal{N} = 4$ super Yang-Mills theory in $3 + 1$ dimensions contains a gauge field, four Weyl fermions and six scalars, all in the adjoint representation. For convenience its Lagrangian can be obtained by dimensional reduction from the more compact Lagrangian density for a $SU(N_c)$ gauge field and a 16 component Majorana-Weyl spinor in $D = 10$ dimensions,

$$\mathcal{L} = \frac{1}{2g_{\rm YM}^2}\mathrm{Tr}\left(F_{\mu\nu}F^{\mu\nu}\right) + i\mathrm{Tr}\left(\bar{\psi}\gamma^\mu D_\mu \psi\right) \ . \tag{1.1}$$

The six real scalar fields emerge from compactification of the extra six dimensions. The Yang-Mills coupling $g_{\rm YM}$ is exactly marginal and the theory is conformal at all couplings. From the gravity side we start by considering type IIB supergravity in $D = 10$ dimensions, containing two scalar fields, two 2-form potentials, a 4-form potential and fermionic supersymmetric partners [35]. Note that the spacetime geometry $AdS_5 \times S^5$ is a solution of this supergravity theory.

There are many arguments supporting the duality. As a first check, the symmetries of the gauge theory, $SO(4, 2)$ symmetry coming from conformal invariance and $SO(6)$ symmetry coming from rotation of the scalars arising from dimensional reduction, agree with those of $AdS_5 \times S^5$ and both theories have 32 supersymmetries. More importantly, it was shown that all linearized supergravity states have a precise description in terms of gauge theory states [36]. Nevertheless, in this specific theory, supergravity states map to a small subset of all the gauge theory states. This suggests that the gravity theory dual to $\mathcal{N} = 4$, $SU(N_c)$ gauge theory in four dimensions *contains* IIB supergravity, but it is actually a more general theory. In fact it was realized that the additional degrees of freedom correspond to the excited states of strings. In this sense, string theory (and hence gravity) *emerges* as natural consequence of the gauge theory. Thus a precise statement of the duality, as originally conjectured by Maldacena [1] is the following:

> *$\mathcal{N} = 4$ supersymmetric $SU(N_c)$ gauge theory in four dimensions is equivalent to type IIB string theory with $AdS_5 \times S^5$ boundary conditions.*

In his original argument Maldacena considered a stack of N_c $D3$-branes, whose coupling to gravity is parametrized by the string coupling g_s. The branes backreact with the spacetime and the dimensionless parameter $g_s N_c$ parametrizes the distortion of the metric. When $g_s N_c \gg 1$ the backreaction dominates and the spacetime describes an extremal black three-brane, whose

near-horizon geometry is $AdS_5 \times S^5$. In the low energy limit, and when $g_s N_c \gg 1$, string states near the horizon decouple. In the same low energy limit, a similar decoupling occurs when $g_s N_c \ll 1$ for excitations of the three-branes, which are described by $U(N_c) = SU(N_c) \times U(1)$ gauge theory. Maldacena conjectured that the decoupled sectors of the low energy limit, *i.e.* the gauge theory at small string coupling and $AdS_5 \times S^5$ closed string theory at large string coupling, can be actually regarded as the same theory as seen at different values of the coupling. Notice that the radial coordinate of the bulk spacetime plays the role of the energy scale in the gauge theory, with the boundary at infinity corresponding to the ultraviolet regime. The precise relation between the parameters of these two theories reads

$$L = \ell_s g_{\rm YM} N_c^{1/4} \,, \tag{1.2}$$

where L is the AdS radius, ℓ_s is related to string tension μ by $\mu^{-1} = 2\pi\ell_s^2$, the Yang-Mills coupling $g_{\rm YM}$ is related to the string coupling by $g_{\rm YM}^2 = 4\pi g_s$ and N_c is the number of colors. Notice that when the *'t Hooft coupling* [37] is large, $g_{\rm YM}^2 N_c \gg 1$, then $L \gg \ell_s$, *i.e.* the spacetime curvature is small in string units. In the large 't Hooft coupling limit the gauge theory remains strongly coupled and is not describable in terms of quasiparticles. Nevertheless its gravitational dual is the small coupling limit of the string theory, which is well approximated by IIB supergravity (in the t' Hooft limit quantum corrections due to graviton loops are suppressed). Although the full quantum string theory is poorly understood, its low energy approximations, *i.e.* supergravity theories, have been extensively studied and can be controlled via classical methods. This explains the appealing strong/weak coupling nature of the duality, mentioned in the previous section.

Finally, we mention that although a rigorous proof of the AdS/CFT equivalence is still lacking, during the last decade the correspondence survived several non-trivial tests [2] and, presently, there is very little doubt that the conjecture is valid. Indeed, some hold the view that a rigorous proof, though urgent, will be rather technical and it will probably not provide any further insights into the physical picture arising from the conjecture.

1.2.1 Basic AdS/CFT dictionary and recipes

A more detailed discussion on the AdS/CFT correspondence is beyond the scope of the present dissertation. However, for later convenience, it is useful to give the prescription for the bulk partition function and for correlation functions of boundary operators in the gauge theory [1, 38, 36]. According to the gravity/gauge duality, the boundary value ϕ_0 of a bulk field Φ is identified with a source that couples to a gauge invariant boundary operator $\mathcal{O}_\Phi$. The on-shell bulk partition function is related to the generating functional of the gauge theory correlation functions via

$$Z_{\rm string} \simeq Z_{\rm SUGRA}[\phi_0] = \int_{\Phi\sim\phi_0} D\Phi\, e^{-S[\Phi]} \equiv Z_{\rm QFT}[\phi_0] = \langle e^{i\int_{\partial{\rm AdS}} d^{D-1}x\,\phi_0\mathcal{O}_\Phi}\rangle_{\rm QFT} \,, \tag{1.3}$$

where $Z_{\rm string}$ and $Z_{\rm SUGRA}$ are the D-dimensional string and supergravity partition functions, S is the supergravity action, ∂AdS is the boundary of the asymptotically AdS space in $D-1$ dimensions and $\langle\cdot\rangle_{\rm QFT}$ is the expectation value of a given quantity over the quantum field theory path integral. In the Eq. (1.3), $\simeq$ stands for the semiclassical (low-energy) approximation and $\equiv$ means that field theory correlators can be effectively computed by differentiating the

on-shell supergravity action $S_{\text{o.s.}}$ as follows

$$\langle \mathcal{O}(x) \rangle = \left. \frac{\delta S_{\text{o.s.}}}{\delta \phi_0(x)} \right|_{\phi_0=0} , \tag{1.4}$$

$$\langle \mathcal{O}(x_1) ... \mathcal{O}(x_n) \rangle = (-1)^{n+1} \left. \frac{\delta^n S_{\text{o.s.}}}{\delta \phi_0(x_1) ... \delta \phi_0(x_n)} \right|_{\phi_0=0} . \tag{1.5}$$

Schematically, the correspondence is illustrated in Table 1.1, where we also list some entries of the AdS/CFT dictionary which will be discussed in the next sections.

Table 1.1: Schematic AdS/CFT dictionary. See Ref. [39] and Section 1.3 for details.

Gravitational bulk		**Boundary gauge theory**
dynamical field Φ	$\leftrightsquigarrow$	gauge invariant operator $\mathcal{O}$
graviton g_{ab}	$\leftrightsquigarrow$	stress-energy tensor $T^{\mu\nu}$
Maxwell field A_a	$\leftrightsquigarrow$	global current J^μ
scalar field ϕ	$\leftrightsquigarrow$	scalar operator $\mathcal{O}_S$
fermionic field Ψ	$\leftrightsquigarrow$	fermionic operator $\mathcal{O}_F$
gauged symmetry	$\leftrightsquigarrow$	global symmetry
AdS black hole	$\leftrightsquigarrow$	thermal quantum field theory
black hole quasinormal modes	$\leftrightsquigarrow$	poles of retarded correlators

1.3 Holographic properties of AdS black holes

Black holes reveal the intimate connection between gravity, quantum mechanics and statistical mechanics. This connection is encoded in the laws of black hole thermodynamics [33]. The Hawking temperature of a Schwarzschild black hole in physical units reads

$$T_H = \frac{\hbar c^3}{8\pi G k_b M} , \tag{1.6}$$

where M is the black hole mass and the formula above contains most of the fundamental physical constants: the Planck constant $\hbar$, the speed of light c, Newton constant G and Boltzmann constant k_b. These constants govern the quantum, gravitational and thermodynamical realms, respectively. Thus it is clear that black holes can help in understanding the overlapping region of these theories and must play a prominent role in the framework of quantum gravity.

Black hole thermodynamics has a natural interpretation within the AdS/CFT duality. The gauge theory described in the previous section, whose holographic dual is asymptotically $AdS_5 \times S^5$, is a quantum field theory at zero temperature. However in several situation we wish to describe quantum field theories at finite temperature. This is the case in Big Bang cosmology for the quantum chromodynamics phase transition at $T \sim 200$ MeV, where a hot gas

of quarks and gluons, the so-called *quark-gluon plasma*, turned into a gas of hadrons. Recent experiments at the Relativistic Heavy Ion Collider (RHIC) aim to reproduce those extreme primordial conditions and to supply further confirmations for the quark-gluon plasma.

Temperature introduces an energy scale T which breaks the conformal invariance. Among other reasons, this makes finite-temperature field theories difficult to compute with standard field theory techniques, even at weak coupling. Thus it is remarkable that a holographic description of strongly coupled gauge theories at finite temperature is not essentially more intricate than that of zero temperature theory: it only involves classical bulk field dynamics in curved spacetime. It is then natural to consider black holes in the bulk and to associate the Hawking temperature to the temperature of the boundary field theory at equilibrium. Equivalently, a black hole can be regarded as the gravitational dual to a hot gas of gauge bosons, scalars and fermions, which are the degrees of freedom of the gauge theory. We shall now discuss this issue in some more detail.

Following the framework discussed in the previous section we consider a Schwarzschild black hole in AdS_5 spacetime, whose metric reads (hereafter we use Planck units, $c = G = \hbar = k_b = 1$)

$$ds^2 = -f(r)dt^2 + f(r)^{-1}dr^2 + r^2 d\Omega_3\,, \qquad f(r) = ds^2 = 1 - \frac{r_0^2}{r^2} + \frac{r^2}{L^2}\,, \tag{1.7}$$

where $d\Omega_3$ is the angular line element, L is the AdS radius and r_0 is a parameter related to the black hole mass. The Hawking temperature of this black hole reads

$$T_H = \frac{L^2 + 2r_H^2}{2\pi r_H L^2}\,, \tag{1.8}$$

where the horizon radius r_H is defined as the largest root of $f(r_H) = 0$. For large ($r_H \gg L$) AdS black holes $T_H \sim r_H/L^2$, whereas for large Schwarzschild black holes in asymptotically flat spacetime Eq. (1.6) gives $T_H \sim 1/r_H$.

Furthermore the entropy of a black hole is remarkably proportional to its area, A, rather than to its volume, as one could expect [33]. This remarkable behavior had inspired 't Hooft's holographic principle [31, 32]. The entropy of the Schwarzschild-AdS_5 black hole reads

$$S_{\rm BH} = \frac{A}{4} \sim \frac{r_H^3 L^5}{g_s^2 \ell_s^8} \sim \frac{T_H^3 L^{11}}{g_s^2 \ell_s^8} \sim N_c T_H^3 L^3\,, \tag{1.9}$$

where we have used Eq. (1.2) in the last step. Remarkably, the entropy $S_{\rm BH}$, computed in a purely gravitational framework, agrees with the field theory entropy $S_{\rm YM}$ at weak coupling. In fact in this regime we have order N_c^2 degrees of freedom on a three sphere of radius L at temperature T_H and by simple dimensional analysis we expect

$$S_{\rm YM} =\sim N_c T_H^3 L^3\,. \tag{1.10}$$

The correspondence between black holes and thermal gauge theories include also dynamical aspects. One of the most relevant examples is the holographic description of the celebrated Hawking-Page transition for black holes in AdS [40]. Below a critical temperature $T \sim 1/L$, Schwarzschild-AdS black holes undergo a phase transition toward a (energetically favored) gas of particle in AdS. In the gauge field side, $\mathcal{N} = 4$ gauge theory on S^3 has an analog confinement/deconfinement transition [36]. Other recent developments of the black hole/thermal gauge theory duality are reviewed below.

1.3.1 Black hole quasinormal modes and AdS/CFT correspondence

Being dual to strongly coupled gauge theories at finite temperature, black holes in AdS have a fundamental role in the gauge/gravity duality and they are widely investigated as *theoretical laboratories*, where our present understanding of the holographic correspondence can be challenged. At the very least, the study of AdS black holes will provide useful theoretical insights on strongly coupled field theories and their relation to quantum gravity. However, as we briefly discuss in the remaining of this chapter, there is the ambitious expectation that gravitational duals to *real world* condensed matter systems could be eventually discovered.

In this framework black hole characteristic oscillations play a crucial role, being holographically related to the linear response of the gauge theory at equilibrium. More precisely, black hole quasinormal modes in the bulk are related to the poles of the retarded correlation function of the corresponding field theory operator (see Refs. [9, 15] for a review). Indeed let us consider a small perturbation of the bulk field, $\Phi = \Phi_0 + \delta\Phi(t, r, \mathbf{x})$. The asymptotic behavior is given by the linearized equations of motion and by imposing purely ingoing waves at the horizon. Typically, the Fourier transform of $\delta\Phi(t, r, \mathbf{x})$ at infinity reads

$$\delta\Phi(\omega, r, k) \to \frac{\mathcal{A}(\omega, k)}{r^{\Delta_-}} + \frac{\mathcal{B}(\omega, k)}{r^{\Delta_+}}, \quad r \to \infty, \tag{1.11}$$

where the frequency ω is the Fourier transform variable (assuming a time dependence $\delta\Phi \sim e^{-i\omega t}$), whereas $k = |\mathbf{k}|$ is the magnitude of the momentum. In the AdS/CFT correspondence Δ_- and Δ_+ are related to the conformal dimension of the boundary operator $\mathcal{O}_\Psi$ and they depend on the spin of the bulk field Φ, on its mass and on the number of spacetime dimensions. Black hole quasinormal modes are complex frequencies satisfying a pair of causally-motivated boundary conditions: the corresponding eigenfunctions describe purely ingoing waves at the horizon and purely outgoing waves at infinity (a more detailed discussion on black hole quasinormal modes in AdS is given in Chapter 4). In Eq. (1.11), quasinormal modes are solutions of $\mathcal{A}(\omega_{\rm QNM}, k) = 0$. On the gauge theory side, the retarded Green's function of the operator $\mathcal{O}_\Psi$, computed by applying the AdS/CFT prescription, reads [41]

$$G^R(\omega, k) \sim \frac{\mathcal{B}(\omega, k)}{\mathcal{A}(\omega, k)} + \text{contact terms}, \tag{1.12}$$

thus it is clear that the poles of the retarded correlator are exactly the quasinormal frequencies $\omega_{\rm QNM}$ (see however Ref. [9] and references therein for some subtleties). Poles of thermal correlators encode important informations about the near-equilibrium behavior of a thermal field theory. For example they are related to transport coefficients and excitation spectra of the boundary theory.

The rest of this chapter is devoted to briefly review some recent topics of black hole physics within the AdS/CM duality, with special care given to the role of black hole perturbations. In particular in Section 1.3.2 we review the universal shear viscosity to entropy ratio for holographic plasma [16] and in Section 1.3.3 we discuss a basic model of holographic superconductor [42]. For completeness, we mention that fermionic perturbations of charged black holes, which are dual to boundary fermionic operators, are currently investigated as strongly coupled analogues of Fermi surfaces [43]. Further attempts to use holographic models of perturbed black holes to approach condensed matter systems include the Fermi gas at unitarity [21], non-Fermi liquids [22], strange metals and the quantum Hall effect.

1.3.2 Quark-gluon plasma via holography

Black holes are known to share many properties with dissipative systems (see, *e.g.* the black hole membrane paradigm [44]). This also agrees with their holographic description, since a hot gauge theory is obviously a dissipative system. It is therefore interesting to analysis hydrodynamic quantities such as the shear viscosity. Quite remarkably, AdS/CFT calculations of shear viscosity in strongly coupled field theories are in good numerical agreement with real features of the quark-gluon plasma observed at the RHIC, see Ref. [17] for a review. This result is notable because standard condensed matter computations, which are difficult to perform in strongly coupled field systems, fail to reproduce the observed properties of the quark-gluon plasma.

Long wavelength dynamics of quantum field theories can be described by the hydrodynamic regime [16]. In this regime the Kubo's formula allows to compute the shear viscosity,

$$\eta = -\lim_{\omega\to 0}\frac{G^R_{xy,xy}(\omega,\mathbf{0})}{\omega}\,, \tag{1.13}$$

from the usual retarded Green's function for the energy momentum $T^{\mu\nu}$,

$$G^R_{xy,xy}(\omega,\mathbf{0}) = \int dtd\mathbf{x}e^{i\omega t}\theta(t)\langle[T_{xy}(t,\mathbf{x}),T_{xy}(0,\mathbf{0})]\rangle\,, \tag{1.14}$$

where $\theta(t)$ is the step function and $\{x,y\}$ are the spacial (flat) directions in the boundary theory. In the low-momentum limit, $k\to 0$, the retarded Green's function has a "shear" pole at

$$\omega_S = -i\frac{\eta}{\epsilon+P}k^2\,,\quad k\to 0 \tag{1.15}$$

where ϵ and P are the plasma energy and pressure respectively. The Green's function (1.14) can be computed by applying the AdS/CFT correspondence. The correlator for T_{xy} are related to the fluctuations δg_{xy} of the background metric. In the small frequency and small momentum limit the perturbation equation for δg_{xy} on a black brane background can be solved analytically [45] and the shear viscosity can be extracted from the form of shear mode (1.15). The famous result is written in term of shear viscosity to entropy density ratio as

$$\frac{\eta}{s} = \frac{1}{4\pi} + \mathcal{O}\left[\left(g^2_{\rm YM}N_c\right)^{-3/2}\right]\,,\quad g^2_{\rm YM}N_c \gg 1 \tag{1.16}$$

where $s = S/V$ is the entropy density and S is the black brane entropy, analog to (1.9). The ratio above is interesting for several reasons. First, to leading order in the 't Hooft coupling, it is a universal result [16]. This follows directly from the relation between graviton absorption cross section and the imaginary part of the Green's function (1.14). Curiously, the same ratio (1.16) has been also obtained in membrane paradigm hydrodynamics, without invoking the holographic correspondence. Secondly, the ratio (1.16) is order one, which implies that all quantum field theories with gravitational duals are strongly coupled. As mentioned in Sect. 1.3.2, this is the case for quark-gluon plasma possibly created in heavy ion collisions. Remarkably, experimental results roughly agree with the AdS/CFT value (1.16) [17].

1.3.3 Holographic superconductors

Phase transitions are a central concept in physics. Usually they occur in the weak coupling regime and involve quasiparticle, pair mechanisms, etc... This is the case for standard superconductors, phenomenologically described by Landau-Ginzburg theory and by Bardeen, Cooper and Schrieffer (BCS) theory at microscopic level. However unconventional materials, such as high-temperature cuprate superconductors, are not adequately explained by BCS theory. Although there is evidence that Cooper pairs still form in these materials, the pairing mechanism is not well understood since, unlike BCS theory, strongly coupled electrons are involved in the condensation mechanism.

Being strongly coupled theories, high-temperature superconductors are natural arenas for the gauge/gravity duality. Indeed a gravitational dual to a strongly coupled superconductor has been recently formulated [19] (see also Ref. [42] for a review). The main ingredient of a superconductor is a charged operator, which acquires a non-vanishing expectation value below a critical temperature T_c and, in the simpler case, breaks an $U(1)$ symmetry. The underlying field theory is usually at finite chemical potential. The holographic correspondence discussed above suggests that, from the bulk perspective, a charged black hole develops a charged "hair" when the Hawking temperature $T < T_c$. The minimal toy Lagrangian describing this configuration is

$$\mathcal{L} = R + \frac{6}{L^2} - \frac{1}{4}F^2 - |\nabla\Psi - iqA\Psi|^2 - m^2\left|\Psi^2\right|\,, \tag{1.17}$$

which is Einstein-Maxwell gravity in Anti de Sitter with a scalar field minimally coupled to the Maxwell potential. The charge and the mass of the scalar field are denoted by q and m respectively. The Reissner-Nordström-AdS (AdS-RN) black hole is solution of the equations of motion stemming from the Lagrangian above. Nevertheless, for sufficiently large values of q and sufficiently low temperature, the AdS-RN black hole is unstable toward scalar perturbations [46]. This can be easily understood by noting that the scalar field Ψ acquires an effective mass

$$m_{\text{eff}}^2 = m^2 + q^2 g^{00} A_0^2\,, \tag{1.18}$$

whose second term is negative near the horizon and contributes with a tachyonic mode, eventually destabilizing the scalar field. In Chapter 2, using neutral scalar fields, we shall discuss a different mechanism to make AdS-RN black holes unstable.

As a consequence of the instability, the AdS-RN black hole develops a scalar hair, which breaks the $U(1)$ symmetry of the Lagrangian (1.17). In the gravitational bulk, depending on the mass m and on the number of dimensions, the scalar field has a specific behavior at infinity, which is holographically related to the conformal dimension of the dual operator (cf. Eq. 1.11). The expectation value of the scalar operator as a function of the temperature shows the typical mean-field behavior of second order phase transitions [19, 47]. This arises from the large 't Hoof limit, which suppresses quantum fluctuations in the gravity theory and allows the latter to be treated semiclassically.

Furthermore, the more striking feature of a superconductor, *i.e.* the infinity DC conductivity, naturally emerges in this holographic framework. In fact, once again transport coefficients can be computed via the AdS/CFT correspondence by perturbing specific bulk fields. In this case, by studying electromagnetic perturbations, one can computed the retarded Green's function. The conductivity is then easily obtained in terms of the asymptotic behavior of the Maxwell perturbations, as explained in detail in Chapter 2 (cf. Section 2.5).

The DC conductivity turns out to be infinite, whereas the AC conductivity shows the typical frequency gap observed in real superconductors. Remarkably, for several holographic superconductor models, the gap frequency $\omega_g/T_c \sim 8$. This value is larger than the corresponding BCS value ($\omega_g/T_c = 3.5$) and it roughly agrees with the experimental gap observed in real high-temperature superconductors.

Summary of subsequent chapters

Here we briefly introduce the topics that we shall explore in detail in Chapters 2, 3, 4 and 5. In Chapter 2 we shall discuss new phase transitions between charged black holes in AdS and construct their holographic duals. In the new phase, we shall investigate scalar and electromagnetic perturbations, relating the former to the onset of the transition and the latter to transport coefficients in the dual field theory. From the holographic perspective, we shall discuss in detail how the condensation of a neutral scalar operator can affect transport properties, such as the electrical conductivity in the boundary theory. Some of the behaviors that we observe in our numerical simulations are reminiscent of electron motion in real materials. For instance the electrical AC conductivity as a function of the frequency shows a typical "Drude peak" at small frequency and, in some cases, the resistivity as a function of the temperature shows a non-monotonic behavior reminiscent of the celebrated Kondo effect. In Chapter 3 we shall generalize these results to the case of dyonic black holes. Correspondingly, in the dual field theory a magnetic field is turned on and we discuss how this affects the phase transition and the trasport properties.

Interestingly, it turns out that, in several situations involving AdS black holes, some specific quasinormal modes become purely real in the regime of interest [39]. The imaginary part of the frequency for a perturbation $\delta\Psi \sim e^{-i\omega t}$ is related to the system response to small solicitations. In fact characteristic perturbations whose frequency has negative imaginary part are damped, i.e. $\delta\Psi \sim e^{-t/\tau}$, where $\tau = |\mathrm{Im}(\omega)|^{-1}$ is the characteristic damping time. Black holes are stable against this class of perturbations, at least at linear level. However, a positive imaginary part signals a perturbation which grows exponentially, $\delta\Psi \sim e^{t/\tau}$. In this case $\tau = \mathrm{Im}(\omega)^{-1}$ is the characteristic instability timescale. After an amount of time of order τ, the small perturbations grows in such a way that its backreaction to the metric is not negligible and it will drastically modify the background metric beyond the linear level. Therefore a vanishing imaginary part of the characteristic frequency signals a marginal stability of the black hole and in turn, a dual theory which is marginally stable. This can mark the critical point of a phase transition, which is relevant both for holographic superconductors and for dilatonic black holes discussed in Chapters 2 and 3. In both cases AdS-RN black holes are unstable against scalar perturbations below a critical temperature T_c. When $T \lesssim T_c$ the imaginary part of the characteristic frequency is small and positive, thus signaling the inset of an instability. On the other hand, as previously mentioned, (stable) quasinormal modes close to the real axis appear in the hydrodynamic limit of quantum field theories and they are relevant for the computation of the shear viscosity in holographic plasma [39]. Thus characteristic frequencies approaching the real axis (both from above and from below) are relevant in a variety of problems within the gauge/string duality.

Due to the importance of quasi-real characteristic frequencies of AdS black holes, in Chapter 4 we develop a numerical method to compute stable long-lived quasinormal modes of Schwarzschild-AdS black holes. These are characteristic frequency whose imaginary part is

much smaller than the real part, hence they characteristic timescale τ is large and indeed they are expected to dominate the thermalization in the boundary field theory.

Finally in Chapter 5 we conclude this part of the thesis by discussing vortex black hole solutions in three-dimensional AdS gravity. Due to the benefit of the three-dimensional field equations, the coupling between AdS black holes and scalar fields can be investigated analytically. In fact we find exact solutions describing vortex-black holes coupled to scalar fields. The vortex interpolates between two AdS_3 geometries with different AdS lengths. In the AdS/CFT language this means that these non-trivial configurations interpolate between two bidimensional CFTs with different central charges.

Chapter 2

Phase transitions between Reissner-Nordström and dilatonic black holes in 4D AdS spacetime

We study Einstein-Maxwell-dilaton gravity models in four-dimensional anti-de Sitter (AdS) spacetime which admit the Reissner-Nordström (RN) black hole solution. We show that below a critical temperature the AdS-RN solution becomes unstable against scalar perturbations and the gravitational system undergoes a phase transition. We show using numerical calculations that the new phase is a charged dilatonic black hole. Using the AdS/CFT correspondence we discuss the phase transition in the dual field theory both for non-vanishing temperatures and in the extremal limit. The extremal solution has a Lifshitz scaling symmetry. We discuss the optical conductivity in the new dual phase and find interesting behavior at low frequencies where it shows a "Drude peak". The resistivity varies with temperature in a non-monotonic way and displays a minimum at low temperatures which is reminiscent of the celebrated Kondo effect.

Contents

2.1 Introduction

The AdS/CFT correspondence [1] provides a deep connection between quantum gravity and quantum gauge theories. When the classical gravity approximation is reliable, it also provides efficient techniques for the computation of the thermodynamical and transport properties of strongly interacting quantum field theories. This holographic approach has been applied both

to gauge theories similar to QCD [16, 48] and, more recently, to condensed matter phenomena [49, 18, 3, 50]. It relies on the identification between the black hole solutions of the bulk theory and the thermal states of the boundary theory. Transport coefficients can be computed at strong coupling by solving the equations governing small perturbations of the black hole background [41].

In the attempt of developing a gravitational description for condensed matter phenomena one is primarily interested in finding black hole solutions that can capture the salient features of realistic many-body systems and in studying the corresponding phase diagram. The existence and the stability properties of a given solution depend on the field content and on the couplings of the bulk action. As an illustration of this point let us consider the simplest example, relevant for the holographic description of systems at finite temperature and charge density. The minimal bulk theory is in this case Einstein-Maxwell theory and the only static charged black hole solution is the AdS-Reissner-Nordström (AdS-RN) black hole [51]. The solution remains stable as we lower the temperature and the ground state of the system corresponds to the extremal AdS-RN black hole. If we include in the action a charged scalar field with a minimal coupling to the gauge field, below a critical temperature new branches of solutions appear which are thermodynamically favored. The resulting instability of the AdS-RN black hole provides a holographic description of a phase transition in the dual theory [52, 47, 19]. Below the critical temperature the new solution is a static charged black hole with a scalar hair. The non-trivial profile of the scalar field corresponds to a charged condensate in the dual theory that breaks spontaneously a global $U(1)$ symmetry. One then expects to observe in the new phase phenomena typical of superfluid or superconducting systems and this is confirmed by the study of the linearized response of the hairy black hole to small perturbations [47, 19].

Most investigations considered so far only the case of scalar fields minimally coupled to the electromagnetic field. Relatively little is known about the stability of the AdS-RN solution in non-minimally coupled models (Einstein-Maxwell-dilaton gravity). Non-minimal couplings of the form $f(\phi)F^2$ between a scalar fields ϕ and the Maxwell tensor are very common in supergravity and in the low-energy effective action of string theory models. In flat spacetime charged black holes solutions of Einstein-Maxwell-dilaton gravity are well-known [53, 54, 55]. These solutions involve a non-constant scalar field and differ significantly from the RN black hole since there is no inner horizon and the event horizon becomes singular in the extremal limit. Examples of charged dilaton black hole solutions with AdS asymptotics are provided by the family of four-charge black holes in $\mathcal{N} = 8$ four-dimensional gauged supergravity [56]. As shown in [57] in the extremal limit these black holes can support an isolated fermion normal mode which signals the presence of a Fermi surface in the dual systems. Quite interestingly the AdS-RN black hole is not a solution of dilaton gravity models with $f = \exp(a\phi)$.

In this chapter we shall consider models where the coupling between the scalar field and the kinetic term of the gauge field starts quadratically. We first investigate the stability of the AdS-RN black hole under scalar perturbations and show that it becomes unstable below a critical temperature. In flat space this kind of instability was studied in [58]. In [59] it was found that the AdS-RN black hole in $\mathcal{N} = 8$ four-dimensional gauged supergravity is unstable against fluctuations involving a scalar and four gauge fields. In [60] a similar instability was found studying scalar fluctuations around a dyonic black hole in order to compute the momentum relaxation time scale induced by the presence of impurities.

In our models AdS-RN and dilaton black holes can coexist. Below a critical temperature the AdS-RN solution undergoes a phase transition toward a new solution, which is a hairy

black hole solution. Following closely the approach of [47, 19] we will construct numerically the hairy black hole solutions. In order to clarify the behavior of the model at low temperatures we will also study the extremal solution. The near horizon form is characterized by a Lifshitz scaling isometry [61] and is a simple generalization of the solution found in [62].

In the new phase a neutral scalar operator acquires a non-vanishing expectation value. The condensate modifies the transport properties of the system in an interesting way. This is clearly illustrated by the behavior we find for the optical conductivity at small frequencies and non-vanishing temperatures: there is a minimum and then the conductivity increases until it reaches a value which can be much higher than the constant value at high frequencies. We can understand this fact by rewriting the equation for the vector fluctuations as a Schrödinger equation [63]. The non-minimal coupling between the scalar and the gauge field induces a term in the potential that is not positive definite. A similar behavior was recently observed in models where the Born-Infeld action of a probe brane is coupled to a geometry with a Lifshitz scaling symmetry [22].

Another interesting feature of the new phase is the fact that the resistivity does not increase monotonically with the temperature but displays a minimum. A similar behavior of the resistivity is observed in metals containing magnetic impurities, an effect explained by Kondo as resulting from the interaction between the magnetic moment of the conduction electrons and the impurity.

The plan of this chapter is as follows. In Section 2.2 we present our model and discuss the stability of the AdS-RN black hole against scalar perturbations, providing approximate criteria to identify the region in parameter space where an instability is likely to occur. In Section 2.3 we construct numerically the charged black hole solutions with a neutral scalar hair and show that they are thermodynamically favored. In Sec. 2.4 we give the analytic form of the near-horizon solution for the extremal and near-extremal black holes. In Section 2.5 we analyze the optical conductivity in the new phase of the dual field theory described by the dilaton black hole. In Sec. 2.6 we present our conclusions.

2.2 Instability of AdS-RN black holes in Einstein-Maxwell-dilaton gravity

In this chapter we consider Einstein gravity coupled to an abelian gauge field A_μ and a real scalar field ϕ. The Lagrangian

$$\mathcal{L} = R - \frac{f(\phi)}{4}F^2 - \frac{1}{2}\partial^\mu\phi\partial_\mu\phi - V(\phi)\,, \tag{2.1}$$

depends on the choice of two functions, a potential $V(\phi)$ and a function $f(\phi)$ that couples the scalar to the kinetic term of the gauge field. Lagrangians of this type are common in supergravity and in the low-energy limit of string theory models. The equations of motion read

$$\begin{aligned}
&\nabla_\mu\left(f(\phi)F^{\mu\nu}\right) = 0\,,\\
&\nabla^2\phi = \frac{dV(\phi)}{d\phi} + \frac{df(\phi)}{d\phi}\frac{F^2}{4}\,,\\
&R_{\mu\nu} - \frac{1}{2}g_{\mu\nu}R = -\frac{f(\phi)}{2}\left(F_{\mu\rho}F^{\rho}{}_{\nu} + \frac{g_{\mu\nu}}{4}F^{\rho\sigma}F_{\rho\sigma}\right) + \frac{1}{2}\left(\partial_\mu\phi\partial_\nu\phi - \frac{g_{\mu\nu}}{2}\partial^\rho\phi\partial_\rho\phi\right) - \frac{g_{\mu\nu}}{2}V(\phi)\,.
\end{aligned} \tag{2.2}$$

We shall restrict the possible choices of $V(\phi)$ and $f(\phi)$ by imposing two requirements. The first is that the potential $V(\phi)$ admits stable AdS vacua. Assuming for simplicity that there is only one extremum at $\phi = 0$, the potential can be expanded for small values of the field as

$$V(\phi) = -\frac{6}{L^2} + \frac{\beta}{2L^2}\phi^2 + \mathcal{O}(\phi^3)\,, \tag{2.3}$$

where L is the AdS radius and β parametrizes the mass of the field, $m^2L^2 = \beta$. The AdS vacuum is stable if the mass parameter satisfies the Breitenlohner-Freedman (BF) bound $\beta \geq -9/4$ [64]. In the following we will limit our discussion to quadratic potentials and to potentials of the form $V(\phi) = -2W_0\cosh(b\phi)$. In the latter case $L^2 = 3/W_0$, $\beta = -6b^2$ and the BF bound becomes $b^2 \leq 3/8$.

The second requirement is that the AdS-RN black hole is a solution of the equations (2.2). This is the case if the first derivative of the coupling function vanishes at the extremum of V, $\frac{df}{d\phi}(0) = 0$. For small values of the field the function f can be expanded as

$$f(\phi) = 1 + \frac{\alpha}{2}\phi^2 + \mathcal{O}(\phi^3)\,, \tag{2.4}$$

where the parameter α is assumed to be non-negative. In the following we will consider mainly quadratic coupling functions and functions of the form $f(\phi) = \cosh(a\phi)$ for which $\alpha = a^2$. In our analysis of the zero temperature limit of the hairy black hole solutions in Section 2.4 we will also consider exponential coupling functions.

We will look for static electrically charged solutions of the equations of motion with translational symmetry in two spatial directions. The metric can be written as

$$ds^2 = -g(r)e^{-\chi(r)}dt^2 + \frac{dr^2}{g(r)} + r^2(dx^2 + dy^2)\,. \tag{2.5}$$

The scalar field is $\phi = \phi(r)$ and only the temporal component of the gauge potential is non-vanishing, $A_0 = A_0(r)$. The equations of motion become

$$\phi'' + \left(\frac{g'}{g} - \frac{\chi'}{2} + \frac{2}{r}\right)\phi'(r) - \frac{1}{g}\frac{dV}{d\phi} + \frac{{A_0'}^2 e^{\chi}}{2g}\frac{df}{d\phi} = 0\,, \tag{2.6}$$

$$(r^2 e^{\frac{\chi}{2}} f(\phi) A_0')' = 0\,, \tag{2.7}$$

$$\chi' + \frac{r\phi'^2}{2} = 0\,, \tag{2.8}$$

$$\frac{\phi'^2}{4} + \frac{{A_0'}^2 e^{\chi} f(\phi)}{4g} + \frac{g'}{rg} + \frac{1}{r^2} + \frac{V(\phi)}{2g} = 0\,, \tag{2.9}$$

where here and in the following a prime will always denote a derivative with respect to r. When the condition (2.4) is satisfied, the equations of motion admit the AdS-RN black hole solution

$$g = -\frac{2M}{r} + \frac{Q^2}{4r^2} + \frac{r^2}{L^2}\,, \qquad \chi = 0\,, \qquad A_0 = \frac{Q}{r} - \frac{Q}{r_h}\,, \qquad \phi = 0\,, \tag{2.10}$$

where M and Q are respectively the mass and the electric charge of the black hole and r_h the radius of the horizon. The black hole temperature is

$$4\pi T_{RN} = \frac{3r_h}{L^2} - \frac{Q^2}{4r_h^3}\,, \tag{2.11}$$

and the solution becomes extremal for $12r_h^4 = Q^2L^2$.

Let us now discuss the stability of the AdS-RN solution (2.10) against small perturbations of the scalar field. Given the planar symmetry of the solution, we can expand the scalar perturbation in Fourier modes

$$\phi_{\omega,\vec{k}} = \frac{R(r)}{r} e^{i(k_1 x + k_2 y - \omega t)} \,. \tag{2.12}$$

The radial function R solves the following equation

$$g^2 R'' + g g' R' + \left[\omega^2 - V\right] R = 0\,, \qquad V = g\left[\frac{\vec{k}^2}{r^2} + \frac{g'}{r} + m_{\text{eff}}^2\right] , \tag{2.13}$$

where we have introduced an effective mass

$$m_{\text{eff}}^2(r) = m^2 - \frac{\alpha}{2} A_0'(r)^2 \,. \tag{2.14}$$

In the presence of an electric background field the non-minimal coupling gives a negative contribution to the effective mass. If the coupling is strong enough it can lower the mass below the BF bound and destabilize the background. This mechanism of instability can be generalized to magnetic and dyonic black holes. In this case whether the solution is stable or unstable depends on the sign of the coupling α and on the relative magnitude of the electric and magnetic charges. In flat space this kind of instability was studied in [58]. In [59] a dynamical instability of the AdS-RN black hole in $\mathcal{N} = 8$ four-dimensional gauged supergravity was found involving fluctuations of both scalar and gauge fields. A similar instability was also found in [60] analyzing scalar fluctuations around a dyonic black hole in order to compute the momentum relaxation time scale induced by the presence of impurities.

Before studying numerically the solutions of Eq. (2.13), it is worth discussing some approximate criteria that point to the instability of the AdS-RN background. When $\beta = -2$ we can in fact provide a simple proof of the instability. In this case the potential $V(r)$ vanishes both at the horizon and at infinity and a sufficient condition for the existence of unstable modes is given by [65]

$$\int_{r_h}^{\infty} dr \frac{V(r)}{g(r)} < 0\,. \tag{2.15}$$

In terms of the parameter α this instability condition becomes

$$\alpha > \frac{3r_h^4}{Q^2L^2} - \frac{1}{4}\,. \tag{2.16}$$

For generic values of β an approximate condition for the instability of the solution follows from the observation that the region where the effective mass is below the BF bound contributes to the formation of a tachyonic mode whereas the region where the effective mass is above the BF bound supports stability. We can characterize the two regions introducing an instability radius r_i

$$r_i^4 = \frac{Q^2L^2}{\gamma}\,, \qquad \gamma = \frac{2}{\alpha}\left(\frac{9}{4} + \beta\right) . \tag{2.17}$$

The region where $m_{\text{eff}}^2 < -9/4$ corresponds to $r < r_i$ while the region where $m_{\text{eff}}^2 > -9/4$ corresponds to $r > r_i$. When $r_i \gg r_h$ the AdS-RN black hole is likely to be unstable and since

$r_i \to \infty$ when $\alpha \to \infty$ or when $\beta \to -9/4$ we expect an instability for large values of α or for masses close to the BF bound. This approximate condition can be expressed in terms of the black hole temperature (2.11) as

$$T_i \gg T_{RN} \ , \qquad T_i = \frac{\sqrt{QL}}{16\pi L^2}\left(\frac{12-\gamma}{\gamma^{1/4}}\right) . \tag{2.18}$$

The instability temperature is shown in Figure 2.1 as a function of the black hole charge Q. The region where an instability is expected to occur is $T_{RN} \ll T_i$, *i.e.* $Q \gg Q_i$, where Q_i is given by the intersection point of the two curves $T_{RN}(Q)$ and $T_i(Q)$.

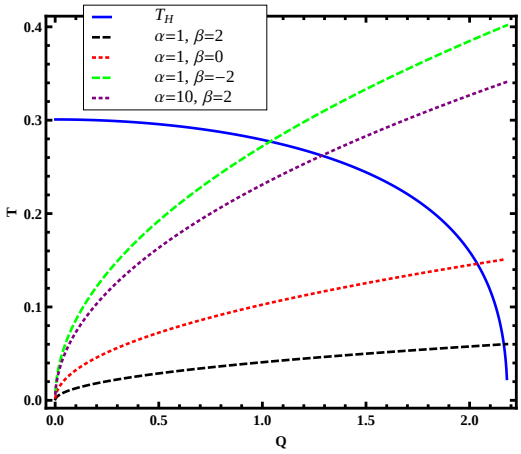

Figure 2.1: The instability temperature T_i and the black hole temperature T_{RN} as functions of Q for $L = M = 1$. Plots extend from $Q = 0$ to $Q_{\rm ext} = M\sqrt{3}(2L/M)^{1/3}$ which corresponds to extremal black holes. The region of instability is $T_{RN} \ll T_i$. Curves are ordered in a counterclockwise sense for decreasing values of γ. The smaller γ the larger the instability region.

In order to confirm the existence of the instability one should find unstable modes of the scalar equation (2.13). Unstable modes correspond to normalizable solutions of (2.13) with purely ingoing boundary conditions at the horizon and complex frequency ω with $\mathrm{Im}(\omega) > 0$ (see [9] for a recent review on black hole perturbations). These modes grow exponentially in time destabilizing the background. Another strong indication of the instability of a gravitational background is provided by the presence of marginally stable modes, namely modes with $\omega = 0$. Setting also $\vec{k} = 0$, Eq. (2.13) reduces to

$$\left(\Box - m_{\rm eff}^2\right)\phi(r) = 0\,. \tag{2.19}$$

We can solve the previous equation by numerical integration starting from a series expansion at the horizon and imposing suitable boundary conditions near the AdS boundary. The expansion at large r of the scalar field is

$$\phi \sim \frac{\mathcal{O}_\Delta}{r^\Delta} \ , \tag{2.20}$$

with $\Delta(\Delta - 3) = m^2$ and Δ chosen in such a way that the scalar mode is normalizable. We solve Eq. (2.19) numerically fixing α and β and varying L until we find a solution with the correct asymptotic behavior (2.20). A solution exists for $L \leq 2\sqrt{3}$ and as we increase L to lower the temperature several marginally stable modes arise. Some examples of marginal modes are shown in Figure 2.2 and 2.3.

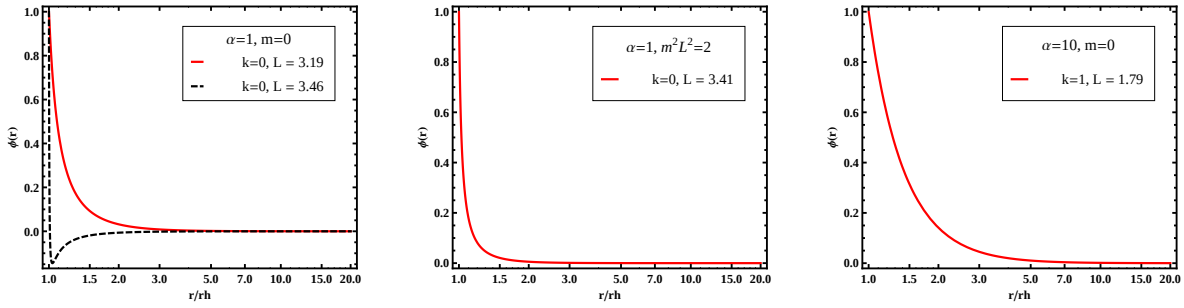

Figure 2.2: Some examples of marginally stable modes with $m^2 \geq 0$

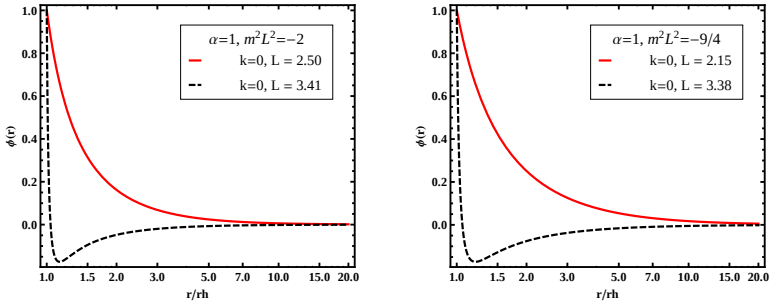

Figure 2.3: Some examples of marginally stable modes with $0 \geq m^2 \geq m^2_{BF}$

The numerical results confirm the qualitative discussion at the beginning of this Section. The instability temperature (2.18) provides a good estimate of the critical temperature at which the first marginal mode actually appears, it overestimates the numerical value by a factor of order one which decreases in the large α limit. Marginal modes appear in a large region of the parameter space and they provide a strong indication of the instability of the AdS-RN black hole.

Finally integrating numerically Eq. (2.13) with $\omega \neq 0$ we found quasinormal modes with $\mathrm{Im}(\omega) > 0$, which provide the main indication for the existence of a dynamical instability. As expected the imaginary part of the frequency of these unstable modes increases as we increase α or consider values of β close to the BF bound.

2.3 Numerical solutions of the field equations

The existence of a perturbative instability for the AdS-RN black hole in models containing a scalar field with a non-minimal coupling to the gauge field suggests that the Lagrangian (2.1) should admit charged dilaton black holes with $T \leq T_c$ and a lower free energy than the AdS-RN black hole. In this Section we show that these solutions exist by solving numerically the full nonlinear equations of motion (2.2). In Appendix 2.7 we discuss a simpler probe limit in which the stress-energy tensors of the Maxwell and of the scalar field decouple from the Einstein equations.

Analytic solutions for static, charged, planar black holes with scalar hairs are difficult to find. Charged black holes with a scalar hair in a similar model were found in flat spacetime [55] and their generalization to AdS spacetime were considered recently in [66]. The asymptotic behavior of the scalar field is however not the one required for the study of phase transitions in the dual theory. In [67] numerical black hole solutions with a scalar hair were found in flat space for models of dilaton gravity coupled to the Born-Infeld action. Charged black hole solutions with scalar hairs in AdS were only found resorting to numerical computations [47, 68] and we shall follow the same approach here.

To set up the numerical procedure we first consider the behavior of the fields near the AdS boundary for $r \to \infty$ and near the horizon for $r \to r_h$. The asymptotic behavior near the AdS boundary of the scalar field is

$$\phi \sim \frac{\mathcal{O}_-}{r^{\Delta_-}} + \frac{\mathcal{O}_+}{r^{\Delta_+}} \,, \tag{2.21}$$

where

$$\Delta_\pm = \frac{3 \pm \sqrt{9 + 4m^2L^2}}{2} \,. \tag{2.22}$$

In order to describe states of the dual field theory with a non vanishing expectation value for the operator dual to the scalar field, the asymptotic expansion (2.21) should contain only normalizable modes [69]. For this reason when $m^2L^2 \geq -5/4$ we impose the boundary condition $\mathcal{O}_- = 0$, corresponding to a vacuum expectation value for an operator of dimension Δ_+. When $-9/4 < m^2L^2 < -5/4$ two distinct choices are possible [70]: $\mathcal{O}_- = 0$, corresponding to a vacuum expectation value for an operator of dimension Δ_+ and $\mathcal{O}_+ = 0$, corresponding to a vacuum expectation value for an operator of dimension Δ_-.

The asymptotic behavior of the gauge field is

$$A_0 \sim \mu - \frac{\rho}{r} \,, \tag{2.23}$$

where μ and ρ specify the chemical potential and the charge density of the dual theory [3]. Finally the asymptotic behavior of the metric functions is given by

$$\chi \sim \frac{\Delta \mathcal{O}_\Delta^2}{4L^2} \frac{1}{r^{2\Delta}} \,, \tag{2.24}$$

and

$$\begin{aligned} g &\sim \frac{r^2}{L^2} + \frac{\Delta \mathcal{O}_\Delta^2}{4L^2} \frac{1}{r^{2\Delta-2}} - \frac{2M}{r} \,, \qquad \text{if } 1 < 2\Delta \leq 2 \,, \\ g &\sim \frac{r^2}{L^2} - \frac{2M}{r} \,, \qquad \text{if } \Delta > 1 \,, \end{aligned} \tag{2.25}$$

where M is the black hole mass. Asymptotically the solution is then characterized by four parameters: μ, ρ, M and $\mathcal{O}_\Delta$.

A power series expansion near the horizon shows that the solutions of the equations (2.6)-(2.9) are completely specified by four parameters [47]: the horizon radius r_h, $A_0'(r_h)$, $\chi(r_h) \equiv \chi_h$ and $\phi(r_h) \equiv \phi_h$. In term of these parameters the black hole temperature is

$$T = \frac{r_h}{16\pi L^2}\left[(12 + 2\phi_h^2)e^{-\chi_h/2} - L^2 A_0'(r_h)^2 e^{\chi_h/2} f(\phi_h)\right] . \tag{2.26}$$

In order to reduce the number of parameters in the numerical analysis one can exploit the following three scaling symmetries of the equations of motion [19]

$$\begin{aligned} r &\mapsto kr , \quad t \mapsto kt , \quad L \mapsto kL , \\ r &\mapsto kr , \quad (t,x,y) \mapsto \frac{1}{k}(t,x,y) , \quad g \mapsto k^2 g , \quad A_0 \mapsto kA_0 , \\ t &\mapsto kt , \quad e^\chi \mapsto k^2 e^\chi , \quad A_0 \mapsto \frac{1}{k}A_0 . \end{aligned} \tag{2.27}$$

We can use the first symmetry to set $L = 1$, the second to set $r_h = 1$ (assuming that the horizon radius is different from zero) and the third to set to zero the asymptotic value of χ at infinity. In this way we are left with two parameters, ϕ_h and $A_0'(r_h)$, that are constrained by the condition that either $\mathcal{O}_+$ or $\mathcal{O}_-$ vanish at infinity. It follows that the numerical solutions of the field equations (2.6)-(2.9) form a one-parameter family. Varying the single free parameter, *e.g.* ϕ_h, one obtains solutions with different values of the temperature (2.26).

By numerical integration we found solutions of the field equations (2.6)-(2.9) that describe charged dilatonic black holes. We considered two types of coupling functions

$$f_1(\phi) = \cosh(a\phi) , \qquad f_2(\phi) = 1 + \frac{\alpha}{2}\phi^2 , \tag{2.28}$$

and two types of potentials

$$V_1(\phi) = -\frac{6}{L^2} + \frac{\beta}{2L^2}\phi^2 , \qquad V_2(\phi) = -\frac{6}{L^2}\cosh(b\phi) . \tag{2.29}$$

In Figure 2.4 we display the field profiles of the numerical solution obtained for a particular choice of f and V. Other choices lead to qualitatively similar results.

Below a critical temperature $T_c \sim \sqrt{\rho}$ we always find charged dilaton black hole solutions. Comparing their free energy with the free energy of the AdS-RN one can verify that they represent more stable states. The free energy $F = M - TS - \Phi Q$ depends on the four asymptotic parameters that characterize the solution, namely μ, ρ, M and $\mathcal{O}_\Delta$. Setting $L = 1$ the free energies of the AdS-RN black hole and of the dilaton black hole read [47]

$$F_{RN} = \frac{V}{r_h}\left(-r_h^4 + \frac{3\rho^2}{4}\right) , \qquad F_{CD} = V\left(-2M + \mu\rho\right) , \tag{2.30}$$

where V is the volume of the (x, y) plane. In Fig. 2.5 we plot the free energy and the specific heat $c = -T\partial_T^2 F/V$ for an AdS-RN black hole and a charged dilatonic black hole with the same mass and charge. Below T_c the dressed solution has a lower free energy and represents a more stable state than the AdS-RN black hole. The free energy is continuous at T_c while the specific heat has a discontinuity, so that the phase transition is second order. For $T > T_c$ the

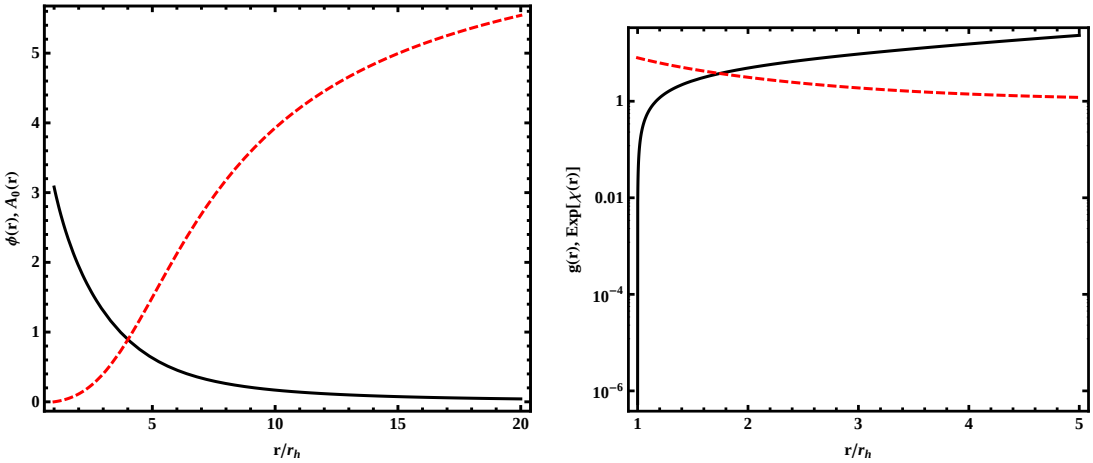

Figure 2.4: Examples of the field profiles of the numerical charged black hole solution for a coupling function $f(\phi) = \cosh(2\phi)$ and a potential $L^2V(\phi) = -6 - \phi^2$. Left panel: the scalar field ϕ (black) and the gauge potential A_0 (dashed red). Right panel: metric function g (black) and e^{χ} (dashed red). $T/T_c \sim 0.2$.

dressed solution is not present anymore, precisely as it happens for the instability induced by the minimal coupling to a charged scalar field [19, 71]. We mention here that for a given choice of f and V there are usually several different black hole solutions with scalar hair and the correct asymptotic behavior. We always choose the solution with a monotonic scalar profile. The other solutions have scalar fields with several nodes and presumably they also have a higher free energy.

2.4 The zero temperature limit

Below the critical temperature the gravitational background describes a charged dilaton black hole. In this section we discuss the properties of the zero temperature ground state. Extremal solutions are not easily found numerically. In order to study their properties one can first look for an ansatz for the leading behavior of the fields near the horizon that contains at least one free parameter. The equations of motion are then integrated numerically and the free parameter varied until one finds the correct asymptotic behavior at infinity. In this way a solution to the equations of motion with the correct boundary conditions is obtained [63]. The zero temperature limit of hairy black holes in models with a minimally coupled charged scalar field was studied in [63]. In [62] a similar analysis was carried out for dilaton black holes with an exponential coupling function $f(\phi) = e^{a\phi}$.

We limit our attention to models with coupling function and potential of the form

$$f(\phi) = 2f_0 \cosh a\phi \ , \qquad V = -2W_0 \cosh b\phi \ . \tag{2.31}$$

A similar analysis could also be performed for other coupling functions as for instance $f(\phi) = 1 + \frac{\alpha}{2}\phi^2$. The action we consider is then

$$S = \int d^4x\sqrt{-g}\left[R - \frac{1}{2}(\partial\phi)^2 - \frac{f_0}{2}\cosh a\phi\, F^2 + 2W_0\cosh(b\phi) - 2\Lambda\right] \ , \tag{2.32}$$

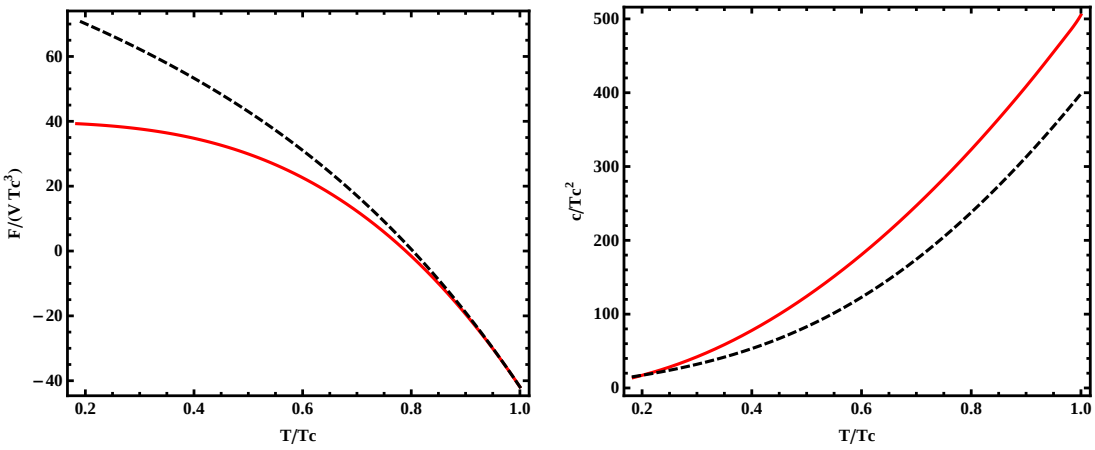

Figure 2.5: Left panel: Free energy of the hairy black hole (red line) and of the AdS-RN (black dashed line). Right panel: specific heat. The data shown are for the operator $\mathcal{O}_-$ and for $f(\phi) = \cosh(2\phi)$ and $V(\phi) = -6/L^2 - \phi^2/L^2$.

where we included a negative cosmological constant $\Lambda < 0$. The radius of the AdS vacuum solution is

$$\frac{3}{L^2} = W_0 - \Lambda \ , \tag{2.33}$$

and stability of the vacuum requires that the parameter b satisfies the Breitenlohner-Freedman bound

$$b^2 \leq b_u^2 \ , \qquad b_u^2 \equiv \frac{3}{8}\left[1 - \frac{\Lambda}{W_0}\right] \ . \tag{2.34}$$

In this section we use the following parametrization for the metric

$$ds^2 = -\lambda(r)dt^2 + \frac{dr^2}{\lambda(r)} + H^2(r)(dx^2 + dy^2) \ . \tag{2.35}$$

The equation of motion of the gauge field can be immediately integrated and gives

$$A_0' = \frac{\rho}{fH^2} \ , \tag{2.36}$$

where ρ is the charge density of the solution. The remaining equations are

$$\begin{aligned}
(\lambda H^2)'' &= -2H^2\,(V + 2\Lambda) \ , \\
(H)'' &= -\frac{H}{4}(\phi')^2 \ , \\
(\lambda H^2 \phi')' &= H^2\left[\frac{dV}{d\phi} - \frac{(A_0')^2}{2}\frac{df}{d\phi}\right] \ , \\
\lambda(H')^2 + \frac{\lambda'}{2}(H^2)' &= H^2\left[\frac{\lambda}{4}(\phi')^2 - \frac{f}{4}(A_0')^2 - \frac{V}{2} - \Lambda\right] \ .
\end{aligned} \tag{2.37}$$

The equation of motion of the scalar field contains an effective potential

$$\tilde{V}(\phi) = V(\phi) + \frac{\rho^2}{2H^4 f(\phi)} \ , \tag{2.38}$$

and one can find $AdS_2 \times \mathbb{R}^2$ solutions with constant $H = H_0$ and $\phi = \phi_0$ provided that

$$\frac{d\tilde{V}}{d\phi}(\phi_0) = 0 \ , \qquad \frac{\rho^2}{2H_0^4 f(\phi_0)} = -V(\phi_0) - 2\Lambda \ . \tag{2.39}$$

For the simple models discussed in this chapter with potentials of the form given in (2.29), this is possible only if $m^2 > 0$ and for $\rho^2 a^2 > 4 f_0 m^2 H_0^4$. In this Section we will focus on models with $m^2 \leq 0$ and therefore we do not consider this possible class of solutions.

We will try instead the following scaling ansatz [62]

$$\lambda = \lambda_0 \, r^w (1 + p_1 \, r^\nu) \ , \qquad H = r^h (1 + p_2 \, r^\nu) \ , \qquad \phi = \phi_0 - \xi \ln r + p_3 \, r^\nu \ . \tag{2.40}$$

This scaling ansatz provides an exact solution to the equations of motion if the parameters are chosen in the following way

$$\xi = \frac{4(a+b)}{4 + (a+b)^2} \ , \qquad w = 2 - b\xi \ , \qquad h = \frac{(a+b)^2}{4 + (a+b)^2} \ , \tag{2.41}$$

$$\lambda_0 \ = \ \frac{2 W_0 e^{b\phi_0}}{(w+2h)(w+2h-1)} \ , \qquad \frac{\rho^2}{f_0} e^{-a\phi_0} = \frac{2 W_0 e^{b\phi_0}}{w+2h} (2 - 2h - b\xi) \ . \tag{2.42}$$

Using the previous relations we can express the parameter ϕ_0 in terms of the charge density and the other parameters of the model

$$\frac{\rho^2}{f_0} e^{-(a+b)\phi_0} = 2 W_0 \frac{2 - b(a+b)}{2 + b(a+b)} \ . \tag{2.43}$$

Finally the other parameters read

$$\begin{aligned} p_3 \ &= \ \frac{2 p_2}{\xi} (2h - 1 + \nu) \ , \qquad (2.44) \\ p_1 (w + 2h + \nu)(w + 2h - 1 + \nu) \ &= \ p_3 b (w+2h)(w+2h-1) - 2 p_2 \left[\nu^2 + \nu (2w + 4h - 1) \right] \ , \end{aligned}$$

and the exponent ν is a real root of the following quartic equation

$$\begin{aligned} &Q(\nu) = (\nu + 1)(\nu + a\xi)(\nu^2 + A\nu + B) \ , \qquad (2.45) \\ &A = 1 + \frac{2(a^2 - b^2)}{4 + (a+b)^2} \ , \quad B = -2A^2 + 2A \frac{(a+b)^2 (1 + ab)}{4 + (a+b)^2} \ . \end{aligned}$$

If we choose the greatest positive root the scaling ansatz describes the near-horizon region of the extreme black hole. It could be interesting to study the backgrounds corresponding to the other real roots of the polynomial (2.45). In Figure 2.6 we show the background fields obtained by integrating the near-horizon behavior discussed above up to infinity and requiring suitable boundary conditions.

The solution is extremal if $b\xi < 1$ which implies

$$b < b_e \ , \qquad b_e \equiv \frac{a}{3} \left[2 \sqrt{1 + \frac{3}{a^2}} - 1 \right] \ . \tag{2.46}$$

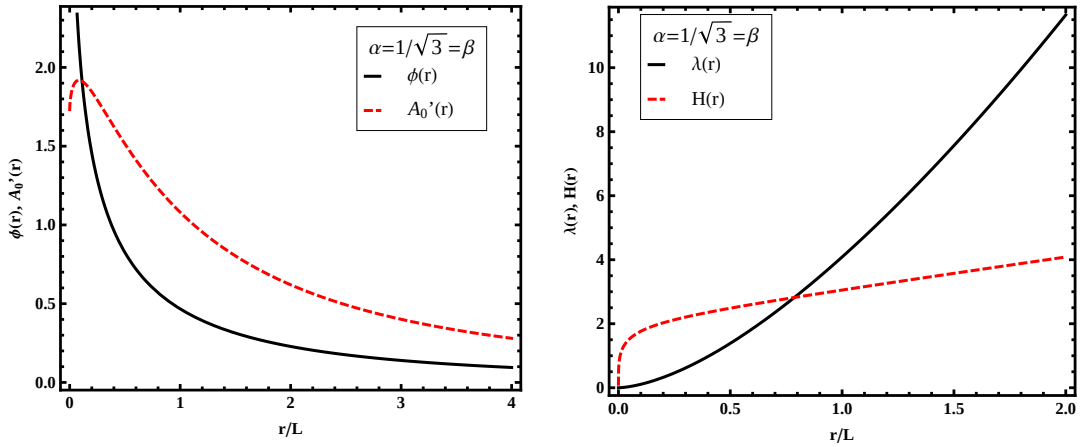

Figure 2.6: Background fields at $T = 0$, Maxwell and scalar field (left) and metric functions (right).

This condition together with the BF bound (2.34) restricts the possible value of b for a given value of a. When $b = 0$ the previous solution reduces to the solution found in [62] upon substituting W_0 with $2(W_0 - \Lambda)$. Since the extremal solution depends on the parameter b, it is not surprising that also the behavior of the conductivity at low frequencies is modified. As we will show in the next Section it vanishes as $\sigma(\omega) \sim \omega^{2+\frac{b\xi}{1-b\xi}}$.

The scaling ansatz in Eq. (2.40) can also capture the near-horizon region of a near-extreme black hole [62]. The near-extreme solution corresponds to a negative value for the parameter $\nu = -\eta$ with

$$\eta = 1 + \frac{\xi}{2}(a - b) \ , \tag{2.47}$$

which implies $p_2 = p_3 = 0$. The parameters λ_0, ρ and φ_0 satisfy the relations already given in (2.42). The solution depends then on a parameter $p_1 \equiv -m$ and the metric is

$$ds^2 = \lambda_0 r^w \left(1 - \frac{m}{r^\eta}\right) dt^2 + \frac{dr^2}{\lambda_0 r^w \left(1 - \frac{m}{r^\eta}\right)} + r^{2-2h}(dx^2 + dy^2) \ . \tag{2.48}$$

The horizon radius is given by $r_0^\eta = m$. We will use this metric in Section 2.5 to clarify the low temperature behavior of the optical conductivity.

We note that since the scalar field diverges logarithmically as it approaches the extremal horizon, the same near-horizon analysis can be applied to the case of exponential coupling functions of the form $f(\phi) = f_0 e^{a\phi}$ and potentials of the form $V(\phi) = -W_0 e^{b\phi}$. Black hole solutions in Einstein-Maxwell-dilaton gravity with exponential coupling functions and Liouville-like potentials are discussed in [72, 73, 74].

2.5 Holographic properties of the new black hole solution

The instability of the AdS-RN black hole toward developing a scalar hair signals a phase transition in the dual field theory defined on the boundary of AdS. When the scalar field is

charged with respect to the $U(1)$ gauge field, in the dual theory there is a phase transition to a superfluid state characterized by the spontaneous breaking of a global $U(1)$ symmetry [19]. In our case the condensate is neutral and we have a phase transition between the state dual to the AdS-RN black hole and the state dual to the dilatonic black hole. As mentioned in the introduction, these two states have markedly different properties, in particular from the thermodynamical point of view.

In order to better illustrate the behavior of the new phase, we will display our results for the four models listed in the Table 2.1.

Table 2.1: Models investigated in detail in our numerical simulations.

	$f(\phi)$	$V(\phi)$	α	β
Model I	$\cosh(\sqrt{3}\phi)$	$-\frac{6}{L^2}-\frac{\phi^2}{L^2}$	3	-2
Model II	$1+\frac{3}{2}\phi^2$	$-\frac{6}{L^2}-\frac{\phi^2}{L^2}$	3	-2
Model III	$\cosh(\sqrt{3}\phi)$	$-\frac{6}{L^2}\cosh\left(\frac{\phi}{\sqrt{3}}\right)$	3	-2
Model IV	$\cosh(10\phi)$	$-\frac{6}{L^2}-\frac{\phi^2}{L^2}$	100	-2

The first three models correspond to different choices for the coupling functions $f(\phi)$ and the potential $V(\phi)$ but they all have the same values for the parameters α and β that enter in the linear perturbation analysis of Section 2.2. The last model illustrates the behavior of the system for large values of the parameter α. As discussed in the previous Section, at low temperatures a simpler pattern appears: when the potential has the form given in (2.29) with $\beta \leq 0$ the properties of the model depend mainly on α and are affected by the presence of the potential only when this is an exponential function of the scalar field.

2.5.1 Phase transitions in the dual theory

Below T_c the new black hole solution develops a scalar hair and therefore the new phase of the dual theory is characterized by a scalar condensate. The temperature dependence of the expectation value of the neutral operator $\mathcal{O}_+$ or $\mathcal{O}_-$ can be determined using Eq. (2.21) and the fact that the black hole temperature depends only on ϕ_h, the value of the scalar field at the horizon. In Figure 2.7 we display the scalar condensate at constant charge density and for different values of the temperature for our four models. The critical temperature is proportional to $\sqrt{\rho}$ where ρ is the charge density. Near the critical temperature the scalar condensate behaves like $\sim (1-T/T_c)^\gamma$, with $\gamma = 1/2$ for both $\mathcal{O}_+$ and $\mathcal{O}_-$, which is the value of the exponent predicted by mean field theory [47, 75].

2.5.2 Electric conductivity in the dual theory

According to the AdS/CFT correspondence, transport phenomena in the dual field theory are related to linear perturbations of the equations of motion of the bulk fields. For instance the electric, thermal and thermoelectric conductivities can be derived from the equations governing the fluctuations of the component g_{tx} of the metric and A_x of the gauge field [3]. Perturbations of g_{tx} and A_x with zero spatial momentum and harmonic time dependence decouple from all

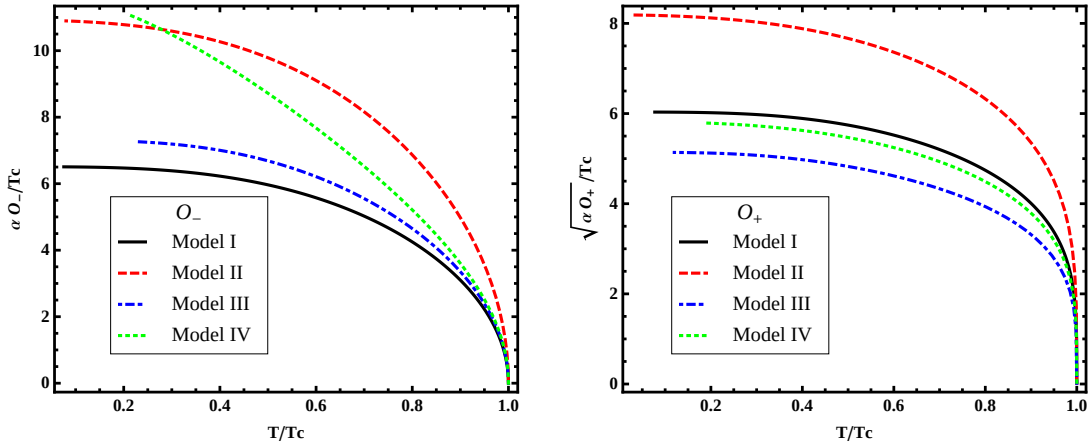

Figure 2.7: Neutral condensate as a function of T for the two different boundary theories and for different models. Left: $\mathcal{O}_- \sim (1 - T/T_c)^{1/2}$ near the critical temperature. Right: $\mathcal{O}_+ \sim (1 - T/T_c)^{1/2}$ near the critical temperature.

the other modes and one is left with a system of just two equations

$$A_x'' + \left[\frac{g'}{g} - \frac{\chi'}{2} + \frac{1}{f(\phi)}\frac{df(\phi)}{d\phi}\phi'\right] A_x' + \frac{\omega^2}{g^2} e^{\chi} A_x = \frac{A_0' e^{\chi}}{g}\left[\frac{2}{r} g_{tx} - g_{tx}'\right], \tag{2.49}$$

$$g_{tx}' - \frac{2}{r} g_{tx} + A_0' A_x f(\phi) = 0\,. \tag{2.50}$$

Substituting the second equation in the first gives the following equation for the fluctuations of the gauge field

$$A_x'' + \left[\frac{g'}{g} - \frac{\chi'}{2} + \frac{1}{f(\phi)}\frac{df(\phi)}{d\phi}\phi'\right] A_x' + \left(\frac{\omega^2}{g^2} - \frac{{A_0'}^2 f(\phi)}{g}\right) e^{\chi} A_x = 0\,. \tag{2.51}$$

We solve Eq. (2.51) with purely ingoing boundary conditions at the horizon. The electric, thermal and thermoelectric conductivities are given by [19]

$$\sigma = -i\frac{A_x^{(1)}}{\omega A_x^{(0)}}\,, \qquad \sigma_{te} = \frac{1}{T}\left(\frac{i\rho}{\omega} - \mu\sigma\right)\,, \qquad \sigma_t = \frac{iM}{4\omega T}\,, \tag{2.52}$$

where $A_x^{(0)}$ and $A_x^{(1)}$ are fixed by the asymptotic behavior of the fluctuation at infinity

$$A_x \sim A_x^{(0)} + \frac{A_x^{(1)}}{r}\,. \tag{2.53}$$

In the following we will consider only the electric conductivity. Figures 2.8, 2.9 and 2.10 show its frequency dependence obtained by numerical integration of eq. (2.51).

The four models display similar qualitative features. In the high-frequency limit the real part of the conductivity becomes constant, a property common to every theory with an AdS_4 dual. Moreover, as a consequence of translation invariance, the imaginary part of σ has a

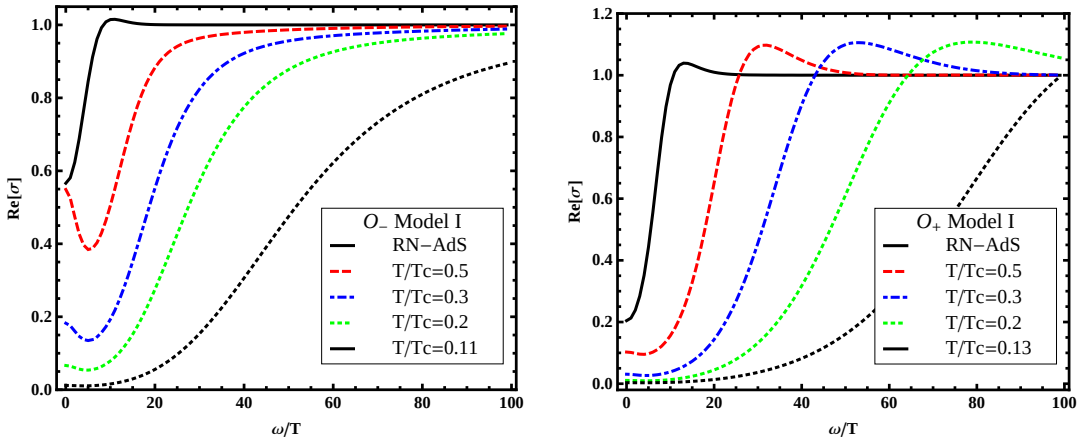

Figure 2.8: Real part of the conductivity as a function of the frequency for different values of T and for the operators $\mathcal{O}_-$ (left) and $\mathcal{O}_+$ (right). We show results for Model I.

simple pole at $\omega = 0$ and therefore the DC conductivity contains a delta function contribution at $\omega = 0$. The conductivity displays interesting behavior at small frequencies. From the plots we see that it develops a minimum and then it tends to a non-zero value as $\omega \to 0$, more pronounced for large values of the non-minimal coupling α, as shown in Fig. 2.9. This non-zero value of $\mathrm{Re}[\sigma]$ at $\omega = 0$ may be seen as an analogue of the Drude peak in the conductivity of ordinary metals. As we lower the temperature this additional contribution to the DC conductivity decreases and at zero temperature $\sigma(\omega)$ vanishes at low frequencies as a power with an exponent fixed by the geometry of the near-horizon region, as we will show below.

The frequency dependence of the conductivity is easier to understand if one rewrites Eq. (2.51) as a Schrödinger equation and expresses σ in term of a reflection coefficient [63]. In order to do so we introduce a new coordinate z defined by

$$\frac{dr}{dz} = g e^{-\frac{\chi}{2}} \,, \tag{2.54}$$

and rescale the gauge field setting $\sqrt{f}A = \Psi$. In the new coordinates the horizon is at $z = -\infty$, the boundary of AdS at $z = 0$ and the field Ψ satisfies the following equation

$$\frac{d^2\Psi}{dz^2} + (\omega^2 - V(z))\Psi = 0 \,, \qquad V(z) = g f (A_0')^2 + \frac{1}{\sqrt{f}} \frac{d^2\sqrt{f}}{dz^2} \,. \tag{2.55}$$

The potential in Eq. (2.55) has two contributions. The second term is due to the non-minimal coupling, it is present also in the probe limit and it is always negative in the near-horizon region. The first term is always positive and corresponds to the backreaction of the metric.

To find solutions of the original problem with ingoing boundary conditions at the horizon it is convenient to extend the definition of the potential $V(z)$ to positive values of z by setting $V(z) = 0$ for $z > 0$. One then solves the one-dimensional Schrödinger equation with potential $V(z)$ for a particle incident on the potential barrier from the right [63]. For $z \geq 0$ the wave function is

$$\Psi(z) = e^{-i\omega z} + \mathcal{R} e^{i\omega z} \,, \qquad z \geq 0 \,, \tag{2.56}$$

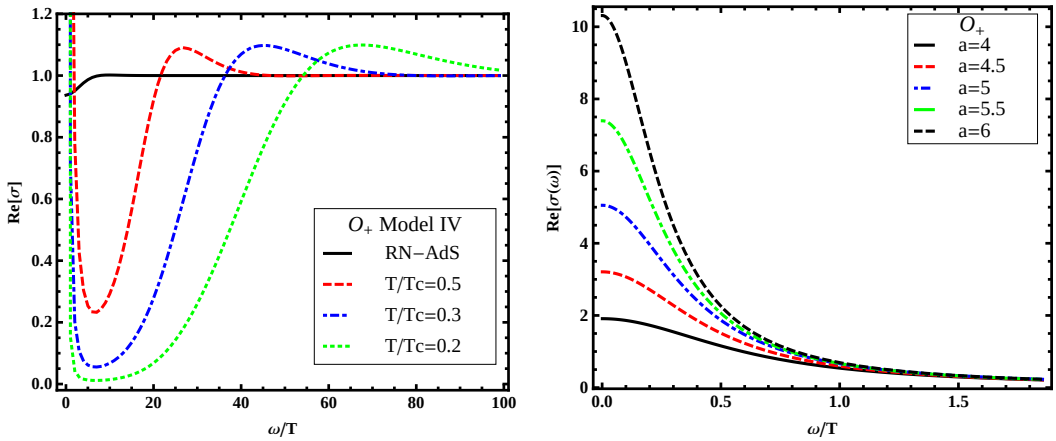

Figure 2.9: Left: Real part of the conductivity as a function of the frequency for different values of T and for the operator $\mathcal{O}_+$. We show results for Model IV. Right: Real part of the conductivity for $\beta = -2$ and $f(\phi) = \cosh(a\phi)$ for increasing values of a.

where $\mathcal{R}$ is the reflection coefficient. Using Eq. (2.53) and (2.52) and the definition $\Psi = \sqrt{f}A$ one obtains

$$\sigma(\omega) = -\frac{i}{\omega}\frac{A_x^{(1)}}{A_0^{(0)}} = \frac{1-\mathcal{R}}{1+\mathcal{R}} - \frac{i}{2\omega}\left[\frac{1}{f}\frac{df}{dz}\right]_{z=0} . \tag{2.57}$$

The second term in the equation above contributes only to the imaginary part of the conductivity. When f starts with a term linear in ϕ this term vanishes for $\Delta > 1$, is constant for $\Delta = 1$ and diverges for $\Delta < 1$. When f starts with a term quadratic in ϕ and therefore satisfies the conditions in Eq. (2.4) it vanishes for $\Delta > 1/2$ and it is constant for $\Delta = 1/2$. The real part of the conductivity is completely determined by the reflection coefficient $\mathcal{R}$, hence by the form of the potential V in the Schrödinger equation.

The behavior of V at large r depends on the asymptotic expansion of the scalar field $\phi \sim O_\Delta / r^\Delta$ and on the coupling function $f(\phi)$. When f starts with a term linear in ϕ, as it is the case for $f = e^{a\phi}$, the potential is

$$V(z) \sim \rho^2 z^2 + \frac{a}{2}\Delta(\Delta-1)O_\Delta(-z)^{\Delta-2} , \tag{2.58}$$

and therefore it vanishes for $\Delta > 2$, is constant for $\Delta = 2$ and diverges for $1/2 < \Delta < 2$. When f starts with a term quadratic in ϕ, as it is the case for $f = \cosh(a\phi)$, the potential is

$$V(z) \sim \rho^2 z^2 + \frac{a^2}{2}\Delta(2\Delta-1)O_\Delta^2(-z)^{2(\Delta-1)} , \tag{2.59}$$

and therefore it vanishes for $\Delta > 1$, is constant for $\Delta = 1$ and diverges for $1/2 < \Delta < 1$.

For non extremal black holes the potential tends to zero exponentially as the coordinate z tends to the horizon, $V(z) \sim V_h e^{4\pi T z}$ where T is the temperature of the black hole. While the potential of a model with a charged scalar minimally coupled to the gauge field is always positive, in our case the sign of the potential is not definite. Although it is always positive near the boundary, it can become negative and reach a minimum before vanishing at the horizon

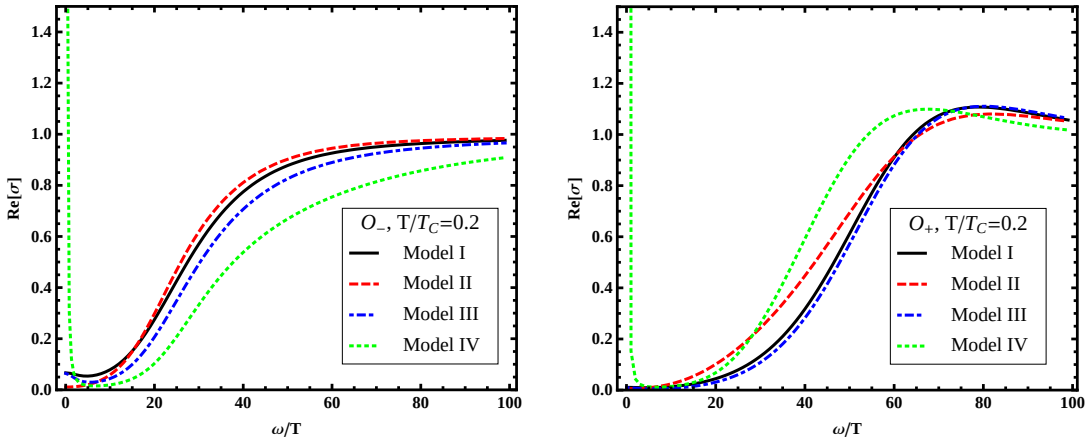

Figure 2.10: Real part of the conductivity as a function of the frequency for different models at $T/T_c \sim 0.2$ and for the operators $\mathcal{O}_-$ (left) and $\mathcal{O}_+$ (right).

with a negative exponential tail. Whether the potential is positive or negative depends on the relative magnitude of the two terms in the Schrödinger potential, the one due to the non-minimal coupling and the one due to the backreaction. As we lower the temperature the effect of the backreaction becomes increasingly important. In fact at $T = 0$ the potential is always positive near the extremal horizon and vanishes like C/z^2, with a positive constant C.

The near-horizon behavior of the potential at $T = 0$ can be determined using the analytic form of the extremal solution found in the previous Section. With the form of the metric used in that Section the new coordinate z is given by

$$\frac{dr}{dz} = \lambda \ , \tag{2.60}$$

and the rescaled gauge field $\Psi = \sqrt{f}A$ satisfies the following equation

$$\frac{d^2\Psi}{dz^2} + (\omega^2 - V(z))\Psi = 0 \ , \qquad V(z) = \lambda f (A_0')^2 + \frac{1}{\sqrt{f}}\frac{d^2\sqrt{f}}{dz^2} \ . \tag{2.61}$$

Substituting the explicit form of the solution one obtains

$$V(z) = \frac{C}{z^2} \ , \qquad C = \frac{(2b\xi - 3)^2}{4(1 - b\xi)^2} - \frac{1}{4} \ . \tag{2.62}$$

Following the approach of [76] one can show that the optical conductivity vanishes at small frequencies and obtain an analytic expression for the leading power in ω by matching the conserved probability current of the Schrödinger equation near the boundary at infinity and near the horizon. The result is

$$\sigma(\omega) \sim \omega^{2+\frac{b\xi}{1-b\xi}} \ , \tag{2.63}$$

and this behavior is observed in our numerical results for the conductivity in the low temperature and low frequency limits. Notice that the existence of extremal solutions requires $b\xi < 1$, hence $\sigma(\omega) \propto \omega^\gamma$, where $\gamma > 1$.

The Schrödinger potential and the related conductivity are shown in Figs. 2.11. As mentioned before, also in this case there are several solutions to the field equations. The Schrödinger potential and the conductivity for these additional solutions can have several maxima and minima in the intermediate region between the horizon and infinity. These features are absent if the coupling function is exponential, $f \sim e^{a\phi}$.

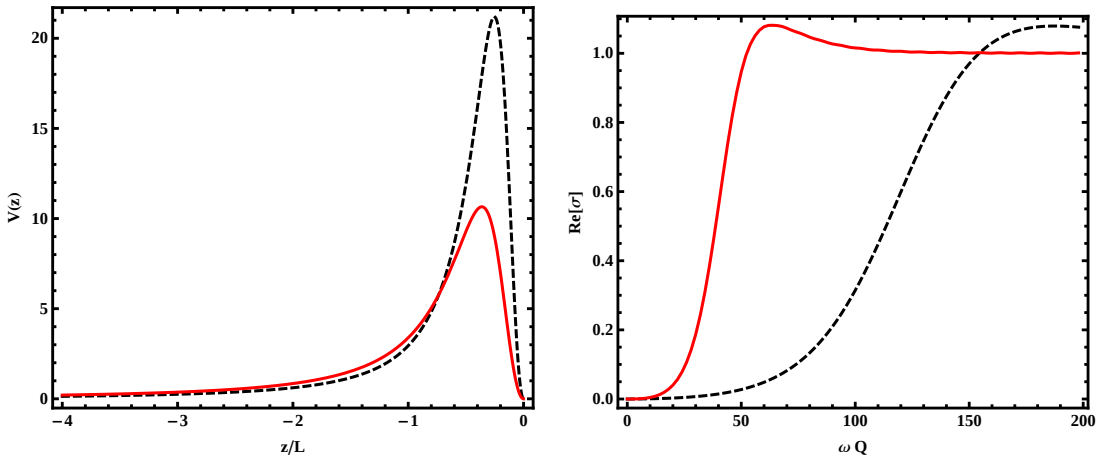

Figure 2.11: Schrödinger potential (left) and electrical conductivity (right) at $T = 0$. Black dashed lines correspond to $b = 0$ and $a = 1$, whereas red straight lines correspond to $b = a = 1/\sqrt{3}$.

The other distinctive feature of the behavior of $\sigma(\omega)$, the presence of a peak at small frequencies when $T > 0$, is due to the fact that the potential of the Schrödinger problem is not positive definite and can support a resonance near $\omega = 0$, causing a sharp increase in the DC conductivity. Using the near-extremal solution (2.48) we can clarify when to expect a peak in $\sigma(0)$ and when this peak will be present even at very low temperatures. The explicit form of the Schrödinger potential near the horizon is in this case

$$V(z) \sim \frac{A^2}{r_0}\left[2 - 2h - \left(b + \frac{a}{2}\right)\xi\right] e^{Az} \ , \tag{2.64}$$

where $A = \lambda_0 \eta r_0^{1-b\xi}$. The potential, as already observed, receives a negative contribution from the term due to the non-minimal coupling between the scalar and the gauge field and a positive contribution from the term due to the backreaction of the metric. From the previous expression we can see that the potential approaches zero with a negative exponential tail as $z \to -\infty$ if $a^2 + 2b^2 + 3ab > 4$. For a given b this happens for

$$a > \frac{1}{2}\left[\sqrt{b^2 + 16} - 3b\right] \ . \tag{2.65}$$

In particular when $b = 0$ this implies that the potential for the quasi-extreme black hole is positive near the horizon for $a < 2$ and negative for $a > 2$. In Figure 2.12 we display the potential for selected values of the temperature and the parameters to confirm that its behavior changes according to Eq. (2.65). When a negative exponential tail is present for the near-extremal solution, the value of the conductivity increases significantly at small frequencies

even at low temperatures, as shown in Fig. 2.10. One can observe a small increase in $\sigma(\omega)$ at low frequencies even when the near-extremal potential is positive. This is due to the fact that at temperatures higher than those corresponding to the near-extremal black hole the term due to the non-minimal coupling can dominate the term due to the backreaction.

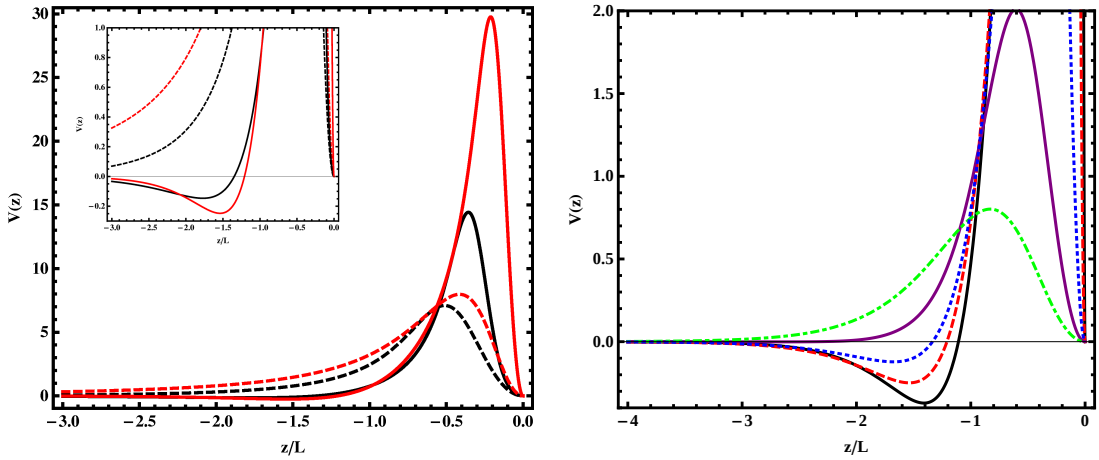

Figure 2.12: Effective potential in Eq. (2.55). Left: different models at fixed $T/T_c \sim 0.3$. Black lines refer to the case $b = 0$ and $a = 3$ (straight line) and $a = \sqrt{3}$ (dashed line). Red lines refer to $b = 1/\sqrt{3}$ and $a = \sqrt{3}$ (straight line) and $a = 1/\sqrt{3}$ (dashed line). According to Eq. (2.65), straight and dashed lines correspond to potentials approaching $z = -\infty$ from below and above respectively, as shown in the inset. Right: the model $a = \sqrt{3}$ and $b = 1/\sqrt{3}$ for different temperature. From below to top $T/T_c \sim 0.2$, 0.3, 0.5, , 0.8, 1. The lower the temperature, the deeper the minimum.

A similar increase in $\sigma(\omega)$ at low frequencies was recently observed in models where the Born-Infeld action of a probe brane is coupled to a geometry with a Lifshitz scaling symmetry [22].

Another interesting feature of our model is that the DC conductivity $\sigma(0)$ depends in a non-monotonic way on the temperature, as shown in Fig. 2.13. This effect becomes more evident as the value of a increases. In terms of the resistivity Fig. 2.13 shows that there is a minimum at low temperature. A minimum in resistivity is observed in metals containing magnetic impurities and its presence was explained by Kondo as resulting from the interaction between the magnetic moment of the conduction electrons and the impurity. It would be interesting to identify in our model what kind of effective interaction is induced among the charge carriers by the scalar condensate which causes the minimum in resistivity.

2.6 Conclusions

We have investigate a broad class of Einstein-Maxwell-dilaton gravity models in 4D AdS spacetime which admit both AdS-RN and charged dilatonic black hole solutions. Below a critical temperature the AdS-RN solution is unstable and it undergoes a phase transition whose endpoint is the charged black hole dressed with a scalar field.

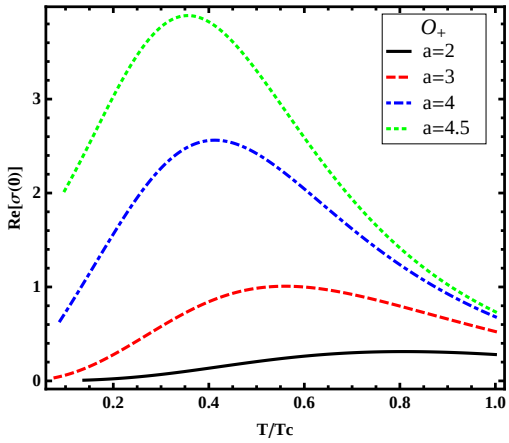

Figure 2.13: DC conductivity for $V = -\frac{6}{L^2}\cosh(\phi/\sqrt{3})$ and $f = \cosh(a\phi)$. From bottom to top $a = 2$, 3, 4, 4.5.

This instability is interesting from a purely gravitational perspective but it acquires a particular relevance when used in the context of the AdS/CFT correspondence to provide a holographic description of condensed matter phenomena. Our model describes a second order phase transition in the dual field theory in which a neutral scalar operator condenses below a critical temperature.

The new phase has interesting electric transport properties, presumably caused by the interactions of the charge carriers with the scalar condensate. When the temperature is not too close to zero, the optical conductivity has a minimum at low frequencies and then a "Drude peak", reaching a constant value at $\omega = 0$ which can be considerably larger than its constant value at high frequency. This effect is particularly evident for large values of the non-minimal coupling between the scalar and the gauge field. Another very interesting feature is that the resistivity does not increase monotonically with the temperature but displays a minimum. This effect is reminiscent of the Kondo effect, caused in real metal with magnetic impurities by the interactions of the magnetic moment of the conduction electrons with the magnetic moment of the impurity. It would be interesting to compute the precise temperature dependence of the resistivity and to clarify what kind of effective interaction causes the minimum in resistivity.

We also studied the extremal limit of the charged dilatonic black hole. The near-horizon metric has a Lifshitz scaling symmetry which is a simple generalization of the one found in [62]. Using the extremal solution we clarified the behavior of the numerical solutions in the zero temperature limit.

The analysis of the fluctuations of fermionic fields in the AdS-RN [77, 78, 79, 80, 43] and in the charged dilaton black hole background [57] provides evidence for the existence of a Fermi surface in the boundary theory. While in the former case the macroscopic ground state entropy prevents a simple interpretation of the dual phase, in the latter case one observes a more conventional behavior, with vanishing zero-point entropy and with a specific heat linear in the temperature. Since the phase transition discussed in this chapter connects the AdS-RN and the charged dilatonic black hole, it may help to clarify the correct interpretation of the corresponding dual theories.

It would be interesting to study models which allow for both the instability studied in this chapter and the instability caused by the minimal coupling of a charged scalar field. One could then investigate the effect of the neutral condensate on the properties of the superconducting phase. Our models can in fact be easily adapted to describe holographic superconductors by interpreting the scalar field as the modulus of a complex scalar and adding to the Lagrangian a coupling between the phase of the scalar and the gauge field. Models of this type were recently discussed in [81].

In order to identify precisely the dual theory and specify its operator content and Hamiltonian, it would be interesting to embed these black hole solutions into ten or eleven dimensional supergravity. For the holographic superconductors examples of this embedding were discussed in [82, 83, 84, 85].

2.7 Appendix: Scalar hairs in the probe limit. Schwarzschild-AdS background

Although in Sect. 2.3 we derived numerically the charged dilatonic black hole solution, it is of some interest to consider the regime in which one can neglect the back reaction of the matter fields on the gravitational field. The results of this Appendix can be compared with similar results obtained for the holographic superconductors in Ref.[19]. We shall follow closely the methods used in that paper, to which we refer for further details. We focus on potential of the form $V(\phi) = -6/L^2 - \phi^2/L^2$. The outcome does not qualitatively change if one chooses a different V as long as Eq. (2.4) is satisfied. The limit in which the dynamics for the scalar and electromagnetic field decouples from the gravitational dynamics is obtained for $\alpha \to \infty$, after the rescaling $\phi \to \phi/\alpha$ and $A_0 \to A_0/\alpha$. The gravitational part of the dynamics, represented by the sourceless Einstein equations, is solved by the planar AdS-Schwarzschild (AdS-S) background

$$ds^2 = -g(r)dt^2 + \frac{dr^2}{g(r)} + r^2(dx^2 + dy^2)\,, \tag{2.66}$$

with $g(r) = r^2/L^2 - 2M/r$. The black hole horizon is located at $r_h = (2ML^2)^{1/3}$, and the temperature is given by $T = \frac{3(2M)^{1/3}}{4\pi L^{4/3}}$. After using eq. (2.36) the dynamics for the scalar field is described by a single equation

$$\phi''(r) + \left[\frac{2}{r} + \frac{g'}{g}\right]\phi'(r) + \frac{1}{g}\left(\frac{\rho^2}{2r^4}\frac{1}{f(\phi)^2}\frac{df}{d\phi} - \frac{dV}{d\phi}\right) = 0\,, \tag{2.67}$$

which has to be numerically integrated. The numerical integration is performed using the method explained in Sect. 2.3. Setting either $\mathcal{O}_- = 0$ or $\mathcal{O}_+ = 0$ in Eq. (2.21), we find a one-parameter family of solutions. Varying the single free parameter ϕ_h we obtain the condensate as a function of the temperature T/T_c. Numerical results are shown in Figure 2.14 and they represent the $\alpha \gg 1$ limit of the exact solution described in the main text. We plot the results for two different choices of the coupling functions: $f(\phi) = \cosh(\phi)$ and $f(\phi) = 1 + \phi^2/2$. The condensate $\mathcal{O}_-$ diverges as $T \to 0$. The divergence is an artifact of the probe limit approximation and it is removed once the backreaction is taken into account, as shown in Figure 2.7.

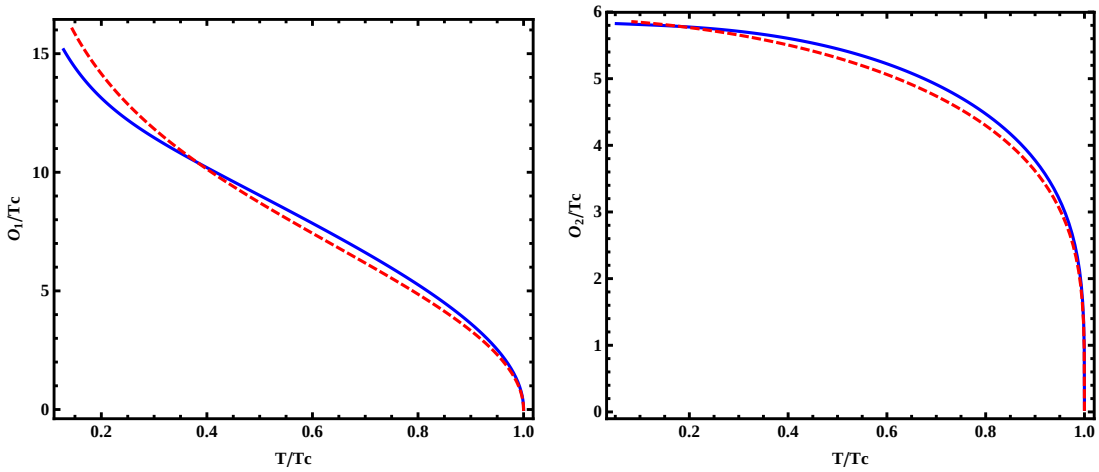

Figure 2.14: Condensate of the scalar operator as a function of the temperature for $\mathcal{O}_-$ (left) e $\mathcal{O}_+$ (right). Straight blue line is $f(\phi) = \cosh(\phi)$ and dashed red line is $f(\phi) = 1 + \phi^2/2$. In both cases the potential is $L^2V(\phi) = -6 - \phi^2$. For the two operators we have $T_c \sim 0.182\sqrt{\rho}$ and $T_c \sim 0.135\sqrt{\rho}$ respectively.

We conclude with a brief discussion of the conductivity in the probe limit. The perturbation equation reads

$$A_x''(r) + \left(\frac{g'}{g} + \frac{1}{f(\phi)}\frac{df(\phi)}{d\phi}\phi'\right) A_x'(r) + \frac{\omega^2}{g^2}A_x(r) = 0\,. \tag{2.68}$$

Using the AdS/CFT definition (2.52) we obtain the results shown in Figure 2.15 for the real and imaginary part of the conductivity and for the condensate $\mathcal{O}_+$. Similar results are obtained for $\mathcal{O}_-$. The increase of $\sigma(\omega)$ at low frequencies, typical of the dilaton black holes considered in this chapter, is evident in the probe limit. In fact it grows exponentially as $T/T_c \to 0$ but this is an artifact of the probe limit and disappears once the back reaction is taken into account (see Fig. 2.8). Finally, since translation invariance is broken by the AdS-S background, the imaginary part does not have a pole but vanishes for $\omega \to 0$. From the dispersion relations it follows that the DC conductivity is finite at $\omega = 0$ in the probe limit.

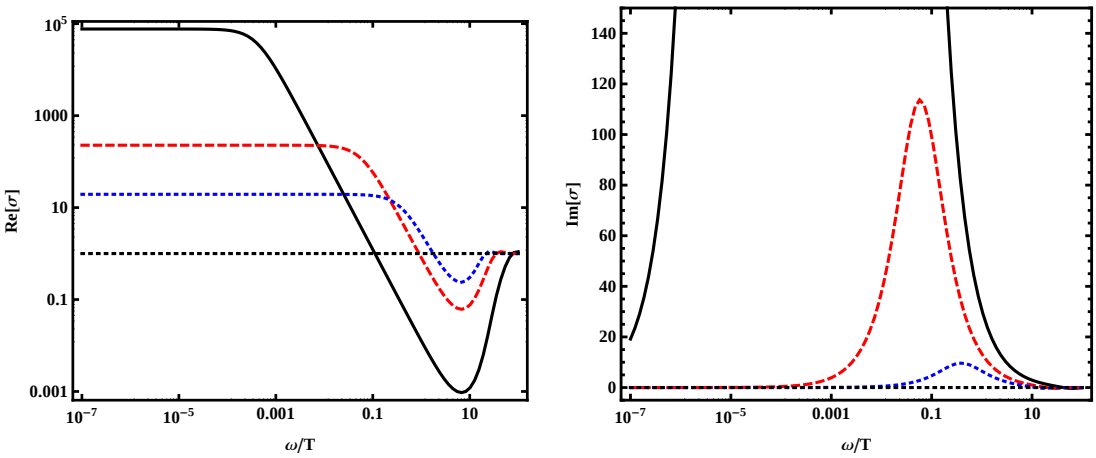

Figure 2.15: Real (left) and imaginary (right) part of the conductivity in a log scale for $\mathcal{O}_+$ and $f(\phi) = \cosh(\phi)$. $T/T_c \sim 0.14\,, 0.3\,, 0.5\,, 1$ from bottom to top.

Chapter 3

Phase transitions and holography of dyonic dilatonic black holes in AdS

Results discussed in the previous chapter are extended by including a constant magnetic field. We study dyonic black holes in Einstein-Maxwell-dilaton gravity in four-dimensional anti-de Sitter spacetime which admit a dyonic Reissner-Nordström black hole solution. The role played by the magnetic field in the inset of the phase transition is discussed. Scalar condensation occurs only below a critical magnetic field. By computing the electrical conductivity we study the Hall effect and cyclotron resonances in the new phase. We also consider purely magnetic solutions, obtained By applying the electromagnetic duality, both at finite and at vanishing temperature.

Contents

3.1 Introduction

In this chapter we extend the results discussed in Chapter 2 by considering dyonic black holes in Einstein-Maxwell-dilaton gravity in Anti de Sitter (AdS) spacetime. Our main motivations are similar to those discussed in Chapter 2 and we refer to Section 2.1 for a general overview of the role of dilatonic black holes within the gauge/string duality.

The inclusion of magnetic fields in the dual field theory is important for several reasons. First, real materials are usually immersed in external– or generate their own – magnetic fields. Second, magnetic fields can be ad-hoc engineered and applied in laboratories and, as we shall see, they can be used to prevent or to catalyze phase transitions. Thus, it is important to discuss their effects in the dual theory and how they affect transport properties such as the electrical conductivity.

Holographic field theories immersed in a magnetic fields are currently investigated in the context of holographic superconductors (HSCs) [86]. Important phenomena observed in real superconductors, such as the Meissner effect and vortex production, can have a holographic description in terms of dyonic black holes. Holographic properties of dyonic black holes in Einstein-Maxwell-dilaton gravity were investigated in Ref. [87]. Many common phenomena, such as the Hall effect or cyclotron resonances, naturally emerge from the dual picture.

Here, as in Chapter 2, we consider the action for Einstein-Maxwell-dilaton gravity

$$S = \int d^4x\sqrt{-G}\,\mathcal{L} = \int d^4x\sqrt{-G}\left(R - \frac{f(\phi)}{4}F^2 - \frac{1}{2}\partial^\mu\phi\partial_\mu\phi - V(\phi)\right), \tag{3.1}$$

and we focus on scalar potentials of the following form:

$$V(\phi) = -\frac{6}{L^2} + \frac{\beta}{2L^2}\phi^2 + \mathcal{O}(\phi^3)\,, \qquad f(\phi) = 1 + \frac{\alpha}{2}\phi^2 + \mathcal{O}(\phi^3)\,. \tag{3.2}$$

Although this choice does not include exponential potentials, $f(\phi) \sim e^{\alpha\phi}$, discussed in Ref. [87], it allows for dyonic Reissner-Nordström Anti de Sitter (AdS-RN) black holes when $\phi \equiv 0$. Building on Chapter 2, we wish to construct hairy dyonic black holes dressed with scalar fields and to investigate phase transitions between these and AdS-RN black holes.

3.2 Instability of dyonic AdS-RN black holes

Let us consider the following ansatz:

$$ds^2 = -g(r)e^{-\chi(r)}dt^2 + \frac{dr^2}{g(r)} + r^2(dx^2+dy^2)\,, \tag{3.3}$$

$$A = A_0(r)dt + A_3(r,x)dy\,, \qquad A_3(x,y) = B(r)C(x) \tag{3.4}$$

$$\phi = \phi_0(r)X(x)\,. \tag{3.5}$$

From the holographic perspective we are interested in a three-dimensional boundary theory at constant charge density and with an external magnetic field $B(r \to \infty)$ perpendicular to the (x,y) plane. It is straightforward to show that the equations of motion stemming from the action (3.1) require $X(x) = 1$ and $A_3(r,x) = Bx$ (where $B = \text{const}$) hence, for convenience, we define $\phi_0 \equiv \phi$. Interestingly, the magnetic field and the scalar condensate are homogeneous at infinity. This is not the case in HSCs, when a minimal coupling $\propto qA_\mu\phi$ between a charged scalar and the Maxwell field is considered [86] (q being the charge of the scalar field). In fact, for HSCs immersed in a magnetic field, the transverse dependence of the scalar field, parametrized by $X(x)$, is that of an harmonic oscillator whose eigenvalues $\propto qB$. Consequently, the scalar field is confined in a boundary region along the x direction, $\Delta x \propto qB$. On the other hand, in the case under consideration, the scalar field is homogeneous on the boundary.

The relevant equations of motion become

$$\phi'' + \left(\frac{g'}{g} - \frac{\chi'}{2} + \frac{2}{r}\right)\phi'(r) - \frac{1}{g}\frac{dV}{d\phi} + \frac{1}{2g}\frac{df}{d\phi}\left({A_0'}^2 e^{\chi} - \frac{B^2}{r^4}\right) = 0\,, \tag{3.6}$$

$$(r^2 e^{\frac{\chi}{2}} f(\phi)A_0')' = 0\,, \qquad \chi' + \frac{r\phi'^2}{2} = 0\,, \tag{3.7}$$

$$\frac{\phi'^2}{4} + \frac{f(\phi)}{4g}\left({A_0'}^2 e^{\chi} + \frac{B^2}{r^4}\right) + \frac{g'}{rg} + \frac{1}{r^2} + \frac{V(\phi)}{2g} = 0\,, \tag{3.8}$$

and the magnetic field B only affects the first and last equation. Due to Eqs. (3.2), the AdS-RN black brane is solution of the equations of motion with

$$g = -\frac{2M}{r} + \frac{Q^2+B^2}{4r^2} + \frac{r^2}{L^2}\,, \qquad \chi = 0\,, \qquad A = \left(\frac{Q}{r} - \frac{Q}{r_h}\right) dt + Bxdy\,, \qquad \phi = 0\,. \quad (3.9)$$

Hereafter, with some abuse of notation, we shall use the term "black holes" in a wider sense, also including solutions with a planar topology (as the one in Eq. 3.9) which are properly black branes.

In Chapter 2 we have shown that the AdS-RN solution is unstable under scalar perturbations. Here, in order to understand the role played by the magnetic field, we again compute scalar perturbations around the AdS-RN black hole (3.9). Fourier-expanding the perturbation as in Eq. (2.12), we find a Schroedinger-like equation in the same form as Eq. (2.13), but in this case the effective mass reads

$$m^2_{\rm eff}(r) = m^2 - \alpha\frac{Q^2-B^2}{2r^4}\,, \quad (3.10)$$

where $m^2 = \beta/L^2$ is the squared mass of the scalar field. Interestingly, the contributions of the magnetic and of the electric field are opposite. While the electric field contributes to a tachyonic mode in the effective mass (hereafter we focus on $\alpha > 0$), the magnetic field gives a *positive* contribution and stabilizes the AdS-RN black hole. For dyonic black holes, these two contributions are competitive and an instability can arise only when $Q^2 > B^2$. Thus, there exists a critical value B_c of the magnetic field above which the effective square mass is positive

$$B_c = \pm Q\,. \quad (3.11)$$

Remarkably, the existence of a critical value, which we shall confirm in the next section by solving numerically the equations of motion, can be related to a sort of Meissner effect, which occurs even in a homogeneous condensate and even if the new phase is not superconducting (the scalar condensate preserves $U(1)$ symmetry of the model (3.1)). As discussed in Ref. [47], electric currents in the dual theory are non-dynamical, *i.e.* they do not generate any electromagnetic field (see however Ref. [88] for an interesting method to introduce dynamical gauge fields in the dual theory). Therefore, strictly speaking the Meissner effect, *i.e.* the expulsion of a magnetic field from a superconductor, cannot occurs in this simple holographic configuration. However, the opposite effect – the expulsion of a scalar condensate by the external magnetic field – can be interpreted in a similar way, as discussed for example in Ref. [86]. In the HSCs, this inverse-Meissner effect depends on the charge q of the scalar field (cf. Fig. 6 in Ref. [47]). On the other hand, in our case the critical magnetic field (3.11) is independent from the coupling α. Regardless the value of α, dyonic AdS-RN black branes with $B > B_c = Q$, are stable against scalar perturbations.

3.3 Dyonic black holes with scalar hairs

Dyonic dilatonic black hole solutions of Eqs. (3.6)-(3.8) can be obtained numerically by using the same procedure discussed in detail in Chapter 2. Namely, we expand the background fields close to the horizon $r = r_h$ and then integrate the system of ODEs up to infinity, where we

impose suitable boundary conditions. As discussed in Chapter 2, the asymptotic behavior of the scalar field near the AdS boundary reads

$$\phi \sim \frac{\mathcal{O}_-}{r^{\Delta_-}} + \frac{\mathcal{O}_+}{r^{\Delta_+}}\,, \qquad \Delta_\pm = \frac{3 \pm \sqrt{9 + 4m^2L^2}}{2} \tag{3.12}$$

and we simply choose one of the independent parameters at the horizon, say $A_0(r_h)$, such that $\mathcal{O}_1 = 0$ or $\mathcal{O}_2 = 0$. When $B = 0$, this is enough to describe the solution in terms of a single parameter, *e.g.* the scalar field at the horizon ϕ_h or, more physically, the black hole temperature T. Numerically, this is implemented by finding the root of a function of a single variable

$$\mathcal{F} : A_0(r_h) \longrightarrow \mathcal{O}_i\,, \tag{3.13}$$

where $\mathcal{O}_i$ is the result of the numerical integration and the solution describes two different boundary theories for $i = 1$ or $i = 2$ respectively. However when $B \neq 0$, the series expansion near the horizon depends on three independent parameters, ϕ_h, $A_0(r_h)$ and B. At given ϕ_h (*i.e.* at given temperature) we find the roots of two functions of two variables,

$$\begin{cases} \mathcal{F}_1 : \{A_0(r_h), B\} \longrightarrow \mathcal{O}_i\,, \\ \mathcal{F}_2 : \{A_0(r_h), B\} \longrightarrow B/\rho - C\,, \end{cases} \tag{3.14}$$

where now both $\mathcal{O}_i$ and B/ρ result from the numerical integration and C is the value of the constant magnetic field in units of ρ. Numerical solutions are characterized by two parameters: the black hole temperature $T/\sqrt{\rho}$ and the magnetic field $C = B/\rho$. The functions $\mathcal{F}_i$ are known only numerically and they are not necessarily polynomials. In order to find their roots we implemented a bidimensional extension of Müller method, recently proposed in Ref. [89]. Building on Chapter 2, we can follow the evolution of the condensate as a function of the temperature at fixed magnetic field. Alternatively, we can also study the evolution of the condensate as a function of the magnetic field at fixed temperature. In this case, we should find the roots of the following functions

$$\begin{cases} \mathcal{F}_1 : \{A_0(r_h), B\} \longrightarrow \mathcal{O}_i\,, \\ \mathcal{F}_2 : \{A_0(r_h), B\} \longrightarrow T/\sqrt{\rho} - C\,, \end{cases} \tag{3.15}$$

where now C is the constant temperature in units of $\sqrt{\rho}$.

We refer to Ref. [89] for further details on the numerical method, now focusing on some results. As discussed in Chapter 2, we focus both on polynomial forms and on hyperbolic cosine forms for the potentials $V(\phi)$ and $f(\phi)$ (cf. Table 2.1). Results are qualitatively similar regardless the precise form of the potentials and they only show a strong dependence on the second derivatives $\beta \equiv V''(\phi)|_{\phi=0}L^2$ and $\alpha \equiv f''(\phi)|_{\phi=0}$. Thus, in presenting results, we shall not discriminate between one or the other form of the potentials. Moreover we shall present solutions obtained by imposing $\mathcal{O}_1 = 0$ and, for concreteness, we focus on $\beta = m^2L^2 = -2$. Nevertheless, analogously to what we found in Chapter 2, imposing $\mathcal{O}_2 = 0$ or choosing different values of β gives qualitatively similar results.

First, we report that this method is successful in constructing dyonic AdS black holes coupled to a neutral scalar field. We name these solutions dyonic and dilatonic black holes (DDBHs). From the holographic point of view, DDBHs are dual to field theories in which a neutral scalar operator acquires a non-vanishing expectation value below a critical temperature

and below a critical magnetic field. In fact, in Fig. 3.1 we show the scalar condensate both as a function of the temperature for several values of constant magnetic field (left panel) and as a function of the magnetic field for several values of constant temperature (right panel). From the left panel of Fig. 3.1, the critical temperature decreases for increasing values of the magnetic field.

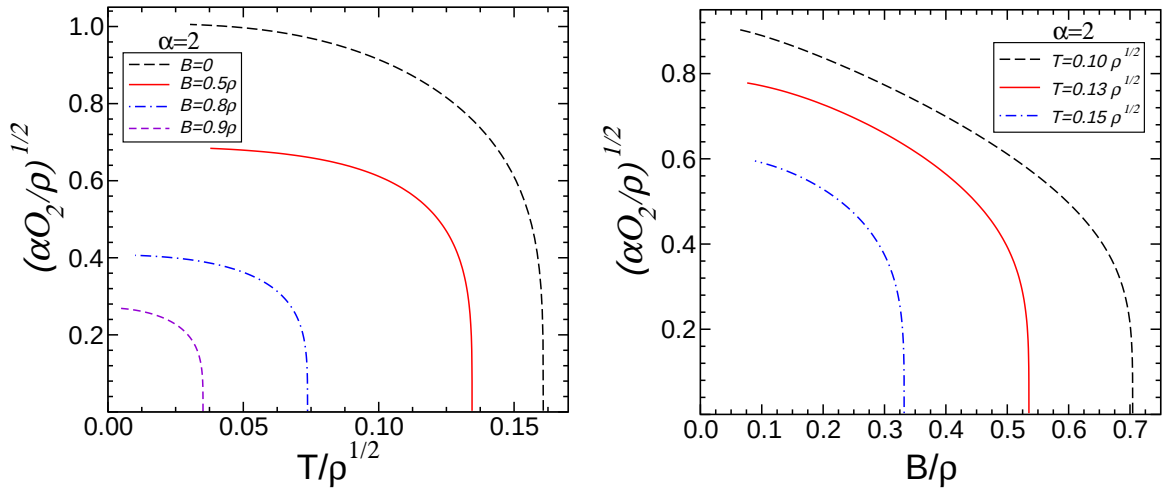

Figure 3.1: Left panel: scalar condensate as a function of the temperature for selected values of the magnetic field B. Right panel: scalar condensate as a function of the magnetic field for selected values of the temperature. In both plots we used $f(\phi) = \cosh(2\phi)$.

More precisely the phase diagram of DDBHs, *i.e.* the critical temperature as a function of the magnetic field, is shown in Fig. 3.2 for several values of the coupling α. Numerical results confirms our analytic expectation: $T_c = 0$ when $B = B_c = \rho$, *i.e.* the scalar operator does not condense at any finite temperature above the critical magnetic field B_c. The critical value B_c does not depend neither on the coupling constant α nor on the precise forms for $f(\phi)$ and $V(\phi)$ (if they behave as prescripted in Eq. (3.2)).

Remarkably, Fig. 3.2 is qualitatively similar to Fig. 8 in Ref. [47], which describes the (qualitative) phase diagram for HSCs immersed in a magnetic field. Conversely, the phase diagram for DDBHs shown in Fig. 3.2 is exact and it is in agreement with the schematic illustration depicted in Ref. [47].

Another interesting issue is the nature of the phase transition shown in the right panel of Fig. 3.1. At $B \sim B_c$ the scalar condensate has the typical behavior for second order phase transitions in the mean-field approximation,

$$O_i \sim (B - B_c)^{1/2} \,. \tag{3.16}$$

In the language of superconductivity, this means that the material is a type II superconductor. The same behavior is observed in real high-T_c superconductors and it is correctly reproduced by holographic models [42]. However, in the case at hand, the new phase is not superconducting, as the neutral scalar operator preserves $U(1)$ symmetry of the action 3.1. Nevertheless, also in this case we observe a sort of inverse-Meissner effect: as we increase an external magnetic field, a second order phase transition occurs, and the condensate disappears.

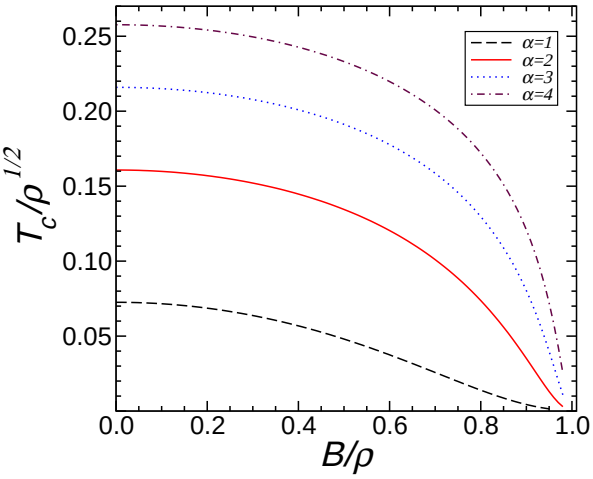

Figure 3.2: Critical temperature as a function of the ratio B/ρ for several coupling constants α. Numerical results confirms our analytical expectation: $T_c = 0$ when $B = B_c = \rho$. Regions below the curves mark the parameter space where the scalar operator condenses.

3.3.0.a Free energy of dyonic and dilatonic black holes

As discussed above, a sufficiently strong magnetic field will destroy the new phase. The critical magnetic field can be also understood in terms of energetics. The difference in free energy between the normal and the dressed phase reads

$$\frac{B_c^2(T)V}{8\pi} = F_{\text{normal}}(T) - F_{\text{dressed}}(T)\,, \tag{3.17}$$

where V is the "volume" of (x, y) plane and F is the free energy. We wish to compare the free energy between different phases – with and without the scalar condensate – and in presence of a magnetic field. As for the normal phase, the free energy of a dyonic AdS-RN black hole (see for instance Ref. [47]) reads

$$\frac{F_{\text{RN}}}{V} = \frac{F_{\text{normal}}}{V} = -r_h^3 + \frac{3(\rho^2 + B^2)}{4r_h}\,, \tag{3.18}$$

where we have set $L = 1$. In order to compute the free energy for DDBHs we start from the Euclidean action

$$S_E = -\int d^4x\sqrt{-g}\mathcal{L}\,, \tag{3.19}$$

where $\mathcal{L}$ is the Lagrangian written in Ref. (3.1) and computed for the numerical DDBH solution. Following Ref. [47] we write the Einstein tensor,

$$G_{xx} = \frac{r^2}{2}(\mathcal{L} - R) + \frac{B^2 f(\phi)}{2r^2}\,, \tag{3.20}$$

thus we obtain

$$\mathcal{L} = -G_t^t - G_r^r - \frac{B^2 f(\phi)}{r^4} = -\frac{1}{r^2}\left[(rg)' + (rge^{-\chi})'e^{\chi}\right] - \frac{B^2 f(\phi)}{r^4}\,, \tag{3.21}$$

where we have used the scalar curvature $R = -G_a^a$ computed for the dressed solution. Then the Euclidean action reads

$$S_E = \int d^3x \int_{r_h}^{\infty} dr \left(2rge^{-\chi/2}\right)' + B^2 \int d^3x \int_{r_h}^{\infty} dr \frac{f(\phi)e^{-\chi/2}}{r^2} \,. \tag{3.22}$$

The first radial integral in the equation above is a total derivative and it is straightforwardly performed. However, it diverges as $r \to \infty$ and must be regularized by suitable counterterms [47]. On the other hand, the contribution arising from the magnetic field is finite. Defining the regularized Euclidean action $\tilde{S}_E$, the thermodynamical potential in the gran-canonical ensemble reads

$$\Omega = T\tilde{S}_E = \int d^2x \left(\frac{-\epsilon L^2}{2} + B^2 \int_{r_h}^{\infty} dr \frac{f(\phi)e^{-\chi/2}}{r^2} \right) , \tag{3.23}$$

where we have defined the (compact) Euclidean time $\int dt = 1/T$, and we have used the boundary conditions ($\mathcal{O}_1 = 0$ or $\mathcal{O}_2 = 0$) for the scalar field.

Finally, the free energy of DDBHs in the canonical ensemble simply reads ($L = 1$)

$$F_{\rm DD} = F_{\rm dressed} = \Omega + \mu Q = V \left(-\frac{\epsilon}{2} + \mu\rho + B^2 \int_{r_h}^{\infty} dr \frac{f(\phi)e^{-\chi/2}}{r^2} \right) . \tag{3.24}$$

In the particular case of AdS-RN black holes ($f(\phi) \equiv 1$ and $\chi \equiv 0$) the integral above is trivial and $F_{\rm DD}$ reduces to Eq. (3.18). In the left panel of Fig. 3.3 we compare $F_{\rm RN}$ and $F_{\rm DD}$ as functions of the temperature for selected values of the constant magnetic field. Free energies refers to solutions with same mass and same charge. Although not shown, for both solutions the specific heat $c = -T\partial_T F/V$ is positive for any value of B. For $T < T_c$ and $B < B_c$, AdS-RN black holes always have a larger free energy, for any value of B and, roughly speaking, the magnetic field shifts up the free energy of both solutions. Therefore, when $T < T_c$ and $B < B_c$, DDBHs are energetically favored. However, the magnetic field contributes to decrease the difference $\Delta F = F_{RN} - F_{\rm DD}$. Such a difference grows as $T \to 0$ but, for fixed temperature, it decreases as the magnetic field increases. This is consistent with our analytical understanding, since we expect $\Delta F = 0$ both when $T = T_c$ and when $B = B_c = \rho$.

Finally, we want to study the magnetic susceptibility

$$\Xi = \left. \frac{\partial^2 F}{\partial B^2} \right|_{\rho,T} , \tag{3.25}$$

where the derivative is performed on solutions at constant temperature and constant charge density. Therefore in the numerical integration, we find the roots of Eqs. (3.15), in order to compute the free energy as a function of the magnetic field at constant temperature and finally we obtain the magnetic susceptibility by performing the derivative in Eq. 3.25. Results are shown in the right panel of Fig. 3.3. The free energy and the magnetic field are normalized as $F \to F/\rho^{3/2}$ and as $B \to B/B_c$, respectively. Hence, the magnetic susceptibility is normalized as $\Xi \to \Xi\rho^{3/2}/B_c^2$.

The magnetic susceptibility Ξ is order 1 and positive. This means that the boundary theory is strongly diamagnetic. This is analog to the AdS-RN case where $\Xi \sim 9/(8\pi T) > 0$ for $B \ll M$ and $\rho \ll M$ [47].

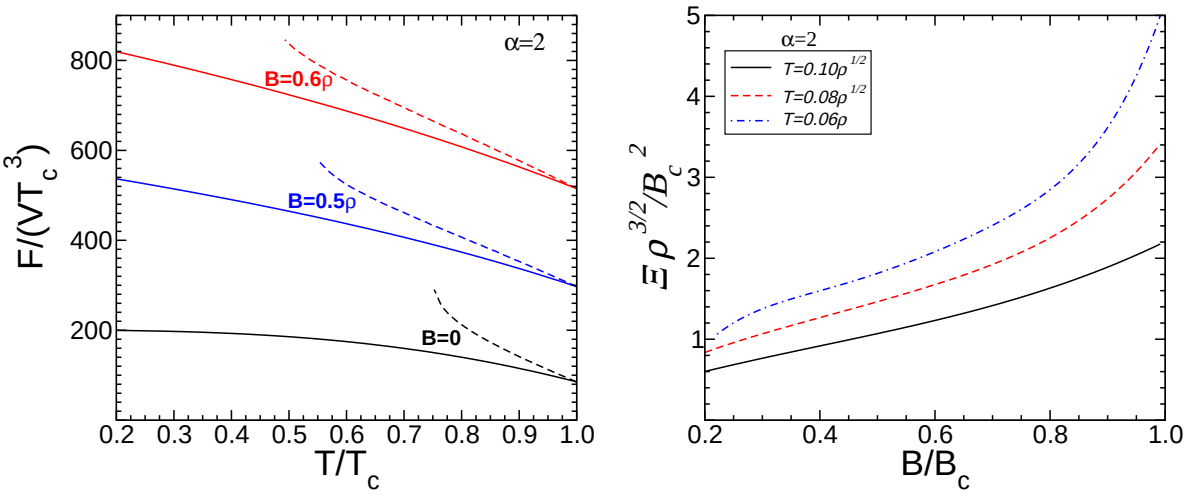

Figure 3.3: Left panel: free energy for DDBHs (straight lines) and for AdS-RN black holes (dashed lines) as a function of the temperature for selected values of the magnetic field. Right panel: normalized magnetic susceptibility for DDBHs as a function of the magnetic field. We use $f(\phi) = \cosh(2\phi)$.

3.4 Holographic properties of DDBHs

In this section we compute some holographic properties of DDBHs. In particular we discuss the effects of the magnetic field on the electrical conductivity in the dual theory, such as the Hall effect and cyclotron resonances. As discussed in detail in Chapter 2, the AdS/CFT correspondence provides a precise prescription for the electrical conductivity, in terms of bulk electromagnetic perturbations.

Electromagnetic perturbations of a dyonic black hole are fairly involved. In fact, following the same notation used in Chapter 2, the minimal set of perturbations includes $A_x(r)$, $A_y(r)$, $g_{tx}(r)$ and $g_{ty}(r)$, which are coupled through the electric and magnetic field. These perturbations have been studied using AdS-RN black holes as background metric [90, 91]. Here we want to extend those calculations to the case of dilatonic background.

Let us consider perturbations with vanishing 3-momentum,

$$A_\mu = (A_0, 0, 0, Bx) + (0, 0, A_x(r), A_y(r))e^{-i\omega t}\,,$$

and similarly for the metric perturbations, $g_{tx}(r)e^{-i\omega t}$ and $g_{ty}(r)e^{-i\omega t}$. Linearized Einstein and Maxwell equations provide a set of four coupled equations. Two of them are

$$A_x'' + A_x'\left(\frac{f'(\phi)}{f(\phi)}\phi' + \frac{g'}{g} - \frac{\chi'}{2}\right) + \omega^2\frac{e^\chi}{g^2}A_x = -e^\chi\left[\frac{iB\omega}{r^2g^2}g_{ty} + \frac{A_0'}{g}\left(g_{tx}' - \frac{2}{r}g_{tx}\right)\right], \quad (3.26)$$

$$g_{tx}' - \frac{2}{r}g_{tx} + f(\phi)A_0'A_x = -\frac{iBf(\phi)}{r^2\omega}\left[A_0'g_{ty} + ge^{-\chi}A_y'\right], \quad (3.27)$$

and the other two can be obtained from those above by changing $x \leftrightarrow y$ and $B \leftrightarrow -B$. Notice that terms proportional to B couple perturbations along the x direction to those along the y direction. When $B = 0$ equations above decouple and reduce to a single Schroedinger-like equation (cf. Section 2.5.2). In the case at hand, such a decoupling does not occur and

we are left with a system of four coupled ODEs. Furthermore notice the presence of terms proportional to B/ω. When $B \neq 0$ these terms diverges in the $\omega \to 0$ limit, whereas they vanish if $B = 0$. Thus, as first noted in Ref. [90], the limits $B \to 0$ and $\omega \to 0$ do not commute.

We integrate the system of ODEs above numerically, starting from a series expansion close to the horizon, where we impose purely ingoing waves. The asymptotical behaviors read

$$A_x \sim a_x^{(0)} + a_x g_h^{\nu}\,, \qquad A_y \sim a_y^{(0)} + a_y g_h^{\nu}\,, \tag{3.28}$$

$$g_{tx} \sim g_x^{(0)} + g_x g_h^{\nu+1}\,, \qquad g_{ty} \sim g_y^{(0)} + g_y g_h^{\nu+1}\,, \tag{3.29}$$

with $g_h = g(r_h) \sim (r - r_h)$, $\nu = -i\omega e^{\chi_h/2}/g'(r_h)$ and where a_x, $a_x^{(0)}$, g_x, $g_x^{(0)}$, a_y, $a_y^{(0)}$, g_y and $g_y^{(0)}$ are constant. Requiring that the expansions above are solutions of the equations of motion at first order provides a relation among some constants

$$g_x^{(0)} = -\frac{i a_y^{(0)}\omega}{r_h^2 B}\,, \qquad g_x = f(\phi_h)\frac{a_y B e^{-\chi_h/2} + a_x A'_{0h} r_h^2}{i e^{\chi_h/2} r_h^2 \omega - r^2 g'_h}\,, \tag{3.30}$$

$$g_y^{(0)} = \frac{i a_x^{(0)}\omega}{r_h^2 B}\,, \qquad g_y = f(\phi_h)\frac{-a_x B e^{-\chi_h/2} + a_y A'_{0h} r_h^2}{i e^{\chi_h/2} r_h^2 \omega - r^2 g'_h}\,, \tag{3.31}$$

Moreover, due to the linearity of Eq. (3.26)-(3.27), one parameter (say a_x) can be rescaled away and the solution will eventually depend on three independent parameters only, say ($a_x^{(0)}$, $a_y^{(0)}$ and a_y). Interestingly, the electrical conductivities turn out to be independent from these three parameters, signaling an underlying symmetry of the perturbation equations.

3.4.1 Conductivity in the dual field theory

Before presenting results of the numerical integration, we briefly review some analytical results obtained in Refs. [90, 91] for the electrical conductivity in theories dual to AdS-RN black holes. In that case, Eqs. (3.26)-(3.27) can be solved analytically in the hydrodynamical limit, *i.e.* when $\omega/T \ll \mu/T, B/T^2$. The linear response in the dual theory is governed by the following equations

$$\begin{pmatrix} \vec{J} \\ \vec{Q} \end{pmatrix} = \begin{pmatrix} \boldsymbol{\sigma} & \boldsymbol{\alpha} \\ \boldsymbol{\alpha} T & \bar{\boldsymbol{\kappa}} \end{pmatrix} \begin{pmatrix} \vec{E} \\ -\vec{\nabla} T \end{pmatrix}\,. \tag{3.32}$$

where $\vec{\nabla} T$ is the temperature gradient, $\vec{E}$ is the electric field, $\vec{J}$ is the electric current and $\vec{Q}$ is the heat current. Defining

$$\sigma_\pm = \sigma_{xy} \pm i\sigma_{xx}\,, \qquad \hat{\alpha}_\pm = \alpha_{xy} \pm i\alpha_{xx}\,, \qquad \bar{\kappa}_\pm = \bar{\kappa}_{xy} \pm i\bar{\kappa}_{xx}\,, \tag{3.33}$$

the response functions read [91]

$$\pm\,\hat{\alpha}_\pm T\omega = (B \mp \mu\omega)\sigma_\pm - \rho\,, \tag{3.34}$$

$$\pm\bar{\kappa}_\pm T\omega = \left(\frac{B}{\omega} \mp \mu\right)\hat{\alpha}_\pm T\omega - sT + mB\,. \tag{3.35}$$

Thus, once $\sigma_\pm$ are computed, the remaining transmission coefficients can be obtained from the equations above. In the hydrodynamical limit the diagonal and off-diagonal components

of the conductivity can be computed via the AdS/CFT duality and they read [91]

$$\sigma_{xx} = \sigma_Q \frac{\omega(\omega + i\gamma + i\omega_c^2/\gamma)}{(\omega + i\gamma)^2 - \omega_c^2}\,, \qquad \sigma_{xy} = -\frac{\rho}{B}\frac{-2i\gamma\omega + \gamma^2 + \omega_c^2}{(\omega + i\gamma)^2 - \omega_c^2}\,,$$

with

$$\omega_c = \frac{B\rho}{\epsilon + \mathcal{P}}\,, \quad \gamma = \frac{\sigma_Q B^2}{\epsilon + \mathcal{P}}\,, \quad \sigma_Q = \frac{(sT)^2}{(\epsilon + \mathcal{P})^2} \tag{3.36}$$

and where $\mathcal{P}$ and ϵ are the pressure and the energy density respectively. Rotational invariance implies $\sigma_{xx} = \sigma_{yy}$ and $\sigma_{xy} = -\sigma_{yx}$. The electrical conductivity has a pole at $\omega = \omega_c - i\gamma$, corresponding to a damped cyclotron frequency. Furthermore, in the $\omega \to 0$ limit, the DC diagonal component σ_{xx} vanished due to the Lorentz invariance, whereas the DC off-diagonal component is the well-known Hall conductivity:

$$\sigma_{xx} = 0\,, \qquad \sigma_{xy} = \frac{\rho}{B}\,. \tag{3.37}$$

Notice that $\sigma_{xy} \to \infty$ as $B \to 0$. This is due to the non-commuting limits $\omega \to 0$ and $B \to 0$.

It is relevant to study whether and how the scalar condensate affects these results. Unfortunately, in our model, the background solution is only known numerically and this prevents to derive explicit formulas. However we can still use the AdS/CFT prescription in order to relate the conductivity to the asymptotic behavior of the numerical solution. Following Ref. [91], the conductivity is

$$\sigma_\pm = \sigma_{xy} \pm i\sigma_{xx} = \frac{\mathcal{B}_x \pm i\mathcal{B}_y}{\mathcal{E}_x \pm i\mathcal{E}_y}\,, \tag{3.38}$$

where

$$\mathcal{B}_i = -\lim_{r\to\infty} \epsilon_{ij} A_j'\,, \qquad \mathcal{E}_i = \lim_{r\to\infty}\left[f(\phi)\left(i\omega A_i - \frac{B}{r^2}\epsilon_{ij} g_{tj}\right)\right]\,, \tag{3.39}$$

are the spatial component of δF and $\delta \star F$ respectively ($F = F_0 + \delta F$ and $\star F = \star F_0 + \delta \star F$ being its dual). The coefficients $A_i^{(0)}$, $A_i^{(1)}$ and $g_{ti}^{(0)}$ are related to the asymptotic behavior of the electromagnetic and metric perturbations at infinity:

$$A_i \to A_i^{(0)} + \frac{A_i^{(1)}}{r}\,, \qquad g_{ti} \to g_{ti}^{(0)} r^2\,, \quad i = x, y \tag{3.40}$$

Thus, once perturbation equations are solved with suitable boundary conditions, Eq. (3.38) gives the AdS/CFT prescription for the conductivity in the dual theory.

3.4.2 Numerical results

In Fig. 3.4 the conductivities σ_{xx} and σ_{xy} as functions of the frequency are shown both for the AdS-RN case ($T = T_c$) and for the DDBH at $T < T_c$. The numerical procedure previously discussed has been tested by reproducing numerical results in Ref. [91] for vanishing scalar field. A general result that can be inferred from our simulations is that, regardless the scalar condensate, the DC conductivities are the same as those computed for AdS-RN black holes [91],

$$\sigma_{xx}(\omega \to 0) = 0\,, \qquad \sigma_{xy}(\omega \to 0) = \frac{\rho}{B}\,, \tag{3.41}$$

at any $T \leq T_c$. While the first result ($\sigma_{xx} = 0$) simply arises from the Lorentz invariance, it is interesting that the Hall effect is not affected by the scalar condensate.

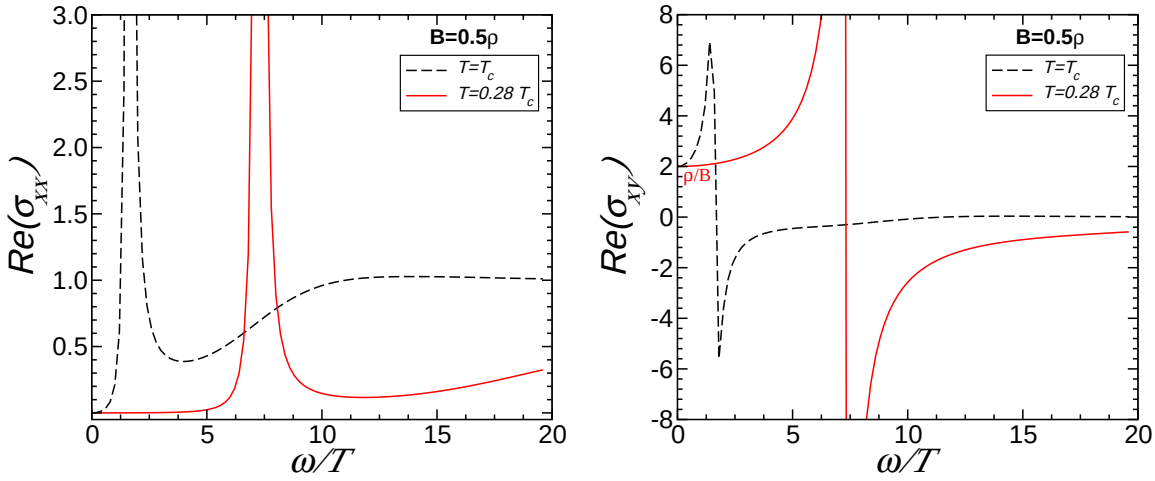

Figure 3.4: Conductivity in the dual theory (left panel: σ_{xx}, right panel: σ_{xy}) as a function of the frequency for $B/\rho = 0.5$ and $f(\phi) = \cosh(2\phi)$. The conductivity in the normal phase at $T = T_c$ (AdS-RN black hole) is compared to that in the dressed phase at $T \sim 0.28 T_c$ (DDBH).

However, as shown in Fig. 3.4, the AC behavior is fairly rich. Depending on the temperature and on the magnetic field, sharp peaks appear in the real part of σ_{xx} and σ_{xy}. These correspond to the cyclotron frequencies discussed in Ref. [91] for AdS-RN black holes. Our results confirm and extend that analysis to the case of DDBHs. Indeed the scalar condensate affects the cyclotron frequency. In Fig. 3.5 we show the location of the pole of σ_{xx} as a function of the temperature for selected values of B. Both the real and the imaginary part of the frequency strongly depend on the magnetic field (notice that plots in Fig. 3.5 are logarithmic). The real part increases exponentially as the temperature is lowered, while the imaginary part, as a function of the temperature, has a less clear behavior, being monotonic at large values of B and having a non-monotic behavior at small values of B.

3.5 Purely magnetic black holes

We now focus on the purely magnetic case, hereafter setting $Q = 0$. Notice that a background solution characterized by coupling function, electric charge and magnetic charge $\{f(\phi), Q, B\}$ is related, via the electromagnetic duality, to the same background solution with $\{1/f, B, -Q\}$. In particular, due to the electromagnetic duality, the charged dilatonic black holes found in Chapter 2 are also valid magnetic solutions with $f \to 1/f$ and $B \to -Q$.

For dyonic AdS-RN black holes, the duality acts on the electromagnetic tensor only

$$\frac{2\pi}{g^2} F \to \star F \equiv \frac{\sqrt{-g}}{4} \epsilon_{\mu\nu\rho\sigma} F^{\rho\sigma} dx^\mu \wedge dx^\nu \,. \tag{3.42}$$

Perturbation equations for δF ($F = F_0 + \delta F$) are most conveniently written in terms of $\mathcal{B}_a$ and $\mathcal{E}_a$, (cf. Eq. (3.39)) which are the spatial component of δF and of $\delta \star F$ respectively. The electromagnetic duality acts as $\mathcal{E} \to \mathcal{B}$ and $\mathcal{B} \to -\mathcal{E}$. It follows from Eq. (3.38) that the

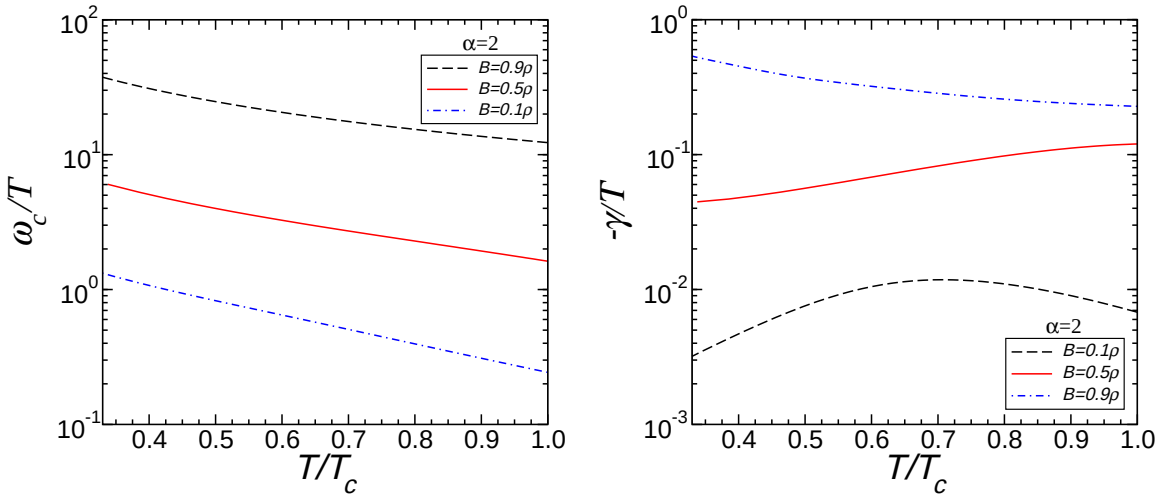

Figure 3.5: Real (left panel) and imaginary (right panel) of the damped cyclotron frequency $\omega = \omega_c + i\gamma$ as functions of the temperature for selected values of the magnetic field B/ρ.

duality transforms the conductivities as

$$\sigma_\pm(Q,B) \to \frac{1}{\sigma_\pm(B,-Q)}\,. \tag{3.43}$$

Equation (3.43) has been recently extended to the case of $SL(2,R)$ invariant theories with a dilaton and an axion [87]. Also in that case, starting from a purely electrical background, a transformation similar to (3.43) holds

$$\sigma_\pm(0,-Q) = \frac{1}{\sigma_\pm(Q,0)}\,, \tag{3.44}$$

which does not explicitly depend on the dilaton and axion fields. Although Eq. 3.44 has been derived for $SL(2,R)$ invariant theories [87] and the action (3.1) is not invariant under $SL(2,R)$, nevertheless the same derivation should apply to our case as well. We shall explicitly confirm this statement below, by computing the conductivity in the purely magnetic case.

3.5.1 Electrical conductivity

Notice that, in the rest of this section, we keep referring to the coupling $f(\phi)$ for convenience, although the duality transformation acts on the action 3.1 by transforming $f \to h = 1/f$. The real non-minimal coupling for solutions obtained by the duality is $h(\phi)$ and not $f(\phi)$.

For purely magnetic background, setting $A_0(r) \equiv 0$, Eqs. (3.26)-(3.27) (and those obtained from them by $x \leftrightarrow y$ and $B \leftrightarrow -B$) decouple pairwise. Equations for A_x and g_{ty} read

$$A_x'' + A_x'\left(\frac{f'(\phi)}{f(\phi)}\phi' + \frac{g'}{g} - \frac{\chi'}{2}\right) + \omega^2\frac{e^\chi}{g^2}A_x + \frac{iB\omega}{r^2 g^2}e^\chi g_{ty} = 0\,, \tag{3.45}$$

$$g_{ty}' - \frac{2}{r}g_{ty} - \frac{iBf(\phi)}{r^2\omega}ge^{-\chi}A_x' = 0\,, \tag{3.46}$$

and those for A_y and g_{tx} can be again obtained by $x \leftrightarrow y$ and $B \leftrightarrow -B$. The two equations above can be written in a single Schroedinger-like equation for $A_x'(r)$, i.e. they are third order in $A_x(r)$. In fact, we define

$$\Psi(r) = A_x'(r) = \frac{e^{\chi/2}}{g(r)\sqrt{f(\phi)}} Y(r)\,, \tag{3.47}$$

and the equation for $Y(r)$ reads

$$Y''(r) + \left(\frac{g'}{g} - \frac{\chi'}{2}\right) Y'(r) + \frac{e^{\chi}}{g^2}\left[\omega^2 - V(r)\right] Y(r) = 0\,, \tag{3.48}$$

or, equivalently,

$$Y''(z) + \left[\omega^2 - V(r)\right] Y(z) = 0\,, \tag{3.49}$$

where z is the tortoise coordinate defined by $dr/dz = e^{\chi(r)/2}/g(r)$ and the explicit form of the potential reads

$$V(r) = g(r)e^{-\chi}\left\{\frac{B^2 f(\phi)}{r^4} - \frac{g}{2}\frac{f'}{f}\left[\phi'' + \left(\frac{f''}{f'} - \frac{3}{2}\frac{f'}{f}\right)\phi'^2 + \left(\frac{g'}{g} - \frac{\chi'}{2}\right)\phi'\right]\right\}\,. \tag{3.50}$$

Interestingly in the equation above, the magnetic field dependence is B^2 and the contribution $\propto 1/\omega$ of Eq. (3.46) cancels out, *i.e.* in the purely magnetic case the limits $B \to 0$ and $\omega \to 0$ commute.

For a magnetic AdS-RN black hole ($\chi \equiv 0$ and $\phi \equiv 0$) the potential simply reduces to

$$V_{RS} = g_{RS}(r)\frac{B^2}{r^4}\,, \tag{3.51}$$

and it is positive defined. Moreover $V_{RS} = 0$ at the horizon and at infinity. From general quantum mechanics theorems it follows that such a Schroedinger potential does not admit bound states, *i.e.* the magnetic AdS-RN black hole is stable. The potential for purely magnetic dilatonic solutions (obtained via the electromagnetic duality) is shown in Fig. 3.6. Also in this case the potential is positive defined and the background solution is stable.

3.5.1.a Numerical results

We have computed the conductivity $\sigma_+(\omega)$ in a purely electrical background and compared it to the inverse of the conductivity in a purely magnetic background $\sigma_+^{-1}(\omega)$ with $f(\phi) \to 1/f(\phi)$. A representative example is shown in Fig. 3.7. The two functions coincide confirming our analytical expectations (cf. Eq. 3.44 and Ref. [87]).

Notice that, although the electromagnetic duality straightforwardly relates the conductivities $\sigma_\pm$ in an electrical and in a magnetic background, nevertheless the transformation is non-trivial. In fact, being $\sigma_\pm$ a complex quantity, the real part of the frequencies σ_{xx} and σ_{xy} in the magnetic case turns out to depend both on the real and on the imaginary part of the frequencies σ_{xx} and σ_{xy} in the electrical case. Namely, the explicit transformations read

$$\sigma^M_{xy} = \frac{\sigma^E_{xy}}{\left(\sigma^E_{xx}\right)^2 + \left(\sigma^E_{xy}\right)^2}\,, \qquad \sigma^M_{xx} = -\frac{\sigma^E_{xx}}{\left(\sigma^E_{xx}\right)^2 + \left(\sigma^E_{xy}\right)^2}\,, \tag{3.52}$$

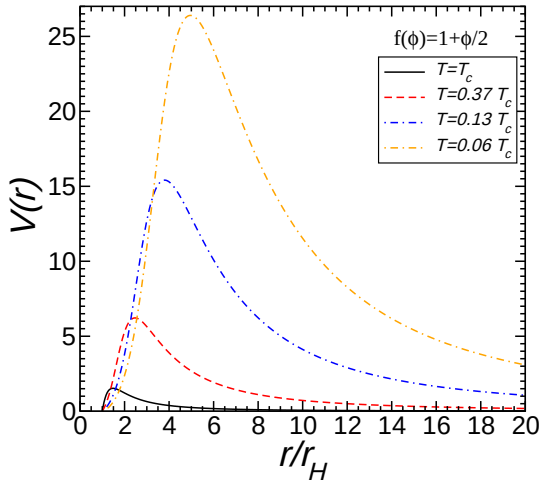

Figure 3.6: Schroedinger potential for electric perturbations around purely magnetic dilatonic black holes (cf. Eq. (3.50).

where σ^M and σ^E are the electrical conductivities in the magnetic and electrical case, respectively and all the quantities are complex. Therefore the explicit dependence of, say, Re $\left[\sigma^M_{xx}\right]$ can be non-trivial. In the left panel of Fig. 3.8 we show the AC conductivity $\sigma_{xx}(\omega)$ for a purely magnetic background solution. From our numerical simulations we can infer the general behavior

$$\sigma_{xy}(\omega) \equiv 0\,, \qquad \sigma_{xx}(\omega = 0) = 0\,, \tag{3.53}$$

that is, for any temperature, also the off-diagonal component of the DC conductivity is vanishing. However, as shown in the left panel of Fig. 3.8, the AC diagonal component has a maximum whose location and height depend on the temperature. These peaks in the conductivity may signal the excitation of some bound state in the dual field theory. Thus σ^M, although related to σ^E by the electromagnetic duality, can show some non-trivial features, which we shall throughly investigate in future works.

3.5.2 Purely magnetic solutions at $T = 0$

As discussed in Chapter 2, extremal black holes are most conveniently studied using the following ansatz

$$ds^2 = -\lambda(r)dt^2 + \frac{1}{\lambda(r)}dr^2 + H^2(r)\left(dx^2 + dy^2\right)\,, \tag{3.54}$$

Purely magnetic background solutions can be again obtained from purely electrical background solutions discussed Chapter 2, via the electromagnetic duality. In this new ansatz perturbation equations around dyonic background solutions read

$$A_x'' + A_x'\left(\frac{f'(\phi)}{f(\phi)}\phi' + \frac{\lambda'}{\lambda}\right) + \frac{\omega^2}{\lambda^2}A_x + \frac{iB\omega}{H^2\lambda^2}g_{ty} + \frac{A_0'}{\lambda}\left(g_{tx}' - \frac{2H'}{H}g_{tx}\right) = 0\,, \tag{3.55}$$

$$g_{tx}' - \frac{2H'}{H}g_{tx} + f(\phi)A_0'A_x + \frac{iBf(\phi)}{H^2\omega}\left[A_0'g_{ty} + \lambda A_y'\right] = 0\,, \tag{3.56}$$

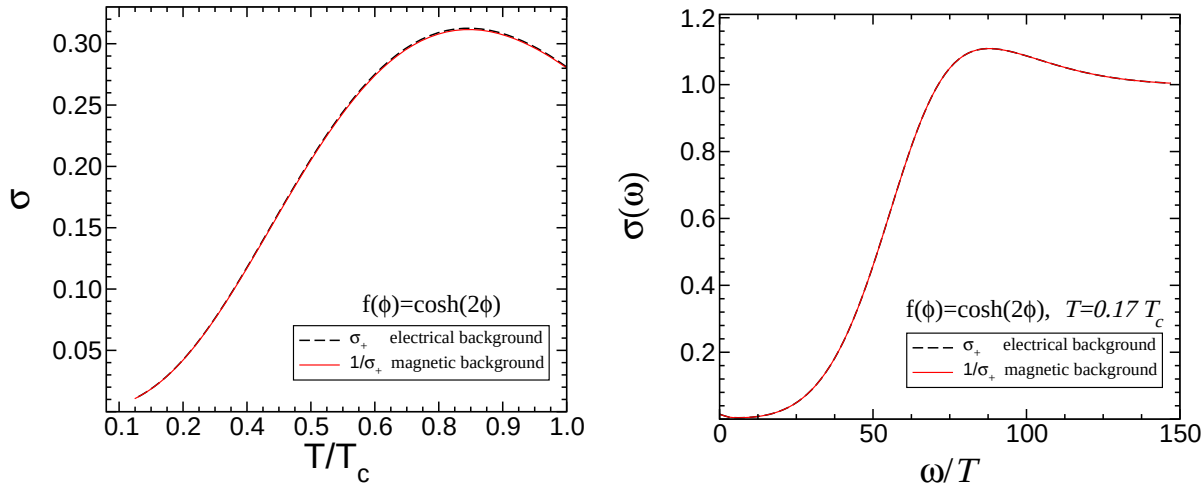

Figure 3.7: Left panel: comparison between the DC conductivity in an electrical and in a magnetic background. The black dashed line is $\mathrm{Re}[\sigma_+(\omega=0)]$ in the purely electrical background, whereas the red straight line is $\mathrm{Re}[{\sigma_+}^{-1}(\omega=0)]$ in the purely magnetic background with $f(\phi)\to 1/f(\phi)$. Right panel: the same but showing the AC conductivity at $T=0.17T_c$ as a function of the frequency. As proved in Ref. [87], the two functions coincide. The magnetic solution is obtained via the electromagnetic duality from an electrical solution with $f(\phi)=\cosh(\alpha\phi)$.

plus those obtained via $x\leftrightarrow y$ and $B\leftrightarrow -B$. As previously discussed, in a purely magnetic background ($A_0(r)\equiv 0$) perturbation equations decouple and can be written as a Schroedinger equation. Following the derivation presented in the previous sections, we obtain

$$Y''(z)+\left[\omega^2-V(r)\right]Y(z)=0\,, \tag{3.57}$$

$$V(r)=\lambda(r)\left\{\frac{B^2 f(\phi)}{H^4}-\frac{\lambda}{2}\frac{f'}{f}\left[\phi''+\left(\frac{f''}{f'}-\frac{3}{2}\frac{f'}{f}\right)\phi'^2+\frac{g'}{g}\phi'\right]\right\}\,. \tag{3.58}$$

where $dr/dz=1/\lambda(r)$ and $Y(r)=\sqrt{f(\phi)}\lambda(r)\Psi(r)$. The conductivity as a function of the frequency at $T=0$ is shown in the right panel of Fig. 3.8.

3.6 Discussion

In this and in the previous chapter we have discussed in considerable detail charged dilatonic black branes arising from the model (3.1) and phase transitions between these and AdS-RN solutions. While in Chapter 2 we focused on purely electrical branes both at finite and vanishing temperature, in this chapter we have investigated the inclusion of a constant magnetic field.

Thermodynamical properties of dilatonic black branes and AdS-RN black branes are quite different. For example at zero temperature, DDBHs have zero entropy, whereas AdS-RN black holes have a finite (and large) entropy. Nevertheless, we found that the scalar condensate does not affect the dual response to the magnetic field. In particular some transport properties of the dual theory, such as the Hall effect, are independent from the condensate, *i.e.* they are

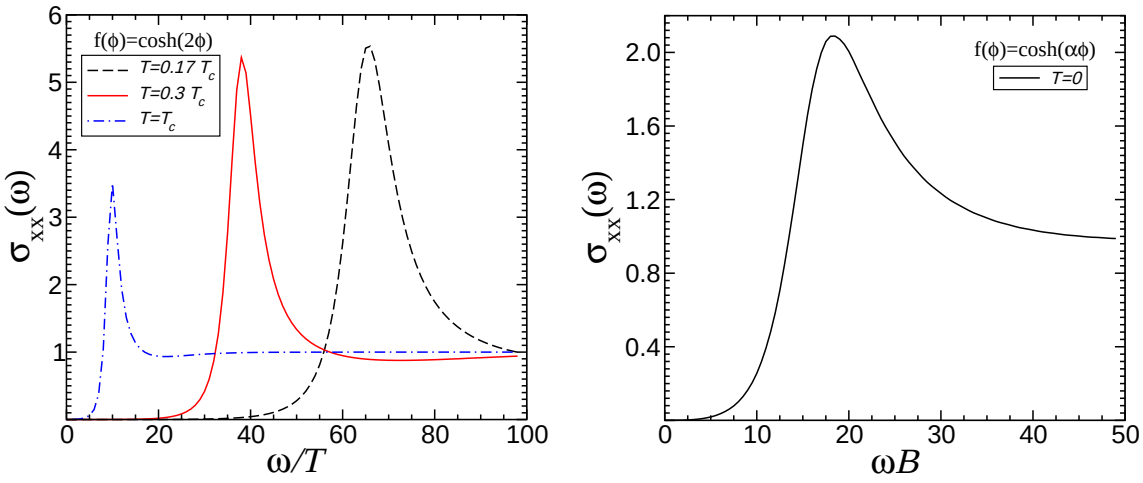

Figure 3.8: Left: AC conductivity in a purely magnetic background for several values of T/T_c and for $f(\phi) = \cosh(2\phi)$. Right: AC conductivity σ_{xx} for a purely magnetic dilatonic black hole at $T = 0$. The off-diagonal component vanishes, *i.e.* $\sigma_{xy} \equiv 0$. The magnetic solution is obtained via the electromagnetic duality from the purely electric dilatonic black hole with $f(\phi) = \cosh(\phi/\sqrt{3})$.

the same for DDBHs and for AdS-RN black branes. Other properties, such as the presence of cyclotron resonances, do not change qualitatively. When a magnetic field is switched on, the DC conductivities read $\sigma_{xx} = 0$ and $\sigma_{xy} = \rho/B$ at any temperature and regardless the scalar condensate. This prevents further investigations of the Drude peak and of the Kondo-like effect, which were observed in Chapter 2 and are reminiscent of a metallic behavior.

In fact the picture emerging from this chapter is more similar to a strongly coupled charged plasma, which behaves quite independently from the scalar condensate [87]. The model with $f(\phi) \sim e^{\alpha\phi}$ is consistent with this picture at $T \sim 0$ [87]. Our model behaves very similarly at $T \sim 0$, because near the horizon $\phi_h \to \infty$ at $T = 0$ and $f(\phi_h) = \cosh(\alpha\phi_h) \sim e^{\alpha\phi_h}$. Since the near-horizon geometry dominates the dynamics of linear perturbations, the zero temperature model loses the details arising from the quadratic expansion (3.2).

However, as discussed in Chapter 2, the model (3.1) is richer at finite temperature and it shows a metallic behavior when $B = 0$. Finally, at $B \neq 0$, the properties of the dual field theory are largely independent from the details of the model and, even at $T > 0$, they are similar to those of a charged plasma. Remarkably, the model at hand seems to interpolate between a metallic and a charged plasma behavior, depending on the temperature and on the magnetic field. This speculation is intriguing and undoubtedly worth pursuing.

Chapter 4

Breit-Wigner resonances and the quasinormal modes of anti-de Sitter black holes

The purpose of this short communication is to show that the theory of Breit-Wigner resonances can be used as an efficient numerical tool to compute black hole quasinormal modes. For illustration we focus on the Schwarzschild anti de Sitter (SAdS) spacetime. The resonance method is better suited to small SAdS black holes than the traditional series expansion method, allowing us to confirm that the damping timescale of small SAdS black holes for scalar and gravitational fields is proportional to r_+^{-2l-2}, where r_+ is the horizon radius. The proportionality coefficients are in good agreement with analytic calculations. We also examine the eikonal limit of SAdS quasinormal modes, confirming quantitatively Festuccia and Liu's [92] prediction of the existence of very long-lived modes in asymptotically AdS spacetimes. Our results are particularly relevant for the AdS/CFT correspondence, since long-lived modes presumably dominate the decay timescale of the perturbations.

Contents

4.1 Introduction

It is well known that quasi-bound states manifest themselves as poles in the scattering matrix, and as Breit-Wigner resonances in the scattering amplitude. Chandrasekhar and Ferrari made use of the form of the scattering cross section near these resonances in their study of gravitational-wave scattering by ultra-compact stars [93, 94]. In geometrical units ($c = G = 1$), the Regge-Wheeler potential $V(r)$ describing odd-parity perturbations of a Schwarzschild black hole (BH) of mass M has a peak at $r \sim 3M$. Constant-density stellar models may have a radius $R/M < 3$ (but still larger than the Buchdal limit, $R/M > 2.25$). When $R/M \lesssim 2.6$,

the radial potential describing odd-parity perturbations of the star (which reduces to the Regge-Wheeler potential for $r > R$) displays a local minimum as well as a maximum. If this minimum is sufficiently deep, quasi-stationary, "trapped" states can exist: gravitational waves can only leak out to infinity by "tunneling" through the potential barrier. Since the damping time of these modes is very long, Chandrasekhar and Ferrari dubbed them "slowly damped" modes [93].

For trapped modes of ultra-compact stars the asymptotic wave amplitude at spatial infinity $\Psi \sim \alpha \cos \omega r + \beta \sin \omega r$ has a Breit-Wigner-type behavior close to the resonance:

$$\alpha^2 + \beta^2 \approx \text{const} \left[(\omega - \omega_R)^2 + \omega_I^2 \right] , \tag{4.1}$$

where ω_I^{-1} is the lifetime of the quasi-bound state and ω_R^2 its characteristic "energy". The example of ultra-compact stars shows that the search for weakly damped quasinormal modes (QNMs) corresponding to quasi-bound states ($\omega = \omega_R - i\omega_I$ with $\omega_I \ll \omega_R$) is extremely simplified. We locate the resonances by looking for minima of $\alpha^2 + \beta^2$ on the $\omega = \omega_R$ line, and the corresponding damping time ω_I can then be obtained by a fit to a parabola around the minimum [93, 94].

Here we show that this "resonance method" can be used very successfully in BH spacetimes. The resonance method is particularly valuable in studies of asymptotically AdS BHs. The QNM spectrum of AdS BHs is related to thermalization timescales in a dual conformal field theory (CFT), according to the AdS/CFT conjecture [95]. Analytic studies of wave scattering in AdS BHs have previously hinted at the existence of resonances (see Fig. 9 in Ref. [96]); here we show that these are indeed Breit-Wigner resonances.

Various analytic calculations recently predicted the existence of long-lived modes in asymptotically AdS BH spacetimes [97, 92, 98]. These modes will presumably dominate the BH's response to perturbations, hence the thermalization timescale in the dual CFT. Since their existence may be very relevant for the AdS/CFT conjecture, we decided to investigate numerically these long-lived modes. In Section 4.2 we confirm the existence of quasi-bound states for small SAdS BHs, first predicted by Grain and Barrau [97], partially correcting some of their predictions. In Section 4.3 we re-analyze the eikonal limit of SAdS QNMs studied by Festuccia and Liu [92], finding excellent agreement with their calculations.

It may be useful to point out that a different but intimately related method (the complex angular momentum approach, a close kin of the theory of Regge poles in quantum mechanics) has been used in the past to study QNMs in asymptotically flat BH spacetimes [99, 100, 101]. Some aspects of the relation between the resonance method and the theory of Regge poles are illustrated, for example, in Ref. [94].

4.2 Quasi-bound states in SAdS black holes

In this chapter we will focus on SAdS BHs in four spacetime dimensions, but our results are trivially extended to higher dimensions. Scalar ($s = 0$), electromagnetic ($s = 1$) and vector-type (or Regge-Wheeler) gravitational perturbations ($s = 2$) of SAdS BHs are governed by a

second-order differential equation for a master variable Ψ [95, 102]:

$$f^2\frac{d^2\Psi}{dr^2}+ff'\frac{d\Psi}{dr}+\left(\omega^2-V_{l,s}\right)\Psi=0\,, \tag{4.2}$$

$$V_{l,s}=f\left[\frac{l(l+1)}{r^2}+(1-s^2)\left(\frac{2M}{r^3}+\frac{4-s^2}{2L^2}\right)\right], \tag{4.3}$$

where $f=r^2/L^2+1-r_0/r$, L is the AdS radius, r_0 is related to the horizon radius r_+ through $r_0/L=(r_+/L)^3+r_+/L$, and we assume that the perturbations depend on time as $e^{-i\omega t}$. As usual, we define a "tortoise" coordinate r_* by the relation $dr/dr_*=f$ (so that $r_*\to-\infty$ as $r\to r_+$) .

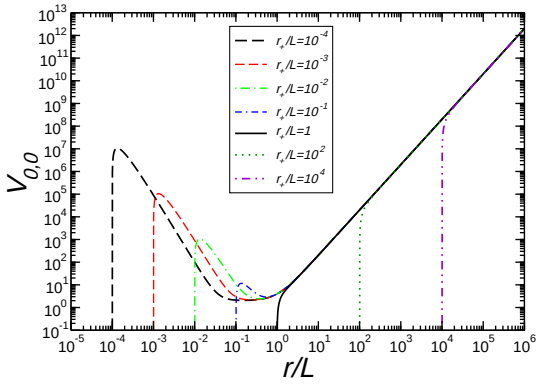

Figure 4.1: Potential for scalar field ($s=0$) perturbations of a SAdS background with $l=0$. Different lines refer to different values of r_+/L. A potential well develops for small BHs ($r_+/L<1$).

The potential for scalar-field perturbations of SAdS BHs is shown in Fig. 4.1 for different values of r_+/L, ranging from "large" BHs with $r_+/L\sim10^4$ to "small" BHs with $r_+/L\sim10^{-4}$. Notice how a potential well of increasing depth and width develops in the small BH limit ($r_+/L\ll1$).

Close to the horizon, where the potential $V_{l,s}\to0$, we require ingoing-wave boundary conditions:

$$\Psi\sim e^{-i\omega r_*}\,,\quad r_*\to-\infty\ (r\to r_+)\,. \tag{4.4}$$

Near spatial infinity ($r\to\infty$) the asymptotic behavior is

$$\Psi_{s=0}\sim Ar^{-2}+Br\,,\quad \Psi_{s=1,\,2}\sim A/r+B\,. \tag{4.5}$$

Regular scalar-field perturbations should have $B=0$, corresponding to Dirichlet boundary conditions at infinity. The case for electromagnetic and gravitational perturbations is less clear, and there are indications that Robin boundary conditions may be more appropriate in the context of the AdS/CFT correspondence [103, 104, 105, 106]. With this caveat, most calculations in the literature assume Dirichlet boundary conditions, so we choose to work with those.

In general, a solution with the correct boundary conditions at infinity behaves near the horizon ($r_* \to -\infty$) as

$$\Psi \sim A_{\rm in} e^{-i\omega r_*} + A_{\rm out} e^{i\omega r_*} \sim \alpha \cos \omega r_* + \beta \sin \omega r_* \,, \tag{4.6}$$

with $\alpha = A_{\rm out} + A_{\rm in}$, $\beta = i(A_{\rm out} - A_{\rm in})$. For increased numerical accuracy, in our calculations we use a higher-order expansion of the form

$$A_{\rm in}(1 + a(r - r_+))e^{-i\omega r_*} + A_{\rm out}(1 + a^*(r - r_+))e^{i\omega r_*} \,, \tag{4.7}$$

with

$$a = \frac{2l(l+1) + (s^2-1)\left((s^2-6)r_+^2/L^2 - 2\right)}{(2r_+/L)(1 + 3r_+^2/L^2 - 2i\omega r_+)} \,. \tag{4.8}$$

The problem is analogous to axial gravitational-wave scattering by compact stars, as long as we replace the "outgoing-wave boundary condition at infinity" in the stellar case by an "ingoing-wave boundary condition at the horizon" in the SAdS case (compare our Fig. 4.1 with Fig. 1 in Ref. [93]). Quasi-bound states for the potential (4.3) should show up as Breit-Wigner resonances of the form (4.1) for *real* ω.

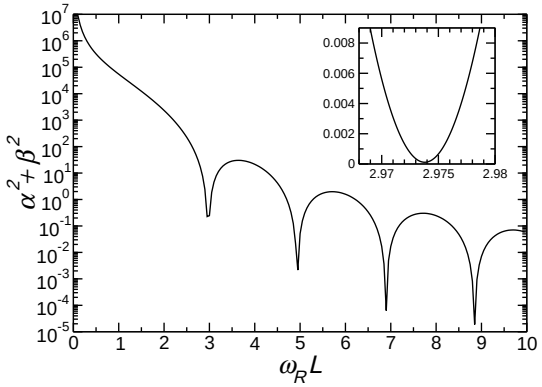

Figure 4.2: A plot of $\alpha^2 + \beta^2$ for scalar field SAdS perturbations with $l = 0$, $r_+/L = 10^{-2}$. Resonances are seen when $\omega_R \simeq 3 + 2n$, *i.e.* close to the resonant frequencies of the pure AdS spacetime. In the inset we show the behavior near the minimum, which allows us to extract the decay time by a parabolic fit.

Fig. 4.2 shows a typical plot of $\alpha^2 + \beta^2$ as a function of $\omega_R L$. The pronounced dips correspond to the location of a resonance, $\omega = \omega_R$, and the inset shows a zoomed-in view of one such particular resonance. Once a minimum in $\alpha^2 + \beta^2$ is located, the imaginary part ω_I can be found by a parabolic fit of $\alpha^2+\beta^2$ to the Breit-Wigner expression (4.1). Alternative (but equivalent) expressions are $\omega_I = -\beta/\alpha' = \alpha/\beta'$, where a prime stands for the derivative with respect to ω_R, evaluated at the minimum [93, 94]. We used these three different expressions to estimate numerical errors in the computed quasinormal frequencies. In the next subsections we briefly report on our results for $s = 0$ and $s = 2$, respectively.

4.2.1 Scalar field perturbations

The series solution method presented by Horowitz and Hubeny [95] was used by Konoplya in Ref. [107] to compute quasinormal frequencies of small SAdS BHs. The series has very poor convergence properties for $r_+/L < 1$, and QNM calculations in this regime take considerable computational time. As seen in Fig. 4.1, the potential for small SAdS BHs is able to sustain quasi-bound states, so we expect the resonance method to be well adapted to the study of small BHs.

Table 4.1: The fundamental $l = 0$ QNM frequencies for small SAdS BHs for selected values of r_+/L. The series solution data is taken from Ref. [107]. In the table, $\delta\omega_R\, L \equiv 3 - \omega_R\, L$.

	series		resonance	
L/r_+	$\delta\omega_R\, L^2/r_+$	$\omega_I\, L^3/r_+^2$	$\delta\omega_R\, L^2/r_+$	$\omega_I\, L^3/r_+^2$
12	3.064	9.533	2.992	9.662
20	2.922	7.720	2.912	7.840
30	2.805	6.660	2.802	6.714
50			2.700	5.952
100			2.610	5.471
200			2.580	5.266
500			2.560	5.158
1000			2.554	5.125
2000			2.550	5.109
5000			2.550	5.100

In Table 4.1 we list QNMs for $l = 0$ scalar field perturbations and for different BH sizes, comparing (where possible) results from the resonance method with Konoplya's series expansion calculation. A cubic fit of our data for $L/r_+ > 30$ yields $\omega_I\, L = 5.00 r_+^2/L^2 + 47.70 r_+^3/L^3$, a quartic fit yields $\omega_I = 5.09(r_+/L)^2 + 33.59(r_+/L)^3 + 485.09(r_+/L)^4$, and fits with higher order terms basically leave a and b unchanged with respect to the quartic fit. The numerical results are consistent with Horowitz and Hubeny's prediction that $\omega_I \propto r_+^2$, and they are in very good agreement with analytic predictions by Cardoso and Dias [108], who derived a general expression for the resonant frequencies of small BHs in AdS for $M\omega_R \ll 1$ regime. Setting $a = 0$ in Eq. (33) of Ref. [108], their result is

$$L\,\omega = l + 3 + 2n - i\omega_I L\,, \tag{4.9}$$

where n is a non-negative integer and

$$\omega_I\, L \simeq -\gamma_0 \left[(l+3+2n)\ (r_+/L)^{\,2l+2}\right]/\pi\,, \tag{4.10}$$
$$\gamma_0 \equiv \frac{2^{-1-6l}\,(l!)^2\,\Gamma\left[-l-1/2\right]^2\,\Gamma\left[5+2l+2n\right]}{(3+2n)(3+2l+2n)\Gamma\left[l+1/2\right]^2\,\Gamma\left[2+2n\right]}\,.$$

For $l = n = 0$ one gets $\omega_I = 16(r_+/L)^2/\pi \sim 5.09(r_+/L)^2$, in excellent agreement with the fits. For general l Eq. (4.9) predicts an r_+^{2+2l} dependence, in agreement with our results

for $l = 0,\ 1,\ 2$. Moreover we find excellent agreement with the proportionality coefficient predicted by Eq. (4.10). Higher overtones are also well described by Eqs. (4.9) and (4.10).

Our results show that the resonant frequency ω_R always approaches the pure AdS value in the small BH limit, generally confirming the analysis by Grain and Barrau [97]. However our numerics disagree with Grain and Barrau's semi-classical calculation of the monopole mode ($l = 0$). We find that all modes including the monopole reduce to pure AdS in the small BH limit. More precisely, as $r_+/L \to 0$ we find

$$\omega_R\, L = l + 3 + 2n - k_{ln}\, r_+/L\,, \quad n = 0,\ 1,\ 2,\ \ldots \tag{4.11}$$

with $k_{l0} \sim 2.6,\ 1.7,\ 1.3$ for $l = 0,\ 1,\ 2$, respectively.

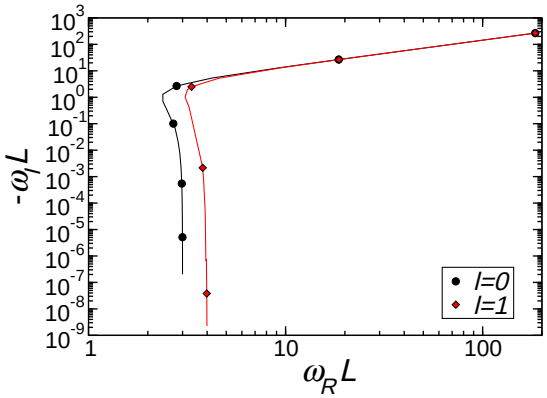

Figure 4.3: Track traced in the complex plane $(\omega_R L, \omega_I L)$ by the fundamental $l = 0, 1$ scalar field QNM frequencies as we vary the BH size r_+/L. Counterclockwise along these tracks we mark by circles and diamonds the frequencies corresponding to decreasing decades in r_+/L ($r_+/L = 10^2, 10^1, 10^0, 10^{-1}, ...$).

Our results for scalar field perturbations are visually summarized in Fig. 4.3, where we combine results from the resonance method and from the series solution (compare *e.g.* Fig. 1 of Ref. [109]). Modes with different l coalesce in the large BH regime (top-right in the plot), as long as $l \ll r_+/L$. As shown in Fig. 4.1, the potential for small SAdS BHs develops a well capable of sustaining quasi-stationary, long-lived modes. It should not be surprising that small and large BH QNMs have such a qualitatively different behavior.

4.2.2 Gravitational perturbations

We have also searched for the modes of Regge-Wheeler or vector-type gravitational perturbations. The potential (4.3) for gravitational perturbations of small BHs does not develop a local minimum. Nevertheless it develops a local maximum which, when imposing Dirichlet boundary conditions [see the discussion following Eq. (4.5)] can sustain quasi-bound states. For this reason we expect the resonance method to be useful also in this case.

For small BHs our numerical results agree with the following analytic estimate, derived under the assumption that $M\omega_R \ll 1$ [110]:

$$\omega_I\, L \simeq -\gamma_2\, (l+2+2n)\ (r_+/L)^{\,2l+2}\ , \tag{4.12}$$

with

$$\gamma_2 \equiv \frac{(l+1)(2+l+2n)\,\Gamma\left[1/2-l\right]\Gamma\left[l\right]^3\Gamma\left[3+l\right]\Gamma\left[2(2+l+n)\right]}{(l-1)^2(2n)!\Gamma\left[l+3/2\right]\Gamma\left[2l+1\right]\Gamma\left[2l+2\right]\Gamma\left[-1/2-l-2n\right]\Gamma\left[7/2+l+2n\right]} \tag{4.13}$$

For $n=0$ and $l=2$ this implies $\omega_I = 1024(r_+/L)^6/45\pi \simeq 7.24(r_+/L)^6$, while a fit of the numerics yields $\omega_I \sim 7.44(r_+/L)^6$. Again, $\omega_R\, L$ approaches the pure AdS value in the limit $r_+/L \to 0$:

$$\omega_R\, L = l+2+2n-k_{ln}\, r_+/L\,, \quad n=0,\,1,\,2,\,\ldots \tag{4.14}$$

For the fundamental $l=2$ mode we find $k_{20} \sim 1.4$.

4.3 Long-lived modes in the eikonal limit

A recent study of the eikonal limit ($l \gg 1$) of SAdS BHs suggests that very long-lived modes should exist in this regime [92]. Define $r_b > r_c$ to be the two real zeros (turning points) of $\omega_R^2 - p^2 f/r^2 = 0$. Then the real part of a class of long-lived modes in four spacetime dimensions is given by the WKB condition

$$2\int_{r_b}^{\infty} \frac{\sqrt{r^2\omega_R^2 - p^2 f}}{rf}\, dr = \pi\,(2n+5/2)\ , \tag{4.15}$$

where $p = l+1/2$. Their imaginary part is given by

$$\omega_I = \frac{\gamma\Gamma}{8\omega_R}\,, \quad \log\Gamma = 2i\int_{r_b}^{r_c} \frac{\sqrt{r^2\omega_R^2 - p^2 f}}{rf}\, dr\,. \tag{4.16}$$

The prefactor γ, not shown in Ref. [92], can be obtained by standard methods [111, 112] with the result

$$\begin{aligned} \gamma &= \left[\int_{r_b}^{\infty} \frac{\cos^2\chi}{\sqrt{\omega_R^2 - p^2 f/r^2}}\frac{dr}{f}\right]^{-1}\ , \\ \chi &\equiv \int_r^{\infty} \sqrt{\omega_R^2 - p^2 f/r^2}\,\frac{dr}{f} - \frac{\pi}{4}\,. \end{aligned} \tag{4.17}$$

The resonance method is well suited to analyze the eikonal limit, especially for small BHs (for large BHs the existence of a dip in the potential well requires very large values of l, which are numerically hard to deal with). In Table 4.2 we compare the WKB results against numerical results from the resonance method. Unfortunately machine precision limitations do not allow us to extract extremely small imaginary parts. The agreement with the WKB condition of Ref. [92] is remarkable, even for relatively small values of l. Our numerics conclusively confirm the existence of very long-lived modes in the SAdS geometry, but the numerical results for the damping timescales disagree by orders of magnitude with the corresponding results by Grain and Barrau [97]. A reanalysis of the assumptions implicit in their method would be useful to understand the cause of this disagreement.

Table 4.2: The QNM frequencies for a $r_+/L = 0.1$ BH for selected values of l, and comparison with the corresponding WKB prediction.

	WKB		resonance	
(l, n)	$\omega_R L$	$\log \omega_I L$	$\omega_R L$	$\log \omega_I L$
3,0	5.8668	-16.40	5.8734	-17.03
3,1	7.6727	-12.61	7.6776	-12.97
3,2	9.4189	-9.40	9.4219	-9.60
4,0	6.8830	-22.13	6.8889	-22.84
4,1	8.7139	-18.30	8.7184	-18.41
4,2	10.4960	-14.65	10.4996	-14.72
5,0	7.8945	-28.64	7.8997	-28.76
5,1	9.7426	-23.97	9.7466	-24.02
5,2	11.5482	-20.03	11.5516	-20.06

4.4 Conclusions and outlook

The method described here provides a reliable and accurate alternative to the series solution method [95], to be used in regimes where the former has poor convergence properties. Together, the two methods allow an almost complete characterization of the spectrum of BHs in AdS backgrounds, encompassing both small and large BHs. As an application of the method, we have explicitly confirmed the existence of the weakly damped modes predicted by Refs. [97, 92].

Extensions of the resonance method to higher-dimensional [95] and charged geometries [109, 113] should be trivial. Our techniques may be useful to verify the existence of the highly-real modes predicted by Ref. [98]. Finally, it would be interesting to investigate whether the resonance method described here is of any use to investigate the eikonal limit of QNMs in asymptotically flat BH spacetimes.

Chapter 5

Scalar hairs and exact vortex solutions in 3D AdS gravity

We investigate three-dimensional (3D) Anti-de Sitter (AdS) gravity coupled to a complex scalar field ϕ with self-interaction potential $V(|\phi|)$. We show that the mass of static, rotationally symmetric, AdS black hole with scalar hairs is determined algebraically by the scalar charges. We recast the field equations as a linear system of first order differential equations. Exact solutions, describing 3D AdS black holes with real spherical scalar hairs and vortex-black hole solutions are derived in closed form for the case of a scalar field saturating the Breitenlohner-Freedman (BF) bound and for a scalar field with asymptotic zero mass. The physical properties of these solutions are discussed. In particular, we show that the vortex solution interpolates between two different AdS_3 vacua, corresponding respectively to a $U(1)$-symmetry-preserving maximum and to a symmetry-breaking minimum of the potential V.

Contents

5.1 Introduction

One of the most striking features of black hole solutions in any space-time dimension is their uniqueness. Typically, they are characterized by a bunch of parameters, which are asymptotic charges associated with global symmetries of the solution. One question that has been debated since a long time is the uniqueness of black hole solutions in the presence of scalar fields. The issue is rather involved and a precise formulation of the no-hair conjecture, i.e the absence of nontrivial scalar field configurations in a black hole background, has not yet been given

[13, 114, 115]. In this context the relevant question concerns not only the presence of scalar hairs but also the possibility of having scalar charges independent from the black hole mass.

In recent years the investigation on black hole solutions with scalar hairs has been mainly focused on asymptotically AdS solutions [116]. The obvious reason behind such interest is the anti-de Sitter/conformal field theory ($\mathrm{AdS}_d/\mathrm{CFT}_{d-1}$) correspondence. The dynamics of scalar fields in the AdS_d background gives crucial information about the dynamics of the dual $(d-1)$-dimensional field theory. For instance, scalar hair configuration may interpolate between two different AdS geometries (one asymptotic and the other near-horizon) [117] similarly to what happens for charged AdS black holes [118, 119, 120].

An other important example is given by the recently discovered holographic superconductors [19, 47]. It is exactly a nontrivial scalar hair black hole solution of four-dimensional (4D) AdS gravity that breaks the $U(1)$ symmetry and is responsible for the superconducting phase transition in the dual three-dimensional (3D) field theory.

No-hair theorems for asymptotically AdS_d black hole have been discussed in Ref. [116] for the case $d > 3$. In that paper Hertog has shown that AdS black hole solutions with spherical scalar hairs can only exist if the positive energy theorem is violated. He was also able to construct numerical black hole solution with scalar hairs [116]. This result has played an important role for the development of holographic superconductors. In fact, the existence of 4D black holes dressed with a scalar hair is a necessary condition for having a phase transition in the dual theory.

In this chapter we will consider the $d = 3$ case. We will investigate the existence of black hole solutions with spherical scalar hairs in 3D AdS spacetime. Because three spacetime dimensions may allow for topologically non trivial global vortex configuration for the scalar field, we consider the case of a complex scalar field. The interest for global vortex solutions is not only motivated by the search for nontrivial scalar hairs. The study of black holes formed by global vortex is interesting by itself, as a particular case of black hole solutions supported by solitons. This kind of solutions may have some relevance in cosmology (as viable cosmic string candidates [121]), in the context of the AdS/CFT correspondence as nonperturbative 3D bulk solutions interpolating between different AdS vacua [117] and also as possible gravitational duals of condensed matter systems [122].

As a first step we analyze the dynamics of a complex scalar field ϕ with an arbitrary potential $V(|\phi|)$ in AdS_3 . We demonstrate a theorem stating that for static, rotationally symmetric black hole solutions with scalar hairs the black hole mass is determined algebraically by the scalar charges. As a second step we show that the field equations can be recast in the form of a system of first order linear differential equations for the scalar potential V and the spacetime metric. In principle, this allows us to find exact solutions of the field equations once the form of the scalar field is fixed. We use this method to find exact black hole solutions with spherical scalar hairs (both real and vortex-like) in the case of a scalar field saturating the BF bound [64] and for a scalar field with zero mass. These dressed black hole solutions are completely characterized by a scalar charge c and a vortex winding number n, the black hole mass being determined by c and n.

In the case of a scalar field saturating the BF bound, the potential $V(|\phi|)$ has a W, Higgs-like, form and a global $U(1)$ symmetry. We find that the black hole-vortex solutions interpolates between two AdS_3 geometries with different AdS lengths. Choosing appropriately the parameters of the potential these AdS_3 geometries correspond respectively to the $U(1)$-symmetry-preserving maximum and to the symmetry-breaking minimum of the Higgs

potential.

The structure of the chapter is as follows. In Sect 2. we discuss the dynamics of a complex scalar field in 3D AdS spacetime. In Sect. 3. we discuss no-hair theorems and prove the theorem stating that the mass of AdS_3 black holes with spherical scalar hairs is determined by c and n. In Sect. 4 we recast the field equations in linear form. In Sect. 5 we derive and discuss exact solutions of our system describing AdS_3 black holes endowed with a real scalar hair saturating the BF bound. We also investigate their thermodynamics and show that their free energy is always higher then the free energy of the Bañados-Teitelboim-Zanelli (BTZ) black hole [123]. In Sect. 6 we derive and discuss exact black hole-vortex solutions obtained for two different choices of the scalar field profile ($|\phi| = c/r$ and $|\phi| = c/r^2$) and discuss the linear stability of the BTZ background. Finally in Sect. 7 we present our concluding remarks.

5.2 Dynamics of a complex scalar field in 3D AdS spacetime

Let us consider 3D Einstein gravity coupled to a complex scalar field ϕ:

$$I = \frac{1}{2\pi}\int d^3x\sqrt{-g}\left[R - V(|\phi|) - \frac{1}{2}\partial_\mu\bar{\phi}\partial^\mu\phi\right], \tag{5.1}$$

where $V(|\phi|)$ is the potential for the scalar and for convenience we set the 3D gravitational constant G equal to $\frac{1}{8}$. The action (5.1) is invariant under global $U(1)$ transformations acting on the scalar field as $\phi \to e^{i\beta}\phi$. We are only interested in solutions for the 3D metric that are spherically symmetric and asymptotically AdS. Therefore, we require that V has a local extremum at $\phi = 0$ (corresponding to $r = \infty$), such that

$$V(0) = -\frac{2}{L^2}, \tag{5.2}$$

where L is the AdS length. For a scalar field in the AdS_d spacetimes stability of the asymptotic solution does not necessarily requires $\phi = 0$ to be a minimum. Only the weaker BF bound, $m^2L^2 \geq -(d-1)^2/4$, involving the squared mass $m^2 = V''(0)$ of the scalar (the prime denotes derivation with respect to $|\phi|$), must be satisfied. The scalar field must behave asymptotically as [a]

$$\varphi = \frac{c_-}{r^{\lambda_-}} + \frac{c_+}{r^{\lambda_+}} + ..., \tag{5.3}$$

where $\lambda_\pm = \frac{1}{2}\left(d - 1 \pm \sqrt{(d-1)^2 + 4m^2L^2}\right)$.

The field equations following from the action (5.1) are,

$$\begin{aligned} R_{\mu\nu} - g_{\mu\nu}V(|\phi|) - \frac{1}{4}\partial_\mu\bar{\phi}\partial_\nu\phi - \frac{1}{4}\partial_\mu\phi\partial_\nu\bar{\phi} &= 0, \\ \frac{1}{2\sqrt{-g}}\partial_\mu(\sqrt{-g}\partial^\mu\bar{\phi}) - \frac{\partial V(|\phi|)}{\partial\phi} &= 0, \\ \frac{1}{2\sqrt{-g}}\partial_\mu(\sqrt{-g}\partial^\mu\phi) - \frac{\partial V(|\phi|)}{\partial\bar{\phi}} &= 0. \end{aligned} \tag{5.4}$$

[a] When the BF bound is saturated the asymptotic behavior of the scalar field may involve a logarithmic branch, whose back reaction also modifies the asymptotic behavior of the metric [124]. However, throughout this chapter we will not consider this logarithmic branch.

We are interested in static, spherically symmetric solutions of these equations, therefore we choose the following ansatz for the metric:

$$ds^2 = -e^{2f(r)}dt^2 + e^{2h(r)}dr^2 + r^2 d\theta^2. \tag{5.5}$$

The most general form of the complex scalar compatible with spherical symmetry of the metric is given in terms of a real modulus field $\varphi(r)$ depending only on r and a phase depending linearly on θ. This is a consequence of the global $U(1)$ symmetry of the action (5.1). For topologically nontrivial spacetimes the phase becomes physically relevant and the proportionality factor is quantized. We will therefore use for ϕ the ansatz for static global vortices:

$$\phi(r,\theta) = \varphi(r)e^{in\theta}, \tag{5.6}$$

where n is the winding number of the vortex.

Using Eqs. (5.5) and (5.6) in the field equations (5.4) we obtain:

$$\begin{aligned}
V + \frac{1}{r}e^{-2h}\dot{f} + e^{-2h}\dot{f}^2 - e^{-2h}\dot{f}\dot{h} + e^{-2h}\ddot{f} &= 0 \\
-V + \frac{1}{r}e^{-2h}\dot{h} - e^{-2h}\dot{f}^2 + e^{-2h}\dot{f}\dot{h} - e^{-2h}\ddot{f} - \frac{1}{2}e^{-2h}\dot{\varphi}^2 &= 0 \\
-V - \frac{1}{r}e^{-2h}\dot{f} + \frac{1}{r}e^{-2h}\dot{h} - \frac{1}{2}\frac{n^2}{r^2}\varphi^2 &= 0 \\
-V' + e^{-2h}\left(\frac{1}{r} + \dot{f} - \dot{h}\right)\dot{\varphi} + e^{-2h}\ddot{\varphi} - \frac{n^2}{r^2}\varphi &= 0,
\end{aligned} \tag{5.7}$$

where the dot indicates the derivative with respect to the radial coordinate r. Only three of the four Eqs. in (5.7) are independent. For $\phi \neq const.$ the system can be drastically simplified by combining the first and second equation and multiplying the fourth by $\dot{\varphi}$,

$$\begin{aligned}
&\dot{h} + \dot{f} = \frac{1}{2}r\dot{\varphi}^2 \\
&\dot{h} - \dot{f} = r\left(V + \frac{1}{2}\frac{n^2}{r^2}\varphi^2\right)e^{2h} \\
&e^{-2h}\left[\left(\frac{1}{r} + \dot{f} - \dot{h}\right)\dot{\varphi}^2 + \dot{\varphi}\ddot{\varphi}\right] - \frac{1}{2}\frac{n^2}{r^2}(\dot{\varphi^2}) - \dot{V} = 0
\end{aligned} \tag{5.8}$$

5.3 Scalar hairs

In this section we will discuss no-hair theorems for the black solutions of 3D AdS gravity coupled with a scalar field. The field equations (5.7) admit as solution the BTZ black hole. This is obtained by setting $\varphi = 0$. Requiring that $V'(0) = 0$ and using Eq. (5.2), one easily finds:

$$e^{2f} = e^{-2h} = \frac{r^2}{L^2} - M, \tag{5.9}$$

where M is the black hole mass. One important question one can ask concerns the existence of 3D AdS black holes with scalar hairs, *i.e.* solutions of the system (5.8) with a non-constant

scalar, $\varphi \neq const.$ Furthermore, assuming such black holes with scalar hairs to exist, one would also like to know whether the scalar charges $c_{\pm}$ (see Eq. (5.3)) are independent from the black hole mass M.

In the 4D case it has been shown that the existence of AdS black holes with scalar hairs is crucially related with the violation of positive energy theorem [116]. Generically, this will be also true for the 3D case. Therefore, we expect black holes with scalar hairs to exist when the scalar mass squared m^2 becomes negative. In the next sections we will derive in closed form, exact black hole solutions with scalar hairs in the case of m^2 saturating the BF bound and for $m^2 = 0$. In this section we will be concerned with the second part of the question above. We will show that the following theorem holds:

If we couple 3D AdS gravity with a complex scalar field, the mass of static, rotationally symmetric solutions of the theory is determined algebraically by the scalar charges $c_{\pm}$ and by the winding number n.

In order to demonstrate this theorem we first solve for e^{2f} the system (5.8). One easily finds,

$$e^{2f} = a_0 e^{\int dr r\dot{\varphi}^2} \left[\dot{V} + r\left(V + \frac{1}{2}\frac{n^2}{r^2}\varphi^2\right)\dot{\varphi}^2 + \frac{1}{2}\frac{n^2}{r^2}(\dot{\varphi^2})\right]\left(\frac{1}{r}\dot{\varphi}^2 + \ddot{\varphi}\dot{\varphi}\right)^{-1}, \tag{5.10}$$

where a_0 is an integration constant, which can be scaled away by a rescaling of the time coordinate t. Because the g_{tt} component of the metric is a function of V, φ, n the mass of the solution is determined by $c_{\pm}, n$. This can be explicitly verified using in the previous equation the asymptotic expansion for the scalar field (5.3) and that for g_{tt},

$$e^{2f} = \frac{r^2}{L^2} - M + \mathcal{O}(\frac{1}{r}), \tag{5.11}$$

one immediately finds that M is determined, algebraically, by $c_{\pm}$ and n. If only a single fall-off mode for the scalar (only one independent scalar charge c) is present in Eq. (5.3), the black hole mass M is completely determined by the scalar charge c and by the winding number n.

5.4 Linear form of the field equations

In order to find exact solutions of the system (5.8) one has to choose a form of the potential $V(\varphi)$ for the scalar field. Alternatively, one can choose a form for the scalar field $\varphi(r)$ and solve (5.8) in terms of $h(r), f(r), V(r)$. This method has two main advantages. It allows to fix from the beginning the asymptotic behavior of the field φ. The field equations (5.8) can be rewritten in the form of a system of first order linear differential equations. This can be achieved introducing in Eqs. (5.8) the new variables S, Z

$$S = \alpha e^{-2h}, \quad Z = \alpha(V + \frac{1}{2}\frac{n^2}{r^2}\varphi^2 - Y_0), \tag{5.12}$$

where $\alpha(r) = e^{\int dr r\dot{\varphi}^2}$ and Y_0 is a solution of the equation $\dot{Y_0} + r\dot{\varphi}^2 Y_0 + \frac{n^2}{r^3}\varphi^2 = 0$. After eliminating f and using Eqs. (5.12), the second and third equations in (5.8) can be written in the form

$$\dot{S} - p(r)S + rZ + q(r) = 0, \quad \dot{Z} - g(r)S = 0, \tag{5.13}$$

where $p(r) = \frac{1}{2}r(\dot{\varphi})^2$, $q(r) = r\alpha Y_0$, $g(r) = \frac{1}{2r^2}(d/dr)(r^2\dot{\varphi}^2)$. This is a first order system of linear differential equations, which allows to determine the potential V and the metric function h once $\varphi(r)$ is given. The metric function f then follows just by integrating the first equation in (5.8).

Although this method for solving Eq. (5.8) can be used for a generic $\varphi(r)$, in this chapter we will mainly apply it to the case of a scalar field that saturates the BF bound in 3D, this implies $\lambda_+ = \lambda_- = 1$, $m^2 = -1/L^2 = m^2_{BF}$, i.e [a]

$$\varphi = \frac{c}{r}, \quad V''(0) = \frac{1}{2}V(0). \tag{5.14}$$

In the next sections we will derive in closed form exact black hole and vortex solutions corresponding a scalar field given by Eq. (5.14). We will also briefly consider solutions of Eqs. (5.8) in the case of scalar field with $m^2 = 0$, i.e for $\varphi = c/r^2$.

5.5 Black hole solutions with real scalar hairs

For a real scalar field, *i.e.* for $n = 0$, and φ given by Eq. (5.14) the method described in the previous section allows us to find the following solution of the system (5.8),

$$\begin{aligned} V(\varphi) &= -2\lambda_1 e^{\frac{\varphi^2}{2}} + \frac{\lambda_1}{2}\varphi^2 e^{\frac{\varphi^2}{2}} - 2\lambda_2 e^{\frac{\varphi^2}{4}}, \\ e^{-2h} &= r^2 e^{\frac{c^2}{4r^2}}\left(\lambda_1 e^{\frac{c^2}{4r^2}} + \lambda_2\right), \\ e^{2f} &= e^{-\frac{c^2}{2r^2}} e^{-2h}. \end{aligned} \tag{5.15}$$

where $\lambda_{1,2}$ are parameters entering in the potential. They define the cosmological constant of the AdS spacetime. In fact using Eq. (5.2) one finds

$$L^{-2} = \lambda_1 + \lambda_2. \tag{5.16}$$

Thus, AdS solution exist only for $\lambda_1 > -\lambda_2$. For $\lambda_1 > 0$ the potential has the W form typical of Higgs potentials. The maximum of the potential, corresponds to an AdS_3 vacuum with $\varphi = 0$ and $V(0) = -2/L^2$. It preserves the global $U(1)$ symmetry of the action (5.1). Conversely, the minimum of the potential corresponds to an other AdS_3 vacuum with $\varphi = \varphi_m$ and a different AdS length l, $-2l^{-2} = V(\phi_m)$. This vacuum breaks spontaneously the $U(1)$ symmetry of the action (5.1). The shape of the potential for $\lambda_1 > 0$ is shown in figure 1 (left).

For $\lambda_1 < 0$ the potential has only the symmetry preserving maximum at $\varphi = 0$ and no symmetry breaking minima. The shape of the potential for $\lambda_1 < 0, \lambda_2 > 0, \lambda_2 > |\lambda_1|$ is shown in figure 1 (right).

Let us now consider the metric part of the solution (5.15). The solution describes a black hole only for $\lambda_1 < 0, \lambda_2 > 0$, which in view of Eq. (5.16) requires $\lambda_2 > |\lambda_1|$. As expected, the black hole mass M is determined in terms of the scalar charge c by the asymptotic expansion (5.11) of e^{2f},

$$M = \frac{\lambda_2 c^2}{4}. \tag{5.17}$$

[a] We do not consider the logarithmic branch (see footnote 1)

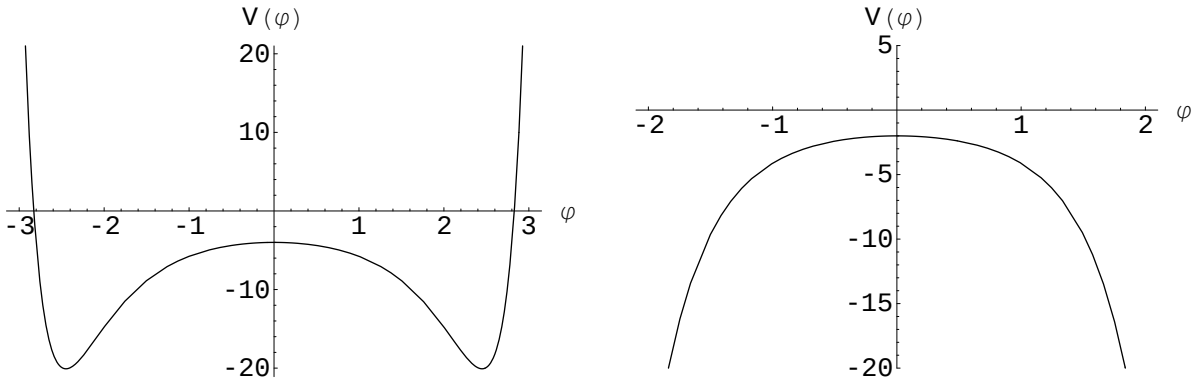

Figure 5.1: *Left.* The form of the potential $V(\varphi)$ for the case $\lambda_1, \lambda_2 > 0$. The picture shows the potential for $\lambda_1 = \lambda_2 = 1$. *Right.* The form of the potential $V(\varphi)$ for the case $\lambda_1 < 0, \lambda_2 > 0, \lambda_2 > |\lambda_1|$. The picture shows the potential for $\lambda_1 = -1, \lambda_2 = 2$.

The event horizon is located at

$$r_h = \gamma\sqrt{M}, \quad \gamma = \left[\lambda_2 \ln(-\frac{\lambda_2}{\lambda_1})\right]^{-\frac{1}{2}}. \tag{5.18}$$

$r = 0$ is a curvature singularity with the scalar curvature behaving as $R \sim \exp(2M/(r^2\lambda_2))/r^4$.

For $\lambda_1 > 0$ the solution (5.15) describes a naked singularity. Because black hole solutions exist only in the range of parameters for which the potential V has no minima, it follows that there is no $n = 0$ black hole solution interpolating between the $U(1)$-symmetry preserving vacuum at $\varphi = 0$ and the symmetry breaking vacuum at $\varphi = \varphi_m$. The symmetry-preserving and the symmetry-breaking vacua seem therefore gravitationally disconnected. Black hole solutions with scalar hairs exist only for the potential shown in right hand side of figure 1.

It is also interesting to have a short look at the thermodynamics of the black hole described by the solution (5.15). Temperature and entropy are given by

$$T = \frac{1}{2\gamma\pi}\sqrt{M}, \quad S = 4\pi\gamma\sqrt{M}, \tag{5.19}$$

where γ has been defined in Eq. (5.18). One can easily show that M, T, S satisfy the first principle, $dM = TdS$. The thermodynamical behavior of our black hole follows closely that of the BTZ black hole, which is given by the same equations (5.19) with $\gamma = L$. If we compute the free energy of the BTZ black hole and that of the scalar-hair black hole (5.15) one finds respectively:

$$F_{BTZ} = -4\pi L^2 T^2, \quad F_{SH} = -4\pi\gamma^2 T^2. \tag{5.20}$$

Because in the range of existence of the black hole solutions ($\lambda_2 > |\lambda_1|$), we have always $\gamma < L$, it follows that $F_{SH} > F_{BTZ}$. This is consistent with the stability the BTZ black hole in the presence of a real scalar field with mass satisfying the BF bound and with the interpretation of the scalar hair solution (5.15) as an excitation of AdS_3.

5.6 Vortex solutions

Before considering vortex-like, black hole solutions, let us first consider the vacuum, $n = 0$, solutions of a model with a potential for the scalar of the form:

$$V(\varphi) = -4\Lambda^2 - \Lambda^2\varphi^2 - \frac{\Lambda^2}{2}\varphi^4 - 2\lambda_1 e^{\frac{\varphi^2}{2}} + \frac{\lambda_1}{2}\varphi^2 e^{\frac{\varphi^2}{2}} - 2\lambda_2 e^{\frac{\varphi^2}{4}}, \tag{5.21}$$

where $\Lambda, \lambda_1 > 0, \lambda_2 < 0$ are parameters. Also in this case the maximum of the potential, corresponds to a AdS_3, $U(1)$-symmetry preserving vacuum, with $\varphi = 0$ and

$$V(0) = -\frac{2}{L_1^2} = -4\Lambda^2 - 2\lambda_1 - 2\lambda_2, \tag{5.22}$$

where as usual L_1 is the AdS length. Existence of this AdS_3 vacuum obviously requires $2\Lambda^2 + \lambda_1 + \lambda_2 > 0$.

The mass of the scalar excitation near $\varphi = 0$ saturates the BF bound, in fact we have $m^2 = V''(0) = (1/2)V(0) = -1/L_1^2 = m_{BF}^2$. We have also a minimum of the potential describing a $U(1)$-symmetry breaking AdS_3 vacuum at $\varphi = \hat{\varphi}_m$ with AdS length l_1 given by $-2l_1^{-2} = V(\hat{\varphi}_m)$.

Using the method described in Sect. 4, a $n \neq 0$ vortex-like, black hole solution of the field equations (5.8) can be obtained for a profile of the complex scalar field given by

$$\phi = \frac{c}{r}e^{in\theta}, \tag{5.23}$$

when the parameter Λ of the potential is fixed in terms of c and n: $\Lambda = n/c$ and $\Lambda^2 \leq \frac{\lambda_2^2}{8\lambda_1}$.

The potential (5.21) with $\Lambda = n/c$ has the physical meaning of the effective potential seen by a vortex with scalar charge c and winding number n. The metric part of the black hole solution turns out to be,

$$e^{-2h} = \lambda_1 r^2 e^{\frac{c^2}{2r^2}} + \lambda_2 r^2 e^{\frac{c^2}{4r^2}} + \frac{2n^2}{c^2}r^2, \quad e^{2f} = e^{-\frac{c^2}{2r^2}}e^{-2h}. \tag{5.24}$$

The black hole mass is given in terms of the scalar charge c and the winding number n:

$$M = \frac{\lambda_2 c^2}{4} + n^2. \tag{5.25}$$

The black hole solution (5.24) has an outer and inner horizon located respectively at

$$r_\pm = \frac{c}{2}\left(\ln\left\{\frac{1}{2\lambda_1}\left[-\lambda_2 \mp \sqrt{\lambda_2^2 - \frac{8\lambda_1 n^2}{c^2}}\right]\right\}\right)^{-\frac{1}{2}}. \tag{5.26}$$

The black hole solution exists for

$$\frac{M}{n^2} \leq 1 - 2\frac{\lambda_1}{|\lambda_2|}, \qquad |\lambda_2| > 2\lambda_1. \tag{5.27}$$

The black hole becomes extremal (single event horizon) when the bound (5.27) is saturated. In general the radial coordinate r_m corresponding to the minima of the potential (5.21) can

lie either outside or inside the event horizon. The requirement $r_m \geq r_h$ implies $M/n^2 \geq 1-(9/4)(\lambda_1/|\lambda_2|)$.

Thus the vortex black hole solution (5.24) interpolates between a symmetry-preserving AdS_3 vacuum at $\varphi = 0$ and a symmetry breaking AdS_3 vacuum at $\varphi = \varphi_m$ for

$$1 - \frac{9\lambda_1}{4|\lambda_2|} \leq \frac{M}{n^2} \leq 1 - 2\frac{\lambda_1}{|\lambda_2|}. \tag{5.28}$$

Notice that differently from the usual case the vortex connects a maximum of the potential in the $r \to \infty$ asymptotic region with a minimum of the potential in the interior region. This is related with the fact that the energy of the vortex although finite is always negative. The energy E of the vortex is given by

$$E = \int_{r_+}^{\infty} r dr d\theta (T_t^t) - E_{\text{vacuum}}, \tag{5.29}$$

where T_t^t is the stress energy tensor of the complex scalar field ϕ and we have subtracted the contribution of the $\phi = 0$ vacuum. We find after a little algebra,

$$E = \frac{c^2}{4}(\lambda_2 + 2\lambda_1) = (M - n^2)(1 - 2\frac{\lambda_1}{|\lambda_2|}). \tag{5.30}$$

The energy of the vortex measured with respect to the vacuum is finite and always negative.

5.6.1 Stability of the solutions

Let us first consider the solutions with a real scalar field. In this case the potential $V(\varphi)$, given in Eq. (5.15) with $\lambda_1 < 0$, admits as solution both the BTZ black hole and a dressed black hole with a real scalar field $\varphi = c/r$. The dressed black hole always has a free energy which is larger than that of the BTZ black hole. Correspondingly, the dressed black hole is always unstable and it will decay to the stable BTZ black hole, losing its real scalar hair. This is confirmed by a linear stability analysis. In the BTZ background scalar perturbations, $\delta\phi$, decouple from the metric. The equation of motion for the scalar perturbation is given by the Klein-Gordon equation for a scalar field propagating in AdS with a mass $m^2 = -1/L^2$ which saturates the BF bound of AdS_3. Thus the BTZ solution is (at least linearly) stable.

The story does not change so much if we consider solutions with a complex scalar field. In this case the potential $V(\varphi)$, supporting vortex solutions, $\phi = (c/r)e^{in\theta}$ in given in Eq. (5.21). We can consider scalar perturbations around the BTZ black hole, which is again solution of the equations of motions. Because the potential only depends on $\varphi = |\phi|$, at the linear level the equation for scalar perturbations near extrema of the potential always decouple in a holomorphic and antiholomorphic part:

$$\frac{1}{\sqrt{-g}}\partial_\mu(\sqrt{-g}\partial^\mu\delta\phi) + \frac{1}{L^2}\delta\phi = 0, ,$$
$$\frac{1}{\sqrt{-g}}\partial_\mu(\sqrt{-g}\partial^\mu\delta\bar{\phi}) + \frac{1}{L^2}\delta\bar{\phi}\,, = 0,$$

i.e. we have two independent real scalar perturbations, propagating in the BTZ background with the same mass saturating the BF bound, $m^2 = -1/L^2 = m_{BF}^2$. This again ensures linear stability of the BTZ black hole.

5.6.2 Other Vortex solutions

Let us now briefly consider a scalar field with $m^2 = V''(0) = 0$. From equation (5.3) it follows that φ must have the form $\varphi = \frac{c}{r^2}$. We will therefore look for a complex scalar field of the form:

$$\phi = \frac{c}{r^2} e^{in\theta}. \tag{5.31}$$

In this case the method described in Sect. 4 gives the following solution for the potential $V(\varphi)$,

$$\begin{aligned} V(\varphi) &= -2\lambda_1 e^{\varphi^2} - \frac{n^2}{2c}\varphi + 2\sqrt{\frac{2}{\pi}}\lambda_2 \varphi e^{\frac{\varphi^2}{2}} + 2\lambda_1 \varphi^2 e^{\varphi^2} + \\ &\frac{n^2\sqrt{\pi}}{4c}\varphi^2 e^{\varphi^2}\left[1 - \mathrm{erf}\left(\varphi\right)\right] - \frac{n^2\sqrt{\pi}}{4c} e^{\varphi^2}\left[1 - \mathrm{erf}\left(\varphi\right)\right] \\ &-2\lambda_2 e^{\varphi^2}\,\mathrm{erf}\left(\frac{\varphi}{\sqrt{2}}\right) + 2\lambda_2\varphi^2 e^{\varphi^2}\,\mathrm{erf}\left(\frac{\varphi}{\sqrt{2}}\right) - \frac{n^2}{2c}\varphi^3, \end{aligned} \tag{5.32}$$

where λ_1, λ_2 are constants.

The metric part of the solution is given by

$$e^{2f} = r^2\left\{\lambda_1 + \lambda_2\,\mathrm{erf}\left(\frac{c}{\sqrt{2}r^2}\right) + \frac{n^2\sqrt{\pi}}{8c}\left[1 - \mathrm{erf}\left(\frac{c}{r^2}\right)\right]\right\},\ e^{-2h} = e^{\frac{c^2}{r^4}} e^{2f}, \tag{5.33}$$

whereas for the AdS length we have,

$$V(0) = -\frac{2}{L^2} = -2\lambda_1 - \frac{n^2\sqrt{\pi}}{4c}. \tag{5.34}$$

Hence, the solutions are asymptotically AdS for $\lambda_1 > -\frac{n^2\sqrt{\pi}}{8c}$.

The mass M of the solution can be easily computed using the asymptotic expansion of $\exp(2f)$. One has,

$$M = -\sqrt{\frac{2}{\pi}}\lambda_2 c + \frac{n^2}{4}. \tag{5.35}$$

The question about the presence of event horizon in the generic, $n \neq 0$, solution given by Eq. (5.33) is rather involved. We will not address this problem here, but we will just consider the $n = 0$ solutions. The solutions are asymptotically AdS for $\lambda_1 > 0$. They describe a black hole for $\lambda_2 < 0$, $|\lambda_2| \geq \lambda_1$. The position of event horizon r_h is the solution of the equation

$$\mathrm{erf}(\frac{c}{\sqrt{2}{r_h}^2}) = \frac{\lambda_1}{|\lambda_2|}.$$

5.7 Conclusions

In this chapter we have derived and discussed exact, spherically symmetric, solutions of 3D AdS gravity coupled with a complex scalar field ϕ. Our method allows to determine the potential $V(|\phi|)$ once the form of $|\phi(r)|$ is fixed. A scalar field profile corresponding to the saturation of the BF bound requires a Higgs-like potential V, which allows both for BTZ black holes solutions - corresponding to a constant scalar field- and for black hole solutions with scalar hairs.

A generic feature of 3D black holes with scalar hairs is that the black hole mass is determined algebraically by the scalar charges and by the winding number of the vortex. The main difference between 3D black hole solutions with real scalar hairs and the BTZ black hole is the presence of a curvature singularity at $r = 0$, where the scalar curvature behaves as $R \sim e^{2M/(r^2\lambda_2)}/r^4$. On the other hand, the thermodynamical behavior of these dressed black hole solutions is very similar to that of the BTZ black hole. They share the same mass/temperature relation $M \sim T^2$ and we were able to show that the BTZ black hole remains always stable, being the free energy of the dressed solution always bigger than that of the BTZ black hole.

Conversely, the black hole-vortex solutions we have derived in this chapter share many feature with both rotating [117] and electrically charged [118] 3D black hole solutions. They are characterized by the presence of an inner and outer horizon and the vortex interpolates between two AdS_3 geometries with different AdS lengths. For some choice of the parameters, these AdS_3 geometries correspond respectively to the $U(1)$-symmetry-preserving maximum and to the symmetry-breaking minimum of the Higgs potential. In the AdS/CFT language this means that the vortex interpolates between two 2D CFTs with different central charges. It is interesting to notice that these interpolating features of the vortex solution are more similar to those of the rotating solution of Ref. [117] (both interpolated geometries are AdS_3) then to those of the electrically charged solutions of Ref. [118] (the solution interpolates between AdS_3 and $AdS_2 \times S^1$).

Also the non trivial solution for the scalar field could have an interesting holographic interpretation. The scalar charge c has to be thought of as a nonvanishing vacuum expectation value for some boundary operator. This could be a signal of a phase transition in the dual 2D boundary field theory. However, this is a rather involved issue because of the well-known results about phase transitions in statistical systems with only one spacelike dimension [125].

Part II

Signatures of black holes beyond General Relativity

Chapter 6

Black holes in alternative theories of gravity

6.1 Do we really need some alternative to General Relativity?

During the last century General Relativity (GR) passed numerous and stringent tests [23], which proclaimed it as the standard theory of gravity. It provides us with a full control of gravitational phenomena at terrestrial, solar and galactic scale, in a range between $10^{-5}m$ and 10^{8}parsec [126]. Some of GR predictions has been confirmed with an astonishing precision, which is comparable or better than the celebrated precision in perturbative quantum electrodynamics. Commenting on this fact, Roger Penrose provokingly stated that, since GR is such a precise theory, we should extend our knowledge of quantum field theories in order to accommodate them within GR and not viceversa [127].

Therefore the investigation of alternative theories of gravity seems at least a peripheral problem, due to the enormous success that GR has reached. However, modifications to GR are pursued vigorously for two main reasons. First, from a theoretical standpoint, an ultraviolet completion of GR is highly desiderable. Such a completion, arising from quantum gravity theories such as String Theory or Loop Quantum Gravity, would lead to higher-curvature corrections in the action, *i.e.* higher powers of scalar invariants constructed upon to the Riemann tensor. Although quantum gravity effects could be negligible for practical purposes, nevertheless it is quite disappointing that we know *a priori* the existence of an energy scale – presumably the Planck scale – at which our understanding of the Laws of Nature fails. Secondly, from an experimental standpoint there are strong evidences that the deep infrared gravity regime is dominated by some form of dark energy [128, 129]. To reconcile theoretical predictions with recent cosmic microwave background measurements by WMAP [130] roughly 74% of the Universe is *assumed* to be composed by a completely unknown form of dark energy, which leaves no imprint in any other phenomena so far. One possibility to accommodate dark energy is to consider a small positive cosmological constant, $\Lambda \sim 10^{-3}eV^4$. This is indeed the choice in the standard Lambda-Cold Dark Matter (Λ-CDM) cosmological model. However, quantum field theory predictions for Λ overestimate its experimental value by a factor 10^{56} in the most optimistic case! This is the famous Cosmological Constant problem [131]. Apart from this problem, in the Λ-CDM cosmological model, ordinary matter contributes with only $\sim$ 4% to the total amount of energy-matter of the universe. These observations suggest

that something fundamental is still missing in our understanding of gravitational phenomena. Indeed the long-standing Cosmological Constant, Dark Matter and Dark Energy problems (see, *e.g.* Refs. [132], [133] and references therein) might be due to truly quantum gravitational effects or simply to a modification of GR at large distances. In fact another possibility to accommodate dark energy is to consider nonlinear couplings to curvature invariants in the action [134, 135]. These couplings are also similar in spirit to the corrections that we expect from an ultraviolet completion of GR.

Alternative theories of gravity are developed with the aim to extend the validity region of GR, eventually resolving its infrared and ultraviolet regimes, but without giving any observable modification in the range where GR has been tested with excellent precision. Hence in these theories the weak gravity regime is the same as in GR, and it is difficult to tell an alternative theory from Einstein's gravity by means of, for example, Solar System experiments. More precisely, in the weak gravity regime the Newtonian gravitational potential, velocities and related variables are much smaller than unity. In this regime a parametrized post-Newtonian (PPN) expansion [23, 136] is usually appropriate. Therefore alternative theories of gravity usually have the same PPN expansion as in GR, at first orders. However observable differences may presumably arise when strong curvature effects are taken into account [137]. This is the case for cosmology or for strongly relativistic objects, such as black holes, whose astrophysical imprints in the framework of gravity theories beyond GR are the main topic of the present discussion.

Black holes (BHs), probing the strong curvature regime of any gravity theory, provide a means of possible high-energy corrections to GR. Unfortunately, the majority of quantum gravity theories are vastly more complex than GR in their full-fledged form. It is thus not surprising that progresses in understanding the exact differences between one and the other (and specially differences one can measure experimentally) have been slow and mostly focusing on the weak-, far-field behavior. Therefore our approach will be different. We shall focus on selected and well-established modifications of GR and we investigate *effective actions* arising as low-energy approximations of more fundamental quantum gravity theories. These effective theories are much more tractable than their exact versions, and the imprint of their modifications to GR can already leave some signature in astrophysical phenomena, such as strong gravity effects taking place around astrophysical BHs. One of the most important of such effects is the emission of gravitational waves, whose detection is one of the main scientific goals of current experimental physics. During the 20th century spectroscopy has open a new era in quantum physics, via the precise detection of electromagnetic radiation from atoms, molecules and quantum systems. In the same way the detection of gravitational waves from BHs, neutron stars and other astrophysical objects can open a new era in gravitational physics and enhances our knowledge of gravity to unprecedented levels.

At present there are several gravitational wave observatories worldwide: LIGO in the U.S. [24], VIRGO [138] and GEO600 in Europe, TAMA300 in Japan. They have reached (or are approaching to reach) the design sensitivity and, in a near future, they will open a new opportunity to probe the strong curvature regime of gravity via gravitational wave detection. Gravitational wave detection will provide us with high-precision tests of GR and hopefully with evidences of physics beyond it. Thus it is of fundamental importance to investigate astrophysical properties of BHs in alternative theories of gravity and, in particular, to infer corrections to GR from the gravitational wave imprint of BHs [139, 140].

6.2 The hairy black holes zoo

It is now almost 40 years from Wheeler's celebrated sentence *"Black holes have no hair"* [141]. His conjecture was inspired by a series of uniqueness theorems for static and stationary asymptotically flat vacuum BHs in Einstein-Maxwell theory [142, 143, 144], which, loosely speaking, establish that properties of BHs in GR are uniquely determined by precisely three "hairs" at spatial infinity: their Arnowitt-Deser-Misner mass, spin and charge [145, 13]. However this is true only in GR and BHs do indeed have extra hairs in theories where the coupling with dilatons or Higgs fields is considered, *e.g.* in Einsten-Maxwell-dilaton gravity [54], in Einstein-Yang-Mills [146] and in Einstein-Skyrme [147] theory. Furthermore, when the spacetime is not asymptotically flat, several stable hairy BHs exist [58, 148, 46]. This is the case of dilatonic BHs in asymptotically AdS spacetime discussed in Part I. Finally uniqueness theorems mostly hold in four spacetime dimensions, but the situation changes in higher dimensions. In this case, even within Einstein-Maxwell theory without cosmological constant, stationary axisymmetric solutions are degenerate. BHs in higher dimensions may play a role in BHs produced by high energy cosmic rays and in particle accelerators [149, 150, 151, 152].

However our purpose here is to discuss *hairy* BHs as viable astrophysical candidates. For astrophysical purposes, we can focus on four dimensional solutions in asymptotically flat spacetime. Moreover astrophysical BHs are likely to be electrically neutral, as their electrical charge is shorted out by the surrounding plasma [153]. Thus we restrict ourselves to four dimensional theories schematically described by the following field equations

$$G_{\mu\nu} = T_{\mu\nu} + \gamma M_{\mu\nu}(\Psi, g_{\mu\nu}) = T^{(\text{eff})}_{\mu\nu}(\Psi, g_{\mu\nu})\,, \tag{6.1}$$

where $G_{\mu\nu}$ is the Einstein tensor and $T_{\mu\nu}$ is the usual matter stress-energy tensor. The tensor $M_{\mu\nu}(\Psi, g_{\mu\nu})$ encodes corrections to GR and depends on the metric $g_{\mu\nu}$ and on any further field (schematically written as Ψ) which must be supplied by its own equations of motion. For instance, if Ψ is a scalar field, Eqs. (6.1) must be supplied by the Klein-Gordon equation for Ψ.

Typically equations of motion arising from alternative theories of gravity can be exactly written in the form (6.1). This is the case for the two alternative theories we shall explore in detail in Chapters 7 and 8. However for other theories, Eqs. (6.1) are not exact field equations, but can be obtained as first order expansion from more intricate equations of motion, hence they are only valid in the limit $\gamma \ll 1$. Corrections to GR are typically forced to be small in order to agree with Solar System observations. Furthermore, as we discuss in Section 6.4, some alternative theories arise from *effective* actions, which are themselves only valid in the limit $\gamma \ll 1$. Thus, Eqs. (6.1) include most of the astrophysically viable corrections to Einstein gravity.

The field equations (6.1) are conveniently written as Einstein equations with an effective stress-energy tensor $T^{(\text{eff})}_{\mu\nu}(\Psi, g_{\mu\nu})$. Due to high energy corrections to GR, the effective stress energy tensor can bypass the no-hair theorem. For example, for spherically symmetric solutions in GR gravity, the time-component of the stress-energy tensor is positive definite and the relation $T^r_r \equiv T^\theta_\theta$ holds. These are both conditions used in the proof of the theorem [115]. However the effective stress-energy tensor $T^{(\text{eff})}_{\mu\nu}(\Psi, g_{\mu\nu})$ gets contributions from the gravitational field itself, as well as from any other extra field, and it can typically evade these conditions. Therefore, when the theory of matter has sufficient structure, matter fields can

develop non-trivial configurations outside the black hole horizon. The resulting black hole is "hairy" in that it possesses an extra conserved "charge", which can be independent from the mass and the spin (primary hair) or can be related to those (secondary hair).

Low-energy degrees of freedom arising from String Theory can provide the necessary non-trivial structure for the matter fields. Thus black holes non-trivially coupled to dilaton, axion, Abelian or Yang-Mills fields have been recently discovered and obviously evade classical no-hair theorems. However, although these theorems properly refer to the existence of black hole solutions and not to their stability, they are often seen in a wider perspective as if they prescribed that *no stable hairy black holes exist*. For this reason some hairy black holes, which turn out to be unstable, are not regarded as proper violations of the theorems. From the astrophysical standpoint this problem is purely academical, as unstable black hole solutions are not viable astrophysical candidates. Therefore, the investigation of linear perturbations of hairy black holes in alternative theories of gravity is relevant both for practical purposes and for more theoretical insights on the no-hair theorems in GR.

Correspondingly to the numerous low-energy effective theories, supergravities and scalar-tensor theories (see Section 6.4 for a brief discussion) also the number of different hair black hole solutions has rapidly increased over the last decades. For the sake of concreteness, among the existing plethora of hairy BHs, we shall focus on those which can be viable astrophysical candidates and which arise from minimally modified theories of gravity. This is the case for Einstein gravity coupled to a scalar field. The actual form of the coupling and of the action are dictated by low energy effective corrections arising from quantum gravity, as discussed in Section 6.4. Non-trivial scalar fields may be relevant in cosmology [154], galaxy rotation curves [155] and inflationary models [156]. Furthermore neutral scalar fields, such as the dilaton, do not leave any direct imprint in the electromagnetic sector, but nevertheless they modify the gravitational properties of astrophysical objects in the strong curvature regime.

In order to check viability of hairy black holes, a fundamental issue concerns their stability. Thus in Chapter 7 and 8, among other properties, we shall throughly investigate the linear perturbation spectrum of black holes in two representative effective theories: Dynamical Chern-Simons gravity and Einstein-Dilatonic-Gauss-Bonnet gravity. These theories are briefly introduced in Section 6.4.

6.3 No-hair theorem tests

As mentioned above no-hair theorems establishes that properties of BHs in GR are uniquely determined by precisely three parameters: their mass, spin and charge [145]. In the most general case these Einstein BHs are described by the Kerr-Newman metric, which reduces to the Kerr metric in the uncharged case. Kerr BHs are commonly believed to be the final states of the evolution of sufficiently massive stars [157, 158], as any extra signature of the progenitor star other then its mass and its spin is radiated away by gravitational emission [159]. No-hair theorems rely on the physically reasonable assumptions that GR is the correct theory of gravity, that no closed timelike curves (CTCs) exist in the exterior metric and on the cosmic censorship conjecture [160] as well. Thus possible tests of no-hair theorems may confirm or rule out some of the fundamental hypothesis our understanding of gravity is based on.

More technically, the exterior spacetime of a BH is defined in terms of its multipole moments, the mass and the spin being identified as the first two of such moments. No-hair

theorems state that higher moments are completely specified by the first two. In Newtonian gravity the gravitational potential satisfies Laplace equation $\nabla^2\phi = 4\pi\rho$, ρ being the mass density. The potential ϕ can always be expanded in spherical harmonics Y_{lm} as

$$\phi = -\sum_{l=0}^{\infty} \frac{4\pi}{2l+1} \sum_{m=-l}^{l} \frac{M_{lm} Y_{lm}}{r^{l+1}} \tag{6.2}$$

where $M_{lm} = \int_0^r dy\, y^{l+2} \oint d\Omega\, Y^*_{lm}(\Omega)\rho(y,\Omega)$, $d\Omega$ being the infinitesimal solid angle. The expansion above relies on the linearity of the Laplace equation, but it does not apply to Einstein equations, which are highly non-linear. However an expansion in orthogonal polynomials is possible also in GR for stationary and axisymmetric spacetimes [161]. In this case the multipole moments are given by the mass multipole moments M_l and the current multipole moments S_l. Then the no-hair theorem can be easily formulated as

$$M_l + iS_l = M(ia)^l\,, \tag{6.3}$$

where M_l are nonzero for even values of l, whereas S_l are nonzero for odd values of l. The mass and the angular momentum of a Kerr BH are $M = M_0$ and $J \equiv aM = S_1$ respectively. Thus, from Eq. (6.3) higher ($l \geq 2$) multipole moments are uniquely defined in terms of M and J, *i.e.* any observable can ultimately depend on those two moments only. A promising strategy for testing no-hair theorem consists in measuring at least the first multipole moments and check if Eq. (6.3) holds [162]. These observations could be possible in a near future, due to Earth-based interferometers and specially to Space-based interferometers, such as the Laser Interferometer Space Antenna (LISA) [140].

6.4 Alternative theories of gravity. Two cases studies.

Let us suppose that future observations will signal a deviation from Eq. (6.3), *i.e.* suppose that the no-hair theorem does not hold. Among other reasons, this would presumably mean that the compact object we were probing is not a Kerr BH. Due to uniqueness theorems, this would also likely suggest that GR is not the ultimate theory of gravity, even at classical level. Similarly, another possibility is that the probed compact object is indeed a Kerr BH, but the underlying theory of gravity is not GR and this also affects the no-hair theorem relation (6.3). Motivated by this scenario this part of the thesis is devoted to the study of BHs in viable alternative theories of gravity.

Theorists have conceived numerous alternative theories of gravity. In 1960s, Jordan, Brans and Dicke attempted to modify Einstein gravity by introducing a scalar field [134, 163, 164]. These theories are ancestors of modern scalar-tensor theories of gravity, which have been further generalized by introducing vector fields (see the book by Will [165] and references therein). Other proposed alternatives are bimetric theories [166], massive gravity [167] and extensions of them. Recently, so-called $f(R)$ gravities, *i.e.* theories containing some function of the Ricci curvature R in the action, have been extensively studied [135] together with their generalizations which include generic functions of higher curvature invariants. Interestingly, by introducing an auxiliary field, $f(R)$ gravity is shown to be equivalent to a scalar-tensor theory.

However, experimental tests on the Einstein Equivalence Principle and on the weak field regime have strongly bounded (if not completely ruled out) some of these alternative theories.

Some examples of (still) viable theories include Modified Newtonian Dynamics (MOND) [168] and one of its relativistic version, Tensor-Vector-Scalar gravity [169]. Moreover, rather then being derived from first principles, some of these theories contains *ad-hoc* corrections to GR and their theoretical foundations are questionable. Thus, among this plethora of alternative theories, we chose to investigate the role of BH solutions in two well-motivated effective theories: *Dynamical Chern-Simons* (DCS) gravity and *Einstein-Dilaton-Gauss-Bonnet* (EDGB) gravity, which have recently attracted a considerable attention. This is due to the fact that both are natural and well-motivated extensions of GR, whose validation comes from low-energy approximations of String Theory and, for the case of DCS gravity, also from Loop Quantum Gravity and Standard Model particle physics. Moreover these theories modify GR in a minimal way, adding two different contributions to the action, which can be thought as the minimal, most plausible, corrections to GR. In our approach corrections to GR arising from these effective theories should be seen as prototypes of string-inspired corrections. Possible gravitational signatures of these corrections can provide useful insights on the strong curvature regime of gravity and give indirect confirmations (or disapprovals) to String Theory. In the following we give a brief introduction to DCS gravity and EDGB gravity, whereas we shall discuss them in the framework of BH physics in Chapter 7 and 8 respectively.

Before entering in the specifics of our study it is worth to comment on the range of viability of such alternative theories. It has been argued that effective theories arising from String Theory are *de facto* indistinguishable from GR, because corrections to the Einstein-Hilbert action would be quantum suppressed. In fact String Theory suggests that the couplings in DCS gravity or in EDGB gravity should be suppressed at the electroweak scale or (even worst) at the Planck scale. Of course, if this were the case, effective theories would be completely undetectable by any future observation. However there are other quantities which are predicted to be related to the Planck scale by String Theory, whereas direct observations suggest they play a role much below the Planckian regime. The most important example of these quantities is the Cosmological Constant, Λ. As mentioned above, String Theory predicts $\Lambda \sim 10^{45} eV^4$ or $\Lambda \sim 10^{112} eV^4$ if the supersymmetry breaking occurs at the electroweak scale or at the Planck scale respectively. Nevertheless, observations in the deep infrared suggest $\Lambda \sim 10^{-3} eV^4$, which completely invalidates the String Theory predictions. Therefore either we assume that some quantities which (according to String Theory) seem related to Planckian physics, are instead related to larger scales (lower energy) or we admit that present observations are inconsistent, presumably because they implicitly assume the validity of GR at the scale they probe. In both cases the study of alternative theories assumes a fundamental relevance, as it might shed new light on the "dark sector" of gravity still missing by our present knowledge.

6.4.1 Dynamical Chern-Simons gravity

Chern-Simons (CS) gravity is an effective extension of GR in which the gravitational field is coupled to a neutral scalar field through a parity-violating CS term (for an excellent review on CS gravity see Ref. [26]). The CS modified action reads

$$S = \kappa \int d^4x\sqrt{-g}R + \frac{\alpha}{4}\int d^4x\sqrt{-g}\vartheta\, {}^*RR - \frac{\beta}{2}\int d^4x\sqrt{-g}\left[g^{ab}\nabla_a\vartheta\nabla_b\vartheta + V(\vartheta)\right] + S_{\rm mat}\,.$$

The first term in the action above is the usual Einstein-Hilbert action. The second term introduces the parity-violating coupling between gravity and the scalar field ϑ, via the Pontryagin

density

$$ {}^*RR = \frac{1}{2} R_{abcd} \epsilon^{baef} R^{cd}{}_{ef} \,. \tag{6.4} $$

where ϵ^{abcd} is the 4-dimensional Levi-Civita tensor. The third term in the action above is the usual kinetic and self-potential term of the scalar field. Originally CS gravity was formulated with a non-dynamical "a priori" scalar field. This first version of CS gravity is obtained when $\beta = 0$. Although non-dynamical CS gravity is a well-justified theory and deserves its own right, recently great effort has been spent on its dynamical version (DCS gravity), *i.e.* $\beta \neq 0$ (see Ref. [26] for some references related to non-dynamical CS gravity). The Pontryagin term can be expressed as the divergence of a CS topological current. Thus, if the scalar field ϑ =const, by an integration by parts, the CS modified action reduces identically to Einstein-Hilbert action.

The most interesting ingredient of CS gravity is that it introduces parity-violating corrections to GR. Indeed the Pontryagin density is the only parity-violating term which is second order in the curvature. In DCS gravity the scalar field θ, which is sourced by the Pontryagin density ${}^*RR$ via the scalar field equation stemming from Eq. (6.4), is a pseudo-scalar under a parity (purely spatial) transformation [26]. Thus for parity-symmetric backgrounds (such as spherically symmetric solutions) in DCS gravity the Pontryagin density vanishes, ${}^*RR = 0$, and this forces the scalar field to be constant. Therefore parity-even metrics, *e.g.* Schwarzschild BHs, do not get CS corrections. On the other hand, for parity-odd solutions, such as stationary axisymmetric solution (including rotating black holes) the Pontryagin density is non-vanishing and it sources a non-trivial scalar field. This implies that rotating black holes in DCS gravity develop a "scalar hair" and they differs from their GR counterparts.

DCS gravity is a well motivated effective theory. The CS modification arises from Standard Model particle physics via the gravitational anomaly, from the heterotic string theory via the Green-Schwarz anomaly canceling mechanism and even from Loop Quantum gravity if the Barbero-Immirzi parameter is promoted to a dynamical scalar field [26]. A more detailed introduction to DCS gravity is given in Chapter 7.

6.4.1.a No-hair theorem for spinning BHs in DCS gravity

Here we discuss modifications of the no-hair theorem in the DCS gravity briefly introduced in the previous section. As discussed above, the Schwarzschild BH (with vanishing scalar field) persist as solution of DCS gravity, due to the vanishing of the Pontryagin density, while the Kerr BHs is *not* a solution of the modified Einstein equations. Recently an approximate solution has been independently derived by Yunes and Pretorius [170] and by Konno et al. [155]. This solution is valid in the slow-rotation approximation ($a/M \ll 1$) and in the small-coupling approximation up to the second order. In Boyer-Lindquist coordinates the CS coupling affects the Kerr metric by introducing an extra off-diagonal term

$$ g^{(CS)}_{t\phi}(r,\theta) = \frac{5}{8} \frac{\alpha^2}{M^4} \frac{a}{M} \frac{M^4}{r^4} \left(1 + \frac{12M}{7r} + \frac{27M^2}{10r^2} \right) \sin^2\theta \,, \tag{6.5} $$

where α is the CS coupling. The rest of the metric is $\mathcal{O}(\alpha^0)$ and it is given by the slowly-rotation approximation of the well-known Kerr metric. Due to the CS coupling, rotating BHs

in DCS gravity are coupled to a stationary and axisymmetric scalar field

$$\vartheta(r,\theta) = \frac{5}{8}\frac{\alpha a \cos\theta}{M r^2}\left(1 + \frac{2M}{r} + \frac{18M^2}{5r^2}\right) . \tag{6.6}$$

Notice that this solution does not contain any extra "hair", *i.e.* the BH is completely defined by its mass and its spin and the scalar charge can be written in terms of M, a and the fundamental coupling constant α. In DCS gravity, therefore, the idea of "two-hairs" theorem is preserved. However the classical no-hair theorem (cf. Eq. (6.3)) is violated, as the CS coupling introduces a hecadecapole corrections [171] due to the r^{-4} dependence of the correction shown in Eq. (6.5). In fact, by applying the multipolar formalism [172], it can be proved that the leading-order correction to relation (6.3) occurs for the S_4 multipole. This would require high accuracy in no-hair theorem tests and challenges the future LISA [139] sensitivity. In fact LISA observations are expected to give accurate measures of the first $3-5$ multipole moments [173, 174], which is at the boundary of DCS gravity detectability. For this reasons, investigations of further CS corrections to GR are highly desiderable. In Chapter 7 we investigate the proper perturbation spectrum of Schwarzschild BHs in DCS gravity and contrast it with that of Schwarzschild BHs in GR. We shall show that the characteristic perturbation spectrum, *i.e.*, the "quasinormal mode ringing", gives the very imprint of the CS coupling and might be potentially detectable.

6.4.2 Einstein-Dilatonic-Gauss-Bonnet gravity

Here we discuss one of the most viable examples of astrophysical Dilatonic Black Holes, arising in the framework of Gauss-Bonnet couplings and one-loop corrected four-dimensional effective theory of heterotic superstrings at low energies. The low-energy effective action for the heterotic string [27] in the Einstein frame reads

$$S = \frac{1}{2}\int d^4x\sqrt{-g}\left(R - \frac{1}{2}\partial_\mu\phi\partial^\mu\phi + \frac{\alpha' e^\phi}{4g^2}\mathcal{R}^2_{GB}\right) , \tag{6.7}$$

where

$$\mathcal{R}^2_{GB} = R_{\mu\nu\rho\sigma}R^{\mu\nu\rho\sigma} - 4R_{\mu\nu}R^{\mu\nu} + R^2 , \tag{6.8}$$

is the GB invariant, α' is the Regge slope and g^2 is some gauge coupling constant. Being the GB invariant a topological term in four dimensions, the action (6.7) can be proved to be ghost-free. In Eq. (6.7) we have neglected the usual field strength $F_{\mu\nu}$, since for astrophysical applications we can restrict ourselves to uncharged BHs. Moreover we are also neglecting modulus and axion fields, which can arise from low energy truncations of some string theory. Thus the action (6.7) can be considered as a minimal modification to GR and as a prototype for squared curvature corrections arising from the coupling to a dilaton field. Finally we note that there is an ambiguity between the effective action of the heterotic string theory in the string frame and in the Einstein frame [175]. A conformal transformation maps the action from one frame to the other and, in absence of the GB term, the two formulation are equivalent. However, in presence of the GB term, if the string frame is taken as "fundamental", than extra contributions proportional to α arise when moving to the Einstein frame [176].

When the scalar field ϕ is constant over the spacetime, the GB term can be integrated out and the EDGB action reduces to Einstein-Hilbert action. Thus, as in DCS gravity, BH modifications due to the GB coupling only arise if the BH can support a non-trivial scalar

field, *i.e.* if the no-scalar-hair theorem fails. Indeed there is a simple reason to expect that no-hair theorems can be bypassed. In fact the modified Einstein equations can be schematically written as Eqs. (6.1) supplied by the Klein-Gordon equation for the dilaton. In EDGB gravity the coupling γ in Eqs. (6.1) is related to the GB coupling (see Chapter 8) (whereas in DCS gravity it depends on the CS coupling, see Chapter 7). Thus, due to high energy corrections to GR, the effective stress energy tensor $T^{(\rm eff)}_{\mu\nu}$ can evade the conditions for no-hair theorems to apply. In particular, for spherically symmetric solutions in EDGB gravity, both the time-component of this tensor is not positive definite and the relation $T^r_r \equiv T^\theta_\theta$ does not hold.

It is therefore not surprising that scalar (dilaton) hairs indeed exist for BHs in EDGB gravity, although they can be only computed numerically [177] or in the small-coupling expansion [178]. These solutions are interesting prototypes of BHs in alternative, yet well-behaved gravity theories: they evade the no-hair theorem but were proved to be stable against radial perturbations [179]. Further generalizations of this models, including black holes in non-asymptotically flat spacetimes and with unconventional topologies, were recently investigated in a series of works by Guo, Ohta and Torii (see Ref. [175] and subsequent works in the series). In Chapter 8 we discuss the stability issue for static BHs in EDGB, we numerically construct slowly rotating black hole solutions and we critically discuss them as viable astrophysical candidates.

6.4.3 Black holes and strong curvature regime

BHs are natural candidates to investigate strong curvature corrections to GR. The reason for that can be easily understood by computing some scalar invariant at the black hole horizon. For concreteness, we shall focus on the GB invariant (6.8). For a Kerr BH in GR the GB invariant on the equatorial plane ($\theta = \pi/2$) in Boyer-Lindquist coordinates reads

$$\mathcal{R}^2_{GB}(r) = \frac{48M^2}{r^6}\,, \tag{6.9}$$

where M is the BH mass. The curvature scalar is a monotonic function of the radial distance and it diverges on the singularity as $r \to 0$. However, for astrophysical purposes we are only interested in the region outside the horizon and, in particular, in the near-horizon region, where the curvature is stronger. For a Schwarzschild black hole the horizon is located at $r_H = 2M$ and $\mathcal{R}^2_{GB}M^4 = 3/4$. However for extremal Kerr BHs the horizon is located at $r_H = M$ and the scalar invariant is much larger, $\mathcal{R}^2_{GB}M^4 = 48$. Therefore the imprints of strong curvature corrections are expected to be strong for those processes taking place close to the horizon of near-extremal rotating black holes. Unfortunately, highly rotating black hole solutions in alternative theories are difficult to obtain and analytical solutions are usually known in the slow-rotation limit only. In particular no highly rotating black hole has been yet constructed for DCS gravity and EDGB gravity. Such solutions – if they exist – are expected to introduce much larger corrections, *i.e.* better observable imprints, than those we shall discuss in Chapters 7 and 8. We leave this interesting topic for future investigations.

Chapter 7

Gravitational signature of Schwarzschild black holes in Dynamical Chern-Simons gravity

Dynamical Chern-Simons gravity is an extension of General Relativity in which the gravitational field is coupled to a scalar field through a parity-violating Chern-Simons term. In this framework, we study perturbations of spherically symmetric black hole spacetimes, assuming that the background scalar field vanishes. Our results suggest that these spacetimes are stable, and small perturbations die away as a ringdown. However, in contrast to standard General Relativity, the gravitational waveforms are also driven by the scalar field. Thus, the gravitational oscillation modes of black holes carry imprints of the coupling to the scalar field. This is a smoking gun for Chern-Simons theory and could be tested with gravitational-wave detectors, such as LIGO or LISA. For negative values of the coupling constant, ghosts are known to arise, and we explicitly verify their appearance numerically. Our results are validated using both time evolution and frequency domain methods.

Contents

7.1 Introduction

In Chern-Simons gravity [180, 181, 182] the Einstein-Hilbert action is modified by adding a parity-violating Chern-Simons term, which couples to gravity via a scalar field. This correction could explain several problems of cosmology [183, 184, 185, 186, 155]. Furthermore, a Chern-Simons term arises in many versions of string theory [35] and of loop quantum gravity [187,

188, 189], and Chern-Simons gravity can be recovered by truncation of low energy effective string models [190, 191].

When Chern-Simons gravity was first formulated, the scalar field was considered as a prescribed function. Later on, it was understood that this *a priori* choice is not really motivated (see the discussion in Ref. [170]). Then, dynamical Chern-Simons (DCS) gravity has been formulated [190], in which the scalar field is treated as a dynamical field.

Since DCS gravity has a characteristic signature (the Chern-Simons term violates parity), there is the exciting prospect of testing its predictions against astrophysical observations. This has motivated a large body of work on the subject (for a review on DCS gravity and its astrophysical consequences see Ref. [26]). In this context, the study of black hole (BH) perturbations is very promising, since astrophysical black holes are probably the most appropriate objects to probe the strong field regime of General Relativity [171].

The first study of BH perturbations in the context of DCS gravity has been carried out in Ref. [192], where it was found that, if the background solution contains a (spherically symmetric) scalar field, polar and axial perturbations of DCS BHs are coupled, and the equations describing them are extremely involved. Recently, in Ref. [193] (hereafter, Paper I), some of us found that, when the background scalar field vanishes, polar and axial gravitational perturbations of a Schwarzschild BH decouple, and only axial parity perturbations are affected by the Chern-Simons scalar field. We also found that under this assumption the gravitational and scalar perturbations are described by a coupled system of two second order ordinary differential equations (ODEs). The numerical integration of this system to find the quasi-normal modes (QNMs) of Schwarzschild DCS BHs is challenging, due to the same asymptotic divergence which prevented for many years the numerical computation of QNMs for Schwarzschild BHs [194, 7, 9, 195]. Therefore, in Paper I the QNMs of Schwarzschild DCS BHs were not investigated thoroughly. It is remarkable that there are very few studies of this kind of system, *i.e.*, QNMs described by coupled ODEs (one interesting work is presented in Ref. [196]). In Paper I we also claimed that Schwarzschild DCS BHs are unstable for a specific range of the parameters of the theory. This result was the consequence of a sign error in the derivation of the perturbation equations; on the contrary, as we discuss in this chapter, there is strong evidence that these spacetimes are stable.

In this chapter we complete the study of Schwarzschild DCS perturbations, performing a thorough numerical analysis of the perturbation equations. We employ two different – and completely independent – numerical approaches: time evolution and a formulation of the frequency domain approach [197] which has never been applied before to the study of instability in black hole spacetimes. The results of the two independent methods agree very well, typically within an accuracy of 0.1%, validating each other.

The main result we find is that any perturbation decays at late-time as a damped sinusoid. This is known as the ringdown phase, where the black hole radiates all excess hairs in its lowest QNMs [9, 195]. What is new here, and with important implications for tests of DCS gravity, is that the gravitational sector has two distinct sets of QNMs. For large values of the constant β (associated to the dynamical coupling of the scalar field), these two sets coincide with the usual gravitational QNMs and scalar field QNMs of General Relativity. This result enables simple, yet fundamental tests on DCS gravity. By measuring (or not) these two different modes, one could effectively constrain DCS gravity through gravitational-wave observations. For instance, detection of ringdown modes with a signal-to-noise ratio $\gtrsim 6$ (feasible with both the Earth-based LIGO and the space-based detector LISA), could allow one to test DCS gravity if the

mass of the BH is known, for instance through observations of the inspiral phase of black hole binaries. For signal-to-noise ratios $\gtrsim 150$ one could be able to discriminate between DCS gravity and standard General Relativity without any further knowledge of the BH parameters.

A summary of our results

For the reader wishing to skip the technical details of the rest of the chapter, the following is a brief summary of our results.

(i) Two complementary numerical methods were developed and employed. They are completely independent and their concordance is very good.

(ii) For small values of the coupling constant ($M^4\beta \lesssim 0.5$), the perturbative dynamics is characterized by a stable exponentially decaying phase. The intermediate late time evolution is dominated by

$$\Phi(t, r_{\rm fixed}) = e^{\omega_{\rm no}\, t} \begin{pmatrix} a \\ b \end{pmatrix} \tag{7.1}$$

with $\mathrm{Re}[\omega_{\rm no}] = 0$ and $\mathrm{Im}[\omega_{\rm no}] < 0$ (with our sign conventions, a QNM is stable if $\mathrm{Im}[\omega] < 0$). Our results for the non-oscillatory frequency values are compatible with the expression:

$$\omega_{\rm no} = -0.04024 (M^4\beta)^{0.44} \ell \left(1 + \frac{2.0953}{\ell} - \frac{3.4460}{\ell^2}\right) . \tag{7.2}$$

(iii) For intermediate values of $M^4\beta$, field evolution is dominated by a stable oscillatory phase. We have detected two oscillatory modes, named here "gravitational" and "scalar" modes. Although the time profiles of the gravitational perturbation Ψ and of the scalar field Θ are usually different, they consist on different superpositions of the *same* modes.

(iv) In the $\beta \to \infty$ limit, these "gravitational" and "scalar" branches coincide with actual gravitational and scalar modes of Schwarzschild BHs in General Relativity. In this regime, we report that for $\ell = 2$, we find that the gravitational perturbation oscillates with a combination of the two modes

$$M\omega_{\rm grav}(\Psi) = 0.3736 - \mathrm{i}\ 0.08899\,, \tag{7.3}$$

$$M\omega_{\rm sc}(\Psi) = 0.4837 - \mathrm{i}\ 0.09671\,. \tag{7.4}$$

These numbers correspond to the lowest mode of pure gravitational and scalar quasi-normal frequencies in Einstein's theory [9]. The scalar field perturbation, instead, oscillates with the mode $\omega_{\rm sc}$ only. This behavior can be easily understood by looking at the form of the equations in this limit.

(v) At late times, the field decays with a power-law tail, as $t^{-(2\ell+3)}$. The tails do not depend on β or M. Note that the same behavior characterizes Schwarzschild BHs [198], implying that a gravitational-wave observation of the tail would not be able to discriminate DCS gravity from General Relativity.

(vi) An extensive investigation of BH oscillations, performed using two different numerical approaches, only yields stable modes, either oscillating or non-oscillating. This gives strong indications that Schwarzschild BHs in DCS modified gravity are stable against axial and polar perturbations.

(vii) We also discuss how the inclusion of a non-vanishing scalar potential in the Lagrangian affects the QNM spectrum. We focus on potentials of the form

$$V(\vartheta) = m^2\vartheta^2 + \mathcal{O}(\vartheta^3) \tag{7.5}$$

and find that in the $\beta \to \infty$ limit this inclusion only affects the scalar branch of QNMs, while the gravitational branch is unaltered. When $M^4\beta \lesssim 100$, also the gravitational sector is affected by the scalar potential.

The chapter is organized as follows. In Section 7.2 we briefly review the derivation of the perturbation equations in DCS gravity. In Section 7.3 we describe the time domain and frequency domain numerical approaches that we have employed to solve the perturbation equations. In Section 7.4 we present our results in the time and frequency domains. In Section 7.5, a possible observational signature of DCS gravity is discussed. Implications and final remarks are presented in Section 7.6.

In Appendix 7.7 we discuss ghost-like instabilities arising when the wrong sign of the kinetic term in the action is chosen, *i.e.* when $\beta < 0$ in Eq. 7.6 below.

7.2 Perturbation equations and dynamical stability

The action of DCS gravity is [170]

$$S = \kappa\int d^4x\sqrt{-g}R + \frac{\alpha}{4}\int d^4x\sqrt{-g}\vartheta\,{}^*RR - \frac{\beta}{2}\int d^4x\sqrt{-g}\left[g^{ab}\nabla_a\vartheta\nabla_b\vartheta + V(\vartheta)\right] + S_{\rm mat}\,, \tag{7.6}$$

where ϑ is the scalar field and

$${}^*RR = \frac{1}{2}R_{abcd}\epsilon^{baef}R^{cd}{}_{ef}\,. \tag{7.7}$$

We use geometrical units $c = G = 1$ so that $\kappa = 1/16\pi$. Furthermore, we neglect $V(\vartheta)$ (this assumption will be relaxed in Section 7.4.5), and consider the vacuum solutions ($S_{\rm mat} = 0$). The equations of motion are

$$R_{ab} = -16\pi\alpha C_{ab} + 8\pi\beta\vartheta_{,a}\vartheta_{,b} \tag{7.8}$$

$$\Box\vartheta = -\frac{\alpha}{4\beta}\,{}^*RR \tag{7.9}$$

where

$$C^{ab} = \vartheta_{;c}\epsilon^{cde(a}\nabla_e R^{b)}{}_d + \vartheta_{;dc}\,{}^*R^{d(ab)c}\,. \tag{7.10}$$

In a spherically symmetric background, ${}^*RR = 0 = C^{ab}$ and Eqs. (7.8), (7.9) reduce to usual Einstein gravity minimally coupled to a scalar field

$$R_{ab} = 8\pi\vartheta_{,a}\vartheta_{,b}\,, \quad \Box\vartheta = 0\,. \tag{7.11}$$

No-hair theorems [13] state that the Schwarzschild solution, with vanishing scalar field, is the only static spherically symmetric solution of the equations above. We then consider perturbations of a Schwarzschild BH with a vanishing background scalar field. We expand

the gravitational perturbations in tensor spherical harmonics, building the Zerilli and Regge-Wheeler functions. The scalar field is expanded in scalar spherical harmonics as

$$\vartheta = \frac{\Theta^{\ell m}}{r} Y^{\ell m} e^{-\mathrm{i}\omega t} \,. \tag{7.12}$$

Eq. (7.8) implies (see Paper I) that polar parity gravitational perturbations (described by the Zerilli function) are not affected by the Chern-Simons scalar, and then the corresponding QNMs are the well-known modes of Schwarzschild BHs. Axial parity gravitational perturbations $\Psi^{\ell m} = \mathrm{i} Q^{\ell m}/\omega$ (where $Q^{\ell m}$ is the Regge-Wheeler function, defined as in Paper I) are instead coupled with the scalar field. From here onwards, we will drop the $^{\ell m}$ superscripts.

Eqs. (7.8), (7.9) reduce to the following set of coupled ordinary differential equations for the perturbations $\Theta(r)$ and $\Psi(r)$, in terms of which one can completely characterize the axial parity metric perturbations and the scalar field respectively:

$$\frac{d^2}{dr_\star^2}\Psi + \left\{\omega^2 - f\left[\frac{\ell(\ell+1)}{r^2} - \frac{6M}{r^3}\right]\right\}\Psi = \frac{96\pi\, M f}{r^5}\alpha\Theta \,, \tag{7.13}$$

$$\frac{d^2}{dr_\star^2}\Theta + \left\{\omega^2 - f\left[\frac{\ell(\ell+1)}{r^2}\left(1 + \frac{576\pi M^2\alpha^2}{r^6\beta}\right) + \frac{2M}{r^3}\right]\right\}\Theta = f\frac{(\ell+2)!}{(\ell-2)!}\frac{6M\alpha}{r^5\beta}\Psi \tag{7.14}$$

with $f(r) = 1 - 2M/r$ and $r_\star \equiv r + 2M\ln(r/2M - 1)$. Note that third time-derivatives (*i.e.* terms proportional to ω^3) do not arise in the perturbation equations above (although they are generally expected from Eqs. (7.8)-(7.9)) because of the vanishing of the background Ricci tensor in Eq. (7.10). Therefore the Schwarzschild background does not suffer from problems related to ill-posedness of the theory, the so-called Ostrogradski instability (see Refs. [26, 199]). We also remark that the instability found in Paper I for $\beta M^4 \lesssim 2\pi$ was an artifact of a wrong sign in the definition of ${}^*RR$, that has yield a change in the sign of β in the perturbation equations. This is equivalent to consider the equations of the DCS theory with $\beta < 0$, which is indeed expected to be unstable, as discussed in Appendix 7.7.

Re-scaling and the General Relativity limit

Under the replacement $\beta \to \alpha^2\beta$ and $\Theta \to \Theta/\alpha$, one can set $\alpha = 1$ in the perturbation equations (7.13) and (7.14), which we will hereafter assume. Indeed, as discussed in [26], the parameters of the theory are redundant, and it is always possible to fix one of them.

We remark, however, that there is a subtle formal difference between the theory with α, β and the theory with $\alpha = 1$. Indeed, the General Relativity limit of the former is obtained by taking $\beta \to \infty$ and $\alpha \to 0$; the General Relativity limit of the latter is obtained by taking $\beta \to \infty$ and by considering the solutions with $\Theta \equiv 0$. In other words, once we fix $\alpha = 1$, General Relativity is not simply a limit of the DCS theory: it is a particular subset of the solution space of the $\beta \to \infty$ limit of the theory.

7.3 Numerical approach

7.3.1 Time domain evolution

The system (7.13), (7.14) can be written as

$$\left(-\frac{\partial^2}{\partial t^2} + \frac{\partial^2}{\partial r_\star^2}\right)\Phi = V\,\Phi \tag{7.15}$$

where we have defined

$$\Phi = \begin{pmatrix} \Psi \\ \Theta \end{pmatrix}, \quad V = \begin{pmatrix} V_{11} & V_{12} \\ V_{21} & V_{22} \end{pmatrix}, \tag{7.16}$$

and the elements of the matrix potential V are given by

$$V_{11} = f(r)\left[\frac{\ell(\ell+1)}{r^2} - \frac{6M}{r^3}\right], \tag{7.17}$$

$$V_{12} = f(r)\frac{96\pi M}{r^5}, \tag{7.18}$$

$$V_{21} = f(r)\frac{6M(\ell+2)!}{\beta(\ell-2)!}\frac{1}{r^5}, \tag{7.19}$$

$$V_{22} = f(r)\left[\frac{\ell(\ell+1)}{r^2}\left(1+\frac{576\pi M^2}{\beta\, r^6}\right)+\frac{2M}{r^3}\right]. \tag{7.20}$$

Using the light-cone variables $u = r_\star - t$ and $v = r_\star + t$ one can write

$$4\frac{\partial^2}{\partial u \partial v}\Phi = -V\,\Phi\,. \tag{7.21}$$

A discretized version of Eq. (7.21) is

$$\Phi(N) - \Phi(E) - \Phi(W) + \Phi(S) = \frac{\Delta u \Delta v}{8}\, V(S)\, [\Phi(E) + \Phi(W)]\,, \tag{7.22}$$

where the points N, E, W, S are defined as follows: $N = (u+\Delta, v+\Delta)$, $W = (u+\Delta, v)$, $E = (u, v+\Delta)$ and $S = (u, v)$. With the expression (7.22), the region of interest in the $u-v$ plane is covered, using the value of the field at three points in order to calculate the fourth one. As the integration proceeds, the values of $\Psi(t, r_{\rm fixed})$ are extracted [200, 113].

The initial data consist of the expressions on the sub-manifolds $(u > 0, v = 0)$ and $(u = 0, v > 0)$ for the vector

$$\Phi(u, v) = \begin{pmatrix} \Psi(u,v) \\ \Theta(u,v) \end{pmatrix}. \tag{7.23}$$

For most of the numerical evolutions presented here the initial data have the form

$$\Phi(u, 0) = \begin{pmatrix} 0 \\ 0 \end{pmatrix}, \tag{7.24}$$

$$\Phi(0, v) = e^{-(v-v_c)^2/2\sigma}\begin{pmatrix} 1 \\ 1 \end{pmatrix}, \tag{7.25}$$

with $v_c = 10.0$ and $\sigma = 1.0$.

From results on BH oscillations in General Relativity [7] we expect that the main characteristics of the time-evolution profiles (after a transient initial regime) are insensitive to the choice of the initial data, provided that they are localized. To check if this actually occurs in the present case, and rule out any eventual influence of initial data on late time results, we have considered different choices for the initial data:

- Gaussian initial data

$$\Phi(0, v) = \begin{pmatrix} A_1\, e^{-(v-v_{c1})^2/2\sigma_1} \\ A_2\, e^{-(v-v_{c2})^2/2\sigma_2} \end{pmatrix}, \quad \Phi(u, 0) = \begin{pmatrix} 0 \\ 0 \end{pmatrix}. \tag{7.26}$$

The initial v-functions are localized, with different peaks for the Ψ and Θ components. Although strictly speaking they do not have compact supports, they are (numerically) zero far away from the peaks.

- Compact support pulses

$$\Phi(0,v) = f(v)\begin{pmatrix} 1 \\ 1 \end{pmatrix}, \quad \Phi(u,0) = \begin{pmatrix} 0 \\ 0 \end{pmatrix}. \tag{7.27}$$

We have chosen two different functions $f = f_1(v), f_2(v)$. The first choice corresponds to

$$f_1(v) = \left[4\frac{(v-v_2)\,(v-v_1)}{(v_2-v_1)^2}\right]^8, \; v_1 < v < v_2 \tag{7.28}$$

and zero elsewhere. This is a localized and smooth pulse with a compact support. Our second choice corresponds to

$$f_2(v) = 1\,, \qquad v_1 < v < v_2\,, \tag{7.29}$$

and zero elsewhere. It is a localized but not continuous pulse with a compact support.

We have verified that the numerical results (after a transient regime) do not depend on the initial data.

7.3.2 Iteration scheme in the frequency domain

We now present an alternative, and complementary, numerical method, which is an application of Newton's iteration scheme to the shooting method [197].

Let us define ω_0 as the trial eigenfrequency of the eigenvalue problem defined by Eqs. (7.13), (7.14). The corresponding solutions Ψ_0 and Θ_0 satisfy the following set of equations

$$\Psi_0''(r_\star) + (\omega^2 - V_{11})\Psi_0(r_\star) = V_{12}\Theta_0(r_\star)\,, \tag{7.30}$$
$$\Theta_0''(r_\star) + (\omega^2 - V_{22})\Theta_0(r_\star) = V_{21}\Phi_0(r_\star)\,, \tag{7.31}$$

and it is hereafter understood that all these quantities are evaluated at the trial frequency ω_0. In order to compute QNMs we require the following boundary conditions

$$\Phi_0(\pm\infty) = \begin{pmatrix} \Psi_0(\pm\infty) \\ \Theta_0(\pm\infty) \end{pmatrix} \sim \begin{pmatrix} A_\pm \\ B_\pm \end{pmatrix} e^{\pm i\omega r_\star}\,. \tag{7.32}$$

When $\mathrm{Im}[\omega] < 0$ Eq. (7.32) defines (stable) QNMs, while when $\mathrm{Im}[\omega] > 0$ we have "bound-state-like" boundary conditions, *i.e.* $\Phi_0 \to 0$ at $r_\star \to \pm\infty$ (see Paper I) and the corresponding modes are unstable. The numerical method described in the rest of this section is capable to find both stable and unstable modes.

The idea is to "shoot" from each of the boundaries to a matching point where the wave functions and their derivatives are required to be continuous. In general, ω_0 is not the true eigenfrequency, and one of the continuity equations for Ψ_0 and Θ_0 is not satisfied. Without loss of generality, we can choose either Θ_0 or Θ_0' to be the function which does not satisfy the

continuity condition. Moreover we consider the matching point to be at $r_\star = 0$. Namely we assume that

$$[[\Psi_0]] = [[\Psi_0]] = [[\Theta_0]] = 0\,, \qquad \left[\left[\Theta_0'\right]\right] \neq 0\,, \tag{7.33}$$

where we define $[[\dots]]$ as the difference between the limits of the corresponding quantity as $r_\star \to 0_\pm$. We checked that our numerical results do not depend on the choice of the matching point within a wide range around $r_\star = 0$. We perform two integrations: one starting at $+\infty$ (numerically, at $r_\star = r_\star^{(1)} \gg M$) inward to $r_\star = 0$, and the other one starting at $-\infty$ (numerically, at $r_\star = r_\star^{(2)} \ll -M$) outward to $r_\star = 0$. At both infinities, we expand solution in series as follows

$$\begin{pmatrix} \Psi \\ \Theta \end{pmatrix} \sim \begin{cases} \begin{pmatrix} A_H \\ B_H \end{pmatrix} e^{-i\omega r_\star} \left[1 + \sum_{n=1}^{N} \begin{pmatrix} a_H^{(n)} \\ b_H^{(n)} \end{pmatrix} (r-2M)^n\right], \\ \\ \begin{pmatrix} A_\infty \\ B_\infty \end{pmatrix} e^{i\omega r_\star} \left[1 + \sum_{n=1}^{N} \begin{pmatrix} a_\infty^{(n)} \\ b_\infty^{(n)} \end{pmatrix} r^{-n}\right], \end{cases} \tag{7.34}$$

at $r_\star \ll -M$ and at $r_\star \gg M$, respectively. In computing QNMs this way it is important to choose appropriate values of numerical infinities, because numerical instabilities may arise by considering too large values for $r_\star^{(1)}$ and $r_\star^{(2)}$ [194]. In fact at both infinities the general solution will be a mixture of exponentially growing and exponentially suppressed modes and (in order to compute QNMs) we must select pure exponentially growing modes. Problems arise when too large values for $r_\star^{(1)}$ and $r_\star^{(2)}$ are chosen, because in that case contributions from unwanted exponentially suppressed modes can be significant after the integration, due to numerical errors. This problem can be circumvented by choosing small enough values of numerical infinities, say $|r_\star^{(i)}| \sim 10M$, and by considering large enough order of series expansion N, say $N \gtrsim 10$. In this way, though $\sim 10M$ is not very large (typically, for the modes we find, $|10M\omega| \sim 3-5$) the series well approximates the correct solution. This problem does not arise in the computation of unstable modes (see Appendix 7.7), since in that case we simply impose Dirichlet conditions at both infinities.

In order to obtain solutions satisfying continuity conditions (7.33) at the matching point, we compute two *linear independent* solutions and we construct an appropriate linear combination of them, which satisfies the required conditions. The first solution is obtained by choosing $A = 1$ and a generic value $B = B_0$ in the series expansion, whereas the second solution is obtained by choosing $B = 1$ and a generic value of $A = A_0$. We shall denote the first solution as Ψ_+ and the second one as Ψ_-. In order to have two linear independent solutions we also require $A_0 B_0 \neq 1$.

The procedure outlined above is adopted twice: once for A_∞ and B_∞ and once for A_H and B_H. Accordingly, we perform four numerical integrations: two from $r_\star^{(1)}$ and two from $r_\star^{(2)}$ up to $r_\star = 0$ and we obtain $(\Psi_\pm^{\rm right}(r_\star), \Theta_\pm^{\rm right}(r_\star))$ and $(\Psi_\pm^{\rm left}(r_\star), \Theta_\pm^{\rm left}(r_\star))$ respectively. Finally we construct a linear combination of solutions:

$$\begin{pmatrix} \Psi_0 \\ \Theta_0 \end{pmatrix} = \begin{cases} a \begin{pmatrix} \Psi_+^{\rm right} \\ \Theta_+^{\rm right} \end{pmatrix} + b \begin{pmatrix} \Psi_-^{\rm right} \\ \Theta_-^{\rm right} \end{pmatrix}, & r_\star > 0\,, \\ \\ c \begin{pmatrix} \Psi_+^{\rm left} \\ \Theta_+^{\rm left} \end{pmatrix} + d \begin{pmatrix} \Psi_-^{\rm left} \\ \Theta_-^{\rm left} \end{pmatrix}, & r_\star < 0\,, \end{cases}$$

and we choose a, b, c, d in order to satisfy the continuity conditions, Eqs. (7.33). The net result of this procedure is a set of solutions $\{\Psi_0(r_\star), \Theta_0(r_\star)\}$ which have the correct boundary conditions and which are continuous everywhere with Ψ_0' also continuous everywhere. The discontinuity $[[\Theta_0']] \neq 0$ is related to the choice of a trial eigenvalue ω_0, which is not the *correct* eigenfrequency.

Let us now denote with ω_1 the correction to the trial eigenvalue, *i.e.* $\omega = \omega_0 + \omega_1$. If ω_1 is a small correction, *i.e.* $\omega_1 \ll \omega_0$, then [197]

$$\omega_1 = \frac{\mu_0(0)\,[[\Theta_0']]}{\int dr_\star \left[\lambda_0\left(\frac{\partial P}{\partial\omega_0}\Psi_0+\frac{\partial R}{\partial\omega_0}\Theta_0\right)+\mu_0\left(\frac{\partial Q}{\partial\omega_0}\Theta_0+\frac{\partial S}{\partial\omega_0}\Psi_0\right)\right]} \tag{7.35}$$

where we have defined $P(r_\star) = -\omega^2 + V_{11}$, $Q(r_\star) = -\omega^2 + V_{22}$, $R(r_\star) = V_{12}$, $S(r_\star) = V_{21}$. In our case $\partial P/\partial\omega_0 = \partial Q/\partial\omega_0 = -2\omega_0$ and $\partial R/\partial\omega_0 = \partial S/\partial\omega_0 = 0$. Moreover in the Eq. (7.35) λ_0 and μ_0 are the solutions of the conjugate equations of Eqs. (7.30)-(7.31)

$$\lambda_0''(r_\star) + (\omega^2 - V_{11})\lambda_0(r_\star) = V_{21}\mu_0\,, \tag{7.36}$$

$$\mu_0''(r_\star) + (\omega^2 - V_{22})\mu_0(r_\star) = V_{12}\lambda_0\,. \tag{7.37}$$

The correction (7.35) has been computed in Ref. [197] for the case of "bound-state like" boundary conditions. Interestingly enough, it is also valid for the more general case of boundary conditions defined in Eq. (7.32). In fact it is straightforward to show that contributions to Eq. (7.35) arising from boundary conditions (7.32) cancel each others out, if the same boundary conditions are also imposed on λ_0 and μ_0. Therefore Eq. (7.35) can be used in an iteration scheme until we reach the required accuracy. We find that convergence usually occurs, within the required precision (typically $|[[\Theta_0']]\,/\Theta_0'(+0)| < 10^{-6}$), in less then 50 iterations. However, we cannot find the entire QNM spectrum using this method. Indeed even the single equation version of this method fails to find first overtones of Schwarzschild BHs in General Relativity [194]. This is the reason why, as discussed in the next section, we can find QNMs with this approach only for $M^4\beta \gtrsim 0.5$. For smaller values of β the iteration scheme ceases to converge.

7.4 Numerical results

In this Section we present the results of our numerical integrations, performed using both the time domain approach and the iteration scheme approach in the frequency domain. The results for time domain evolutions refer to Gaussian initial data, with a Gaussian wave-packet characterized by $v_c = 10.0$ and $\sigma = 1.0$ in Eq. (7.25); the field is extracted at $r_\star = 50.0M$.

7.4.1 Small $M^4\beta$ limit

For small values of $M^4\beta$ ($\lesssim 0.5$), the perturbative dynamics is characterized by a stable exponential mode phase. The intermediate late time evolution is dominated by

$$\Phi(t, r_{\rm fixed}) = e^{\omega_{\rm no}\, t}\begin{pmatrix} a \\ b \end{pmatrix} \tag{7.38}$$

with $\mathrm{Re}[\omega_{\rm no}] = 0$ and $\mathrm{Im}[\omega_{\rm no}] < 0$.

After an extensive numerical exploration performed using the time domain approach, the non-oscillatory frequencies $\omega_{\rm no}$ obtained are consistent with the expression

$$M\omega_{\rm no} = -0.04024(M^4\beta)^{0.44}\ell\left(1+\frac{2.0953}{\ell}-\frac{3.4460}{\ell^2}\right), \tag{7.39}$$

which is illustrated in Fig. 7.1.

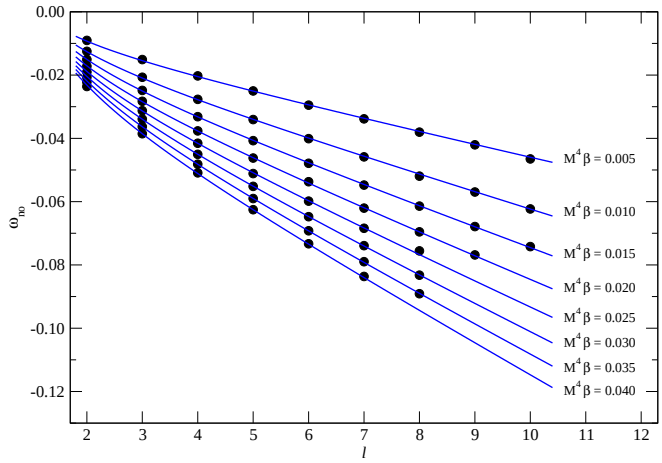

Figure 7.1: $\omega_{\rm no}$ as a function of ℓ for different values of $M^4\beta \leq 0.4$. The dots indicate data from our numerical methods, continuous lines indicate the fit (7.39).

7.4.2 Intermediate values of $M^4\beta$

For $M^4\beta \gtrsim 0.5$, the system evolves with damped oscillations. The transition between non-oscillating and oscillatory mid-late time behavior can be seen in Fig. 7.2, where we show the time evolution of the Ψ and Θ components with $\ell = 2$ for $\beta = 5{\cdot}10^{-3}, 0.25, 1$. The behavior for higher values of ℓ is qualitatively similar.

In this oscillatory regime we have found, for each value of $M^4\beta$, two modes. In Table 7.1 we present the corresponding QNM frequencies (for $\ell = 2$), computed using both numerical methods described above; we find that the agreement between the two approaches is always better then 0.4%. As we discuss in Section 7.4.3, these two modes belong to two different branches, which we term "gravitational" and "scalar"; thus we can consider them as the "fundamental" modes, *i.e.* the lowest lying modes of these two branches. We stress that these names refer to the large β limit of the modes, but both perturbations, Ψ and Θ, oscillate with both modes[a].

The three different $\ell = 2$ modes are shown, for $10^{-2} \lesssim M^4\beta \lesssim 10^5$, in Fig. 7.3, where the dotted-dashed line refers to the non-oscillating mode, the continuous line to the "gravitational" oscillating mode, and the dashed line to the "scalar" oscillating mode. We can see that, for small values of β, the non-oscillating mode $\omega_{\rm no}$, which dominates the time profile, is excited

[a]This happens for $M^4\beta \lesssim 100$; for larger values of $M^4\beta$, the scalar perturbation Θ oscillates with one mode only, as discussed in Section 7.4.3.

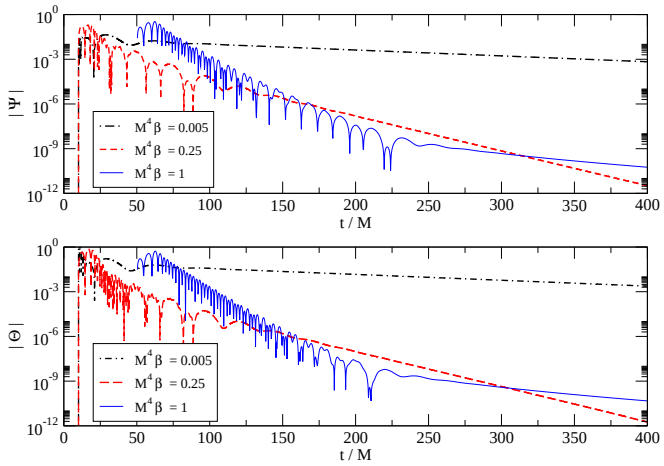

Figure 7.2: Time-profiles for the $|\Psi|$ (upper panel) and $|\Theta|$ (lower panel) components with $\ell = 2$ and $M^4\beta = 5{\cdot}10^{-3}, 0.25, 1$.

together with the gravitational oscillating mode; for $\beta = 0.3$ all three modes are present, and for larger values of β the two oscillating modes are present. Qualitatively similar plots can be found for also for $\ell = 3$ and $\ell = 4$. The time evolution of Ψ for $M^4\beta = 0.3$, which is a combination of the three modes, is shown in in Fig. 7.4.

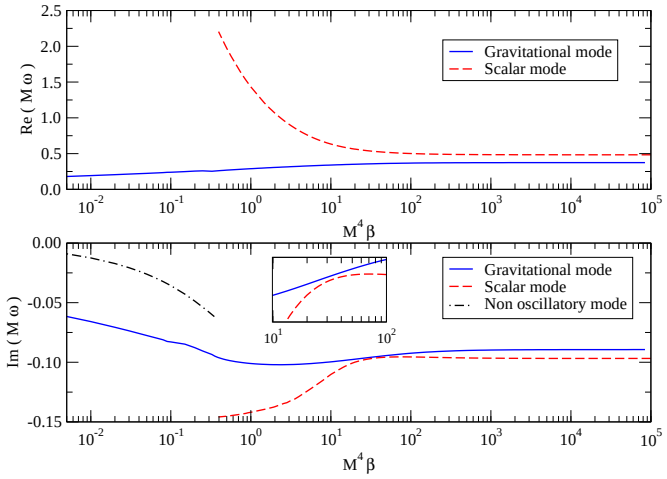

Figure 7.3: Real (upper panel) and imaginary (lower panel) parts of the fundamental QNMs as functions of β for $\ell = 2$.

It should be mentioned that the numerical determination of the different modes for the same value of $M^4\beta$ is not an easy task. For instance, neither of the two approaches is able to find the scalar non-oscillating mode for $M^4\beta \sim 0.5$. The numerical difficulties are related to the fact that the convergence of the iteration scheme in the frequency domain approach is more difficult for small values of β. On the other hand, the time-profiles are usually available for all the β range considered, but the extraction of the frequencies from them is not always

Table 7.1: Quasinormal frequencies for the oscillatory modes with several values of $M^4\beta$ and $\ell = 2$. We compare the results obtained with the time domain (TD) approach with those obtained with the frequency domain (FD) approach.

	$M\omega$, $\ell = 2$	
$M^4\beta$	TD	FD
0.50	0.276 - 0.0967 i	0.276 -0.0936 i
	1.98 - 0.145 i	1.97 - 0.144 i
1.00	0.291 - 0.0970 i	0.292 -0.0971 i
	1.43 - 0.142 i	1.43 - 0.142 i
10.0	0.340 - 0.0980 i	0.340 - 0.0983 i
	0.634 - 0.110 i	0.634 - 0.110 i
100	0.366 - 0.0921 i	0.367 - 0.0919 i
	0.501 - 0.0952 i	0.501 - 0.0954 i
∞	0.374 - 0.0890 i	0.374 - 0.0890 i
	0.484 - 0.0967 i	0.484 - 0.0967 i

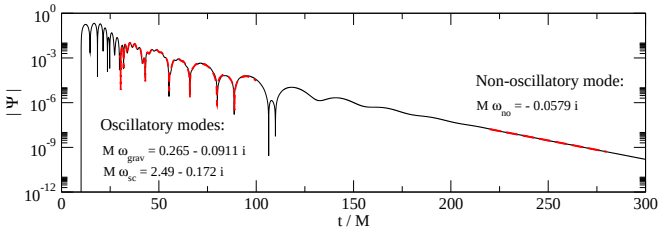

Figure 7.4: Time profile for the Ψ component from the time-evolution approach (solid line) for $M^4\beta = 0.3$ and $\ell = 2$, compared with a combination of oscillatory and non-oscillatory modes (dashed line).

possible. However, we remark that the concordance of the two methods is very good in a wide range of parameter space.

7.4.3 Large $M^4\beta$ limit

A time-profile for the wave function for $M^4\beta = 100$ and $\ell = 2$ is presented in Fig. 7.5. The data for the Ψ component are consistent with a two-mode fit. The values obtained are

$$M\omega_{\rm grav} = 0.3736 - 0.08899\,{\rm i} \tag{7.40}$$

$$M\omega_{\rm sc} = 0.4837 - 0.09671\,{\rm i}\,, \tag{7.41}$$

which coincide, up to numerical precision, with the complex frequencies of the (lowest lying) QNMs of Schwarzschild BHs in Einstein's theory for gravitational ($\omega_{\rm grav}$) and scalar ($\omega_{\rm sc}$) perturbations [9]. The data for the Θ component, instead, is consistent with a single mode fit, with frequency $\omega_{\rm sc}$. The obtained frequencies fit the numerical data very accurately. We can conclude that in the $\beta \to \infty$ limit and for low multipole numbers ℓ, the gravitational perturbations and the scalar field oscillate with the QNMs of Schwarzschild BHs: the former,

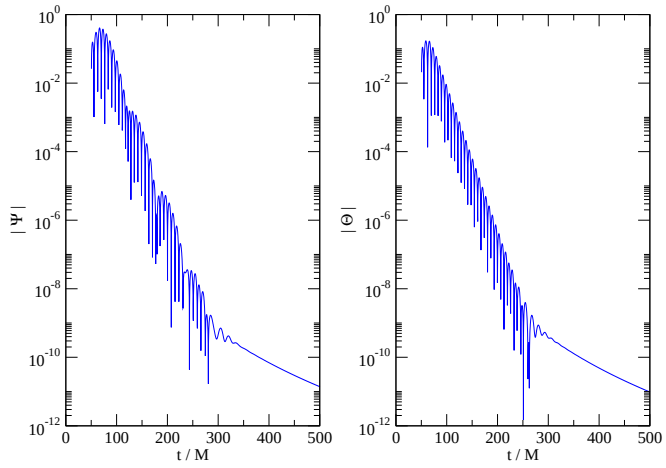

Figure 7.5: Time evolution of $|\Psi|$ and $|\Theta|$, for $M^4\beta = 100$ and $\ell = 2$.

with a combination of the scalar QNM and of the gravitational QNM; the latter, with the scalar QNM. This behavior can be easily understood if we consider the $\beta \to \infty$ limit of the perturbation equations:

$$\frac{d^2}{dr_\star^2}\Psi + \left\{\omega^2 - f\left[\frac{\ell(\ell+1)}{r^2} - \frac{6M}{r^3}\right]\right\}\Psi = \frac{96\pi\, M f}{r^5}\Theta\,, \tag{7.42}$$

$$\frac{d^2}{dr_\star^2}\Theta + \left\{\omega^2 - f\left[\frac{\ell(\ell+1)}{r^2} + \frac{2M}{r^3}\right]\right\}\Theta = 0\,. \tag{7.43}$$

These equations show that, as discussed in Section 7.2, the limit $\beta \to \infty$ does not correspond to the General Relativity limit. Indeed, the gravitational field is coupled with the scalar field: equation (7.42) for Ψ is sourced by Θ. To recover General Relativity, one should restrict to the solutions with $\Theta \equiv 0$; note that $\Theta \equiv 0$ is solution of the $\beta \to \infty$ equations (7.42), (7.43), not of the general equations (7.13), (7.14).

Eq. (7.43) coincides with the equation for scalar field perturbations of a Schwarzschild BH in General Relativity. It does not depend on Ψ, and can be solved separately, yielding the well known scalar QNM frequencies of Schwarzschild BHs [9]. Once Eq. (7.43) is solved, one can solve Eq. (7.42), treating it like the equation of a forced oscillator, since $\Theta(r)$ can be considered as "known". The homogeneous equation associated to (7.42) yields the gravitational QNM frequencies, like $\omega_{\rm grav}$ [9], whereas the source oscillates with frequency $\omega_{\rm sc}$. Its solution $\Psi(r)$, at very late times, oscillates with $\omega_{\rm sc}$ only, but at earlier times it is a combination of the two frequencies, as we have found in our numerical integrations. Furthermore, if $\Theta \equiv 0$, Eq. (7.42) is trivially satisfied, whereas Eq. (7.43) simply becomes the Regge-Wheeler equation for gravitational perturbations of a Schwarzschild BH. This explains why in the $\beta \to \infty$ limit *both* scalar and gravitational QNMs are eigenfrequencies of perturbation equations. Therefore, no matter how large the coupling constant β is, DCS gravity leaves a peculiar signature in the gravitational spectrum of a Schwarzschild BH. The actual detectability of this signature is discussed in Section 7.5.

7.4.4 Late time power-law tails

Our results clearly indicate that, for large enough values of the coupling constant β, there is a power-law tail dominating the signal of the first multipolar numbers at very late times (after the ringdown). Typical time profiles are shown in Fig. 7.6. The observed late time power-law tails are consistent with the expression

$$\Phi(t, r_{\rm fixed}) = t^{-(2\ell+3)} \begin{pmatrix} a \\ b \end{pmatrix} . \tag{7.44}$$

The result (7.44) can be analytically considered in the large r limit. In this limit, the equations decouple and previous results in the literature [201] are applicable. The tails are universal, in sense that they show no dependence on the parameters M and β. Note that the same

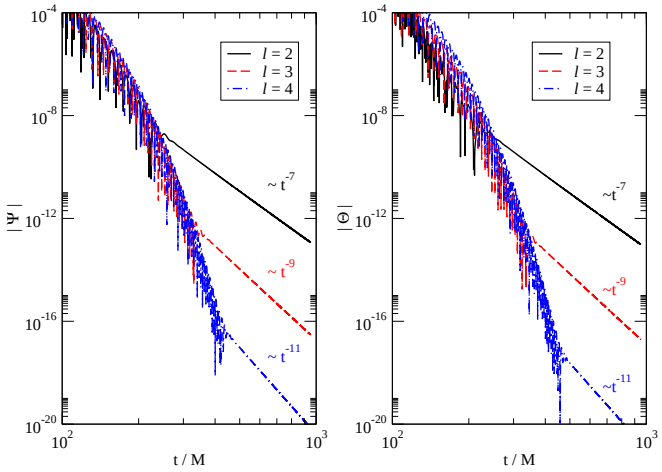

Figure 7.6: Time evolution of $|\Psi|$ and $|\Theta|$ for several values of ℓ. Straight lines indicate power-law decay.

behavior (7.44) characterizes also Schwarzschild BHs [198], implying that a gravitational-wave observation of the tail would not be able to discriminate DCS gravity from General Relativity.

7.4.5 Inclusion of a mass term in the Lagrangian

A relevant question is how the inclusion of a non-vanishing potential $V(\vartheta)$ in the action (7.6) affects results discussed above. Here we consider the simplest potential, by ing a mass term for the scalar field, *i.e.* $V(\vartheta) = m^2\vartheta^2$, with $m = G\mathcal{M}/(\hbar c)$ and $\mathcal{M}$ the physical mass of the field. We note that, if we consider a solar mass BH, $\mathcal{M} = 10^{-16}(mM)$ MeV; therefore, $mM = 0$ for a massless field, $10^{-13} \lesssim mM \lesssim 1$ for ultra-light axions [202], $mM \sim 10^{18}$ for a pion field, and $mM \sim 10^{21}$ for a scalar field at the electroweak scale.

We note that the inclusion of a mass term destroys the shift symmetry of DCS gravity, *i.e.*, invariance under $\vartheta \to \vartheta + k$, with k a constant. If one takes this as a fundamental symmetry, which could presumably be broken only at the electroweak scale, it would imply that m is of the electroweak size [203]. Nevertheless, for generality we do not impose any *a priori* constraint on the mass of the scalar field.

The mass term affects only the perturbation equation for the scalar field. In particular only V_{22} in Eq. (7.20) is affected, and its general form for massive scalars is

$$V_{22} = f\left[\frac{\ell(\ell+1)}{r^2}\left(1+\frac{576\pi M^2}{r^6\beta}\right)+\frac{2M}{r^3}+m^2\right]. \tag{7.45}$$

Note that any scalar potential $V(\vartheta)$ whose expansion for $\vartheta \ll M^2$ starts at least quadratically, *i.e.* $V(\vartheta) \sim m^2\vartheta^2 + \mathcal{O}(\vartheta^3)$, would give the same potential V_{22} as Eq. (7.45). This is also the case of the periodic potential $V(\vartheta) \sim \cos\vartheta$ for ultra-light axions [202].

Moreover the inclusion of a mass term affects the boundary conditions (7.32) for the scalar field. In fact at infinity we have

$$\Theta \sim e^{i\sqrt{\omega^2-m^2}r_\star}. \tag{7.46}$$

Our numerical methods are capable of computing QNMs for massive scalar perturbations whose mass is $mM \lesssim 0.2$, which includes the case of ultra-light axions. We report that numerical results perfectly agree with our analytical expectations in Section 7.4.3. In fact, in the large β limit, the inclusion of the potential only affects Eq. (7.43) and in turn it modifies only the scalar branch of modes: the QNM spectrum consists in the usual gravitational modes plus *massive* scalar modes of a Schwarzschild BH.

For smaller values of the coupling constant ($M^4\beta \lesssim 100$) the analytical limit discussed in Section 7.4.3 breaks down and both gravitational and scalar modes are affected by the scalar potential. Qualitatively, the spectrum for massive scalar perturbations is analogous to the one shown in Fig. 7.2. However, for gravitational modes, the dependence on the scalar mass is very mild. The real part is almost insensitive to m (at least for $mM \lesssim 0.2$), whereas the imaginary part changes as much as 5% for $M^4\beta \sim 1$ and $mM \sim 0.2$. Thus, as expected, DCS gravity leaves a signature in the QNM spectrum of a Schwarzschild BH even if a scalar potential of the form (7.5) is included. Presumably similar results hold for larger values of mM and for more general potentials $V(\vartheta)$.

7.5 Discriminating the QNMs: no-hair tests

Let us now consider what kind of information one can extract from gravitational-wave observations of black hole ringdowns, *i.e.*, from the observation of the quasinormal modes of black holes [14, 204, 9].

What we ideally would like to do is to use gravitational-wave measurements to test General Relativity and/or to rule out alternative candidate theories. The detection of two modes in General Relativity would probably mean these modes are the $\ell = 2$ and $\ell = 3$ fundamental modes, with frequencies $M\omega = 0.37367 - 0.08896\,\mathrm{i}$ and $M\omega = 0.59944 - 0.09270\,\mathrm{i}$, respectively [9]. On the other hand, two-mode measurements in DCS gravity could stand for the lowest $\ell = 2$ modes, which in DCS gravity with large $M^4\beta$ are $M\omega_{\rm grav} = 0.3736 - 0.08899\,\mathrm{i}$ and $M\omega_{\rm sc} = 0.4837 - 0.09671\,\mathrm{i}$. The question we now address is the following: what minimum signal-to-noise ratio is required in order to be able to discriminate two ringdown signals, and then to test DCS gravity? In other words, how can we tell if there really are two or more modes in the signal, and can we resolve their parameters? If the noise is large and the amplitude of the weaker signal is very low, or the two signals have almost identical frequencies, the two modes could be difficult to resolve. If we can resolve the two modes, then tests of Chern-Simons predictions can be performed.

A crude lower limit on the SNR required to resolve frequencies and damping times was presented in [14, 204, 9]. The analysis uses the statistical uncertainty in the determination of each frequency and damping time, which a standard Fisher Matrix calculation estimates to be [14, 204, 9],

$$\rho\sigma_f \lesssim \frac{0.1}{M}\,, \tag{7.47}$$

$$\rho\sigma_\tau \lesssim 65M\,. \tag{7.48}$$

Here, ρ is the signal-to-noise ratio (SNR), $f \equiv \mathrm{Re}[\omega]/2\pi$ and $\tau \equiv 1/\mathrm{Im}[\omega]$ and σ_k is the rms error for variable k. The numbers above assume white-noise for the detector, and equal amplitudes for the two modes. A natural criterion (*á la* Rayleigh) to resolve frequencies and damping times is

$$|f_1 - f_2| > \max(\sigma_{f_1}, \sigma_{f_2})\,, \qquad |\tau_1 - \tau_2| > \max(\sigma_{\tau_1}, \sigma_{\tau_2})\,. \tag{7.49}$$

In interferometry this would mean that two objects are (barely) resolvable if "the maximum of the diffraction pattern of object 1 is located at the minimum of the diffraction pattern of object 2". We can introduce two "critical" SNRs required to resolve frequencies and damping times,

$$\rho^f_{\rm crit} = \frac{\max(\rho\sigma_{f_1}, \rho\sigma_{f_2})}{|f_1 - f_2|}\,, \qquad \rho^\tau_{\rm crit} = \frac{\max(\rho\sigma_{\tau_1}, \rho\sigma_{\tau_2})}{|\tau_1 - \tau_2|}\,. \tag{7.50}$$

We find the following estimates,

$$\rho^f_{\rm crit} \sim 6\,, \tag{7.51}$$

$$\rho^\tau_{\rm crit} \sim 150\,. \tag{7.52}$$

Thus, for SNRs larger than 6, one *can* distinguish the two vibration frequencies in the signal, and is also able to discriminate between the General Relativistic and the DCS prediction. For SNRs larger than 150, one can also measure and discriminate the two different lifetimes. In other words, SNRs larger than 6 allow one to discriminate between the $\ell = 3$ ringing frequency and the "scalar-field-type" gravitational mode in CS gravity with large β. SNRs larger than 150 would allow one to disentangle even the lifetime of each mode. We also note from Table 7.1 and from Fig. 7.3 that for smaller values of β the frequency of the (fundamental, "scalar") mode is larger and then closer to the $\ell = 3$ mode of General Relativity; to discriminate between them, a larger SNR would be required.

The results and discussion above assume that both modes have the same amplitude. In that sense, the results above represent a *lower* limit for the two modes to be discernible. In general the relative amplitude of the two modes depends on the physical process exciting them *and* on the coupling parameters of the theory. For instance, the relative amplitude has a strong dependence on the initial amplitude of each wavepacket, as defined by equation (7.26). This is depicted in Fig. 7.7 for $\ell = 2$ and $\beta = 100$. This plot shows that when $A_1/A_2 = 1$ the scalar and gravitational modes compete and the result is a damped beating pattern. When $A_1/A_2 = 1000$ the gravitational mode dominates the intermediate-time evolution. It would be very interesting to determine the relative amplitudes of these modes for physically interesting situations, like extreme-mass-ratio inspirals, but this is outside the scope of the present work.

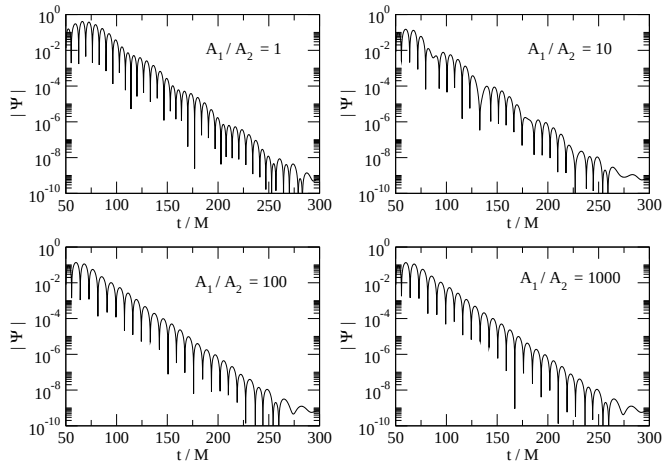

Figure 7.7: Dependence of the gravitational-wave signal on the relative amplitude of the initial gaussian profile, for $\beta = 100$ and $\ell = 2$.

7.6 Conclusions

We have found that Schwarzschild BHs in DCS modified gravity are stable against axial and polar perturbations. Indeed, an extensive investigation of BH oscillations, performed using two different numerical approaches, only yields stable modes, either oscillating or non-oscillating.

Polar perturbations obey exactly the same master equation as in General Relativity, and therefore BHs in DCS gravity oscillate at the same polar frequencies. Axial perturbations, instead, couple to a scalar field, enlarging the spectrum of resonances in the gravitational sector. In particular, the ringdown of a BH in DCS gravity is a superposition of two different QNM sectors. For large values of the constant β, which is associated to the dynamical coupling of the scalar field, one of these sectors corresponds to the gravitational and the other sector to scalar-field QNMs of Schwarzschild BHs in General Relativity. Thus, a golden opportunity to test these theories is by detection of BH ringdowns. As shown in Section 7.5, a modest SNR ($\gtrsim 6$) could be sufficient to discriminate between General Relativity and DCS modified gravity. These estimates assume very special relative amplitudes between the modes. Accurate estimates, as well as constraints on the coupling parameters, require the calculation of accurate waveforms for physically interesting processes exciting these ringdown modes.

The problem dealt with here is also interesting for a number of other reasons, in particular because we expect such kind of problems, *i.e.* QNMs described by a system of coupled second order ODEs, to be a general feature of alternative and more intricate theories; surprisingly there are very few studies of this kind of system in General Relativity.

Finally, we detail in Appendix 7.7 how ghost-instabilities develop in this theory when $\beta < 0$, by a careful analysis of the instability timescale and other features.

Generalization of our results to rotating black holes is of utmost importance, given that many astrophysical black holes are rapidly rotating. Rotating solutions in DCS gravity are only partially understood [170, 205], we hope to come back to this issue in the near future.

7.7 Appendix: Ghost-like instabilities for $\beta < 0$

In this Appendix we study unstable modes for the system (7.13),(7.14), which arise for $\beta < 0$, *i.e.* for the wrong sign for the kinetic energy in the action (7.6). In particular we discuss a peculiar instability, arising at *large* multipoles ℓ, which we believe may be seen as a general signature of ghost-like instabilities at linear level.

For $\beta < 0$, our numerical approaches both show that the amplitudes of the gravitational and scalar field grow exponentially with time: the spacetime is unstable. The agreement between the two methods is excellent (to within the last significant digit), thus results presented here can be reproduced by both methods.

For small values of $M^4|\beta|$ the growth is purely exponential, $\sim e^{\omega_{\rm no} t}$. The non-oscillatory exponential coefficient $\omega_{\rm no}$ depends on β and ℓ, as presented in Table 7.2

Table 7.2: Non-oscillatory exponential coefficient $M\omega_{\rm no}$ for several values of $M^4\beta$ and ℓ.

$\ell = 2$		$\ell = 3$		$M^4\beta = -1$	
$M^4\beta$	$M\omega_{\rm no}$	$M^4\beta$	$M\omega_{\rm no}$	ℓ	$M\omega_{\rm no}$
-0.05	5.894	-0.05	8.391	2	1.115
-0.10	4.111	-0.10	5.871	3	1.629
-0.50	1.706	-0.50	2.467	4	2.142
-1.00	1.115	-1.00	1.629	5	2.655
-2.00	0.6666	-2.00	0.9930	10	5.215
-3.00	0.4382	-3.00	0.6710	20	10.31
-4.00	0.2650	-4.00	0.4358	30	15.30
-4.791	0.0547	-5.233	0.0752	50	24.69

$$M\omega_{\rm no} \approx -0.22 - 0.19\ell + \frac{0.30 + 0.69\ell}{(M^4|\beta|)^{0.45}}\,, \tag{7.53}$$

for any ℓ and small enough $M^4|\beta|$. We notice that the instability timescale $\tau = 1/{\rm Im}[\omega]$ is shorter (the instability is stronger) for smaller β and for larger ℓ. From the expression above one expects that, for large enough $|\beta|$, pure exponentially-growing modes cease to exist ($\omega_{\rm no}$ is negative for large enough $|\beta|$). In fact if $\beta < -|\beta_{\rm no}|$, the late time decay is dominated by an oscillatory exponential mode. This is depicted in Fig. 7.8.

Furthermore our results show that, for fixed ℓ and as β further increases, there exists a critical value $\beta_{\rm crit}$, such that

$$ {\rm Im}\left[\omega(\beta_{\rm crit})\right] = 0\,, \tag{7.54}$$

and for $\beta < -|\beta_{\rm crit}|$ the modes change from unstable to stable. This critical value depends on ℓ and its dependence is very well fitted by a quadratic function

$$M^4\beta_{\rm crit} = -2.77\,\ell^2\,. \tag{7.55}$$

Expression (7.55) implies that the complete perturbation (taking into account all multipole components) is always unstable: for any $\beta < 0$ there is always a multipole ℓ for which $\omega_I > 0$.

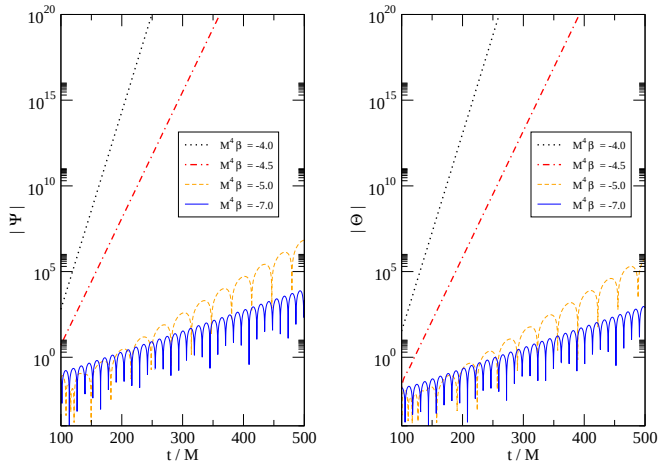

Figure 7.8: Evolution in time of $|\Psi|$ and $|\Theta|$ for $\ell = 2$ and negative values of $M^4\beta$.

Table 7.3: Fundamental unstable mode for different values of β and taking into account the multipole components up to $\ell = 30$

	Fundamental unstable mode, $\omega = \omega_R + \mathrm{i}\,\omega_I$							
	$M^4\beta = -10$		$M^4\beta = -20$		$M^4\beta = -30$		$M^4\beta = -40$	
ℓ	$M\omega_R$	$M\omega_I$	$M\omega_R$	$M\omega_I$	$M\omega_R$	$M\omega_I$	$M\omega_R$	$M\omega_I$
3	0.5387	0.0034	0.5835	0.0060	-	-	-	-
4	0.7342	0.0540	0.7771	0.0371	0.7973	0.0177	0.8074	0.0037
5	0.9154	0.0964	0.9656	0.0676	0.9885	0.0443	1.0002	0.0278
10	1.7929	0.2884	1.8862	0.2186	1.9251	0.1732	1.9456	0.1422
20	3.5266	0.6625	3.7061	0.5188	3.7794	0.4291	3.8181	0.3686
30	5.2563	1.0362	5.5216	0.8186	5.6295	0.6848	5.6865	0.5947

In Table 7.3 we present the fundamental, unstable mode, for large values of β and different values of ℓ. The imaginary part of the fundamental unstable mode grows linearly with ℓ, *i.e.* the instability timescale decays linearly with ℓ.

Generically our results imply that for any value of $\beta < 0$ there is an *instantaneous* instability which develops once all the multipolar components are taken into account. This is related to the choice of the wrong sign for the kinetic term of the scalar field in the action, and it is the signature of ghost-like states at the linear level.

Chapter 8

Black holes in Einstein-Dilatonic-Gauss-Bonnet gravity

It is generally accepted that Einstein's theory will get some as yet unknown corrections, possibly large in the strong field regime. An ideal place to look for these modifications is around the vicinities of compact objects such as black holes. Our case study here are Dilatonic Black Holes, which arise in the framework of Gauss-Bonnet couplings and one-loop corrected four-dimensional effective theory of heterotic superstrings at low energies. These are interesting objects as a prototype for alternative, yet well-behaved gravity theories: they evade the "no-hair" theorem of General Relativity but were proved to be stable against radial perturbations.

We investigate the viability of these black holes as astrophysical objects and try to provide some means to distinguish them from black holes in General Relativity. We start by extending previous works and establishing the stability of these black holes against axial perturbations. We then look for solutions of the field equations describing slowly rotating black holes and study geodesic motion around this geometry. Depending on the values of mass, dilaton charge and angular momentum of the solution, one can have differences in the ISCO location and orbital frequency, relatively to black holes in General Relativity. In the most favorable cases the difference amount to a few percent. Given the current state-of-the-art, we discuss the difficulty to distinguish the correct theory of gravity from EM observations or even with gravitational wave detectors.

Contents

8.1 Introduction

Einstein's theory of General Relativity (GR) has passed numerous consistency and experimental tests in a spectacular way [23]. Nevertheless, it is a general consensus that GR will get modified at some scale, if only because GR has resisted all attempts at its quantization. Moreover, other theories of gravity also pass the experimental tests, some with a better "quantum behavior" and should be taken as serious candidates. Unfortunately, the majority of these alternative theories are vastly more complex than GR in their full-fledged form. Thus the differences between one and the other and specially differences one can measure experimentally are difficult to probe and present investigations mostly focus on the weak-, far-field behavior.

One of the candidates for a theory of quantum gravity is string theory [206]. Since it is still difficult to study geometrical settings in superstring theories, most analyses have been performed by using low-energy string-inspired effective theories [207]. Thus, quantum gravity predictions can be tested by studying modifications of GR due to some low-energy truncation of string theory [208]. Typically the effective theories are supergravities involving not only the metric but also a scalar field (the dilaton) as well as several gauge fields [27]. One of such theories is the one-loop corrected four-dimensional effective theory of the heterotic superstrings at low energies and a simple particular case is known as Einstein-Dilatonic-Gauss-Bonnet (EDGB) theory (see for instance Ref. [209] and references cited therein for a nice and concise introduction to this theory). In EDGB theory the gauge fields are neglected and only the (spacetime-dependent) coupling between the dilaton and the gravity is considered, with the anomaly-canceling Chern-Simons term also neglected (see for instance [210, 190, 211, 212] for work taking this term into account). At the first order in the Regge slope, α', higher-derivative gravitational terms such as the Gauss-Bonnet (GB) curvature-squared term are present in the action, hence the name. The GB terms avoid some pathological features, for example the theory is ghost-free. Since the equations of motions are still of second order, EDGB theory provides one of the simplest consistent high-energy modifications to GR. Even though it does not seem to be a viable cosmological model [213], the Parametrized Post-Newtonian [214] expansion of this theory is identical (to lowest order) to that of GR [215, 216], which means that it passes all Solar system-like experimental tests of gravity. Differences arise only from full nonlinear effects and the ideal place to look for these is near compact objects such as black holes.

Dilatonic Black Holes (DBHs) do exist in EDGB theory [177, 217, 218]. They have a regular event horizon and the geometry is asymptotically flat at infinity (recently DBHs in higher dimensions [175] and with non-flat asymptotical geometries [219] have also been studied). In what follows we refer to DBHs in EDGB theory only. DBHs are interesting for many theoretical and practical reasons. DBHs can evade the classical "no-scalar-hair" theorem [145], and be dressed with classical non-trivial dilaton hair. This is a direct consequence of the GB term [177] and opens up the exciting possibility of ruling out such objects and theories by testing the no-hair theorem, either by gravitational-wave observations of ringdown [14] or by observations of highly eccentric orbits around supermassive black holes [220]. The lack of experimental data and some problems on the theoretical side make it very difficult to explore string theory and other theories of quantum gravity. Since quantum gravity effects are expected to play a significant role in strong gravity regime such as in cosmology [221] and in black hole physics, the investigation of BHs in EDGB theory can shed new light on some aspects of quantum gravity and/or be used to develop testable predictions of the theory.

8.1.1 Astrophysical implications

Our purpose here is to begin exploring differences between GR and alternative theories that could be experimentally tested through astrophysical observations, in the strong field regime. Thus, even though the theory with which we will work is only a first order truncation of the full action, we will elevate it to the status of a complete theory, therefore we place no restriction on the Regge slope. The first important problem concerns the stability of DBHs. Credible alternatives to the Schwarzschild and Kerr metric of GR must be stable spacetimes. It has been shown [179, 222] that DBHs are stable against a small subset of all possible perturbations, linear *radial* perturbations. In this work we characterize completely half of the possible degrees of freedom, by studying general *axial* perturbations. We find that DBHs are stable also against these perturbations. By itself this is an interesting result confirming that high-energy contributions lead to viable alternatives to classical BHs arising in GR. The viability of DBHs poses the following question: can one devise observational tests to discern a DBH from a classical BH? In classical Einstein-Maxwell theory BHs are characterized by three parameters [223]: mass M, electric charge Q and angular momentum $J \equiv aM \leqslant M^2$. Astrophysical BHs are likely to be electrically neutral because of the effect of surrounding plasma [224], and therefore tests of alternative theories of gravity can in general focus on rotation alone. The task is still highly non-trivial and as we mentioned earlier, strong-field effects must be searched for in theories that are not already ruled out by Solar-system experimental data [216].

Most if not all of present-day astrophysical observations related to compact objects, concern directly or indirectly the motion of matter. Thus, a study of geodesic motion around compact objects in alternative theories is of utmost importance. Geodesics convey very important information on the background geometry. In particular circular orbits whose radius is close to the horizon may be extremely useful, because they already probe strong field regions. They can be used to compute the "innermost-stable-circular-orbit" (ISCO), a notion which is very important for interpretation of the experimental data concerning astrophysical black holes. For the Schwarzschild spacetime, $r_{\rm ISCO} = 6M$, while for an extremal rotating Kerr geometry, $r_{\rm ISCO} = M$, $9M$ for co- and counter-rotating circular orbits respectively. Measurements of the ISCO are also useful to evaluate the angular momentum of Kerr BHs [225]. Current methods to measure the ISCO include spectral fitting, quasi-periodic oscillations and relativistic iron line measurements [225]. Here we show that differences in the ISCO of slowly rotating DBHs and classical Kerr black holes can be significant, depending on the coupling parameter. These differences, which may be detectable in near-future experiments, are likely to increase for highly spinning black holes (which are unfortunately out of the scope of this work). In fact, it seems an exciting possibility that the GRAVITY experiment [226], designed to make precision measurements of orbits of stars in the neighborhood of the black-hole in the center of our galaxy, might already be able to discriminate between these black hole solutions and GR solutions, or otherwise impose stringent bounds on the coupling parameter.

Current techniques to evaluate the angular momentum of astrophysical compact objects are based only on ISCO measurements [225]. One needs to *assume* a particular theory of gravity in order to evaluate J. Thus discerning a DBH from a Kerr black hole by ISCO measurements is not an easy task. Future gravitational wave experiments will provide a viable method to measure M and J independently [139]. The analysis below suggests that a *possible* deviation from the expected ISCO in GR can be explained in term of dilatonic charged BH. Therefore

in a near future, gravitational wave astronomy may offer a the possibility to explore string theory-inspired modifications of GR.

Finally, null unstable geodesics are closely related to the appearance of compact objects to external observers [227, 228] and have been associated with the characteristic, or quasi-normal modes (QNMs) of BHs [229, 9]. Quasinormal modes are very important in devising experimental tests of GR and for gravitational wave astronomy. Measuring QNM frequencies may provide a definitive proof of the existence of BHs in GR and it could be useful to study corrections to GR too. Thus the analysis of geodesic motion around a DBH can shed new light on various and important aspects of high-curvature corrections to gravity.

Other theories might also suggest a different ISCO location, different quasinormal modes, etc. Thus, a deviation in these quantities is not a verification of a particular theory, but is a first step in understanding what different theories and scenarios predict in the strong field regime, which could potentially discriminate GR from other alternatives.

The chapter is organized as follows. In Section 8.2 we briefly review the main aspects of BHs in EDGB theory. In Section 8.3 we prove the linear stability of DBHs against axial perturbations. We proceed by studying slowly rotating DBHs in Section 8.4. We prove that such slowly rotating solutions do exist and we characterize them, including a discussion on the ergoregion in these spacetimes. Section 8.5 discusses geodesics in both spherically symmetric and slowly rotating DBHs as well as the possible experimental tests which can be performed to discern a DBH from a Kerr BH. We compute the ISCO dependence on the angular momentum and the QNM frequencies for a spherical symmetric DBH in the eikonal limit. Conclusions are discussed in Section 8.6. In our notation, we use the signature $(+---)$ and the curvature tensor is defined by $R^a_{ijk} = \partial_j \Gamma^a_{ik} + ...$

8.2 Spherically symmetric BHs in Einstein-Dilaton-Gauss-Bonnet theory

We consider the following low-energy effective action for the heterotic string [27]

$$S = \frac{1}{2}\int d^4x\sqrt{-g}\left(R - \frac{1}{2}\partial_\mu\phi\partial^\mu\phi + \frac{\alpha' e^\phi}{4g^2}\mathcal{R}^2_{GB}\right), \tag{8.1}$$

where

$$\mathcal{R}^2_{GB} = R_{\mu\nu\rho\sigma}R^{\mu\nu\rho\sigma} - 4R_{\mu\nu}R^{\mu\nu} + R^2, \tag{8.2}$$

is the GB invariant, α' is the Regge slope and g^2 is some gauge coupling constant. We set $g = 1$ for the rest of this chapter. String-inspired $\mathcal{O}(\alpha')$ corrections to Einstein's gravitation are included in the action (8.1), while gauge fields and matter are omitted for simplicity. We also note that there is some arbitrariness in the coupling, depending on which frame we take as fundamental [175], we choose to keep the e^ϕ coupling in line with previous works. We shall refer to the action (8.1) as EDGB theory.

The dilaton field and Einstein's equations derived from (8.1) are

$$\frac{1}{\sqrt{-g}}\partial_\mu[\sqrt{-g}\partial^\mu\phi] = \frac{\alpha'}{4}e^\phi\mathcal{R}^2_{GB}, \tag{8.3}$$

$$G_{\mu\nu} = \frac{1}{2}\partial_\mu\phi\partial_\nu\phi - \frac{1}{4}g_{\mu\nu}(\partial_\rho\phi)^2 - \alpha'\mathcal{K}_{\mu\nu}, \tag{8.4}$$

where $G_{\mu\nu} = R_{\mu\nu} - \frac{1}{2}g_{\mu\nu}R$ is the Einstein tensor and

$$\mathcal{K}_{\mu\nu} = (g_{\mu\rho}g_{\nu\lambda} + g_{\mu\lambda}g_{\nu\rho})\eta^{\kappa\lambda\alpha'\beta}\nabla_g[\tilde{R}^{\rho g}{}_{\alpha'\beta}\partial_\kappa f]\,. \tag{8.5}$$

Here,

$$\eta^{\mu\nu\rho\sigma} = \epsilon^{\mu\nu\rho\sigma}(-g)^{-\frac{1}{2}}\,, \qquad \epsilon^{0ijk} = -\epsilon_{ijk}\,,$$
$$\tilde{R}^{\mu\nu}{}_{\kappa\lambda} = \eta^{\mu\nu\rho\sigma}R_{\rho\sigma\kappa\lambda}\,, \qquad f = \frac{e^\phi}{8}\,.$$

From the right-hand-side of the modified Einstein's equation (8.4), one can construct a conserved "energy momentum tensor", $\nabla_\mu T^{\mu\nu} = 0$,

$$T_{\mu\nu} = -\frac{1}{2}\partial_\mu\phi\partial_\nu\phi + \frac{1}{4}g_{\mu\nu}(\partial_\rho\phi)^2 + \alpha'\mathcal{K}_{\mu\nu}\,. \tag{8.6}$$

In Ref.[177] is shown that the time component of $-T_{\mu\nu}$, which in Einstein's gravity would correspond to the local energy density $\mathcal{E}$, *can be negative*. The reason is that, as a result of the higher derivative GB terms, there are contributions of the gravitational field itself to $T_{\mu\nu}$. The positiveness of $-T_{00}$ is one of the main assumptions of the no-scalar-hair theorem [145] which can be (and indeed is) evaded in EDGB theory.

We now focus on BH solutions in EDGB theory, considering the following spherically symmetric ansatz for the metric

$$ds^2 = e^{\Gamma(r,t)}dt^2 - e^{\Lambda(r,t)}dr^2 - r^2(d\theta^2 + \sin^2\theta\, d\varphi^2)\,. \tag{8.7}$$

The equations of motion derived from (8.3) and from (8.4) can be found in Ref. [179]. In a static, asymptotically flat geometry, black hole solutions exist only if [177]

$$e^{\phi_h} \leq \frac{r_h^2}{\alpha'\sqrt{6}}\,, \tag{8.8}$$

where r_h and ϕ_h are quantities evaluated on the horizon. In particular black hole solutions may exist only for $\alpha' > 0$. From the asymptotic behavior of the fields one can extract the ADM mass, M and the charge D. As shown in Ref. [177] M and D are not independent quantities, thereby leading to the secondary nature of the dilaton hair [230]. These black hole solutions are uniquely characterized by two parameters (ϕ_h, r_h), which correspond to a unique choice of (M, D). The equations of motion remain invariant under a shift $\phi \to \phi + \phi_0$ and a simultaneous radial rescaling $r \to re^{\phi_0/2}$. As a consequence of the radial rescaling, the two other asymptotic parameters, M and D, are also rescaled according to the rule $M \to Me^{\phi_0/2}$ and $D \to De^{\phi_0/2}$. Due to the above invariance it is sufficient to vary only one of r_h and ϕ_h. Following [179] we choose to keep r_h fixed and to vary ϕ_h. Typical background fields are shown in Fig. 8.1. Differences in the metric coefficients occur only very close to the horizon. We checked our numerical solutions reproducing results shown in the Table 1 of Ref. [177].

After the rescaling, equation (8.8) can be written in terms of the coupling constant

$$0 < \frac{\alpha'}{M^2} \lesssim 0.691\,. \tag{8.9}$$

The maximum value $\alpha'/M^2 \sim 0.691$ corresponds to $D/M \sim 0.572$. For larger values of the coupling constant no DBH solution exists. The dilaton charge, D, as a function of α'/M^2 is shown in Figs. 8.2, where it is compared with the analytical solution in the $\alpha' \to 0$ limit, $D/M = \alpha'/(2M^2)$ [178].

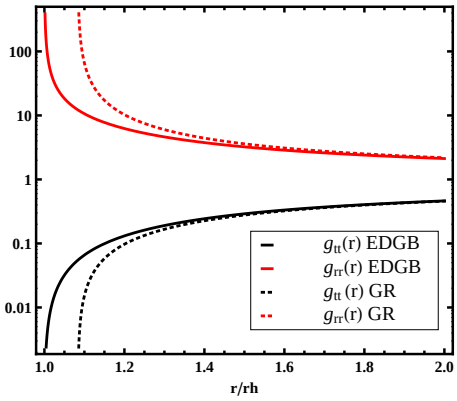

Figure 8.1: Metric components g_{tt} and g_{rr} for a DBH (solid lines) compared with an equal mass Schwarzschild hole (dotted lines) ($\alpha'/M^2 \sim 0.691$, which corresponds to $D/M \sim 0.572$).

8.3 Linear stability analysis

The framework for a linear stability analysis of black holes in theories with Gauss-Bonnet terms was laid down by Dotti and Gleiser [65, 231, 232] in higher dimensions (with no dilaton), and generalized by Moura and Schiappa [209] in the context of Riemann tensor, $\mathcal{R}^2$, corrections. Perturbations of four-dimensional DBHs were considered by Kanti *et al* [179] and Torii and K. i. Maeda [222]. Unfortunately these authors considered only a very specific type of perturbations, here we want to generalize their results. Consider therefore perturbing the spacetime in the following linear way

$$\begin{aligned} g_{\mu\nu}(x^\rho) &= g^{(0)}_{\mu\nu}(x^\rho) + \epsilon\, h_{\mu\nu}(x^\rho)\,, \\ \phi(x^\rho) &= \phi_0(x^\rho) + \epsilon\, \delta\phi(x^\rho)\,, \end{aligned} \tag{8.10}$$

where $\epsilon \ll 1$, $g^{(0)}_{\mu\nu}$ and $\phi_0(x^\rho)$ are the background fields, while $h_{\mu\nu}$ and $\delta\phi(x^\rho)$ are the perturbations. The background metric $g^{(0)}_{\mu\nu}$ and dilaton field $\phi_0(x^\rho)$ are given by the numerical static black hole solution described above [177].

8.3.1 General formalism

To study this problem we use the approach first described by Regge and Wheeler [4]. After a decomposition in tensorial spherical harmonics [5, 233], the perturbations fall into two distinct classes: *axial* (odd) with parity $(-1)^{l+1}$ and *polar* (even) with parity $(-1)^l$, where l is the angular momentum of the particular mode. The theory described by (8.1) is invariant under diffeomorphisms[a], as Einstein's theory is. We can then use the gauge freedom in order to simplify the elements $h_{\mu\nu}$. In the classical Regge-Wheeler gauge the canonical form for the metric perturbations is (see also Ref. [234]):

[a]Despite the covariant derivative in Eq. (8.5), equations of motion *do not* contain higher derivatives of the metric $g_{\mu\nu}$ because of the GB term (see equation (4) in [222]). This allows one to use the same gauge transformations first proposed in Ref. [4].

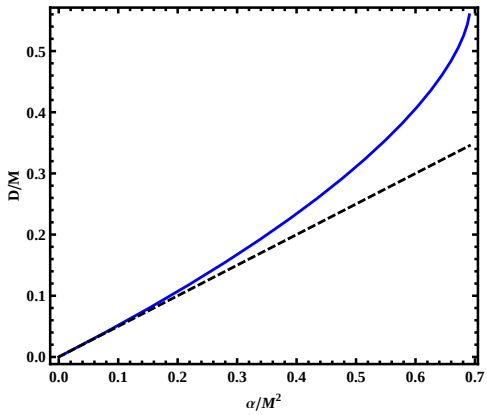

Figure 8.2: The dilaton charge, D, as a function of (re-scaled) α'/M^2 (solid line). The whole range of α'/M^2 in which a black hole solution exists is shown. Numerical solution behaves as $D/M \sim \alpha'/(2M^2)$ in the $\alpha' \to 0$ limit [178] (dashed line).

- axial perturbations:

$$h_{\mu\nu} = \begin{bmatrix} 0 & 0 & 0 & h_0 \\ 0 & 0 & 0 & h_1 \\ 0 & 0 & 0 & 0 \\ h_0 & h_1 & 0 & 0 \end{bmatrix} e^{-i\omega t} \left(\sin\theta \partial_\theta\right) P_l \,, \tag{8.11}$$

- polar perturbations:

$$h_{\mu\nu} = \begin{bmatrix} H_0 e^{\Gamma(r)} & H_1 & 0 & 0 \\ H_1 & H_2 e^{\Lambda(r)} & 0 & 0 \\ 0 & 0 & r^2 K & 0 \\ 0 & 0 & 0 & r^2 K \sin^2\theta \end{bmatrix} e^{-i\omega t} P_l.$$

Where $P_l = P_l(\cos\theta)$ is the Legendre polynomial with angular momentum l and h_0, h_1, H_1, H_2 and K are unknown radial functions.

Perturbations of the dilaton field, $\delta\phi$, do not appear in the axial equations (see also [235]). The linear stability analysis proceeds by mapping the system of the equations of motion for the perturbation fields under consideration to a stationary one-dimensional Schrödinger problem, in an appropriate potential well, in which the 'squared frequencies' ω^2 are the "energy eigenvalues". Instabilities, then, correspond to bound states, *i.e.* to negative energy eigenstates or equivalently to frequencies ω with a positive imaginary component.

Presumably because polar perturbations are extremely complex to analyse, Kanti et al. [179] focused on a certain subset, the radial perturbations. They found that the spacetime was stable against radial perturbations, their results being confirmed in Ref. [222]. Thus, there are good indications that the spacetime is stable under polar perturbations. We thus focus here on the other set of perturbations, axial perturbations, which as far as we know are not dealt with in the literature.

8.3.2 Axial perturbations

For axial perturbations only 3 nontrivial Einstein equations can be obtained by substituting (8.11) and (8.10) into (8.4). The zeroth-order equations are identically zero, due to the background solution, while the equations for the perturbations, h_0 and h_1, read:

$$(\varphi,\theta): \qquad h_0(r) + A_1\, h_1(r) + A_2\, h_1'(r) = 0\,, \tag{8.12}$$

$$(\varphi,r): \qquad h_0'(r) - \frac{2}{r}\, h_0(r) + 1, l\, h_1(r) = 0\,, \tag{8.13}$$

$$(\varphi,t): \qquad C_{1,l}\, h_0(r) + C_{2,l}\, h_1(r) + C_{3,l}\, h_0'(r) + C_{4,l}\, h_1'(r) + C_{5,l}\, h_0''(r) = 0\,, \tag{8.14}$$

where A_i, $B_{i,l}$ and $C_{i,l}$ depend on the radial background function $\Gamma, \Gamma', \Gamma'', \Lambda, \Lambda', \phi_0, \phi_0'$ and ϕ_0'' found in [177]. Their explicit form can be found in Appendix 8.7. We observed numerically that equation (8.14) is automatically satisfied as a consequence of the other two equations and of background solutions. So we are left with a system of two ODEs for two unknown functions $h_0(r)$ and $h_1(r)$. Eliminating h_0 from the first order equation (8.12) we obtain a second order differential equation for h_1 which can be recast (see Appendix 8.7 for details) in the following Schrödinger-like equation,

$$u''(r) + \left[V(r) + \omega^2 K(r)\right]\, u(r) = 0\,, \tag{8.15}$$

These functions are shown in Fig. 8.3.

The asymptotic behavior of equation (8.15) (see Appendix 8.7 for details) is

$$u''(r) + \left[\frac{V_h + \omega^2 K_h}{(r-r_h)^2}\right]\, u(r) = 0\,, \qquad r \to r_h\,, \tag{8.16}$$

$$u''(r) + \omega^2\, u(r) = 0\,, \qquad r \to \infty\,. \tag{8.17}$$

The asymptotic solutions are

$$u(r) \;\sim\; u_0 (r-r_h)^{\frac{1}{2} \pm \sqrt{\frac{1}{4} - V_h - \omega^2 K_h}}\,, \quad r \to r_h\,, \tag{8.18}$$

$$u(r) \;\sim\; u_\infty e^{\pm i\omega r}\,, \quad r \to \infty\,. \tag{8.19}$$

Figure 8.4 shows the coefficients V_h and K_h as functions of α'/M^2. For a Schwarzschild BH, $V_h \equiv 1/4$ and $K_h \equiv 4M^2$. In the EDGB case one finds one finds $V_h \sim 1/4$ and $K_h \lesssim 4M^2$ in the whole range (8.9). Thus the asymptotic solution (8.18) simplifies

$$u(r) \sim u_0 (r-r_h)^{\frac{1}{2} \pm i\,\omega M \sqrt{\frac{K_h}{M^2}}}\,, \quad r \to r_h\,, \tag{8.20}$$

Since ω is complex, the sign in equations (8.19) and (8.20) above has to be chosen so that the solution is regular on the horizon and at infinity. For unstable modes $\mathrm{Im}(\omega) > 0$, thus the choice of the minus and the plus sign in Eqs. (8.19) and (8.20) respectively guarantees that the corresponding eigenfunctions will vanish at infinity and at the horizon. We have searched for unstable modes using these boundary conditions. We integrated equation (8.15) outward starting from the horizon until we found the eigenfrequency corresponding to a vanish field at infinity. We used a Runge-Kutta 4th order method, considering $r_h = 1$ and different ϕ_h

values corresponding to different BH solutions [177]. We systematically span the whole range (8.9) for $l = 2$, 3, 4. We also randomly span other values for α' and l to no avail: no unstable modes were found. We checked the numerical accuracy of our results by changing numerical parameters such as r_∞. Our results strongly suggest that EDGB black holes are stable against axial perturbations. This completes the previous linear stability analysis [179, 222] performed for radial perturbations. It would be of great interest to understand also polar perturbations

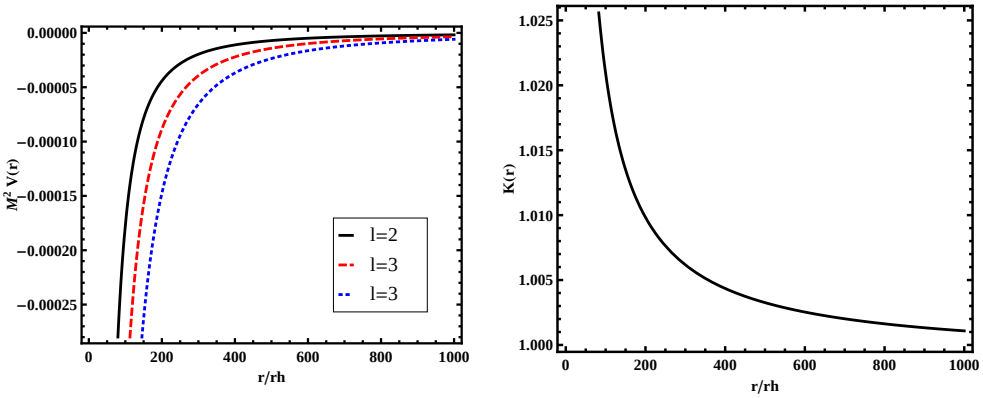

Figure 8.3: Left Panel: The potential $V(r)$ for the axial perturbations for a EDGB black hole. Different values of the angular momentum l are shown for $\alpha'/M^2 \sim 0.691$, which corresponds to $D/M \sim 0.572$. Right Panel: The function $K(r)$ for the axial perturbations equation for a EDGB black hole for $\alpha'/M^2 \sim 0.691$.

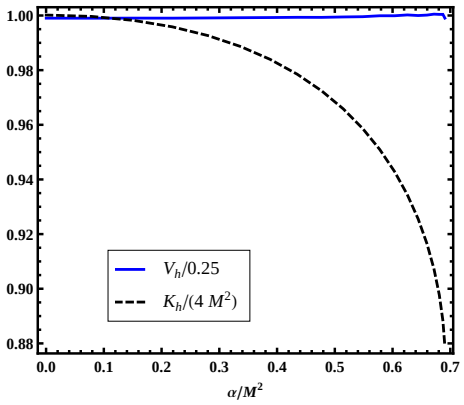

Figure 8.4: The coefficients V_h (solid line) and K_h (dashed line) as functions of α'/M^2 in the whole range (8.9). As for a Schwarzschild BH, $V_h \equiv 1/4$, whereas K_h is always smaller than its Schwarzschild counterpart, $K_h \lesssim 4M^2$.

and reduce them to a single master ordinary differential equation. Due to the complexity of the equations involved we did not perform such an analysis. We note that the present analysis is only possible because axial and polar perturbations decouple in this theory, unlike for instance in Chern-Simons theory [192].

8.4 Slowly rotating BHs in EDGB theory

Astrophysical black holes are expected to be highly spinning because of accretion and merger events [236, 237, 238, 239]. Unfortunately the GB term is very hard to deal with for generic axisymmetric metrics and thus general rotating black holes are difficult to study without a full numerical integration of Einstein's equations. Expansion in α' is another promising approach, which has been successfully implemented for non-rotating DBHs [178]. Here we use another method, searching for solutions describing rotating BHs at every order in α', but in a slow rotation approximation. This method allow us to prove that such (slowly) rotating BHs do exist in EDGB theory. This strongly suggests that, in general, rotating DBHs exist. In alternative high energy modifications of GR, such as Chern-Simons modified gravity BHs, rotating black hole solutions are harder to find [240, 241].

We follow Hartle's approach [242] which is based on axisymmetric perturbations of a spherically symmetric equilibrium solution and on an expansion of the perturbed quantities in a power series of the angular velocity Ω for frame dragging. The equilibrium solution is the one developed in Ref. [177] and explored in the previous sections. To first order in Ω the perturbed metric is

$$ds^2 = e^{\Gamma(r)}dt^2 - e^{\Lambda(r)}dr^2 - r^2\left[d\theta^2 + \sin^2\theta\,(d\varphi - \Omega dt)^2\right]\,, \tag{8.21}$$

where $\Omega \equiv \Omega(r,\theta)$ is the angular velocity $d\phi/dt$ of an observer at (r,θ) freely falling from infinity. Since we consider only axisymmetric perturbations, we neglected the ϕ dependence and we can expand $\Omega(r,\theta)$ in terms of Legendre polynomials

$$\Omega(r,\theta) = \sum_{l=1}^{\infty}\Omega_l(r)\left(-\frac{1}{\sin\theta}\frac{dP_l(\cos\theta)}{d\theta}\right)\,. \tag{8.22}$$

Both the metric and dilaton perturbations are functions of even powers of the angular velocity Ω, thus we can use the unperturbed metric and the unperturbed dilaton field to find Ω-order corrections neglecting Ω^2-order terms. Using the expansion (8.22) only the $\{t,\varphi\}$ component of modified Einstein equations (8.4) is first order in Ω and, interestingly enough, it gives a separable differential equation as follows

$$\Omega_l''(r) + \frac{G_2(r)}{G_3(r)}\Omega_l' + \left[e^{\Lambda}\frac{G_1(r)(2-l(l+1))}{G_3(r)}\right]\Omega_l = 0\,, \tag{8.23}$$

where

$$\begin{aligned} G_1(r) &= 2e^{\Lambda} + \alpha' e^{\phi}\left(\Lambda'\phi' - 2(\phi'^2 + \phi'')\right)\,,\\ G_2(r) &= -e^{\Lambda}r(-8 + r(\Lambda' + \Gamma')) - \alpha' e^{\phi}\left(\phi'(6 - r(3\Lambda' - 2\phi' + \Gamma')) + 2r\phi''\right)\,,\\ G_3(r) &= 2r^2 e^{\Lambda} - 2\alpha' r e^{\phi}\phi'\,, \end{aligned} \tag{8.24}$$

and Λ, ϕ, Γ are zeroth-order in Ω, therefore given by the spherically symmetric background [177]. For $\alpha' = 0$ equation (8.23) is equivalent to the standard GR form (equation (43) in Ref. [242] with vanishing stress tensor).

To solve the above equation we must specify the boundary condition for large r. Since the scalar field vanishes asymptotically, the solution should approach flat space solution. Thus for large r we can define the angular momentum of the BH via the following behavior,

$$\Omega_l(r) \sim \frac{2J}{r^3}\,. \tag{8.25}$$

It is worth to note that the dilaton field can introduce order $1/r^3$ corrections to the off-diagonal metric coefficients. In the slowly rotating approach we use, these corrections are neglected. The asymptotic behavior of equation (8.23) is

$$\Omega_l'(r) + \frac{4}{r}\Omega_l'(r) + \frac{2 - l(l+1)}{r^2}\Omega_l(r) = 0\,, \tag{8.26}$$

whose general solution is

$$\Omega_l(r) \sim \alpha\, r^{-2-l} + \beta\, r^{-1+l}\,, \tag{8.27}$$

where α and β are constant. With the asymptotic behavior (8.25), the equation above implies that only the $l = 1$ mode is allowed. Thus the equation to solve is

$$\Omega_1''(r) + \frac{G_2(r)}{G_3(r)}\Omega_1' = 0\,. \tag{8.28}$$

The solution of the above equation is

$$\Omega_1(r) = C_1 + C_2 \int_{r_h}^{r} dt\, e^{-\int_{r_h}^{t} ds\,(G_2(s)/G_3(s))}\,, \tag{8.29}$$

where the constants C_1 and C_2 are fixed asking for the asymptotic condition at infinity, Eq. (8.25). The analogous procedure to find slowly rotating Kerr solutions in classical GR is presented in Appendix 8.8 for completeness, which is basically a reproduction of the results of Hartle [242]. There we show that this procedure leads to the Kerr metric in lowest order and furthermore that the $l = 1$ term is the only possible term in the expansion. Applying the same procedure to a static boson star [243], one can prove that such slowly rotating solutions do not exist [244].

In what follows we shall drop the index, $\Omega \equiv \Omega_1$. The angular velocity $\Omega(r)$ for different slowly rotating BHs is shown in Figs. (8.5). In the limit $\alpha' \to 0$, one recovers the results for a small rotating BH in General Relativity, obtained perturbing a Schwarzschild BH, as described in the section below. Interestingly, the angular velocity of a BH in the EDGB can be $\sim 40\%$ larger than the one for a slowly rotating Kerr BH (see the bottom panel in Fig.(8.5)) with the same angular momentum. A numerical relation which can be computed from Fig.(8.5) is

$$M\Omega_h \equiv\ M\Omega(r_h) \sim 0.37\frac{J}{M^2}\,, \tag{8.30}$$

while for a slowly rotating Kerr BH the above relation is $M\Omega_h = 0.25\, J/M^2$. Thus, a DBH is more "compact" than a BH with same mass and angular momentum.

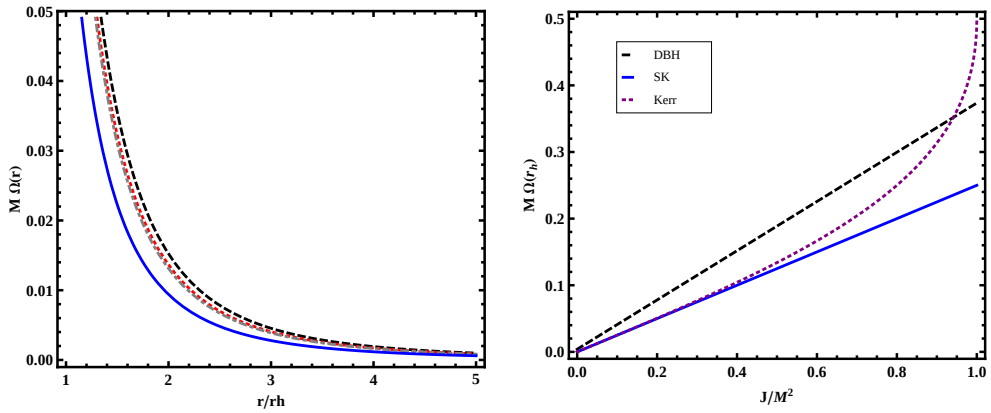

Figure 8.5: Left Panel: Angular velocity Ω as a function of r for different slowly rotating BHs in EDGB theory. From top to bottom: decreasing values for α'/M^2. For $\alpha' \to 0$ or $D \to 0$ solutions approach the slowly rotating Kerr BH (solid line). Right Panel: Angular velocity of the BH, $\Omega_h = \Omega(r_h)$, for a DBH (dashed line) with $\alpha'/M^2 \sim 0.691$ compared to the same for a slowly rotating Kerr BH (solid line) and a Kerr BH (dotted line). Up to $J/M^2 \sim 0.5$ results for the slowly rotating Kerr BH reproduce the exact ones. The difference in the angular velocity between slowly rotating DBHs and slowly rotating Kerr BHs and can be as large as $\sim 40\%$.

8.4.1 Ergoregion and superradiance

Ergoregions can develop in rotating spacetimes. The ergoregion is found by computing the surface on which g_{tt} vanishes. An approximate equation to the location of the ergoregion [245] is

$$0 = -e^{\Gamma(r)} + \Omega^2(r) r^2 \sin^2\theta \,, \tag{8.31}$$

which is expected to be a good approximation specially for very compact objects, such as BHs. The solution of Eq. (8.31) is topologically a torus. In the equatorial plane we have

$$r\Omega(r) = \sqrt{e^{\Gamma(r)}} \,. \tag{8.32}$$

The existence and the boundaries of the ergoregions can be computed from the above equations. The ergoregion width for a DBH compared to both a slowly rotating and a full rotating Kerr BH is shown in Figure 8.6 for different J values. The ergoregion width, W, for a Kerr BH on the equatorial plane is $W/M = 1 - \sqrt{1-(a/M)^2}$. The ergoregion width for a DBH can be $\sim 50\%$ larger than the width for a slowly rotating Kerr BH. Therefore BH superradiance in EDGB is expected to be stronger than in GR. As expected the difference between slowly rotating DBHs and slowly rotating Kerr BHs tends to zero in the $\alpha' \to 0$ limit.

8.5 BH Geodesics in EDGB theory

In this section geodesics in the exterior of both non-rotating and slowly rotating EDGB black holes are discussed. If we neglect back-reaction effects, which we do in the following, the geodesics in this spacetime correspond to paths followed by time-like or null particles. In

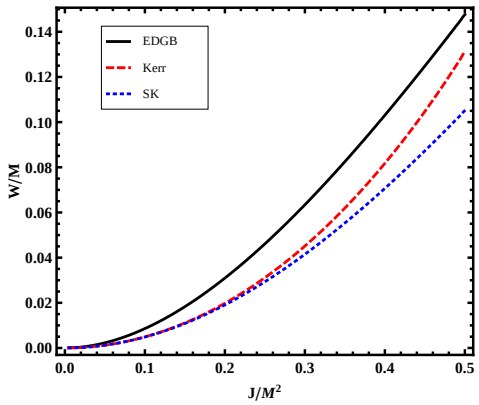

Figure 8.6: Ergoregion width, $\frac{W}{M}$, for a DBH (solid line), a Kerr BH (dashed line) and a slowly rotating Kerr BH (dotted line) as function of the angular momentum J for $\alpha'/M^2 \sim 0.691$. Up to $J/M^2 \sim 0.3$ results for the slowly rotating Kerr BH reproduce the exact ones. The ergoregion width for a rotating DBH can be $\sim 50\%$ larger than the one for a Kerr BH.

principle back-reaction effects should be important for large bodies or strong dilaton fields. However, for small point particles around DBH black holes they should be negligible. From the analysis of the geodetic motion we compute orbital frequencies related to the ISCO for both non-rotating and slowly rotating DBHs and the QNM frequencies for spherically symmetric BHs in EDGB theory in the eikonal limit. These quantities can be directly measured and can be used as a promising tool to study high-energy modifications of GR.

The motion of test particles around a DBH is deeply related to the coupling between matter and the dilaton. However it turns out that the coupling depends on the choice between two different frames, namely the string frame and the Einstein frame (for a discussion in scalar-tensor theories see Ref. [246] and references therein). The two frames are inequivalent. In the string frame the coupling between matter and the dilaton field is minimal, but Newton constant, G_N, depends on the coordinates and light bending is not correctly reproduced [247]. Conversely, in the Einstein frame the light bending is correctly reproduced, since G_N is constant, but particles non-minimally couple to the dilaton field. This leads to a violation of the equivalence principle. This violation is small and compatible with the available tests of the equivalence principle [246] and it is indeed regarded as an important test in discerning the two frames. Which of the two frames is the physically relevant is an open question, which will eventually be settled by experiments.

Following Refs. [177] and [217] we always assume the Einstein frame. In this frame the total action reads

$$S_{\rm TOT} = S + S_c + S_{ts} = S + S_c - m \int dt\, e^{b\phi} \sqrt{-g_{\mu\nu} \frac{\partial x^\mu}{\partial t} \frac{\partial x^\nu}{\partial t}}\,, \tag{8.33}$$

where S is the EDGB action, Eq. (8.1), m is the mass of the test particle and S_c is the action which describes some coupling between the test particle and the dilaton field. The constant b in the equation above is the coupling between the matter and the dilaton field. Its particular value depends on the specific theory from which the low energy theory comes. For low energy

modifications from heterotic string theory, $b = 1/2$. We shall discuss the motion of a test particle keeping a general value of b and we only specialize to $b = 1/2$ when we discussing numerical results. As already mentioned, in the equation above we neglect gauge fields, such as Maxwell fields. Furthermore we neglect any coupling between the dilaton field and the test particle, S_c=0, as well as any back-reaction of the background fields.

The string frame and the Einstein frame are related by a Weyl transformation [248]. Since null geodesics equations are Weyl invariant, the motion of massless particles is the same in both frames and it is described by the standard geodesics equations.

8.5.1 Geodesics: non-rotating case

Following Chandrasekhar [249] and Ref. [229] we consider a four-dimensional stationary, spherically symmetric line element

$$ds^2 = f(r)dt^2 - \frac{1}{g(r)}dr^2 - r^2(d\theta^2 + \sin^2\theta d\varphi^2)\,. \tag{8.34}$$

We also take a spherically symmetric dilaton and set $H(r) = 2b\,\phi(r)$. Due to the symmetry of the above background fields, the trajectory of a particle is planar, say $\theta = \pi/2$ and the following conserved quantities can be defined: the (dimensionless) specific energy of the test particle, $E = e/m$ and the specific angular momentum, $L = \ell/(m)$, where e, ℓ and m are the energy, the angular momentum and the mass of the test particle respectively. Let us restrict attention to circular orbits, for which the Lagrangian is

$$2\mathcal{L} = e^{H(r)}\left(f(r)\,\dot{t}^2 - \frac{1}{g(r)}\dot{r}^2 - r^2\dot{\varphi}^2\right)\,, \tag{8.35}$$

From the Lagrangian above, the equations of motion for the coordinates $x^\mu = (t, r, \theta, \phi)$ read

$$\dot{r}^2 = V(r) = \frac{g(r)}{e^{2H(r)}}\left[\frac{E^2}{f(r)} - \frac{L^2}{r^2} - \delta_1\, e^{H(r)}\right]\,, \tag{8.36}$$

$$\dot{\varphi} = \frac{L}{r^2}e^{-H(r)}\,, \qquad \dot{t} = \frac{E}{f(r)}e^{-H(r)}\,, \tag{8.37}$$

where $\delta_1 = 0, 1$ for light-like and timelike geodesics respectively and the derivative is intended to respect with the proper time.

8.5.1.a Time-like geodesics

We set $\delta_1 = 1$ in equation (8.36). The requirement for a circular orbit at $r = r_t$ is $V(r_t) = V'(r_t) = 0$, thus

$$E^2 = e^{H_t}\frac{2f_t^2(1 + r_t H_t'/2)}{2f_t - r_t f_t'}\,, \quad L^2 = e^{H_t}\frac{r_t^3 f_t'(1 + H_t' f_t/f_t')}{2f_t - r_t f_t'}\,.$$

We choose the notation $f_t \equiv f(r_t)$, with the subscript t standing for timelike. Since the energy must be real we require

$$\frac{2 + r_t H_t'}{2f_t - r_t f_t'} > 0\,. \tag{8.38}$$

The condition for a stable circular orbit is

$$V_t'' = 2\frac{g_t}{f_t}e^{-H_t}\times\left(\frac{(2(f_t')^2 - f_t f_t'')(1+r_t H_t'/2) - 3f_t f_t'/r_t(1+H_t' f_t/f_t')}{2f_t - r_t f_t'} - \frac{f_t}{2}[H_t'' + (H_t')^2]\right) < 0\,. \tag{8.39}$$

From equations (8.37) we define the orbital angular velocity

$$\Omega_t = \frac{\dot{\varphi}}{\dot{t}} = \sqrt{\frac{f_t'}{2r_t}\left(\frac{1+H_t' f_t/f_t'}{1+r_t H_t'/2}\right)}\,. \tag{8.40}$$

Equations above reduce to the usual ones for $H(r) \equiv 0$.

For the well known Schwarzschild case we have $f(r) = g(r) = 1 - 2M/r$ and $H(r) = 0$. In this case the condition (8.38) reads $r_t > 3M$ and from condition (8.39) for stable orbits, we find $r_t > 6M$. For $3M < r_t < 6M$ only unstable orbits exist, hence the radius $r = r_{\rm ISCO} = 6M$ is known as "innermost-stable-circular-orbit" (ISCO). The orbital angular velocity at the ISCO is $M\Omega_{\rm ISCO} = 1/(6\sqrt{6})$.

To compute the above quantities in EDGB theory we set $f(r) = e^{\Gamma(r)}$, $g(r) = e^{-\Lambda(r)}$ and $H(r) = \phi(r)$, where $\Gamma(r)$, $\Lambda(r)$ and $\phi(r)$ represent the spherically symmetric BH solution found in Ref. [177]. We also specialize to the case $b = 1/2$. Numerical results for a EDGB non-rotating BH are shown in Table 8.1 and Fig. 8.7. The comparison with Schwarzschild BH (with the same mass) and inclusion of null geodesics is discussed in the section below. For completeness we show results both for $b = 1/2$ and $b = 0$. The effect of a non-vanishing coupling is leading and it makes the angular frequency for a DBH smaller than in the Schwarzschild case (conversely the ISCO is larger). We find that the difference between the orbital frequency in GR and in EDGB theory can be as large as $\sim 20\%$, depending on the coupling constant α'/M^2. In the $\alpha' \to 0$ limit Schwarzschild results are recovered. The largest deviations occur when relation (8.8) is saturated by choosing the appropriate ϕ_h. This corresponds to the maximum value $\alpha'/M^2 \sim 0.691$, or equivalently to $D/M \sim 0.572$. It is worth noticing that the same occurs for a Reissner-Nordström BH, for which we have a relation between the electrical charge and the mass, $Q/M < 1$. Qualitatively, taking in account the coupling b, in EDGB theory the ISCO is always larger than it is for a Schwarzschild BH and the orbital frequency for a timelike geodesic is always smaller. Results for null geodesics do not depend on the coupling b, as explained in the section below. In Table 8.1 we also show the quantity

$$\eta = \frac{E_\infty - E_{\rm ISCO}}{E_\infty}\,,$$

which is the binding energy per unit rest-mass at the ISCO. Because the accretion inside the ISCO is assumed to be in free-fall, this is equal to the integrated luminosity per unit rest-mass accreted, *i.e.* the radiative efficiency of accretion. This efficiency ranges from $\sim 5.7\%$ for a Schwarzschild black hole hole to $\sim 42\%$ for an extremal Kerr hole.

Finally, we searched for static equilibrium solutions (following Maki and Shiraishi [250]), *i.e.*, a point particle at rest at a distance say, $r = r_0$. For this, we set $L = 0$ in Eq. 8.36 and ask for $V(r_0) = V'(r_0) = 0$. We find no solution to these equations, meaning such a configuration does not seem to be possible for this theory.

8.5.1.b Null geodesics

We now consider null circular geodesics, labeled by a "c" subscript. It is easy to show that, setting $\delta_1 = 0$ in equation (8.36), the dilaton field, $H(r)$, gives no contribution. Requiring

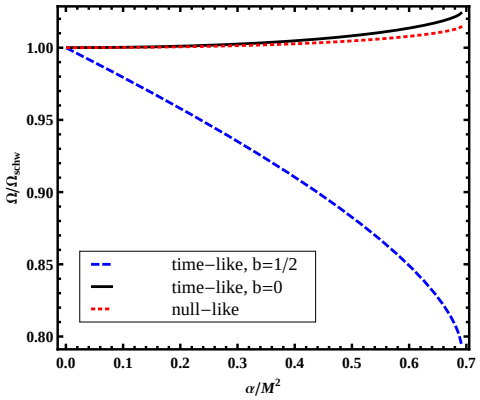

Figure 8.7: Angular frequency for circular timelike, $\Omega_{\rm ISCO}$, for $b = 0$ (solid line) and for $b = 1/2$ (dashed line) and for null-like, Ω_c (dotted line) geodesics, normalized to the Schwarzschild value.

Table 8.1: Some geodesics-related quantities for a spherically symmetric EDGB BH: orbital frequencies for timelike ($\Omega_{\rm ISCO}$), and null (Ω_c) circular orbits and the radiative efficiency, η. We compare to the Schwarzschild case, for different values of α'/M^2 covering whole spectrum $0 < \alpha'/M^2 \lesssim 0.691$. We also give the percentage (%) difference between EDGB and GR and we show results both for the coupling $b = 1/2$ and $b = 0$. Null-like geodesics do not depend on the coupling b.

α'/M^2	D/M	$M\Omega_{\rm ISCO}$ $(b=0)$ $(\pm\%)$	$M\Omega_{\rm ISCO}$ $(\pm\%)$	$M\Omega_c$ $(\pm\%)$	η $(b=0)$ $(\pm\%)$	η $(\pm\%)$
0	0	$0.0681 \sim \frac{1}{6\sqrt{6}}$	$0.0681 \sim \frac{1}{6\sqrt{6}}$	$0.1925 \sim \frac{1}{3\sqrt{3}}$	$0.0572 \sim \frac{3-2\sqrt{2}}{3}$	$0.0572 \sim \frac{3-2\sqrt{2}}{3}$
3×10^{-6}	10^{-6}	0.0681 ($\sim 0\%$)	0.0681 ($\sim 0\%$)	0.1925 ($\sim 0\%$)	0.0572 ($\sim 0\%$)	0.0572 ($\sim 0\%$)
3×10^{-3}	2×10^{-3}	0.0681 ($\sim 0\%$)	0.0680 (-0.1%)	0.1925 ($\sim 0\%$)	0.0572 ($\sim 0\%$)	0.0571 (-0.1%)
0.027	0.013	0.0681 ($\sim 0\%$)	0.0677 (-0.5%)	0.1925 ($\sim 0\%$)	0.0572 ($\sim 0\%$)	0.0567 (-0.9%)
0.238	0.129	0.0681 ($+0.2\%$)	0.0646 (-5.0%)	0.1926 ($+0.1\%$)	0.0572 ($+0.1\%$)	0.0525 (-8.3%)
0.417	0.246	0.0684 ($+0.5\%$)	0.0617 (-9.4%)	0.1930 ($+0.3\%$)	0.0574 ($+0.3\%$)	0.0484 (-15.4%)
0.545	0.350	0.0687 ($+1.0\%$)	0.0591 (-13.1%)	0.1936 ($+0.6\%$)	0.0575 ($+0.6\%$)	0.0449 (-21.6%)
0.630	0.441	0.0691 ($+1.6\%$)	0.0569 (-16.3%)	0.1942 ($+0.9\%$)	0.0577 ($+0.9\%$)	0.0419 (-26.7%)
0.677	0.516	0.0695 ($+2.1\%$)	0.0552 (-18.9%)	0.1948 ($+1.2\%$)	0.0579 ($+1.2\%$)	0.0396 (-30.8%)
0.691	0.572	0.0697 ($+2.5\%$)	0.0539 (-20.9%)	0.1953 ($+1.5\%$)	0.0580 ($+1.3\%$)	0.0378 (-33.9%)

$V_c = V_c' = 0$ we find

$$\frac{E}{L} = \pm\sqrt{\frac{f_c}{r_c^2}}\,, \quad 2f_c = r_c f_c'\,. \tag{8.41}$$

The condition for a circular orbit reads

$$V_c'' = 2\frac{L^2 g_c e^{-2H_c}}{r_c^4 f_c}\left(2f_c - r_c f_c''\right)\,, \tag{8.42}$$

whose sign does not depend on $H(r)$. The orbital angular velocity is

$$\Omega_c = \frac{1}{b_c} = \frac{\dot\varphi}{\dot t} = \frac{\sqrt{f_c}}{r_c}\,, \tag{8.43}$$

where $b_c = L/E$ is the impact parameter. In the Schwarzschild case the condition (8.41) restricts the null circular orbits to $r_c = 3M$. The orbital angular velocity is $M\Omega_c = 1/(3\sqrt{3})$.

Table 8.2: Real and imaginary part of the QNM frequencies defined by the formula $\omega_{QNM} = \Omega_c\, l - i\,(n+1/2)|\lambda|$ in the eikonal approximation [229]. Terms between parenthesis are the differences with respect to the Schwarzschild case, for which $M\Omega = M\lambda = 1/(3\sqrt{3})$.

α'/M^2	D/M	$M\Omega_c$ ($\pm\%$)	$M\lambda$ ($\pm\%$)
3×10^{-6}	10^{-6}	0.1925 ($\sim 0\%$)	0.1925 ($\sim 0\%$)
3×10^{-3}	2×10^{-3}	0.1925 ($\sim 0\%$)	0.1925 ($\sim 0\%$)
0.027	0.013	0.1925 ($\sim 0\%$)	0.1925 ($\sim 0\%$)
0.238	0.129	0.1926 ($+0.1\%$)	0.1924 (-0.1%)
0.417	0.246	0.1930 ($+0.3\%$)	0.1921 (-0.2%)
0.545	0.350	0.1936 ($+0.6\%$)	0.1916 (-0.4%)
0.630	0.441	0.1942 ($+0.9\%$)	0.1909 (-0.8%)
0.677	0.516	0.1948 ($+1.2\%$)	0.1901 (-1.3%)
0.691	0.572	0.1953 ($+1.5\%$)	0.1892 (-1.7%)

Results for a EDGB spherically symmetric BH are summarized in Table 8.1. In this case there is no effect from the coupling b and the difference between EDGB and GR theory is of the order 1%. From (8.42) we find that $V_c'' > 0$ and therefore only unstable null circular orbits exist. Hence also in EDGB case null geodesics are always unstable against small perturbations.

8.5.1.c QNMs in the large l limit for spherically symmetric EDGB BHs

Particularly promising for gravitational-wave detection are the characteristic vibration modes of black holes [14, 9]. These modes, called quasinormal modes (QNMs), are exponentially damped sinusoids and carry an imprint of the black hole, its features being independent on what exactly excited the modes. QNMs are excited to a large amplitude for instance in the inspiral and subsequent merger of black hole or neutron star binaries. In fact, the ringdown phase of supermassive black holes can have a larger signal-to-noise ratio than any other signal [251, 14, 9, 204], justifying dedicated searches for ringdown in current gravitational-wave detectors such as LIGO or TAMA [252, 253].

It was recently shown [229] that there is a simple relation between QNMs and circular null geodesics in general spacetimes in the eikonal, *i.e.* large-l limit,

$$\omega_{QNM} = \Omega_c\, l - i\,(n+1/2)|\lambda|\,, \tag{8.44}$$

where Ω_c is defined in Eq. (8.43) and

$$\lambda = \sqrt{\frac{g_c}{2r_c^2}\,(2f_c - r_c^2 f_c'')}\,, \tag{8.45}$$

is the Lyapunov exponent, describing the inverse of the instability timescale of the geodesic. For circular null geodesics the argument of the square root in Eq. (8.45) is always positive. QNMs are easily computed from the equation above and again the difference between the real and imaginary part of the QNM frequency for a DBH and for a Schwarzschild BH is order 1%, as shown in Table 8.2. We have not attempted to compute the least damped

QNMs for these black holes, but we will assume they behave in the same way as the coupling constant varies [9]. Discriminating such small percentage differences is *in principle* doable with the gravitational-wave detector LISA [14, 204], though it may be very challenging due to systematic errors [254, 255, 9, 14, 204]. As far as we know, the QNMs of DBHs have not been considered in the literature, even though their computation is extremely relevant. Nevertheless, the computation of QNMs of black holes in higher-dimensional Gauss-Bonnet theories without a dilaton, or purely dilatonic black holes has been done [256, 257, 258], we expect the four-dimensional case to proceed along similar lines.

8.5.2 Geodesics: rotating case

We will now consider geodesics in the the slowly rotating DBHs spacetime studied earlier in Section 8.4. For that, let's take the general four-dimensional static axisymmetric spacetime on the equatorial plane

$$ds^2 = f(r)dt^2 - \frac{1}{g(r)}dr^2 - h(r)d\varphi^2 + 2j(r)dtd\varphi\,, \tag{8.46}$$

where we specialize to $\theta = \pi/2$ and $d\theta = 0$. We also consider the dilaton field on the equatorial plane and set $H(r) = 2b\phi(r)$. Some interesting special cases of the metric above are listed in Table 8.3. Following Chandrasekhar [249] we consider planar orbits, for which the Lagrangian is

$$2\mathcal{L} = e^{H(r)}\left(f(r)\dot{t}^2 - \frac{1}{g(r)}\dot{r}^2 - h(r)\dot{\varphi}^2 + 2j(r)\dot{t}\dot{\varphi}\right)\,. \tag{8.47}$$

The generalized momenta are

$$\begin{aligned} p_t &= \text{const} = e^{H(r)}\left[f(r)\dot{t} + j(r)\dot{\varphi}\right] \equiv E\,,\\ -p_\varphi &= \text{const} = e^{H(r)}\left[-j(r)\dot{t} + h(r)\dot{\varphi}\right] \equiv L\,,\\ -p_r &= \frac{e^{H(r)}}{g(r)}\dot{r}\,, \end{aligned}$$

and the Hamiltonian is

$$2\mathcal{H} = 2(p_t\dot{t} + p_\varphi\dot{\varphi} + p_r\dot{r} - \mathcal{L}) = E\dot{t} - L\dot{\varphi} - \frac{e^{H(r)}}{g(r)}\dot{r}^2 = \delta_1\,, \tag{8.48}$$

where again $\delta_1 = 1,\ 0$ for time-like and null geodesics respectively. Using the integrals of motion E and L the equations of motion read

$$\begin{aligned} \dot{r}^2 &= V(r) = g(r)e^{-2H(r)} \times \left[\frac{h(r)\,E^2 - f(r)\,L^2 - 2j(r)\,E\,L}{j^2(r) + f(r)h(r)} - \delta_1 e^{H(r)}\right]\,, \qquad (8.49)\\ \dot{\varphi} &= \frac{j(r)\,E + f(r)\,L}{j^2(r) + f(r)h(r)}e^{-H(r)}\,,\\ \dot{t} &= \frac{h(r)\,E - j(r)\,L}{j^2(r) + f(r)h(r)}e^{-H(r)}\,. \end{aligned}$$

Table 8.3: Some particular cases of interest of the metric (8.46) along the equatorial plane: axially and spherically symmetric spacetimes. Then we specialize to the Kerr metric, and its slow rotation limit (Slow Kerr, SK) discussed in Appendix 8.8, and finally to the general slowly rotating metric described in Section 8.4 and then we compare this to the slowly rotating Kerr solution, discussed.

Axial Sym	Sph. Sym	Kerr	SK	Slow rot
$f(r)$	$f(r)$	$1-\frac{2M}{r}$	$1-\frac{2M}{r}$	$f(r)$
$g(r)$	$g(r)$	$1-\frac{2M}{r}+\frac{a^2}{r^2}$	$1-\frac{2M}{r}$	$g(r)$
$h(r)$	r^2	$r^2+a^2+\frac{2a^2M}{r}$	r^2	r^2
$j(r)$	0	$\frac{2aM}{r}$	$\frac{2J}{r}$	$r^2\Omega(r)$
$H(r)$	$H(r)$	0	0	$H(r)$

8.5.2.a Time-like geodesics

Setting $\delta_1 = 1$ in Eq. (8.49) and requiring $V = V' = 0$ at the radius $r = r_t$ we find a system of non-linear algebraic equations for E and L

$$\begin{aligned} 0 &= h_t\,E^2 - f_t\,L^2 - 2j_t\,E\,L - e^{H_t}(j_t^2 + f_t\,h_t)\,, \\ 0 &= h_t'\,E^2 - f_t'\,L^2 - 2j_t'\,E\,L - e^{H_t}[2\,j_t\,j_t' + f_t'\,h_t + f_t\,h_t' + H_t'(j_t^2 + f_t\,h_t)]\,. \end{aligned}$$

The system above can be solved analytically but the form of the solutions is not particularly useful. Solutions of the system above can be substituted in

$$\begin{aligned} V_t'' = \frac{g_t\,e^{-2\,H_t}}{j_t^2 + f_t\,h_t}\,\big[&h_t''\,E^2 - f_t''\,L^2 - 2\,j_t''\,E\,L - e^{H_t}\times \\ &\times\big([H_t'' + (H_t')^2](j_t^2 + f_t\,h_t) + 2\,H_t'(2\,j_t\,j_t' + f_t'\,h_t + f_t\,h_t') \\ &+2\,j_t'^2 + 2\,j_t\,j_t'' + f_t''\,h_t + 2\,f_t'\,h_t' + f_t\,h_t'')\big)\big] \end{aligned} \tag{8.50}$$

and in

$$\Omega_t = \frac{\dot\varphi}{\dot t} = \frac{j_t\,E/L + f_t}{h_t\,E/L - j_t}\,.$$

From Eq. (8.50) above we can find the ISCO for a generic rotating BH asking for $V_t'' \leq 0$. Setting $h(r) \equiv r^2$ and $j(r) \equiv 0$ equations above reduce to ones for a spherically symmetric spacetime. The requirement for the energy E to be real imposes a constraint $r_t > r_{\rm MIN}$. Results for circular time-like geodesics are shown in Table 8.4 for co-rotating orbits. For $r_{\rm MIN} < r_t < r_{\rm ISCO}$ only unstable circular orbits are permitted. For $r_t > r_{\rm ISCO}$ circular orbits are stable, while for $r_t < r_{\rm MIN}$ no circular orbits exist. Measurements of the ISCO can be used to evaluate the angular momentum of an astrophysical BH [225]. Figure 8.8 shows how the ISCO and the orbital frequency, Ω_t depend on J for slowly rotating BHs both in EDGB theory and in GR. Figure 8.8 can be used to evaluate the angular momentum once the ISCO has been measured (see Fig. 2 in Ref. [225] for details). Again the role of the coupling b is leading for timelike geodesics. As a qualitative result the orbital frequency is smaller for a slowly rotating EDGB BH than the one for a Kerr BH and the ISCO is larger. Differences range from 10% to $\sim 20\%$ depending on the angular momentum J/M^2 and on the dilatonic charge D/M. The

Table 8.4: Results for co-rotating time-like (at the ISCO) and null geodesics in slowly rotating EDGB BH spacetimes compared to the slowly rotating Kerr case.

α'/M^2	J/M^2	$M\Omega_{\rm ISCO}$ $(b=0)$ $(\pm\%)$	$M\Omega_{\rm ISCO}$ $(\pm\%)$	$M\Omega_c$ $(\pm\%)$
3×10^{-3}	0.3	0.0901 ($\sim 0\%$)	0.0900 (-0.1%)	0.2220 ($\sim 0\%$)
3×10^{-3}	0.2	0.0808 ($\sim 0\%$)	0.0807 (-0.1%)	0.2101 ($\sim 0\%$)
3×10^{-3}	0.1	0.0737 ($\sim 0\%$)	0.0736 (-0.1%)	0.2005 ($\sim 0\%$)
0.027	0.3	0.0901 ($\sim 0\%$)	0.0896 (-0.6%)	0.2220 ($\sim 0\%$)
0.238	0.3	0.0903 ($+0.3\%$)	0.0855 (-5.1%)	0.2224 ($+0.2\%$)
0.417	0.3	0.0910 ($+1.0\%$)	0.0818 (-9.2%)	0.2232 ($+0.5\%$)
0.417	0.1	0.0742 ($+0.6\%$)	0.0668 (-9.3%)	0.2012 ($+0.4\%$)
0.545	0.3	0.0919 ($+2.0\%$)	0.0787 (-12.6%)	0.2244 ($+1.1\%$)
0.545	0.1	0.0746 ($+1.2\%$)	0.0641 (-13.0%)	0.2019 ($+0.7\%$)
0.630	0.3	0.0929 ($+3.2\%$)	0.0763 (-15.3%)	0.2258 ($+1.7\%$)
0.630	0.2	0.0827 ($+2.4\%$)	0.0681 (-15.8%)	0.2129 ($+1.3\%$)
0.630	0.1	0.0751 ($+1.9\%$)	0.0619 (-16.1%)	0.2027 ($+1.1\%$)
0.677	0.3	0.0939 ($+4.3\%$)	0.0744 (-17.4%)	0.2272 ($+2.4\%$)
0.677	0.2	0.0834 ($+3.2\%$)	0.0661 (-18.1%)	0.2139 ($+1.8\%$)
0.677	0.1	0.0756 ($+2.5\%$)	0.0600 (-18.6%)	0.2035 ($+1.5\%$)
0.691	0.3	0.0947 ($+5.1\%$)	0.0729 (-19.0%)	0.2284 ($+2.9\%$)
0.691	0.2	0.0839 ($+3.8\%$)	0.0647 (-19.9%)	0.2148 ($+2.2\%$)
0.691	0.1	0.0759 ($+3.0\%$)	0.0586 (-20.4%)	0.2041 ($+1.8\%$)

difference is monotonically decreasing for larger rotations, it strongly depends on b but not on J. The effect of rotation seems to be subleading.

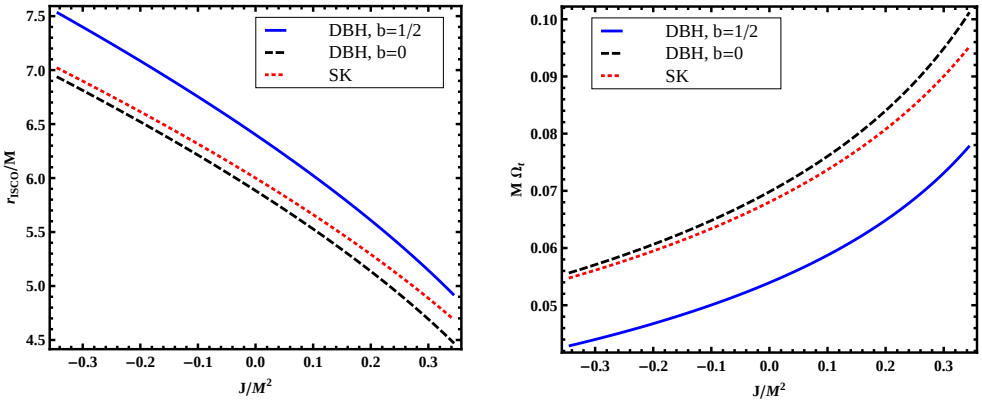

Figure 8.8: Left Panel: The innermost-stable-circular orbit radius, $r_{\rm ISCO}/M$ as a function of the angular momentum, J/M^2 for a slowly rotating DBH with $\alpha'/M^2 \sim 0.691$ for $b = 1/2$ (solid line), $b = 0$ (dashed line) and in the GR limit, $\alpha'/M^2 \sim 0$ (dotted line). From these plots and from the measurements of $r_{\rm ISCO}$ the value of the angular momentum J/M^2 can be evaluated (see Fig. 2 in Ref. [225]). Right Panel: the orbital frequency at the ISCO $\Omega_{\rm ISCO}$ as a function of the angular momentum, J/M^2 for a slowly rotating DBH with $\alpha'/M^2 \sim 0.691$ for $b = 1/2$ (solid line), $b = 0$ (dashed line) and in the GR limit, $\alpha'/M^2 \sim 0$ (dotted line). Negative values for J correspond to counter-rotating orbits.

8.5.2.b Null geodesics

Focusing on circular orbits ($\delta_1 = 0$), we require $V = V' = 0$ at the radius $r = r_c$. These two conditions read

$$\frac{E}{L} = \frac{j_c}{h_c} \pm \sqrt{\left(\frac{j_c}{h_c}\right)^2 + \frac{f_c}{h_c}}\,, \tag{8.51}$$

$$h_c' \left(\frac{E}{L}\right)^2 - f_c' + 2\, j_c' \frac{E}{L} = 0\,. \tag{8.52}$$

In this case

$$V_c'' = \frac{L^2 g_c e^{-2H_c}}{j_c^2 + f_c\, h_c} \left[h_c'' \left(\frac{E}{L}\right)^2 - f_c'' - 2\, j_c'' \frac{E}{L} \right]\,, \tag{8.53}$$

which is positive at $r = r_c$. As expected the positiveness of equation above does not depend on the dilaton $H(r)$. Therefore only unstable null circular orbits are allowed. The angular velocity is

$$\Omega_c = \frac{1}{b_c} = \frac{j_c}{h_c} \pm \frac{\sqrt{j_c^2 + f_c\, h_c}}{h_c}\,, \tag{8.54}$$

where $b_c = L/E$ is the impact parameter. The double sign in the above equation is related to orbits which are co-rotating and counter-rotating with the BH. Results for co-rotating null

orbits are shown in Table 8.4 and in Fig. 8.9. As we expect, results for $J/M^2 \to 0$ smoothly tend to the ones for the non-rotating case. Interestingly enough, percentual differences between GR results can be larger than order 5% for co-rotating orbits. The radius for circular null orbits is always smaller for a rotating EDGB BH than for a Kerr BH in GR.

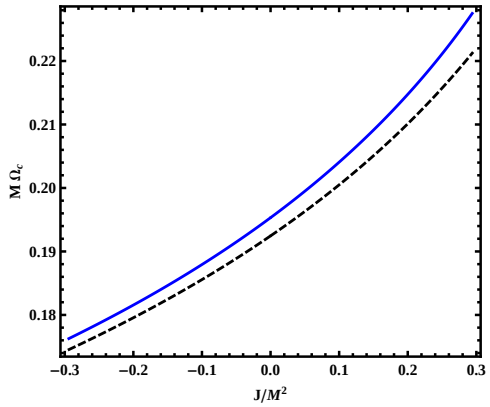

Figure 8.9: The orbital frequency, Ω_c, for circular null-like orbits as a function of the angular momentum, J/M^2 for a slowly rotating DBH with $\alpha'/M^2 \sim 0.691$ (solid line) and in the GR limit, $\alpha'/M^2 \sim 0.03$ (dashed line). Negative values for J correspond to counter-rotating orbits.

8.6 Discussion

Einstein-Dilatonic-Gauss-Bonnet theories are viable theories of gravity, which share many features in common with Einstein's gravity but have a better understood quantum limit. We have improved the linear stability analysis for static black holes in this theory. We found that they are stable and can *in principle* be used to discriminate between the two theories. For the slowly rotating black holes we studied here, the differences in measurable quantities amount to a few percent in the most favorable cases (large coupling constant). Given the current state-of-the-art, it does not seem possible to distinguish the correct theory of gravity from measurements of either the ISCO (from EM observation) or even of ringdown modes with future gravitational wave detectors.

There are at least two important extensions to be made, which could prove to be very relevant:

(i) Consider highly spinning black holes. One could attempt to extend the small rotation expansion to second order in Ω, but we found such procedure to be extremely complex, due to the symbolic manipulations required. If carried through, it would allow a computation of other multipole moments of the hole, which could potentially lead to important tests [14, 220]. Given that many of the astrophysical black hole candidate have a large spin, this could be a promising way of discriminating EDGB and Einstein's theory. To find a highly spinning DBH solution most likely requires a full numerical integration of the field equations (see for instance Ref. [259] for a concise overview of possible methods to handle this).

(ii) Waveforms of inspiralling particles. The calculation of waveforms is highly non-trivial:

it includes either a re-derivation of the PN expansion, or a full-blown numerical solution of the problem. The pay-off is huge: particles orbiting around black holes are able to probe the background geometry in its entirety [162]. The resulting gravitational-waveform *should* be sensitive enough to the field equations, specially at late stages in the inspiral, when the particle is about to merge. Indeed, the particle spends a large number of cycles near the ISCO, which could potentially increase by orders of magnitude the ability to probe the geometry better, if compared to ringdown.

Of course much more remains to be done. For instance, it would be desirable to have a quantitative analysis of the lowest lying ringdown modes. Most of all, it would be extremely important to understand how general theories of gravity affect the strong field regime, the ISCO location and frequency, etc. Perhaps then one might understand how to discriminate between the correct theory of gravity with future electromagnetic or gravitational-wave observations. We hope to tackle these issues in future works.

8.7 Appendix: Linear stability analysis: axial perturbations

In this appendix we derive the Schrödinger-like equation which represents a eigenvalue problem for the complex frequency ω. Detailed calculations can be found in the online MATHEMATICA notebooks which are available at `http://paolo.casadiale.com/EDGB_BHs.zip`.

The coefficients in eqns. (8.12)-(8.14) read

$$
\begin{aligned}
A_1(r) &= \frac{i\,e^{-\Lambda+\Gamma}\left(2e^{\Lambda}\left(\Lambda'-\Gamma'\right)-\alpha' e^{\phi_0}\left(\Gamma'\left(-\phi_0{}'\left(-3\Lambda'+2\phi_0{}'+\Gamma'\right)-2\phi_0{}''\right)-2\phi_0{}'\Gamma''\right)\right)}{2\omega\left(2e^{\Lambda}+\alpha' e^{\phi_0}\left(\Lambda'\phi_0{}'-2\left(\phi_0'^{\,2}+\phi_0{}''\right)\right)\right)}\,,\\
A_2(r) &= \frac{i\,e^{-\Lambda+\Gamma}\left(-2e^{\Lambda}+\alpha' e^{\phi_0}\phi_0{}'\Gamma'\right)}{\omega\left(2e^{\Lambda}+\alpha' e^{\phi_0}\left[\Lambda'\phi_0{}'-2\left(\phi_0{}'^{2}+\phi_0{}''\right)\right]\right)}\,,\\
B_{1,l}(r) &= -\frac{ie^{-\Lambda}}{2r\omega\left(e^{\Lambda}r-\alpha' e^{\phi_0}\phi_0{}'\right)}\Big\{\alpha' e^{\phi_0}\Big[-2e^{\Gamma}r\phi_0'^{\,2}\Gamma'-2e^{\Gamma}r\Gamma'\phi_0{}''+\\
&\quad+\phi_0{}'\left(2e^{\Lambda}r\omega^2-e^{\Gamma}\left(\left(e^{\Lambda}\left(l(l+1)-2\right)-3r\Lambda'\right)\Gamma'+r\Gamma'^{2}+2r\Gamma''\right)\right)\Big]+\\
&\quad+e^{\Lambda}\Big[-2e^{\Lambda}r^2\omega^2+e^{\Gamma}\left(2e^{\Lambda}\left(l(l+1)-2\right)+r\left(r\phi_0'^{\,2}+\left(2+r\Gamma'\right)\left(\Gamma'-\Lambda'\right)+2r\Gamma''\right)\right)\Big]\Big\}\,.
\end{aligned}
$$

The explicit for of the $C_{i,l}$ coefficients is not shown here. One can numerically prove that equation (8.14) is automatically satisfied as a consequence of the other two equations and of background solutions. So we are left with a system of two ODEs for the unknown functions $h_0(r)$ and $h_1(r)$. Eliminating h_0 from the first order equation (8.12) we obtain a second order differential equation for h_1,

$$
A(r)\,h_1''(r)+2B(r)\,h_1'(r)+C(r)\,h_1(r)=0\,, \tag{8.55}
$$

where $A(r)=A_2$, $B(r)=\frac{1}{2}(A_1+A_2'-\frac{2A_2}{r})$ and $C(r)=A_1'-\frac{2A_1}{r}-B_{1,l}$. The function $C(r)$ can be decomposed in $C(r)=Q(r)+\omega^2 E(r)$, where $Q(r)$ and $E(r)$ don't depend on ω. The functions A, B, E and Q depend on the radial background functions $\Gamma, \Gamma', \Gamma'', \Lambda, \Lambda', \phi_0, \phi_0', \phi_0''$ and on ϕ_0'''.

In order to eliminate the term proportional to h_1' we define

$$F = \exp\left(\int_{r_h}^{r} dr' \, \frac{B(r')}{A(r')}\right). \tag{8.56}$$

Setting $u = Fh_1$, equation (8.55) takes the Schrödinger-like form

$$u''(r) + \left[V(r) + \omega^2 K(r)\right] \, u(r) = 0\,, \tag{8.57}$$

which is Eq. (8.15) with

$$V(r) = \frac{Q}{A} - \left(\frac{B}{A}\right)^2 - \frac{d}{dr}\left(\frac{B}{A}\right)\,, \quad K(r) = \frac{E}{A}\,. \tag{8.58}$$

In the limit $r \to r_h$ the coefficients A, B, Q and E take the form

$$A = A_h + \mathcal{O}\left(r - r_h\right), \quad B = \frac{B_h}{(r - r_h)} + \mathcal{O}\left(1\right), \tag{8.59}$$

$$Q = \frac{Q_h}{(r - r_h)^2} + \mathcal{O}\left(\frac{1}{r - r_h}\right)\,, \tag{8.60}$$

$$E = \frac{E_h}{\gamma_1}\,\frac{1}{(r - r_h)^2} + \mathcal{O}\left(\frac{1}{r - r_h}\right)\,. \tag{8.61}$$

In equations above we have used the following asymptotic behavior near the event horizon

$$e^{-\Lambda(r)} = \lambda_1 (r - r_h) + ...\,, \tag{8.62}$$

$$e^{\Gamma(r)} = \gamma_1 (r - r_h) + ...\,, \tag{8.63}$$

$$\phi(r) = \phi_h + \phi_h' (r - r_h) + ... \tag{8.64}$$

where

$$\lambda_1 = \frac{2}{(\frac{\alpha'}{g^2} e^{\phi_h} \phi_h' + 2 r_h)}\,, \tag{8.65}$$

and γ_1 is an arbitrary finite *positive* integration constant, which cannot be fixed by the equations of motion, since the latter involve only $\Gamma'(r)$ and not $\Gamma(r)$. This constant is fixed by the asymptotic limit of the solutions at infinity. The asymptotic behavior near the event horizon for $V(r)$ and $K(r)$ is

$$V = \frac{V_h}{(r - r_h)^2}\,, \qquad K = \frac{K_h}{(r - r_h)^2}\,,$$

where $V_h \sim 1/4$ and $K_h \lesssim 4M^2$. The constants A_h, B_h, Q_h, E_h, V_h and K_h depend on r_h, ϕ_h and ϕ_h'. For a Schwarzschild BH, $V_h \equiv 1/4$ and $K_h \equiv 4M^2$. When $r \to \infty$, $V \to 0$ and $K \to 1$. The asymptotic behavior for equation (8.15) is described by Eqs. (8.16) and (8.17).

8.8 Appendix: Slowly rotating Kerr black holes in the Hartle approximation

A useful check on the method described in Section 8.4 is to consider classical GR, and repeat the calculation adding rotation to a Schwarzschild black hole. Perturbing the Schwarzschild metric and retaining only first order terms in Ω, equation (8.23) reduces to

$$\Omega_l''(r) + \frac{4}{r}\Omega_l' + \frac{2 - l(l+1)}{r(r-2M)}\Omega_l = 0\,, \tag{8.66}$$

which can be solved analytically in terms of special functions

$$\Omega_l(r) = C_1\ F(1-l, 2+l, 4; \frac{r}{2M}) + C_2\ G^{20}_{20}\left(\frac{r}{2M}\,\middle|\,\begin{matrix} -1-l, l \\ -3, 0 \end{matrix}\right) \tag{8.67}$$

where F is the hypergeometric function and G is the Meijer function. The asymptotic behavior of equation (8.66) is the same as Eq. (8.26). The asymptotic behavior (8.25) and the solution at infinity (8.27) imply that only the $l = 1$ mode is allowed. A list of the general solution of the equation above is:

$$\begin{aligned}
&\Omega_1(r) = C_1 + \frac{C_2}{r^3}\,, \quad l = 1\,,\\
&\Omega_2(r) = C_1\left(\frac{r}{M} - 2\right) + C_2\left[\frac{M^3}{r^3} + \frac{M^2}{r^2} + \frac{3M}{2r} - \frac{3}{2} + \frac{3}{4}\left(\frac{r}{M} - 2\right)\log\frac{r}{r-2M}\right], \quad l = 2\,,\\
&\Omega_3(r) = C_1\left(\frac{r}{M} - 2\right)\left(3\frac{r}{M} - 4\right) +\\
&+C_2\left[4\frac{M^3}{r^3} + 10\frac{M^2}{r^2} + 30\frac{M}{r} - 105 + 45\frac{r}{M} - \frac{45}{2}\left(\frac{r}{M} - \frac{4}{3}\right)\left(\frac{r}{M} - 2\right)\log\frac{r}{r-2M}\right], l = 3\,.
\end{aligned}$$

Demanding a correct asymptotic behavior at infinity, Eq. (8.25), we verify that $l = 1$ is the only mode able to satisfy regularity at the horizon (the result extends to $l > 3$ modes, though we do not show those here). We therefore get the exact result $\Omega = 2J/r^3$. This coincides with the expansion (first order in $a = J/M$) of a Kerr metric in Boyer-Lindquist coordinates,

$$ds^2 \;=\; \left(1 - \frac{2M}{r}\right)dt^2 - \left(1 - \frac{2M}{r}\right)^{-1}dr^2 - r^2\left[d\theta^2 + \sin^2\theta\,(d\varphi - \frac{2aM}{r^3}dt)^2\right], \tag{8.68}$$

which we have named Slow Kerr (SK) metric in this work.

Part III

Black hole mimickers

Chapter 9

Are really black holes out there?

Black holes (BHs), once considered as exotic mathematical solutions to Einstein's field equations, have now been widely accepted as astronomical objects [260, 225, 261, 9]. Stellar-mass BHs are believed to be the final stage of the evolution of sufficiently massive stars. Massive BHs seem to populate the center of many galaxies at low redshift, and must have played an important role in the Universe structure formation. Most evidence supporting the astrophysical reality of BHs comes from the weak-gravity region, *i.e.* from observations probing the spacetime several Schwarzschild radii away from the event horizon. Attempts to rule out possible alternatives to BHs usually rely on general relativity being the correct theory of gravity, and on constraints on the equation of state of matter at high densities. For massive BHs the most precise measurements so far come from observations of stellar proper motion at the center of our own galaxy, indicating the presence of a "dark object" of mass $M \simeq (4.1 \pm 0.6) \times 10^6 M_\odot$ [262]. Recent millimeter and infrared observations of Sagittarius A*, the compact source of radio, infrared and X-ray emission at the center of the Milky Way, infer an intrinsic diameter of 37^{+16}_{-10} microarcseconds, even *smaller* than the expected apparent size of the event horizon of the presumed BH [263].

Some of the exotic alternatives to BHs (such as "fermion balls") are incompatible with the observations [264] and any distribution of individual objects within such a small region (with the possible exception of dark matter particles or asteroids, which however should be ejected by three-body interactions with stars) would be gravitationally unstable [265, 266]. In a recent attempt to probe the event horizon, Broderick and Narayan have analyzed the observations of Ref. [263]. If the object at the center of our galaxy had a surface it would be hot enough to glow with a steady emission of infrared light, but no such glow has been detected [267]. This and similar arguments are inevitably dependent on the gas distribution and on details of the accretion process, and they really set lower limits on the gravitational redshift corresponding to the hypothetical surface replacing the event horizon (see *e.g.* [268] for a review). Indeed, some hold the view that an observational proof of the existence of event horizons based on electromagnetic observations is intrinsically impossible [269] (see however Ref. [137]).

In spite of circumstantial evidences, the astrophysical BH picture has become a paradigm [270, 271]. Scientific paradigms are potentially dangerous since it is easy to prove what we actually expect to find [272]. For these reasons, in the following chapters we shall adopt an open-minded approach and we shall discuss model-independent tests of the strong-field BH dynamics and gravitational radiation signatures of event horizons which are necessary to confirm or disprove the BH paradigm.

Gravitational wave detectors offer a new way of observing BHs, complementing the wealth of information from present electromagnetic observations [9]. As first proposed by Ryan [162, 174], an exquisite map of the external spacetime of BHs (outside the innermost stable orbit, if there is any) can be constructed by observing the gravitational waveform emitted when a small compact object spirals into the putative supermassive BH at the center of a galaxy with the Laser Interferometer Space Antenna (LISA). As an extension of Ryan's work, Li and Lovelace considered the small object's tidal coupling with the central object and showed that by studying details of radiation reaction, information about the spacetime region *within* the orbit can also be obtained [273]. Ryan's proposal to map spacetimes using inspiral waveforms is promising, but the data analysis task is affected by a "confusion problem": the possibility of misinterpreting truly non-Kerr waveforms by Kerr waveforms with different orbital parameters [274, 275]. This ambiguity was shown to be resolvable if the orbit is known to be circular [162] or if one only probes the mass, spin and quadrupole moment of the object using waveforms generated in the weak-gravity region [173]. A different approach to test the BH nature of ultra-compact objects is based on measuring several of their free oscillation frequencies ("ringdown waves") and comparing them with the quasinormal mode (QNM) spectrum of BHs [276]. These tests of the "no-hair theorem" require a signal-to-noise ratio which could be achieved by advanced Earth-based gravitational wave interferometers and they are one of the most promising science goals of LISA [14, 204, 277].

In this part of the thesis we explore how to test possible alternatives to the BH paradigm. We retain the "conservative" assumption that general relativity is the correct theory of gravity and we focus on possible tests of the existence (or absence) of an event horizon.

Theorists conceived several families of compact objects with no event horizons. For example, *boson stars* are horizonless compact objects based on plausible models of particle physics at high densities, and they are (still) compatible with astrophysical observations [278, 279]. Being indistinguishable from BHs in the Newtonian regime, boson stars are good "strawmen" for supermassive BHs. The spacetime of nonrotating spherical boson stars can approximate arbitrarily well a Schwarzschild geometry even close to the event horizon, and being very compact it is not easily distinguishable from a BH by electromagnetic observations [279, 280]. Building on Ryan's proposal, Kesden *et al.* showed that the inspiral of a small compact object into a nonrotating boson star will emit a rather different gravitational waveform at the end of the evolution, when the small object falls into the central potential well of the boson star instead of disappearing into the event horizon of a BH [281]. Several authors have computed the QNM spectrum of boson stars, showing that it is remarkably different from the QNM spectrum of BHs and lending support to the feasibility of no-hair tests using QNM measurements [282, 283, 272].

Another proposed alternative to massive BHs, which we shall focus on in Chapter 10, is the *gravastar* model by Mazur and Mottola [284]. The model assumes that the spacetime undergoes a quantum vacuum phase transition in the vicinity of the BH horizon and it effectively replaces the BH event horizon by a transition layer (or shell) and the BH interior by a segment of de Sitter space [285, 286]. In Chapter 10 we shall focus on a simplified version of this model: the so-called thin-shell gravastar model, where the transition layer reduces to an infinitesimally thin shell. We argue that this model effectively retains most of the essential features of the original model and it can be discussed as prototype of static horizonless objects and as a Schwarzschild BH mimicker.

In fact the infinitesimally thin shell can be located arbitrarily close to the would-be event

horizon, so a gravastar might seem indistinguishable from a BH when tests are only performed on its external metric. We shall study the complete set of gravitational perturbations of thin-shell gravastars (both polar and axial perturbations) and show that the QNM spectrum is completely different from that of a Schwarzschild BH, even in the limit when the surface redshift becomes infinite. This result confirms that the replacement of an event horizon by a transition layer, has dramatic consequences on the gravitational perturbation spectrum of a BH mimicker.

In Chapter 10, in order to treat polar perturbations of a nonrotating thin-shell gravastar, we set up a rather generic formalism combining standard perturbation theory with Israel's junction conditions [287]. The formalism can be applied to gravitational perturbations of any spherically symmetric spacetime characterized by regions with different cosmological constants separated by infinitely thin shells with finite surface energy and tension. As a consequence, the polar sector of QNMs depends on the equation of state of matter on the shell. Furthermore, as an application of this generic formalism, late in Chapter 10 we investigate the gravitational wave emission from the quasi-circular inspiral of compact objects of mass m_0 into massive thin-shell gravastars of mass $M \gg m_0$. The power radiated in gravitational waves during the inspiral shows distinctive peaks corresponding to the excitation of the polar oscillation modes of the gravastar and providing a very specific signature of the horizonless nature of the central object.

Chapter 11 is devoted to the stability analysis for *superspinars*, another proposed alternative to highly spinning, compact objects. Superspinars are vacuum solutions of the gravitational field equations whose mass M and angular momentum $J = aM$ violate the Kerr bound, *i.e.* $a > M$ (in geometrical units: $G = c = 1$). These geometries could result from high-energy corrections to Einstein's theory of gravity, such as those that would be present in string-inspired models [29]. Superspinars have been proposed as an alternative to BHs, and they are therefore imagined to have a compactness comparable to that of extremal rotating Kerr BHs and to exist in any mass range. Therefore, the observation of rapidly spinning ultracompact objects could potentially reveal or rule out the existence of these BH mimickers.

The first question about BH mimickers regards their viability. Of course, in order to be viable astrophysical candidates, these objects must pass the same stability test which ordinary BHs pass. In Chapter 10 we shall discuss the stability issue for *static* (*i.e.* nonrotating) thin-shell gravastars and prove they are stable in a broad region of their parameter space. However the situation drastically changes when rotation is considered. In fact rotating horizonless objects which possess an ergoregion, *i.e.* roughly speaking, a region outside the horizon where the metric element $g_{tt} < 0$, are plagued by the so-called "ergoregion instability" [288, 245]. This instability relies on the superradiant scattering of incident waves by the rotating object [289], which is the wave analog of the Penrose's process for particle [290]. The same instability also plagues rotating stars but it has been found to be negligible on the typical stellar evolution timescale [245]. However phenomenologically viable BH mimickers must be much more compact than ordinary stars and the ergoregion instability is much more effective. In fact the instability of rotating boson stars, gravastars, wormholes and other Kerr-like objects have been proved to be effective (*i.e.* to have a typical timescale comparable to or less than the evolution timescale of an astrophysical object) in a wide range of the parameter space [291, 292, 293, 294]. Since astrophysical objects are likely to be rotating (due to accretion processes), the instability against rotation poses a serious challenge on the existence of these objects in nature and may potentially rule them out as alternatives to BHs.

In Chapter 11 we shall throughly investigate the dynamical stability of superspinars to gravitational perturbations and prove that they can unlikely be viable astrophysical alternatives. We shall extend the results of Ref. [292] (which first found that superspinars with a perfectly reflecting surface are unstable due to the ergoregion instability) by considering either purely reflecting or perfectly absorbing boundary conditions at the "surface" of the superspinar. Independently of the boundary conditions, we find several and strong instabilities. This implies that superspinars are very unlikely astrophysical alternatives to BHs. The extension of the same study to other black hole mimickers and possible generalizations of the works done in Refs. [291, 292, 293, 294] are interesting developments that we leave for future works.

Chapter 10

Gravitational-wave signature of a thin-shell gravastar

We discuss how the emission of gravitational waves by ultra-compact objects can be qualitatively different depending on the presence or absence of an event horizon. Our case study are nonrotating thin-shell gravastars. The model has an infinitely thin shell with finite tension separating a de Sitter interior and a Schwarzschild exterior. The shell can be located arbitrarily close to the would-be event horizon, so a gravastar might seem indistinguishable from a black hole when tests are only performed on its external metric. We discuss gravitational perturbations of thin-shell gravastars and show that the spectrum of axial and polar quasinormal modes is completely different from that of a Schwarzschild black hole, even in the limit when the surface redshift becomes infinite. Furthermore, we study gravitational wave emission from the quasi-circular extreme mass ratio inspiral of compact objects of mass m_0 into massive thin-shell gravastars of mass $M \gg m_0$. The power radiated in gravitational waves during the inspiral shows distinctive peaks corresponding to the excitation of the polar oscillation modes of the gravastar. The frequency of these peaks usually depends on the equation of state, but for ultra-compact gravastars it typically lies within the optimal sensitivity bandwidth of LISA, providing a very specific signature of the horizonless nature of the central object.

Contents

10.1 Introduction

One of the most elusive properties characterizing the black hole (BH) solutions of general relativity is the presence of their event horizon. Traditional electromagnetic astronomy can at best yield lower limits on the gravitational redshift corresponding to hypothetical surfaces replacing the event horizon (see [225, 268, 271, 269] for different viewpoints on this delicate issue). However, present and planned gravitational-wave (GW) detectors offer new prospects for "directly" observing BHs and probing their structure [277].

From a gravitational point of view the structure of compact objects is encoded in their free oscillation spectrum, *i.e.* in their quasinormal modes (QNMs) [8, 9]. In an effort to point out the peculiar features of compact objects whose external metric is identical to the Schwarzschild metric, but which do not possess an event horizon, here we studied the free oscillations of one of the simplest ultra-compact horizonless objects: a nonrotating thin-shell gravastar.

The gravastar model assumes that the space-time undergoes a quantum vacuum phase transition in the vicinity of the BH horizon. The model effectively replaces the BH event horizon by a transition layer and the BH interior by a segment of de Sitter space [285, 286]. The thin-shell gravastar model is obtained in the limit where the layer thickness shrinks to zero. Our analysis completes previous investigations [295, 25] by considering the thin shell as a dynamical entity.

Mazur and Mottola argued for the thermodynamic stability of the model. A dynamical stability analysis by Visser and Wiltshire [28] confirmed that a simplified version of the gravastar model by Mazur and Mottola is also stable under radial perturbations for *some* physically reasonable equations of state for the transition layer. Chirenti and Rezzolla [25] first considered nonradial perturbations of gravastars, restricting attention to the relatively simple case of oscillations with axial parity. They computed the dominant axial oscillation modes and found no instabilities. In analogy with previous studies of the oscillation modes of boson stars [282, 283, 272], they confirmed that the axial QNM spectrum of gravastars can be used to discern a gravastar from a BH. In the thin-shell limit, the axial QNM frequencies of Ref. [25] and our own calculations recover Fiziev's calculation of the axial QNMs of ultracompact objects with a totally reflecting surface [295].

Here we throughly study nonradial perturbations of a simplified "thin-shell" gravastar, retaining most of the essential features of the original model. We consider both axial perturbations (reproducing and extending the results of Ref. [25]) and polar perturbations. In the polar case, the matching of interior and exterior perturbations at the gravastar shell requires a more careful analysis because (unlike the axial case) polar perturbations of spherical objects actually induce motions of matter, which in turn couples back to gravitational perturbations. For this reason, nonspherical polar perturbations provide a more stringent test on the gravastar's overall stability. Polar perturbations are also crucial in studying the dynamics of objects orbiting the hypothetical gravastar. In order to treat polar perturbations of a nonrotating thin-shell gravastar we set up a rather generic formalism combining standard perturbation theory (in the Regge-Wheeler gauge) with Israel's junction conditions [287]. The formalism can be applied to gravitational perturbations of any spherically symmetric space-time characterized by regions with different cosmological constants separated by infinitely thin shells with finite surface energy and tension. Because matter is concentrated on these shells, the junction conditions deduced here will be sufficient in describing the linear dynamics of matter. Quite predictably, these conditions depend on the equation of state of the shell. As an application

of the formalism we study the QNM spectrum of polar and axial perturbations of gravastars, exploring the nonradial stability of these objects. Polar QNMs (unlike axial QNMs) depend on the equation of state of matter on the shell: they can be used not only to distinguish a gravastar from a BH, but also to distinguish between different gravastar models. We also find that the imaginary part of some QNMs seems to have a zero crossing when the gravastar is not very compact and the speed of sound on the shell is superluminal, suggesting that some gravastar models may be unstable under nonradial perturbations.

The chapter is formally divided into two parts as follows. In the first part we review our static thin-shell gravastar model (Section 10.2) and we sketch the calculation of axial and polar gravitational perturbations and of the matching conditions at the gravastar shell (Section 10.3). Details of the matching procedure are provided in Appendix 10.8, and details of the QNM calculation are given in Appendix 10.9. Our numerical results for the polar and axial QNM spectra are presented in Section 10.4 and supported by analytical calculations in the high-compactness limit in Appendix 10.10. In the second part, starting from Section 10.5 we apply the formalism developed in the first part to study gravitational radiation from compact objects inspiraling into nonrotating gravastars. In Sec. 10.5.1 we summarize the perturbed Einstein equations in the Bardeen-Press-Teukolsky (BPT) formalism and we write down the source term appearing on the right-hand side of the BPT equation for orbiting pointlike particles of mass $m_0 \ll M$. Then we discuss how the perturbation functions outside the shell (as obtained by the matching conditions derived in the first part of the chapter) can be used to solve numerically the BPT equation with a source given by the orbiting particle and to compute the radiated power. In Sec. 10.6 we compare numerical calculations of the power radiated by BHs and different gravastar models and we stress potentially observable GW signatures of horizonless ultra-compact objects. We conclude by discussing possible extensions of our work.

We use geometrical units ($G = c = 1$). The Fourier transform of the perturbation variables is performed by assuming a time dependence of the form $e^{i\omega t}$. Greek indices ($\mu\,,\nu\,,\dots$) refer to the four-dimensional space-time metric. Latin indices ($i\,,j\,,\dots$) refer to the three-dimensional space-time metric on the shell. Latin indices at the beginning of the alphabet ($a\,,b\,,\dots$) refer to the spatial metric on a two-sphere.

10.2 Equilibrium model

The metric for a static thin-shell gravastar has the form [28, 25]

$$ds_0^2 = -f(r)dt^2 + \frac{1}{h(r)}dr^2 + r^2(d\theta^2 + \sin^2\theta d\varphi^2)\,. \tag{10.1}$$

Here

$$f(r) = \begin{cases} h(r) = 1 - \dfrac{2M}{r}\,, & r > a\,, \\ \\ \alpha\, h(r) = \alpha\left(1 - \dfrac{8\pi\rho}{3}r^2\right)\,, & r < a\,, \end{cases} \tag{10.2}$$

where M is the gravastar mass measured by an outside observer, and $\rho = 3M/(4\pi a^3)$ is the "energy density" of the interior region. The coordinate system (t, r, θ, φ) has been chosen in such a way that the thin shell occupies a coordinate sphere with $r = a$. The space-time

reduces to de Sitter for $r < a$, and to Schwarzschild for $r > a$. The junction conditions on the $r = a$ surface have already partially been chosen by requiring the *induced metric* to be continuous across the shell, which also dictates that $f(r)$ be continuous at $r = a$, or

$$1 - \frac{2M}{a} = \alpha \left(1 - \frac{8\pi\rho a^2}{3}\right) . \tag{10.3}$$

In this chapter we shall usually drop the dependence of $f(r)$ and $h(r)$ on r. From the jump in the radial derivatives of f we could easily obtain the two defining properties of this gravastar model: the surface energy density Σ and surface tension Θ. The junction conditions read [287]:

$$[[K_{ij}]] = 8\pi \left[\left[S_{ij} - \gamma_{ij}\frac{S}{2}\right]\right] , \tag{10.4}$$

where the symbol "[[...]]" gives the "jump" in a given quantity across the spherical shell (or $r = a$), *i.e*

$$[[A]] \equiv A(a_+) - A(a_-) . \tag{10.5}$$

The indices i and j correspond to coordinates t, θ, and φ which parameterize curves tangential to the spherical shell, $K_{ij} = -\nabla_i n_j$ is the extrinsic curvature, $n_\alpha = (0, 1, 0, 0)/\sqrt{g^{rr}}$ is the unit normal vector, and S_{ij} is the surface stress-energy tensor

$$S_{ij} = (\Sigma - \Theta)u_i u_j - \Theta\gamma_{ij} , \tag{10.6}$$

where $u^\alpha = \sqrt{-1/g_{tt}}(1, 0, 0, 0)$ (or $\vec{u} = \sqrt{-1/g_{tt}}\,\vec{\partial}_t$) is the four-velocity of mass elements on the shell and $\gamma_{\alpha\beta} = g_{\alpha\beta} - n_\alpha n_\beta$ is the induced 3-metric on the shell. We then have

$$S_{ij} - \gamma_{ij}\frac{S}{2} = (\Sigma - \Theta)u_i u_j + \frac{\Sigma}{2}\gamma_{ij} . \tag{10.7}$$

In the static, spherically symmetric case,

$$[[K_{ij}]] = \left[\frac{\sqrt{g^{rr}}}{2} g_{ij,r}\right] . \tag{10.8}$$

Discontinuities in the metric coefficients are then related to the surface energy and surface tension as [28]

$$[[\sqrt{h}]] = -4\pi a\Sigma , \quad \left[\left[\frac{f'\sqrt{h}}{f}\right]\right] = 8\pi(\Sigma - 2\Theta) . \tag{10.9}$$

In order to summarize the above relations and reveal the independent parameter space of a thin-shell gravastar we define

$$M_v \equiv \frac{4\pi\rho a^3}{3} , \quad M_s \equiv 4\pi a^2\Sigma , \tag{10.10}$$

which would be the volume- and surface-energy contents of the gravastar. In terms of M_v, M_s and a, we can obviously solve for ρ, Σ, and in addition we have

$$M = M_v + M_s\sqrt{1 - \frac{2M_v}{a}} + \frac{M_s^2}{2a} , \tag{10.11}$$

$$\alpha = \frac{1 - 2M/a}{1 - 2M_v/a} , \tag{10.12}$$

$$\Theta = \frac{1}{8\pi a}\left[\frac{1 - 4M_v/a}{\sqrt{1 - 2M_v/a}} - \frac{1 - M/a}{\sqrt{1 - 2M/a}}\right] . \tag{10.13}$$

As a consequence, gravastar types can be specified by the dimensionless parameters M_v/a and M_s/a. In this chapter we only consider a simplified version of the original Mazur-Mottola gravastar, which has vanishing surface energy ($\Sigma = 0$) and

$$M = M_v, \quad 8\pi a\Theta = -\frac{3M/a}{\sqrt{1-2M/a}}\,. \tag{10.14}$$

However it is convenient to keep our notation general enough, because nonradial oscillations of a gravastar will in general produce nonzero variations of the surface energy (*i.e*, $\delta\Sigma \neq 0$).

10.3 Gravitational perturbations

In both the interior (de Sitter) and exterior (Schwarzschild) background space-times we consider perturbations in the Regge-Wheeler gauge [4], writing

$$ds^2 \;=\; ds_0^2 + (\delta_{\rm RW} g_{\mu\nu}) dx^\mu dx^\nu \tag{10.15}$$

with

$$\|\delta_{\rm RW} g_{\mu\nu}\| = \begin{bmatrix} f(r)H_0(t,r)Y_{lm} & H_1(t,r)Y_{lm} & -h_0(t,r)\dfrac{1}{\sin\theta}\dfrac{\partial Y_{lm}}{\partial\varphi} & h_0(t,r)\sin\theta\dfrac{\partial Y_{lm}}{\partial\theta} \\ * & \dfrac{H_2(t,r)Y_{lm}}{h(r)} & -h_1(t,r)\dfrac{1}{\sin\theta}\dfrac{\partial Y_{lm}}{\partial\varphi} & h_1(t,r)\sin\theta\dfrac{\partial Y_{lm}}{\partial\theta} \\ * & * & r^2K(t,r)Y_{lm} & 0 \\ * & * & * & r^2\sin^2\theta K(t,r)Y_{lm} \end{bmatrix}, \tag{10.16}$$

where $Y_{lm}(\theta,\phi)$ denotes the ordinary spherical harmonics and "$*$" stands for terms obtainable by symmetry. In this gauge the perturbations split into two independent sets: the metric functions h_0 and h_1 are *axial* or *odd parity* perturbations, while $H_0\,, H_1\,, H_2\,, K$ are *polar* or *even parity* perturbations. The linearized Einstein equations automatically require $H_0 = H_2 \equiv H$.

In the rest of this section we work out perturbations of the gravastar space-time, including the dynamics of the shell itself, in three steps. In Sec. 10.3.1, we present the well-known solution of the perturbation equations in de Sitter space-time in terms of hypergeometric functions and choose the solution that is regular at the origin ($r = 0$). In Sec. 10.3.2 we review metric perturbations in the Schwarzschild exterior. Finally, in Sec. 10.3.3 we work out the junction conditions relating the interior and exterior Regge-Wheeler perturbations.

10.3.1 The de Sitter interior

The usual way to obtain the interior solution for perturbed stars is by direct integration of the system of ODEs [296, 297, 298]. Integrating a regular solution from the center would give boundary conditions at the stellar radius (or, in the case of a gravastar, at the location of the shell). For the de Sitter interior ($r < a$) no numerical integrations are required, because a regular solution of the perturbation equations can be obtained in terms of hypergeometric functions [299, 9]. To establish notation we review the basic equations below. Let us express

the metric in terms of a compactness parameter $C \equiv (2M/a)^3$, related to the parameter $\mu = M/a$ of Ref. [25] by $C = 8\mu^3$. Then we have (assuming $\Sigma = 0$)

$$f(r) = 1 - \frac{8\pi\rho}{3}r^2 = 1 - \frac{2M}{a^3}r^2 \equiv 1 - C(r/2M)^2\,. \tag{10.17}$$

In the de Sitter interior *both* axial and polar perturbations can be reduced to the study of the (frequency-domain) master equation

$$\frac{d^2\Psi^{\rm in}}{dr_*^2} + \left[\omega^2 - V_{\rm in}(r)\right]\Psi^{\rm in} = 0\,, \quad r < a\,, \tag{10.18}$$

where

$$V_{\rm in}(r) = \frac{l(l+1)}{r^2}\,f(r) \tag{10.19}$$

and we introduced the tortoise coordinate, defined as usual by the condition $dr/dr_* = f(r)$, which in this case yields

$$r_* = \sqrt{\frac{3}{8\pi\rho}}\text{arctanh}\left[\left(\frac{8\pi\rho r^2}{3}\right)^{1/2}\right]\,, \quad r < a\,. \tag{10.20}$$

In terms of r, the master equation reads

$$\frac{\partial^2\Psi^{\rm in}}{\partial r^2} + \frac{f'}{f}\frac{\partial\Psi^{\rm in}}{\partial r} + \frac{\omega^2 - V_{\rm in}(r)}{f^2}\Psi^{\rm in} = 0\,, \tag{10.21}$$

where a prime denotes a derivative with respect to r. Near the origin, solutions of Eq. (10.21) behave as $Ar^{l+1} + Br^{-l}$. By requiring regularity at the center ($r = 0$) we get, up to a multiplicative constant,

$$\Psi^{\rm in} = r^{l+1}(1 - C(r/2M)^2)^{-i\frac{M\omega}{\sqrt{C}}}F\left[\frac{l+2-i\frac{2M\omega}{\sqrt{C}}}{2}, \frac{1+l-i\frac{2M\omega}{\sqrt{C}}}{2}, l+\frac{3}{2}, \frac{Cr^2}{4M^2}\right], \tag{10.22}$$

where $F(a,b,c,z)$ is the hypergeometric function [300]. From $\Psi^{\rm in}$ and its derivative we can get the axial perturbation variables in the frequency domain [5]:

$$h_1 = \frac{r}{f}\Psi^{\rm in}\,, \qquad h_0 = -\frac{i}{\omega}\frac{d}{dr_*}\left(r\Psi^{\rm in}\right)\,. \tag{10.23}$$

The polar metric functions K and H_1 can be obtained immediately from:

$$K = \frac{l(l+1)}{2r}\Psi^{\rm in} + \frac{d\Psi^{\rm in}}{dr_*}\,, \tag{10.24}$$

$$H_1 = \frac{i\omega r}{f}\left(\frac{\Psi^{\rm in}}{r} + \frac{d\Psi^{\rm in}}{dr_*}\right)\,. \tag{10.25}$$

The quantity $H(= H_0 = H_2)$ and its derivatives can then be found from the algebraic relation

$$\left[\frac{l(l+1)}{2} - \frac{1}{f} - \frac{\omega^2 r^2}{f}\right]K + \left[-i\omega r - i\frac{l(l+1)Cr}{8M^2\omega}\right]H_1 - \frac{(l-1)(l+2)}{2}H = 0\,. \tag{10.26}$$

This procedure fixes all metric quantities and their derivatives in the interior. Here and henceforth in the chapter we drop the dependence of h_0, h_1, H, H_1 and K on ω and r.

10.3.2 The Schwarzschild exterior

In the Schwarzschild exterior, axial and polar perturbations obey different master equations [249]. The determination of the axial perturbation variables can still be reduced to the solution of the Regge-Wheeler equation [4], a Schrödinger-like ODE identical to Eq. (10.21):

$$\frac{\partial^2\Psi^{\rm out}}{\partial r^2}+\frac{f'}{f}\frac{\partial\Psi^{\rm out}}{\partial r}+\frac{\omega^2-V_{\rm out}(r)}{f^2}\Psi^{\rm out}=0\,, \tag{10.27}$$

where

$$V_{\rm out}=f\left(\frac{l(l+1)}{r^2}-\frac{6M}{r^3}\right). \tag{10.28}$$

The metric can then be obtained from Eqs. (10.23), with $f(r)$ given by Eq. (10.2).

The perturbed Einstein equations relate the polar variables (K, H, H_1) via three differential equations:

$$\frac{d}{dr}(fH_1)-i\omega(H+K) = 0\,, \tag{10.29}$$

$$-i\omega H_1+f(H'-K')+f'H = 0\,, \tag{10.30}$$

$$K'-\frac{H}{r}+\left[\frac{1}{r}-\frac{f'}{2f}\right]K+i\frac{l(l+1)}{2\omega r^2}H_1 = 0\,, \tag{10.31}$$

and an algebraic relation:

$$\left[\frac{l(l+1)}{2}-1+\frac{rf'}{2}\left(1-\frac{rf'}{2f}\right)-\frac{\omega^2r^2}{f}\right]K+\left[-i\omega r+i\frac{l(l+1)}{4\omega}f'\right]H_1-\left[\frac{l(l+1)}{2}-f+\frac{rf'}{2}\right]H=0. \tag{10.32}$$

Note that if we make the appropriate choice for $f(r)$, Eqs. (10.29)–(10.31) and the algebraic relation also apply to the interior de-Sitter spacetime [cf. Eq. (10.26)].

The Zerilli function $Z^{\rm out}(r)$ [5], which satisfies a wave equation, and its spatial derivative are also constructed from H_1 and K as

$$Z^{\rm out} = \frac{H_1^{\rm out}-A_3K^{\rm out}}{A_2-A_1A_3}\,, \tag{10.33}$$

$$\frac{dZ^{\rm out}}{dr_*} = \frac{A_2K^{\rm out}-A_1H_1^{\rm out}}{A_2-A_1A_3}\,, \tag{10.34}$$

where

$$A_1 = \frac{6M^2+\lambda/2\,(1+\lambda/2)\,r^2+3/2\lambda Mr}{r^2\,(3M+r\lambda/2)}\,, \tag{10.35}$$

$$A_2 = \frac{i\omega\left(-3M^2-3/2\lambda\,M\,r+r^2\lambda/2\right)}{r\,(3M+r\lambda/2)\,f}\,, \tag{10.36}$$

$$A_3 = i\omega\frac{r}{f} \tag{10.37}$$

and $\lambda=(l-1)(l+2)$. The metric perturbations can then be obtained by integrating the Zerilli equation outwards, starting from $r=a_+$. It is also useful to recall that (in the exterior) we can switch from the Zerilli function $Z^{\rm out}(r)$ (10.34) to the Regge-Wheeler function $\Psi^{\rm out}(r)$

by using a differential relation between polar and axial variables discussed in Chandrasekhar's book [249]:

$$\alpha_- \Psi^{\rm out} = \eta Z^{\rm out} - \frac{dZ^{\rm out}}{dr_*}\,, \qquad \frac{d\Psi^{\rm out}}{dr_*} = \alpha_+ Z^{\rm out} - \eta \Psi^{\rm out}\,,$$

where

$$\alpha_\pm = \frac{\lambda(\lambda+2)}{12M} \pm i\omega\,, \quad \eta = \frac{\lambda(\lambda+2)}{12M} + \frac{6Mf(r)}{r(\lambda\, r + 6M)}\,.$$

From $Z^{\rm out}$ and $dZ^{\rm out}/dr_*$ we can easily compute $\Psi^{\rm out}$ and $d\Psi^{\rm out}/dr_*$ outside the shell and use them as initial conditions to integrate the Regge-Wheeler equation outwards. Leins *et al.* [301] showed that this procedure is convenient to compute polar oscillation modes by the continued fraction method; more details on the QNM calculation are given in Appendix 10.9.

10.3.3 The matching conditions

In this section we discuss the most delicate part of the perturbation problem, namely the junction conditions for the Regge-Wheeler perturbation variables across the shell. Here we only outline our strategy and present the results; more details are given in Appendix 10.8. Technically, the application of Israel's junction conditions is easier if the shell's world tube happens to coincide with a fixed coordinate sphere at constant radius. However this is incompatible with choosing the Regge-Wheeler gauge in both the interior and the exterior, which is convenient to cast the perturbation equations into simple forms. In fact, such a choice of gauge does not leave any freedom. We must explicitly parametrize the 3-dimensional motion of each mass element on the shell and then perform the matching on a moving shell. In order to take advantage of both the simplicity of the field equations and the convenience of matching on a fixed coordinate sphere, we carry out the matching in the following way. We first construct a particular coordinate transformation (for both the exterior and interior space-times) such that in the new coordinate system, any mass on the shell remains static on the coordinate sphere with $r = a$. In this new coordinate system the metric perturbations will no longer be Regge-Wheeler, but will be augmented by quantities that carry information about how masses on the shell move in the Regge-Wheeler gauge. The stress-energy tensor of masses on the shell will correspondingly be modified. We then carry out the matching at $r = a$ and obtain junction conditions relating the interior and exterior metric perturbations, plus equations of motion for matter on the shell. As could be anticipated from the general features of oscillations of nonrotating stars, axial perturbations do not couple to matter motion and the axial junction conditions are very simple, basically imposing continuity of the master variable Ψ and of its first derivative. Polar perturbations, on the other hand, do couple to matter motion, so polar junction conditions do involve the shell dynamics, *i.e* its equation of state.

We parametrize the world line of matter elements on the shell in terms of the coordinates (t, r, θ, φ) as follows:

$$\begin{cases} t = \tau/\sqrt{f(a)} + \delta t(\tau, \theta_*, \varphi_*)\,, \\ r = a + \delta r(\tau, \theta_*, \varphi_*)\,, \\ \theta = \theta_* + \delta\theta(\tau, \theta_*, \varphi_*)\,, \\ \varphi = \varphi_* + \delta\varphi(\tau, \theta_*, \varphi_*)\,, \end{cases} \tag{10.38}$$

where θ_* and φ_* identify physical mass elements on the sphere, while τ parametrizes their proper time. Note that the Lagrangian equations of motion will *not* be the same for the

interior and exterior space-times. Therefore, points with the same $t\,,\theta$ and φ coordinates are not in general the same when viewed from the interior and from the exterior. As shown in Appendix 10.8, the four-velocity of the mass element (θ_*,φ_*) at the scaled proper time $\hat{t}\equiv\tau/\sqrt{f(a)}$ is, to leading order in the perturbation variables:

$$u^\alpha=[f(a)]^{-1/2}\,(1+\delta\dot{t},\delta\dot{r},\delta\dot{\theta},\delta\dot{\varphi})\,. \tag{10.39}$$

We now carry out a gauge transformation which maps the shell to a fixed location (note that two different gauge transformations are required for the exterior and for the interior). For any general gauge transformation $\bar{x}^{\bar{\alpha}}=x^\alpha-\xi^\alpha(x^\mu)$ we have, to first order in ξ^μ,

$$\delta g_{\alpha\beta}=\bar{g}_{\alpha\beta}(\bar{x}^\mu)-g_{\alpha\beta}(\bar{x}^\mu)=\xi_{\beta;\alpha}(\bar{x}^\mu)+\xi_{\alpha;\beta}(\bar{x}^\mu)\,, \tag{10.40}$$

where the semicolon represents a covariant derivative with respect to the four-metric and $\bar{g}_{\alpha\beta}(\bar{x}^\mu)$ is the metric tensor in the new coordinate system. We impose that, when evaluated at $(t,r,\theta,\varphi)=(\hat{t},a,\theta_*,\varphi_*)$, the vector ξ^α coincides with $(\delta t,\delta r,\delta\theta,\delta\varphi)$, so that in the new coordinate system we will have

$$\left\{\begin{array}{lcl}\bar{t}&=&\tau/\sqrt{f(a)}\,,\\ \bar{r}&=&a\,,\\ \bar{\theta}&=&\theta_*\,,\\ \bar{\varphi}&=&\varphi_*\,,\end{array}\right. \tag{10.41}$$

where we are ignoring second-order corrections. The full metric in the new coordinate system is

$$\bar{g}_{\alpha\beta}=g^{(0)}_{\alpha\beta}+\delta_{\rm RW}g_{\alpha\beta}+\delta g_{\alpha\beta}\,, \tag{10.42}$$

where $g^{(0)}_{\alpha\beta}$ is the static gravastar background metric, given by Eq. (10.1). The explicit form of ξ^μ and the corresponding changes in the metric components, Eq. (10.40), are given in Appendix 10.8, where the equations of motion, as well as the gauge transformation, are presented systematically in a multipole expansion. We then match components of $\bar{g}_{\alpha\beta}$ along the shell, which now simply sits at $(\hat{t},a,\theta_*,\varphi_*)$, and apply Israel's junction conditions to the extrinsic curvature given by $\bar{g}_{\alpha\beta}$. For axial perturbations these matching conditions read

$$[[h_0]]=0\,,\quad \left[\left[\sqrt{h}h_1\right]\right]=0\,. \tag{10.43}$$

For thin shell gravastars $h(r)$ is continuous across the shell, implying continuity of the Regge-Wheeler function Ψ and its derivative Ψ' across the shell [cf. Eq. (10.23)]. In more general cases where $h(r)$ may have a discontinuity across the shell the axial junction conditions (10.43) show that Ψ must also be discontinuous.

The treatment of polar perturbations is more involved and it yields the following relations, determining the "jump" of the polar metric functions at the shell:

$$[[K]]=0\,, \tag{10.44}$$

$$[[K']]=-8\pi\frac{\delta\Sigma}{\sqrt{f(a)}}\,, \tag{10.45}$$

$$\frac{2M}{a^2}\,[[H]]-[[H\,f']]-2f(a)[[H']]+4i\omega[[H_1]]=16\pi\sqrt{f(a)}(1+2v_s^2)\delta\Sigma\,. \tag{10.46}$$

Note that $f(r)$ is continuous across the shell [cf. Eq. (10.3)]. The parameter v_s in the equations above depends on the equation of state on the thin shell, $\Theta = \Theta(\Sigma)$:

$$v_s^2 \equiv -\left(\frac{\partial \Theta}{\partial \Sigma}\right)_{\Sigma=0} , \tag{10.47}$$

and it has the dimensions of a velocity. One might naively interpret v_s as the speed of sound on the thin shell and require $v_s \leq 1$, *i.e* that the speed of sound cannot exceed the speed of light. Furthermore, for a shell of ordinary, stable matter we would have $v_s^2 > 0$. The standard argument used to deduce that $v_s^2 > 0$ does not necessarily hold when one deals with exotic matter (as in the case of gravastars and wormholes), so the specification of upper and lower bounds on v_s may require a detailed microphysical model of the exotic matter itself [302, 303]. In our discussion of gravastar stability we will consider the whole range of v_s, but we will primarily focus on the range $0 \leq v_s^2 \leq 1$. The application of the polar junction conditions is more involved than the axial case due to their complexity, which arises from the fact that polar perturbations couple to oscillations of the shell.

Here we note that even though we have three quantities (K, H, H_1) that satisfy a coupled system of first-order ODEs in both the interior and exterior, in each region there is an algebraic relation relating the three quantities. For this reason we only need to impose two independent junction conditions, and Eqs. (10.44)–(10.46) provide exactly two independent relations among K, H and H_1 (after eliminating $\delta\Sigma$). Alternatively, the number of junction conditions can be obtained considering that all metric perturbations can be expressed in terms of $\Psi^{\rm in}$ and $\Psi^{\rm out}$, and that each of these master variables satisfies a second-order ODE. More specifically, we use Eqs. (10.44)–(10.46) to determine two relations among $(\Psi^{\rm in}, \partial_r \Psi^{\rm in})$ and $(\Psi^{\rm out}, \partial_r \Psi^{\rm out})$, plus the corresponding $\delta\Sigma$.

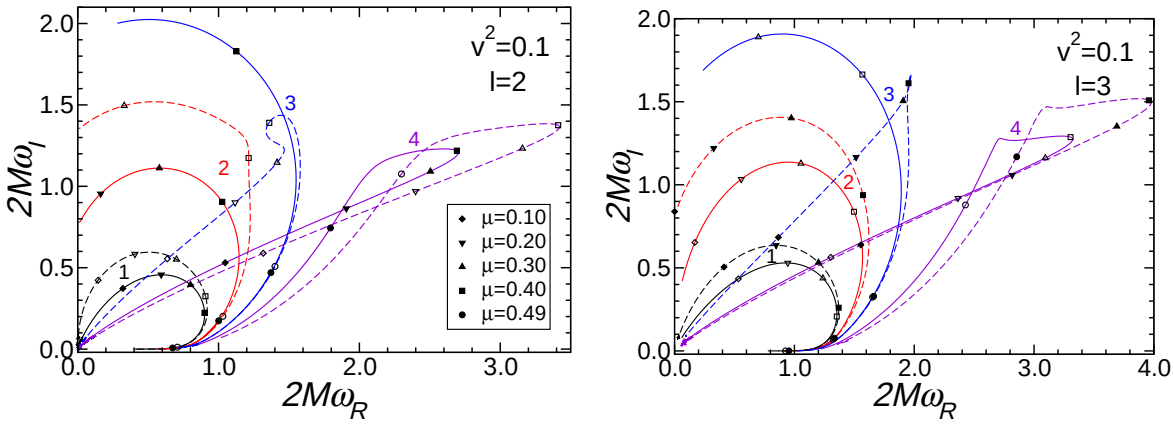

Figure 10.1: First few axial (continuous lines) and polar (dashed lines) QNMs of a thin-shell gravastar with $v_s^2 = 0.1$. In the left panel we follow modes with $l = 2$ as the compactness μ varies. In the right panel we do the same for modes with $l = 3$. Along each track we mark by different symbols (as indicated in the legend) the points where $\mu = 0.1\,, 0.2\,, 0.3\,, 0.4$ and 0.49. Our numerical method becomes less reliable when $2M\omega_I$ is large and when the modes approach the pure-imaginary axis. Numbers next to the polar and axial modes refer to the overtone index N ($N = 1$ being the fundamental mode).

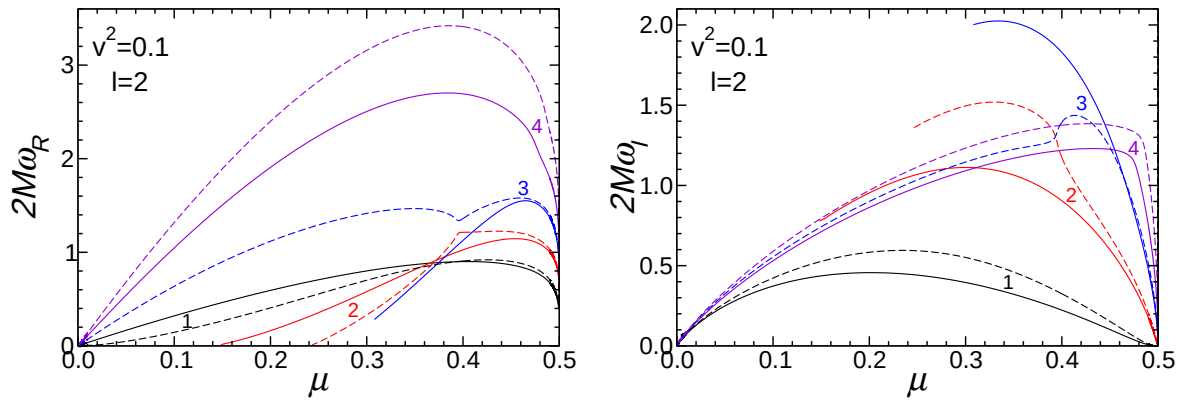

Figure 10.2: Real (left) and imaginary (right) part of polar and axial QNMs with $l = 2$ as functions of μ for $v_s^2 = 0.1$. Linestyles are the same as in Fig. 10.1. Numbers refer to the overtone index.

10.4 Numerical Results

Some axial and polar QNM frequencies for a static thin-shell gravastar, as computed by the continued fraction method, are plotted in Figs. 10.1 and 10.2. The C++ code used for the calculations is an update of the Fortran code used in Ref. [304] to verify and extend results on stellar oscillations by Kokkotas [305] and Leins, Nollert and Soffel [301]. For axial modes, our numerical results are in excellent agreement with the thin-shell limit of the QNM frequencies computed by Chirenti and Rezzolla [25] and with Fiziev's calculation of the axial QNMs of ultracompact objects with a totally reflecting surface (compare figures 3 and 4 of Ref. [295]).

To find the QNM frequencies we adopt the following numerical procedure. We usually fix $\mu = 0.4$ and (for polar perturbations) we choose a constant value of v_s. In the calculations leading to Figs. 10.1 and 10.2 we chose, somewhat arbitrarily, $v_s^2 = 0.1$. Later in this section we will discuss the dependence of polar modes on v_s.

As explained in Appendix 10.9, within the continued fraction method the complex QNM frequencies can be determined as the roots of any of the n equations $f_n(\omega) = 0$ [cf. Eq. (10.126)], where n is the "inversion index" of the continued fraction. To locate QNMs we first fix a value of μ (usually $\mu = 0.4$). We compute the real and imaginary parts of $f_n(\omega)$ for a given inversion index n on a suitably chosen grid of (ω_R, ω_I) values, and make contour plots of the curves along which the two functions are zero. The intersections of these curves are used as initial guesses for the quasinormal frequencies; more precise values are then obtained using Muller's method [306]. For fixed n (say, $n = 0$) this method singles out some spurious roots besides the physical QNM frequencies. The spurious roots can easily be ruled out, since they are not present for different values of n. Looking for roots with $n = 0$ is usually sufficient, but sometimes we get more stable numerical solutions for $n = 1$ and $n = 2$ when the QNMs have large imaginary part ($\omega_I \gtrsim 1.5$ or so).

The QNM spectrum with $\mu = 0.4$ corresponds to the empty (polar) and filled (axial) squares in the left panel of Fig. 10.1, respectively. Starting from $\mu = 0.4$, we follow each QNM as $\mu \to 0$ and as $\mu \to 1/2$ to produce the tracks displayed in the figure. For this value of v_s some of these tracks end at the origin in the limit $\mu \to 0$, while others hit the pure-imaginary

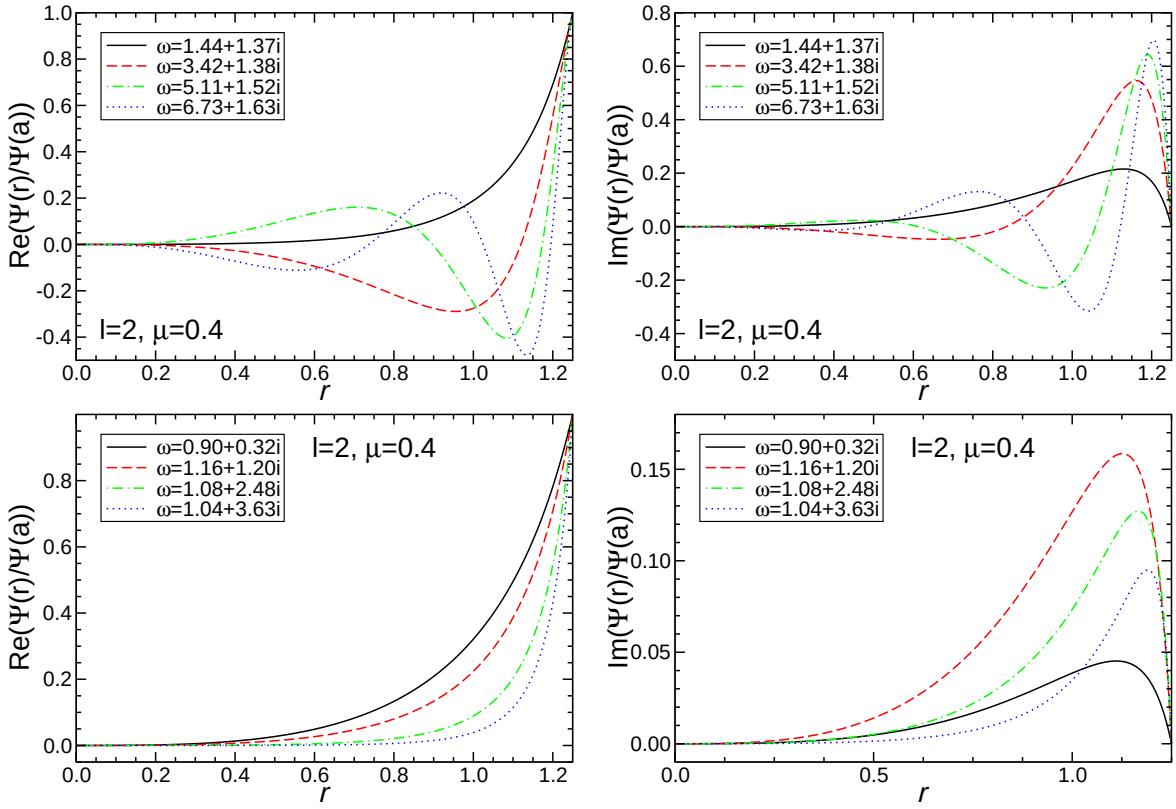

Figure 10.3: Top row: real and imaginary part of the wavefunction in the interior for the first four w-modes. Bottom row: real and imaginary part of the wavefunction in the interior for the first four $w_{\rm II}$-modes. In both cases we consider polar QNMs with $l = 2$ and $v_s^2 = 0.1$.

axis at some finite limiting compactness $\mu_{\rm imag}$ (*e.g.* $\mu_{\rm imag} \simeq 0.24$ for the first polar mode). The mode frequencies usually move clockwise in the complex plane (with the exception of QNMs displaying "loops") as μ is increased. The imaginary part of both axial modes (continuous lines) and polar modes (dashed lines) becomes very small as $\mu \to 1/2$, *i.e* when the gravastar most closely approximates a BH. The behavior is perhaps clearer from Fig. 10.2, where we separately show the real and imaginary parts as functions of μ.

For both axial and polar spectra the dependence of the mode frequencies on the gravastar compactness resembles that of "ordinary" ultracompact stars: see *e.g.* Fig. 3 of Ref. [307]. Intuitive models that capture most of the physics of this problem have been presented in Refs. [308, 309]. In their terminology, modes that emerge from the origin in Fig. 10.1 when $\mu \sim 0$ are w-modes or *curvature* modes, roughly corresponding to waves trapped inside the star. Modes emerging from the imaginary axis at some generally nonvanishing compactness are $w_{\rm II}$-modes [301] or *interface* modes, and they are similar in nature to acoustic waves scattered off a hard sphere [309, 310]. The only qualitative difference with Fig. 3 of Ref. [307] are the "loops" appearing for higher-order w-modes, for which we have no analytical understanding.

The fact that w-modes are effectively waves "trapped inside the star", while $w_{\rm II}$-modes are *interface* modes, similar to acoustic waves scattered off a hard sphere, is also clear from

the behavior of their wavefunctions in the stellar interior. The real and imaginary parts of the wavefunctions are shown in Fig. 10.3 (see Ref. [301] for comparison with the wavefunctions of ordinary stars). This figure shows eigenfunctions computed at the polar QNM frequencies for the first *four* w-modes and $w_{\rm II}$-modes with $l = 2$ and $v_s^2 = 0.1$. The plot shows that w-modes can be thought of as standing waves inside the gravastar, and that the overtone number corresponds to the number of nodes in the real and imaginary parts of the eigenfunction. The situation is different for $w_{\rm II}$-modes, where the wavefunction has a maximum close to the shell, as expected for interface modes.

One of our most important conclusions is that *neither axial nor polar modes of a gravastar reduce to the QNMs of a Schwarzschild BH when* $\mu \to 1/2$. In this limit, the real part of most modes is extremely small (much smaller than the Schwarzschild result, $2M\omega_R \simeq 0.74734$ for the fundamental mode with $l = 2$ [9]). Indeed, the QNM spectrum is drastically different from the QNM spectrum of a Schwarzschild BH: when $\mu \to 1/2$ the entire spectrum seems to collapse towards the origin. This is in sharp contrast with the Schwarzschild BH case and, as first noted in Ref. [25], it can be used to discern a very compact gravastar from a BH. In Appendix 10.10 we prove analytically that the QNM frequencies of a gravastar do not reduce to those of a Schwarzschild BH as $\mu \to 1/2$. The proof is based on the observation that the Zerilli wavefunction for polar modes is continuous in this limit.

It is clear from the figures that axial and polar modes do *not* have the same spectra for general values of μ. However, figures 10.1, 10.2 and 10.4 provide evidence that axial and polar QNMs do become isospectral when the gravastar compactness approaches that of a Schwarzschild BH ($\mu \to 0.5$). An analytic proof of isospectrality in the high-compactness limit is given in Appendix 10.10, where we show that in this limit both the Zerilli and Regge-Wheeler functions are continuous at the shell.

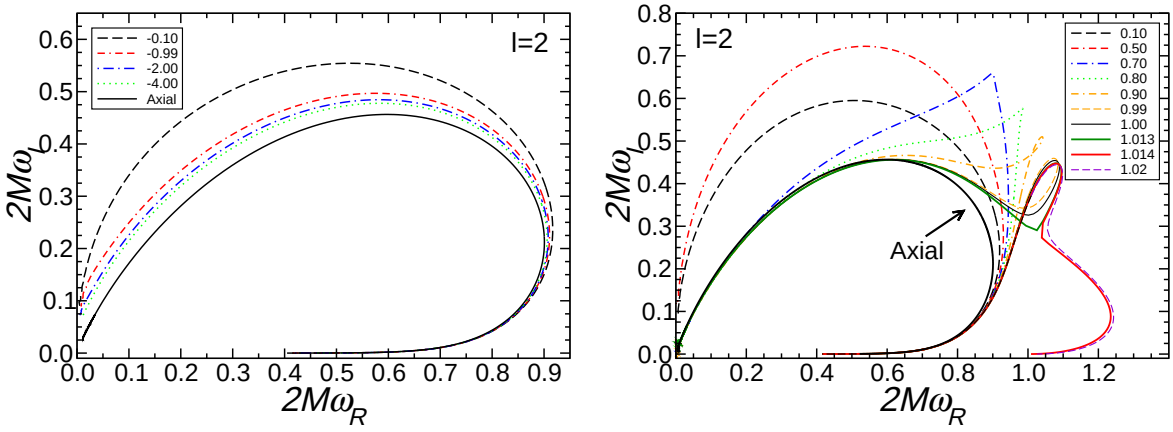

Figure 10.4: Tracks of the fundamental polar and axial w-modes for different values of the "sound speed" parameter v_s when $v_s^2 < 0$ (left) and when $v_s^2 > 0$ (right). Different linestyles correspond to different values of v_s^2, as indicated in the legend.

From the matching conditions (10.43), (10.44), (10.45) and (10.46) it is quite clear that polar QNMs (unlike axial QNMs) should depend on v_s, *i.e* [by Eq. (10.47)] on the equation of state on the shell. This is a new feature that does not arise in the case of axial perturbations [25]. The situation closely parallels the ordinary stellar perturbation problem [298, 93].

The role played by the equation of state in the dynamical stability of gravastars against *spherically symmetric* perturbations was discussed in Ref. [28]. Our calculations extend the considerations of that paper to nonradial oscillations.

The v_s-dependence of the modes is studied in Figs. 10.4, 10.5 and 10.6. In Fig. 10.4 we show the tracks described in the complex plane by the fundamental polar and axial w-mode as we vary the compactness parameter μ. The fundamental axial mode does not depend on the equation of state parameter, as expected, but the polar modes do change as a function of v_s. The standard argument used to deduce that the speed of sound $v_s^2 > 0$ does not necessarily hold when one deals with exotic matter (as in the case of gravastars and wormholes). Therefore, for completeness, in the left panel of Fig. 10.4 we compute polar QNMs when $v_s^2 < 0$. Different linestyles correspond to different values of v_s^2, as indicated in the legend. The solid black line reproduces the fundamental axial w-mode of Figs. 10.1 and 10.2. The dashed black line corresponds to the fundamental polar w-mode for a shell with low sound speed ($v_s^2 = 0.1$), corresponding to the fundamental polar w-mode of Figs. 10.1 and 10.2. The dash-dash-dotted (red), dash-dotted (blue) and dotted (green) lines represent a marginally subluminal, imaginary sound speed ($v_s^2 = -0.99$) and superluminal sound speeds ($v_s^2 = -2$ and $v_s^2 = -4$, respectively). Nothing particularly striking happens in this regime: QNM frequencies for polar and axial perturbations are different in all cases, but for large compactness the results become v_s-independent and modes of different parity become approximately isospectral, in agreement with the analytical results of Appendix 10.10. Furthermore, as $|v_s| \to \infty$ the polar modes seem to approach the axial mode. We can perhaps understand this behavior if we think that the shell is effectively becoming so stiff that matter decouples from the space-time dynamics, and only the "space-time" character of the oscillations survives.

The situation is more interesting in the case $v_s^2 > 0$, displayed in the right panel of Fig. 10.4. At first (when $v_s^2 \leq 0.5$ or so) the modes show a behavior similar to that seen for $v_s^2 < 0$, albeit in the opposite direction (*i.e* the real and imaginary parts of the QNM frequencies *increase* rather than decreasing when $|v_s|$ increases). When $v_s^2 = 0.7$ a cusp develops, and as the speed of sound approaches the speed of light (for $v_s^2 \gtrsim 0.9$ in the figure) the modes "turn around" describing a loop in the complex plane. The area of this loop in the complex plane increases until the sound speed reaches a critical value $1.013 \leq v_{\rm crit}^2 \leq 1.014$ (corresponding to $v_{\rm crit} \simeq 1.007$). For $v_s > v_{\rm crit}$ the QNM behavior changes quite drastically. The complex mode frequencies still approach the $\omega_I = 0$ axis clockwise as $\mu \to 0.5$. However, as μ decreases the modes approach the axis $\omega_I = 0$ very rapidly along tracks which are now tangent to the *lower* branch of the fundamental axial mode.

Even more interestingly, when $v_s^2 > 0$ there is also a *second* family of QNMs with very small imaginary part. A plot of the eigenfunctions shows that these modes are similar in nature to the $w_{\rm II}$-modes. The trajectories described in the complex plane by some of these weakly damped QNMs are shown in the left panel of Fig. 10.5. For comparison, the right panel of Fig. 10.5 shows some of the "ordinary" modes. These ordinary modes are the same as in the right panel of Fig. 10.4, except that this time we use a logarithmic scale for the imaginary part. The second family of QNMs plotted in the left panel has very long damping, and in this sense it is similar to the s-modes of "ordinary" ultra-compact stars discussed by Chandrasekhar and Ferrari [93]. There is, however, an important difference: unlike the s-modes, which exist only when a star is extremely compact, the weakly damped modes of a thin-shell gravastar only exist for *small* compactness $\mu < \mu_{\rm crit}$.

In the left (right) panel of Fig. 10.6 we show the real (imaginary) parts of both families

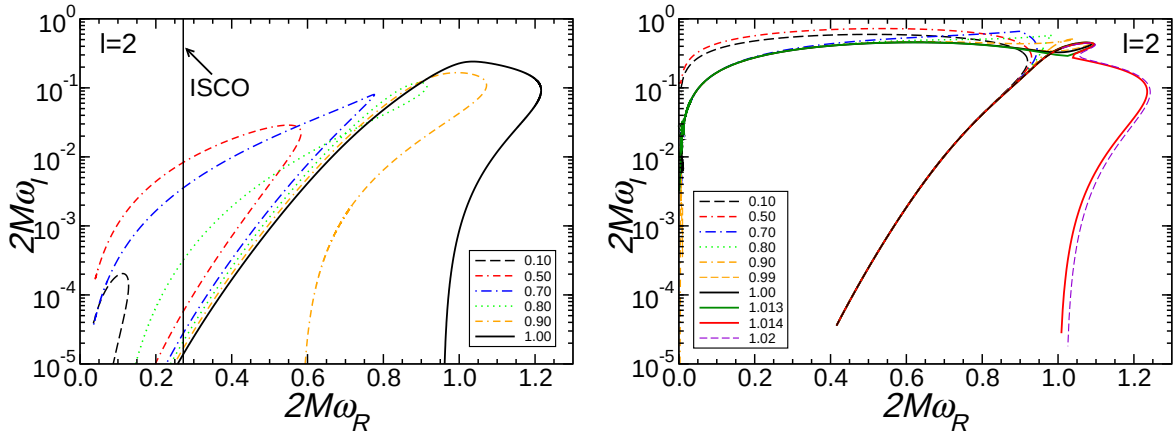

Figure 10.5: Left: spectrum of the weakly damped family of QNMs. The vertical line corresponds to twice the orbital frequency of a particle in circular orbit at the ISCO: as we will discuss below in this chapter, only QNMs to the left of the line can be excited by a compact object inspiralling into the gravastar along quasi-circular orbits. In the case $v_s = 0.8$ the mode "turns around" describing a loop in the complex plane. For $v_s \lesssim 0.8$ the modes move *clockwise* in the complex plane as μ increases. For $v_s \gtrsim 0.8$ they move *counterclockwise* and they cross the real axis at finite compactness. To facilitate comparison, in the right panel we show again the right panel of Fig. 10.4 using a logarithmic scale for the imaginary part.

of QNMs as functions of μ for selected values of v_s. Both the real and imaginary part of the weakly damped modes tend to zero at some finite, v_s-dependent compactness μ. The range where weakly damped modes exist increases with v_s^2. The fact that both the mode frequency and its damping tend to zero at the critical compactness $\mu_{\rm crit}$ suggests that the mode somehow "disappears" there, rather than undergoing a nonradial instability, but this conjecture deserves a more careful analytical study. Plots similar to those shown in Fig. 10.6 show that the imaginary part of "ordinary" modes with $v_s^2 \gtrsim 0.84$ ($v_s \gtrsim 0.92$) rapidly approaches zero at some finite compactness μ while the real part of the modes stays finite. We are unable to track QNMs numerically when $2M\omega_I \lesssim 10^{-5}$ using the continued fraction method, and in any case we cannot really *prove* by numerical methods that $\omega_I \to 0$ at some finite compactness $\mu > 0$. When $v_s^2 = 1.0134$ the two family of modes approach each other along a cusp, but their frequencies and damping times never cross. The "ordinary" family of modes exists all the way up to $\mu = 0.5$ but it becomes unstable (in the sense that the imaginary part of the mode crosses the real axis with the real part remaining finite) at some finite, v_s-dependent value of the compactness μ.

Summarizing, our numerical results suggest that (1) weakly damped QNMs only exist when their compactness is smaller than some v_s-dependent critical threshold and (2) when $v_s > 0$ and $v_s^2 \gtrsim 0.84$, the imaginary part of a QNM crosses the real axis at another critical threshold whose value can be estimated by extrapolation. Nonrotating thin-shell gravastars should be *unstable* against nonradial perturbations when their compactness is smaller than this critical value.

The two thresholds are plotted in Fig. 10.7. Weakly damped QNMs with $l = 2$ exist only below the dashed line and, according to our extrapolation of numerical results, thin-shell

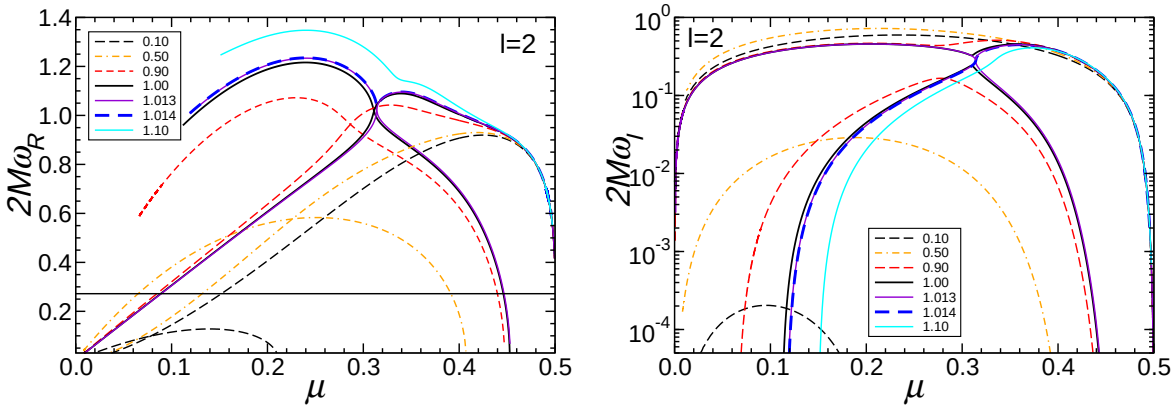

Figure 10.6: Real (left) and imaginary parts (right) of the fundamental polar w-mode for different values of the equation of state parameter v_s. Different linestyles correspond to different values of v_s^2, as indicated in the legend. The horizontal line in the left panel corresponds to twice the orbital frequency of a particle in circular orbit at the ISCO: only modes below the line can be excited during a quasicircular inspiral.

gravastars should be unstable to nonradial perturbations with $l = 2$ below the solid line (we verified that the instability condition for $l = 3$ is less stringent than for $l = 2$). The dashed line extends up to $v_s^2 < 1.0134$, where our numerical search for weakly damped QNMs becomes impractical (the modes trace smaller and smaller loops in the complex plane and they seem to disappear when the compactness is still smaller than $\mu = 0.5$).

To validate results from the continued fraction method we used an independent numerical approach: the resonance method [93, 94, 311], which is applicable to QNMs with $\omega_I \ll \omega_R$. The resonance method was first used by Chandrasekhar and Ferrari in their analysis of gravitational wave scattering by constant-density, ultra-compact stars [93, 94]. Chandrasekhar and Ferrari showed that the radial potential describing odd-parity perturbations of these stars displays a local minimum as well as a maximum when the stellar compactness $\mu \gtrsim 0.39$. If this minimum is sufficiently deep, quasi-stationary, "trapped" states can exist: gravitational waves can only leak out to infinity by "tunneling" through the potential barrier. The damping time of these modes is very long, so they were dubbed "slowly damped" modes (or s-modes) [93].

A straightforward analysis of Eq. (10.19) and an inspection of Fig. 10.8 show that the axial potential for a gravastar develops a minimum when $\mu \gtrsim 0.43$. The compactness of ordinary stars is limited by the Buchdal limit ($\mu < 4/9 \simeq 0.4444$), but since gravastars can be considerably more compact than this limit, s-modes can exist all the way down to the "Schwarzschild limit" ($\mu \to 0.5$). These modes can be computed via the continued fraction method, but since they are long-lived the resonance method, which is computationally very simple, provides very accurate estimates of their frequencies and damping times. We find that the resonance method and the continued fraction method are in very good agreement whenever the resonance method is applicable. In the limit $\mu \to 1/2$ we have $\mathrm{Im}(\omega) \ll \mathrm{Re}(\omega)$, and all QNM frequencies can be interpreted as "trapped" states.

The resonance method essentially confirms our continued fraction results for modes with $\omega_I \ll \omega_R$. In particular, it provides additional numerical evidence for the conjectured nonradial

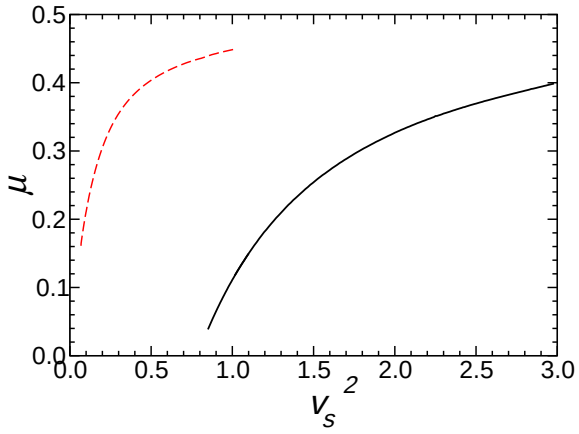

Figure 10.7: Significant thresholds in the $(\mu,\, v_s^2)$ plane. Thin-shell gravastars should be unstable with respect to nonradial perturbations below the solid line, corresponding to "ordinary" QNM frequencies whose imaginary part crosses the zero axis while their real part stays finite. The dashed line corresponds to the "vanishing point" of weakly damped QNM frequencies, *i.e* to the point where both their real and imaginary parts have a zero crossing. We could not find weakly damped modes in the region above the dashed line.

instability of thin-shell gravastars with low compactness. Despite the numerical evidence, an analytic confirmation of our estimates of the instability threshold would be highly desirable.

10.5 Gravitational perturbations by a point particle

As shown in the previous sections, the QNM spectrum of a thin-shell gravastar is complex and profoundly different from that of a BH, mainly because of the different boundary conditions at the surface replacing the event horizon.

Here we use the formalism developed in the first part of this chapter to show that any surface replacing the BH event horizon will produce a very specific signature in the gravitational signal emitted by the orbiting object because of the resonant scattering of gravitational radiation, which can be traced back to the different QNM spectrum of the two objects. In fact, here we show that the QNMs of ultra-compact thin-shell gravastars can be excited *during the inspiral*, whereas Schwarzschild QNMs can only be excited by particles plunging into the BH (see Refs. [312, 313, 314, 315] for a discussion of the analogous problem of particles orbiting neutron stars).

This idea is very similar in spirit to a previous study by Kesden and collaborators [281]. There are two main differences between our work and theirs. The first difference is that Kesden *et al.* considered boson stars rather than gravastars as BH strawmen, so no "hard surface" replaces the event horizon in their case. The second difference is that we compute the radiation in a consistent perturbative framework, instead of using "kludge" waveforms that become increasingly inaccurate in the relativistic regime. In this sense, we present the first "strong-field" calculation of the potential gravitational signatures of inspirals into horizonless objects.

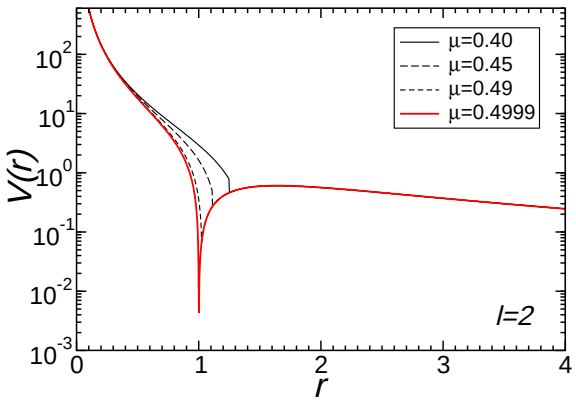

Figure 10.8: The potential governing axial and polar perturbations for different values of the gravastar compactness $\mu \equiv M/a$, where a is the location of the shell (see [93], showing a similar plot for axial perturbations of constant-density stars). The potential develops a minimum when $\mu \gtrsim 0.43$. Note that the polar and axial perturbations in the interior are both governed by the *same* potential, given in Eq. 10.19 below.

10.5.1 The source term and the BPT formalism

A detailed treatment of the perturbative approach used to compute the gravitational emission by a particle orbiting a polytropic neutron star can be found in Refs. [313, 314, 315, 310]. Here we review the original method with an emphasis on the modifications required to deal with thin-shell gravastars.

The radial part $\Psi_{lm}(\omega, r)$ of the perturbation of the Weyl scalar $\delta\Psi_4$ is defined as

$$\Psi_{lm}(\omega, r) = \frac{1}{2\pi} \int d\Omega \; dt \; {}_{-2}S^{*}_{lm}(\theta, \phi) \left[r^4 \; \delta\Psi_4(t, r, \theta, \phi) \right] e^{i\omega t} \,, \tag{10.48}$$

where ${}_{-2}S_{lm}(\theta, \phi)$ is a spin-weighted spherical harmonic of spin -2. The function (10.48) can be expressed in terms of the Zerilli and RW perturbation functions ($Z_l(\omega, r)$ and $Y_l(\omega, r)$, respectively) as follows:

$$\begin{aligned} \Psi_{lm}(\omega, r) &= \frac{r^3 \sqrt{n\,(n+1)}}{4\omega} \left[V^{\rm ax} Y_l + (W^{\rm ax} + 2i\omega)\, \Lambda_+ Y_l \right] \\ &- \frac{r^3 \sqrt{n\,(n+1)}}{4} \left[V^{\rm pol} Z_l + \left(W^{\rm pol} + 2i\omega \right) \Lambda_+ Z_l \right] \,, \end{aligned} \tag{10.49}$$

where $2n = (l-1)(l+2)$, $\Lambda_+ = d/dr_* + i\omega = r^{-2}\Delta d/dr + i\omega$ and

$$W^{\rm ax} = \frac{2}{r^2}(r - 3M) \,, \tag{10.50}$$

$$W^{\rm pol} = 2\frac{nr^2 - 3Mnr - 3M^2}{r^2(nr + 3M)} \,. \tag{10.51}$$

The functions $V^{\rm pol}$ and $V^{\rm ax}$ are the well-known Zerilli and RW potentials:

$$V^{\rm ax}(r) = f\left(\frac{l(l+1)}{r^2}-\frac{6M}{r^3}\right), \tag{10.52}$$

$$V^{\rm pol}(r) = \frac{2f}{r^3}\left(\frac{9M^3+3\lambda^2Mr^2+\lambda^2(1+\lambda)r^3+9M^2\lambda r}{(3M+\lambda r)^2}\right), \tag{10.53}$$

with $\lambda = l(l+1)/2-1$.

The radial part of $\delta\Psi_4$ outside the shell can be computed by solving the perturbation equations in the interior as previously discussed. In Refs. [313, 314, 315, 310] this has been done for polytropic neutron stars by numerically integrating the Tolman-Oppenheimer-Volkoff equation together with the relevant stellar perturbation equations. As previously discussed, for thin-shell gravastars the background spacetime and the perturbation functions in the interior are known analytically. Using the matching conditions derived in Appendix 10.8 we can determine the jump in the perturbation functions across the shell. Therefore we can easily construct the function $\delta\Psi_4(a_+)$ outside the shell. Through the Fourier and angular expansion of Eq. (10.48) we can now impose boundary conditions at a_+ for the integration of the inhomogeneous BPT equation [316, 317]:

$$\begin{aligned}\mathcal{L}_{BPT}\Psi_{lm}(\omega,r) &\equiv \left\{\Delta^2\frac{d}{dr}\left[\frac{1}{\Delta}\frac{d}{dr}\right]+\left[\frac{\left(r^4\omega^2+4i(r-M)r^2\omega\right)}{\Delta}-8i\omega r-2n\right]\right\}\Psi_{lm}(\omega,r) = \\ &= -T_{lm}(\omega,r),\end{aligned} \tag{10.54}$$

where $\Delta = r^2-2Mr$ and the source term $T_{lm}(\omega,r)$ describes the point mass m_0 moving on a given orbit around the gravastar. In Ref. [313] the solution of Eq. (10.54) is constructed in the general case of elliptic orbits. Eccentricity is expected to play an important role in extreme mass ratio inspirals [30, 318]. However, in the remainder of this chapter we focus on circular inspirals. This simplifies our study and it is sufficient to prove our main point: the gravitational radiation from extreme mass ratio inspirals around horizonless objects is drastically different from the BH case. We mention in passing that our numerical code is capable of handling eccentric orbits, and the extension of our study to eccentric inspirals could be an interesting topic for future research.

We further simplify the problem by using the so-called adiabatic approximation (*i.e* we assume that the radiation reaction timescale is much longer than the orbital timescale). Under this assumption the trajectory of the particle is described by the geodesic equations for a mass m_0 moving on a circular orbit of radius R_0:

$$\bar{\gamma}\equiv\frac{dt}{d\tau}=\frac{E}{1-\frac{2M}{R_0}}, \qquad \omega_{\rm K}\equiv\frac{d\varphi}{dt}=\frac{1}{\bar{\gamma}}\frac{d\varphi}{d\tau}, \tag{10.55}$$

where τ is the proper time, E is the energy per unit mass of the particle and $\omega_{\rm K}=\sqrt{M/R_0^3}$ denotes the Keplerian orbital frequency. The source term can be written as

$$T_{lm}(\omega,r)=\delta(\omega-m\omega_K)\Big[{}_0S^*_{lm}(\frac{\pi}{2},0)\,{}_0U_{lm}+{}_{-1}S^*_{lm}(\frac{\pi}{2},0)\,{}_{-1}U_{lm}+{}_{-2}S^*_{lm}(\frac{\pi}{2},0)\,{}_{-2}U_{lm}\Big], \tag{10.56}$$

where the functions ${}_sU_{lm}$ are explicitly given in Refs. [310, 314].

The solution of Eq. (10.54) satisfying the boundary conditions of pure outgoing radiation at radial infinity and matching continuously with the interior solution can be found by the Green's functions technique. The amplitude of the wave at radial infinity can be shown to be [313]

$$A_{lm}(\omega) = -\frac{1}{W_{lm}(\omega)} \int_R^\infty \frac{dr'}{\Delta^2}\, \Psi^1_{lm}(\omega, r')\, T_{lm}(\omega, r')\,, \tag{10.57}$$

where $W_{lm}(\omega)$ is the Wronskian of the two independent solutions of the homogeneous BPT equation

$$W_{lm}(\omega) = \frac{1}{\Delta}\left[\Psi^1_{lm}\partial_r\Psi^0_{lm} - \Psi^0_{lm}\partial_r\Psi^1_{lm}\right]\,. \tag{10.58}$$

The two solutions Ψ^0_{lm} and Ψ^1_{lm} satisfy different boundary conditions:

$$\begin{cases} \mathcal{L}_{BPT}\Psi^0_{lm}(\omega, r) = 0\,, \\ \Psi^0_{lm}(\omega, r\to\infty) = r^3 e^{i\omega r_*}\,, \end{cases} \qquad \begin{cases} \mathcal{L}_{BPT}\Psi^1_{lm}(\omega, r) = 0\,, \\ \Psi^1_{lm}(\omega, a) = \bar{\Psi}_{lm}(\omega, a)\,, \\ \partial_r\Psi^1_{lm}(\omega, a) = \partial_r\bar{\Psi}_{lm}(\omega, a)\,. \end{cases} \tag{10.59}$$

Here $\mathcal{L}_{BPT}$ is the differential operator on the left-hand side of the BPT equation (10.54) and $\bar{\Psi}_{lm}(\omega, a)$ is the radial perturbation of the Weyl scalar, constructed according to Eq. (10.49) in terms of the perturbed metric functions in the interior and evaluated at the (exterior) surface of the gravastar. The crucial point here is that the boundary conditions at the shell of a gravastar are drastically different from the ingoing-wave boundary conditions that must be imposed at the horizon of a black hole. As previously discussed, perturbations near the shell will in general contain a combination of ingoing and outgoing waves, even when the compactness of the gravastar approaches the Schwarzschild value ($\mu \to 1/2$).

The integral in Eq. (10.57) can be written in terms of Ψ^1_{lm} and its derivatives [314]. In Eq. (10.57) it is convenient to isolate the contribution of the Dirac δ function:

$$A_{lm}(\omega) = m_0 \hat{A}_{lm}(\omega)\delta(\omega - m\omega_K)\,. \tag{10.60}$$

Then the time-averaged energy-flux

$$\dot{E}^R \equiv \left\langle \frac{dE_{GW}}{dt} \right\rangle = \lim_{T\to\infty}\frac{E_{GW}}{T} = \lim_{T\to\infty}\frac{1}{T}\sum_{lm}\int d\omega \left(\frac{dE_{GW}}{d\omega}\right)_{lm} \tag{10.61}$$

can be written in terms of $\hat{A}_{lm}(\omega)$ as follows:

$$\dot{E}^R(m\omega_K) = \sum_{lm} \varphi m_0^2 4\pi (m\omega_K)^2\, |\hat{A}_{lm}(m\omega_K)|^2 \equiv \sum_{lm}\dot{E}^R_{lm}. \tag{10.62}$$

In order to evaluate Ψ^0_{lm} and Ψ^1_{lm}, we integrate the BPT equation by an adaptive Runge-Kutta method. Close to a resonance the solutions must be computed very accurately, since the Wronskian (10.58) is the difference between two terms that almost cancel each other. When required, the tolerance parameter in the adaptive integration routines is decreased to achieve convergence. Since the orbital frequency is related to the orbital velocity v and to the semilatus rectum (which for circular orbits is simply $p = R_0/M$) by the relations

$$v = (M\omega_K)^{1/3} = p^{-1/2}\,, \tag{10.63}$$

the energy flux $\dot{E}^R$ can also be considered as a function of v or p. In the following we shall normalize $\dot{E}^R$ to the Newtonian quadrupole energy flux

$$\dot{E}^N = \frac{32}{5}\frac{m_0^2}{M^2}v^{10}\,. \tag{10.64}$$

Then the energy flux emitted in gravitational waves normalized to the Newtonian quadrupole energy flux is given by

$$P(v) \equiv \frac{\dot{E}^R}{\dot{E}^N} = \sum_{lm}\frac{5}{128\pi}\varphi M^2(m\omega_K)^2 v^{10}|\hat{A}_{lm}(m\omega_K)|^2\,. \tag{10.65}$$

The normalized energy flux (10.65) can be computed up to $v \leq 1/\sqrt{6} \simeq 0.408$, which corresponds to the innermost stable circular orbit (ISCO) at $R_0 = 6M$. The post-Newtonian expansion of the energy flux $P(v)$ for particles in circular orbit around Schwarzschild BHs has been studied by several authors [319, 320, 321]. The instability of circular orbits with $R_0 < 6M$ sets an upper bound on the velocity of the point mass. If the radius of the gravastar is larger than the ISCO (this typically occurs for $\mu < 0.1666$) the upper limit in v will be smaller.

From the analytical form of the stress-energy tensor (10.56) it is easy to see that, for each assigned l, a mode of the star is excited when the orbital frequency satisfies the resonant condition

$$m\omega_{\rm K} = \omega_{\rm QNM}\,, \tag{10.66}$$

where $\omega_{\rm QNM}$ is the QNM frequency. Thus we expect sharp peaks to appear at the values of v corresponding to the excitation of the gravastar QNMs for different values of the angular momentum parameter l. This offers an intriguing signature of the absence of event horizons, since the emitted power for a Schwarzschild BH does not show any peak. In fact one can easily check that the frequency of the fundamental QNM of a Schwarzschild BH is *higher* than the critical value $m\omega_{\rm K}$ corresponding to a particle at the ISCO [310]. In other words, Schwarzschild QNMs can only be excited by particles plunging into the BH, while the QNMs of a gravastar can be excited *during the inspiral*. In the following Section we will compare the power emitted by a circular inspiral around a thin-shell gravastar to the power emitted by a circular inspiral around a Schwarzschild BH.

10.6 Gravitational flux from gravastars and black holes

Thin-shell gravastar models are specified by two parameters: the gravastar compactness $\mu = M/a$ and the sound speed parameter v_s that characterizes the EOS on the shell. Thin-shell gravastars are only one of the several possible models that can be explored (see *e.g.* [28, 25]) but we expect the qualitative results of our analysis to apply quite in general. The reason is that the main difference between gravastars and BHs comes from the different *boundary conditions* at the "surface" replacing the BH event horizon, rather than from the specific nature of this surface. Furthermore, as discussed below, peaks in the energy flux are more sensitive to the "global" properties of the gravastar (as determined by the compactness parameter μ) than to the microphysical model determining the matter distribution on the shell (which in our simplified case reduces to the specification of a value for v_s). Our numerical study covers the

whole range in compactness ($0 < \mu < 0.5$). We mainly focused on the most physical range of the EOS parameter ($0 < v_s^2 < 1$) but we also studied the superluminal case ($v_s^2 > 1$), and we even allowed for models with $v_s^2 < 0$ [303].

The gravitational emission of a Schwarzschild BH perturbed by a particle has been studied analytically and numerically in great detail for both circular and eccentric orbits [322, 323, 324, 319]. Our purpose here is to compare and contrast the energy flux from particles orbiting Schwarzschild BHs to the energy flux from particles orbiting thin-shell gravastars. For each value of the gravastar parameters (μ, v_s^2) we integrate the perturbations equations (as described in Section 10.5) for a point-like object of mass m_0 moving on a circular orbit of radius R_0 with orbital velocity v and we compute the energy flux (10.65). Our numerical work uses a modified version of the BPT code described in Ref. [314]. The results obtained by the BPT formalism were verified using an independent code that integrates the Zerilli and Regge-Wheeler equations. A slight variant of these codes was used to compute the flux from a particle orbiting Schwarzschild BHs. The results are consistent with Refs. [319, 323] within an accuracy of about one part in 10^6 (see Ref. [321] for more details).

From previous results (cf. Fig. 10.1), in the Schwarzschild limit $\mu \to 0.5$ the real part of the QNM frequency tends to zero and to a very good approximation it is independent of v_s. For example, for $\mu = 0.49999$ and $l = 2$ we varied v_s^2 in the range $[-2, 2]$ in steps of $\delta v_s = 0.1$ and we found that the real part of the modes is a constant within a part in 10^6 ($\omega_R = 0.235932$), while the imaginary part has tiny variations in the range between $\omega_I = 4.20 \times 10^{-7}$ and $\omega_I = 4.17 \times 10^{-7}$. In order for a QNM to be excited by particles in circular orbits, the QNM frequency must be small enough to allow for the resonant condition (10.66).

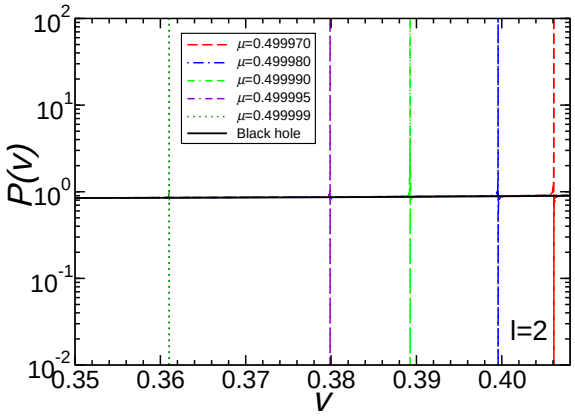

Figure 10.9: Dominant ($l = 2$) contribution to the energy flux for very high compactness and $v_s^2 = 0.1$ (but when $\mu \sim 0.5$ resonances are almost independent on v_s^2). From right to left the resonant peaks correspond to $\mu = 0.49997\,, 0.49998\,, 0.49999\,, 0.499995\,, 0.499999$, respectively.

Figure 10.9 shows the dominant ($l = 2$) contribution to the energy flux for gravastars with very high compactness. The frequencies of the lowest QNMs of a Schwarzschild BH are higher than those of an ultra-compact gravastar, and cannot be excited by particles in stable circular orbits. For this reason the power emitted by a BH (on the scale of this plot) is roughly constant. Resonance peaks do appear for gravastars, as expected, when $\omega_{\rm QNM} = 2\omega_{\rm K}$. Notice that these resonances are extremely narrow and they would get even narrower for $l > 2$. This is because

Table 10.1: Values of the compactness μ, angular momentum number l, QNM frequency, orbital velocity v and GW frequency $\nu_{\rm GW}$ of the circular orbits which would excite the fundamental QNM of the gravastar for the given multipole. The Keplerian frequency is given in mHz and rescaled to a gravastar mass $M_6 = 10^6 M_\odot$.

μ	l	$M\omega_{\rm QNM}$	v	$(M_6/M)\nu_{\rm GW}$ (mHz)
0.49997	2	0.1339	0.4061	4.328
	3	0.1508	0.3691	4.873
0.49998	2	0.1276	0.3996	4.123
	3	0.1429	0.3625	4.616
0.49999	2	0.1180	0.3893	3.812
	3	0.1310	0.3521	4.232
0.499995	2	0.1096	0.3799	3.543
0.499999	2	0.0941	0.3610	3.041

the imaginary part of the excited modes is extremely small ($2M\omega_I \sim 10^{-7}$, 10^{-10} for $l = 2$ and $l = 3$ respectively) in the high-compactness limit $\mu \to 0.5$, leading to a corresponding decrease in the quality factor of the oscillations. Whether these resonances are actually detectable is an interesting question for LISA data analysis. The answer depends on dissipative mechanisms (besides gravitational radiation damping) that could affect the timescale of the oscillations, especially in the non-linear regime: see *e.g.* [315, 325] for discussions of this problem in the context of neutron star binary detection by Earth-based GW interferometers.

Quite interestingly, the gravastars that "try harder" to look like a BH (in the sense that their shell is closer to the Schwarzschild event horizon) are also those that give away their identity at smaller angular velocities: the more compact the gravastar, the smaller the peak frequency in the energy flux. Table 10.1 lists the expected excited modes for different values of μ corresponding to ultra-compact gravastars.

One may worry that the resonance will eventually get out of the LISA band for gravastars having μ *extremely* close to the Schwarzschild value. The following naive argument suggests that this is not the case. The "thick shell gravastar" model by Mazur and Mottola predicts a microscopic but finite shell thickness $\ell \sim \sqrt{L_{\rm Pl} r_{\rm S}} \simeq 3 \times 10^{-14} (M/M_\odot)^{1/2}$ cm, where $L_{\rm Pl}$ is the Planck scale and $r_{\rm S}$ is the Schwarzschild radius, so that the energy density and pressure in the shell are far below Planckian and the geometry can still be described reliably by Einstein's equations [286]. Our simplified model does not allow for a finite thickness of the shell, and a microscopic model of finite shells is required for a careful analysis of this problem. However, for the sake of argument, let us consider $\epsilon = 1/2 - \mu \to 0$ as a "thickness parameter" describing how far the gravastar shell can be relative to the BH horizon. A power-law fit of the QNMs of a thin-shell gravastar in the limit $\epsilon \to 0$ yields $f_{\rm GW} \sim 3.828 \times (\epsilon \times 10^{-5})^{0.1073}$. The lower frequency sensitivity limit for LISA is dictated by acceleration noise. Assuming lower frequency cutoffs of $f_{\rm low} = 10^{-5}, 3 \times 10^{-5}, 10^{-4}$, we find that the peaks will sweep out of the LISA band when $\epsilon = 9.6 \times 10^{-48}, 2.7 \times 10^{-43}, 2.0 \times 10^{-38}$, respectively. This estimate of the "minimum measurable deviation from a BH" is admittedly very sensitive to the fitting function we use and it may change when one considers thick shell gravastars, but it suggests that LISA has the potential to reveal solid surfaces replacing horizons even when these solid

surfaces are very close to the location of the Schwarzschild horizon.

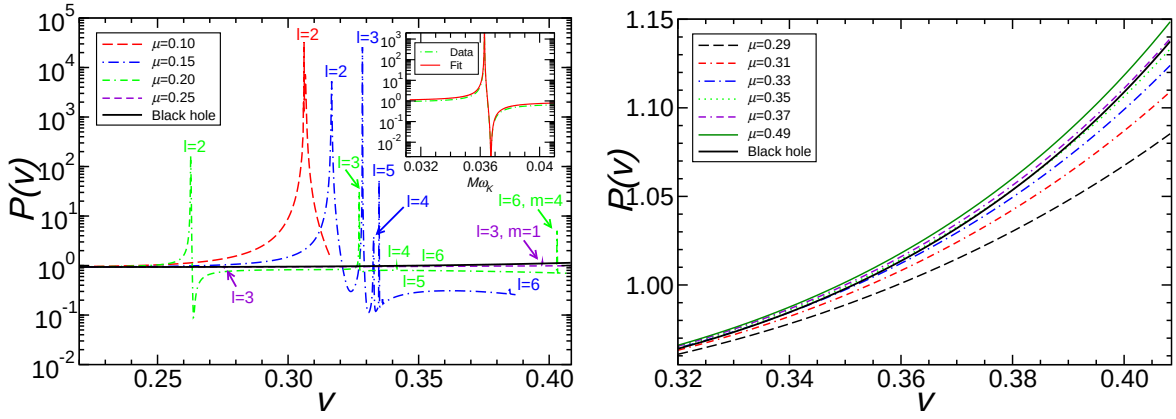

Figure 10.10: Left: The energy flux (summed up to $l = 6$) of GWs emitted by a small mass orbiting thin-shell gravastars with $v_s^2 = 0.1$ and different values of μ (plotted as a function of the particle orbital velocity v) is compared with the flux for a Schwarzschild BH. All peaks (with the exception of the last two peaks on the right) are due to the excitation of QNMs with $l = m$. Right: same for $v_s^2 = 0.1$ and selected values of $\mu \in [0.29, 0.49]$. No QNMs are excited in this range.

A relevant question is whether massive horizonless objects which are compact by the standard of (say) main sequence stars, but "only" as compact as neutron stars, can leave a signature on the gravitational signal emitted by small, inspiralling compact objects. In Fig. 10.10 we plot the normalized energy flux $P(v)$ as a function of the orbital velocity for gravastar models with $v_s^2 = 0.1$ and compactness in the range $0.1 \lesssim \mu \lesssim 0.49$, as well as for a Schwarzschild BH. The total flux was computed by adding all multipoles ($|m| \leq l$) and by truncating the multipolar expansion at $l = 6$. As discussed in Refs. [322, 313, 310, 321], a multipole of order l contributes to the total power as a correction of order p^{2-l}. Roughly speaking, a truncation at $l = 6$ produces a relative error (in the non-resonant regime) of order $p^{-5} = v^{10}$ (but see [321] for a more careful discussion of the convergence properties of the post-Newtonian series). When $\mu \gtrsim 0.166$ the ISCO is located outside the gravastar and we plot the energy flux up to the ISCO velocity $v_{\rm ISCO} \simeq 0.408$ (corresponding to $R_0 = 6M$). For less compact gravastars, plots of the energy flux are truncated at the velocity corresponding to the location of the shell.

The complex structure of the spectrum for values of μ smaller than about 0.2 is best understood by considering the real and imaginary parts of the weakly damped QNM frequencies of a gravastar (see Fig. 10.11). For clarity in Fig. 10.11 we only plot weakly damped QNMs, but our general arguments apply also to the second, "ordinary" family of QNMs. In particular, from Fig. 10.2 and Fig. 10.6 it should be clear that QNMs will be excited for low values of the compactness *and* when μ is very close to the BH value $\mu = 1/2$. Besides these "ultracompact" modes, only QNMs whose real part lies *below* the horizontal line in the left panel (corresponding to twice the ISCO orbital frequency for a particle in circular orbit) can be excited.

Fig. 10.11 clarifies that the range of μ over which QNMs can be excited depends on v_s.

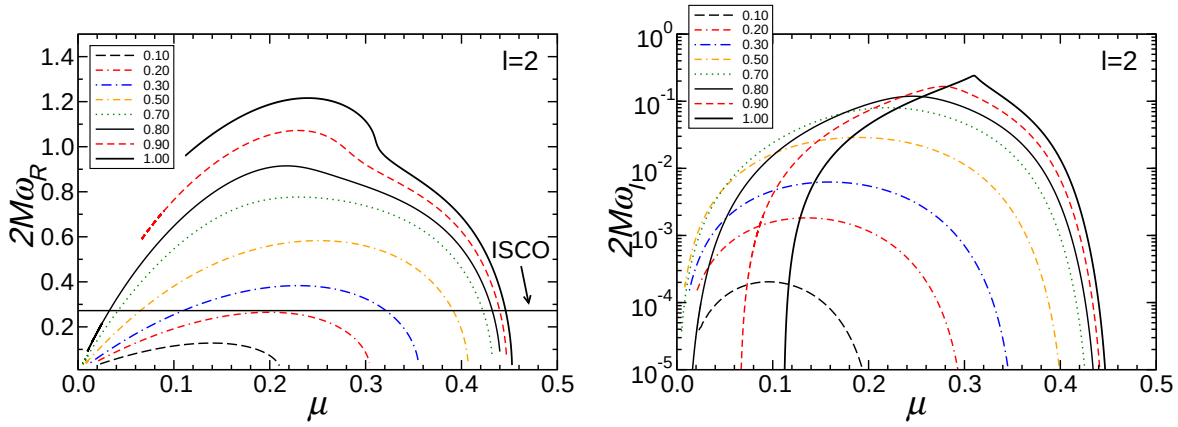

Figure 10.11: Real part (left) and imaginary part (right) of gravastar QNMs with $l = 2$ as a function of compactness for several fixed values of v_s^2 (as indicated in the legend). For clarity in illustrating the "selection rules" that determine QNM excitation during inspiral we only show the weakly damped part of the QNM spectrum (compare Fig. 10.2 and Fig. 10.6). For $v_s^2 > 0.8$ the real part of the frequency is plotted down to the critical minimum compactness at which the imaginary part crosses zero within our numerical accuracy. the horizontal line at $2M\omega_R \simeq 0.2722$ corresponds to twice the orbital frequency of a particle in circular orbit at the ISCO: only QNMs below this line can be excited during a quasi-circular inspiral.

For $v_s^2 = 0.1$ (the case considered to produce the energy fluxes of Fig. 10.10) QNM frequencies that can be excited by resonant inspirals only exist for $\mu \lesssim 0.21$ (left panel of Fig. 10.10) or for $\mu \gtrsim 0.49997$, *i.e* when the thin shell is extremely close to the location of the BH horizon (Fig. 10.9). The real part of the corresponding QNM frequency has a local maximum at $\mu \approx 0.15$. Correspondingly, the $l = 2$ QNM peak visible in the energy flux of Fig. 10.10 occurs later in the inspiral for the $\mu = 0.15$ model than it does for the $\mu = 0.10$ and $\mu = 0.20$ models.

In Fig. 10.10 the $l = 2$ and $l = 3$ peaks for $\mu = 0.20$ are well separated in frequency and an "antiresonance" is visible to the right of the $l = 2$ resonance. The nature of this antiresonance can be explained by a simple harmonic oscillator model [314]. In the inset of the left panel of Fig. 10.10 we plot *both* the resonance and antiresonance as functions of the Keplerian orbital frequency of the particle $M\omega_{\rm K}$ for $\mu = 0.2$ and $l = 2$ (dashed green line). A fit using the simple harmonic oscillator model of Ref. [314] (red line) reproduces the qualitative features of both resonance and antiresonance: in this specific case the fit gives $2M\omega_R \sim 0.07257$ and $2M\omega_I \sim 2\times10^{-6}$, while QNM calculations using the resonance method yield $2M\omega_R \sim 0.07257$ and $2M\omega_I \sim 4 \times 10^{-6}$.

Modes with $l > 2$ are typically harder to excite because of their higher frequencies and lower quality factors. However, because of the complex "selection rules" illustrated in Fig. 10.11 for $l = 2$, sometimes only resonances with $l > 2$ will be visible. When $v_s^2 = 0.1$ and $\mu > 0.21$ only modes with $l > 2$ can be excited, and only narrow $l = 3$ resonances can be seen in Fig. 10.10 when the compactness $\mu = 0.25$ (cf. Fig. 10.12).

When $l = 2$ the imaginary part of one QNM with $v_s^2 = 0.1$ crosses zero within our numerical accuracy at the "critical" compactness $\mu \simeq 0.21$, possibly signaling a (marginal) nonradial instability of the gravastar, and no QNMs can be excited for $0.21 \leq \mu \leq 0.49997$.

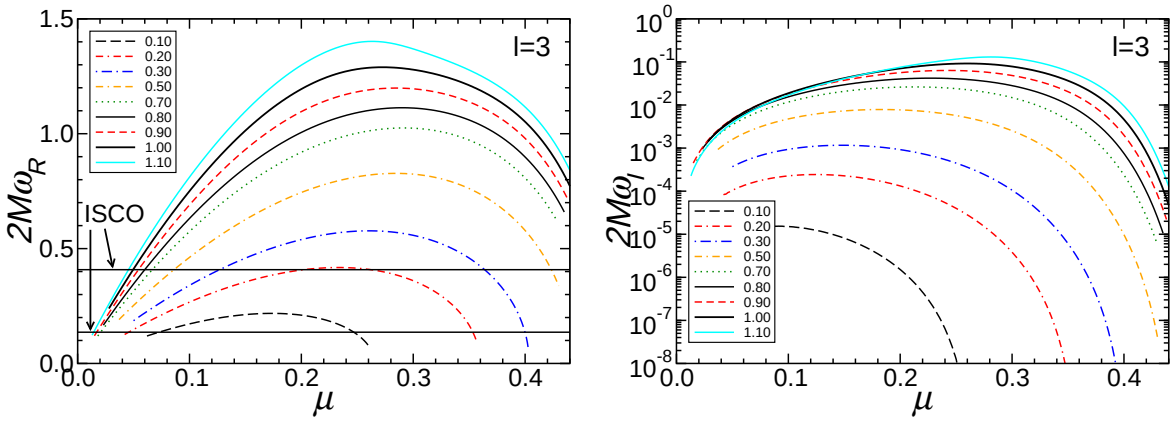

Figure 10.12: Real part (left) and imaginary part (right) of gravastar QNMs with $l = 3$ as a function of compactness for several fixed values of v_s^2 (as indicated in the legend). For clarity in illustrating the "selection rules" that determine QNM excitation during inspiral we only show the weakly damped part of the QNM spectrum. In the left panel, the horizontal lines at $2M\omega_R \simeq 0.1361$ ($2M\omega_R \simeq 0.4082$) correspond to the orbital frequency (or three times the orbital frequency) of a particle in circular orbit at the ISCO. Perturbations with $l = 3, m = 1$ can excite the QNMs below the first line, while perturbations with $l = m = 3$ can excite QNMs below the second line.

In this compactness range the energy flux emitted by either the gravastar or the BH is mostly due to the orbital motion and it only depends on the compactness of the central object. The right panel of Fig. 10.10 shows that the flux emitted by a gravastar approaches the BH flux "from below" as the compactness increases. For $\mu \simeq 0.35$ the gravastar flux is almost indistinguishable from the BH flux and for $\mu > 0.35$ a gravastar radiates slightly more than a BH. This is due to the fact that the emitted power "feels" the contribution of resonances, which in this case correspond to orbits smaller than the ISCO but do nevertheless contribute to increase the slope of the curve. A similar trend can be seen in neutron star calculations in regions of the parameter space where the contribution from resonances is negligible [314].

If gravastars or other horizonless objects have astrophysical reality, the presence or absence of resonant peaks in the GW flux can provide interesting information on the microscopic properties of the physical surface replacing the event horizon. Suppose for example that we can estimate the compactness of a massive object by independent means (*e.g.* by electromagnetic observations). Even within our simple thin-shell model, the range in frequency where resonances in the GW emission from EMRIs are allowed changes with v_s^2. For example, if $v_s^2 = 0.1$ resonances can exist when $\mu \lesssim 0.21$ or $\mu \sim 0.5$, but if $v_s^2 = 0.3$ they can exist when $\mu \lesssim 0.1$, $0.33 \lesssim \mu \lesssim 0.36$ and $\mu \sim 0.5$. Similar results also hold when $l = 3$, as shown in Fig. 10.12. For example, if $v_s^2 = 0.1$ resonances can exist when $\mu \lesssim 0.27$ or $\mu \sim 0.5$, but if $v_s^2 = 0.3$ they can exist when $\mu \lesssim 0.2$, $0.37 \lesssim \mu \lesssim 0.41$ and $\mu \sim 0.5$. So, in general, the range of μ where QNM frequencies can be excited by a circular inspiral depend on the value of l. In the Schwarzschild limit ($\mu \sim 0.5$) QNM frequencies are excited for any l, but higher–l modes have a tiny imaginary part ($2M\omega_I \sim 10^{-10}$ for $l = 3$) and they are more difficult to detect than the dominant ($l = 2$) modes.

If an EMRI is detected, the existence of these selection rules (in the form of compactness regions where resonances can or cannot exist) in principle allows for null tests of the existence of an event horizon for objects of the given compactness. Similar arguments can presumably be made for more complex (or contrived) gravastar models.

We can compare the gravitational energy flux shown in Fig. 10.10 with that emitted by neutron stars of comparable compactness (see for instance Fig. 1 in Ref. [314]). The energy flux for a thin-shell gravastar with $\mu = 0.1$ is shown in Fig. 10.10 by a red dashed line. From the peak position we find that the GW frequency for $l = 2$ is $\nu_{\rm GW} \sim 1.94$ kHz for $M = 0.945 M_\odot$. This is comparable with the value of a polytropic neutron star with the same mass and compactness, $\nu_{\rm GW} \sim 1.53$ kHz (cf. Model A in Ref. [314]). These frequencies depend on the equation of state on the shell of the gravastar and in neutron star interior, respectively. However their range is set by the total mass, so both frequencies lie within the optimal sensitivity bandwidth of LIGO. Therefore even gravastars which are as compact and massive as neutron stars can leave a potentially detectable imprint in the LIGO bandwidth.

10.7 Conclusions and outlook

In this chapter we have studied the nonradial perturbations of nonrotating, thin-shell gravastars. It should not be too hard to extend our formalism to the more complex case of five-layer gravastars of the type originally proposed by Mazur and Mottola (see [25] for a treatment of the axial case).

A presumably less trivial extension concerns rotating gravastars. Slowly rotating gravastars may be unstable against scalar perturbations because of an exponential growth of the perturbations due to superradiance, the so-called "ergoregion instability" [291, 294]. An extension of the present formalism can be used to study nonradial gravitational perturbations of slowly rotating gravastars and to discuss their ergoregion instability, which is believed to be stronger for gravitational perturbations [291]. For gravastars this instability is due to superradiant gravitational wave scattering in the ergoregion, so it is essentially the same as the "w-mode instability" discussed by Kokkotas *et al.* for ultracompact stars [326]. The main difference is that gravastars can be more compact than constant-density stars, so we may expect the instability to be stronger.

Finally, our formalism can be applied to explore nonradial gravitational perturbations of nonrotating wormholes, where the position of the throat plays a role similar to the thin shell of a gravastar. Such an analysis could confirm or disprove some conjectures on the similarity of the QNM spectra of wormholes and BHs [327].

Furthermore we have applied our formalism to shown that gravitational radiation from EMRIs can be used to tell the presence or absence of an event horizon in a compact, massive object. More specifically, we have shown that the resonant excitation of the oscillation modes of a gravastar in the LISA band is a potentially observable signature of the surface replacing the event horizon. For thin-shell gravastar models there is a range of compactness (*e.g.*, $\mu \lesssim 0.21$ and $\mu \gtrsim 0.49997$ for $v_s^2 = 0.1$) where this resonant scattering can occur.

More detailed data analysis studies (possibly including refined microphysical models of this "solid surface") are necessary to determine the detectability of resonant peaks, especially for ultra-compact gravastars.

10.8 Appendix: Perturbation equations and matching conditions

In this appendix we develop the formalism to study polar and axial nonradial (linear) oscillations of an object consisting of a thin spherical shell separating two spherically symmetric regions. Though we are mainly interested in thin-shell gravastars, we shall keep the discussion as general as possible. We focus on a background metric of the form (10.1), keeping $f(r)$ and $h(r)$ generic.

The Regge-Wheeler gauge is incompatible with the requirement that the shell's world tube sits at a fixed location. We deal with this issue in two steps: (i) we choose a coordinate system (system A) such that perturbations in both the interior and exterior are in the Regge-Wheeler gauge; (ii) we write down the equations of motion of mass elements on the shell in this coordinate system (separately for the interior and the exterior), and try to apply matching conditions on the boundary of this moving shell. We then transform to a new coordinate system (system B) in which the shell is fixed, simplifying the matching procedure. System B is an auxiliary tool for matching: when we consider perturbations of the gravastar induced (say) by orbiting particles we will mostly use system A, which is the usual Regge-Wheeler gauge.

Step (i) is a straightforward adaptation of formulas in Section 10.3. In the Regge-Wheeler gauge, polar perturbations are defined by three functions K, H and H_1 for the interior and exterior, respectively. These functions satisfy an algebraic relation and two coupled ODEs, which can be used to reduce the problem to a wave equation. This means that we only need two conditions relating these quantities from the two sides. Similarly, for axial perturbations we have h_0 and h_1, which satisfy a coupled wave equation, and again we need only two conditions connecting the interior and exterior.

Now we go directly to step (ii), and parametrize the shell position as in Eqs. (10.38). Let us define

$$\hat{t} \equiv \tau/\sqrt{f(a)}\,, \tag{10.67}$$

$$\dot{F} \equiv (\partial F/\partial\hat{t}) = \sqrt{f(a)}(\partial F/\partial\tau)\,. \tag{10.68}$$

Note that $\hat{t}$ is simply a re-scaling of proper time of the mass element, and that $f(a)$ is common to the interior and exterior, due to the requirement that the induced metric is continuous. In the absence of perturbations, $\hat{t}$ coincides with t. Henceforth, we will use $(\hat{t},\theta_*,\varphi_*)$, to parametrize the mass element. As a consequence, the four-velocity u^α of the mass element (θ_*,φ_*) would be as in Eq. (10.39). Imposing that $g_{\alpha\beta}u^\alpha u^\beta=-1$, we actually have to require that

$$\frac{(1+2\delta\dot{t})g_{tt}(\hat{t}+\delta t, a+\delta r, \theta_*+\delta\theta, \varphi_*+\delta\varphi)}{f(a)} = -1\,, \tag{10.69}$$

which, to leading order, is

$$f'(a)\delta r(\hat{t},\theta_*,\varphi_*) + 2f(a)\delta\dot{t}(\hat{t},\theta_*,\varphi_*) - \delta_{\rm RW}g_{tt}(\hat{t},\theta_*,\varphi_*) = 0\,. \tag{10.70}$$

Here $\delta_{\rm RW}g_{tt}$ is the tt-component of the metric perturbation in the Regge-Wheeler gauge.

We will now carry out a gauge transformation, both in the exterior and in the interior, which maps the shell to a fixed sphere. As explained in the main text, for any general gauge

transformation $\bar{x}^{\bar{\alpha}} = x^\alpha - \xi^\alpha(x^\mu)$ we have

$$g_{\alpha\beta}(x^\mu) = \bar{g}_{\mu\nu}(\bar{x}^\rho)\left(\frac{\partial \bar{x}^\mu}{\partial x^\alpha}\right)\left(\frac{\partial \bar{x}^\nu}{\partial x^\beta}\right) = \left[\bar{g}_{\alpha\beta} - \bar{g}_{\alpha\nu}\xi^\nu{}_{,\beta} - \bar{g}_{\mu\beta}\xi^\mu{}_{,\alpha}\right]_{\bar{x}^\rho}, \tag{10.71}$$

where we have ignored terms of second order in ξ^μ. Noting that

$$g_{\alpha\beta}(x^\mu) = g_{\alpha\beta}(\bar{x}^\mu + \xi^\mu), \tag{10.72}$$

we obtain Eq. (10.40). This is the desired form, because we want to use ξ^μ to transform to a coordinate system $\bar{x}^\mu$ where mass elements on the shell are fixed in spatial location and move uniformly in the time direction: *i.e*, for mass elements on the shell, $\bar{x}^\mu = (\hat{t}, a, \theta_*, \varphi_*)$. Then Israel's junction conditions will be applied to the Regge-Wheeler metric evaluated at a fixed coordinate location $(\hat{t}, a, \theta_*, \varphi_*)$, and in terms of the transformation generators (which are related to the motion of the shell in the Regge-Wheeler gauge).

Let us make four consecutive transformations

$$\begin{aligned}
\xi^\alpha_{(0)} &= [-f^{-1}(r)y(t)Y_{lm}, 0, 0, 0], \\
\xi^\alpha_{(1)} &= [0, h(r)z(t)Y_{lm}, 0, 0], \\
\xi^\alpha_{(2)} &= \left[0, 0, \frac{w(t)}{r^2}Y_{lm,\theta}, \frac{w(t)}{r^2\sin^2\theta}Y_{lm,\varphi}\right], \\
\xi^\alpha_{(3)} &= \left[0, 0, \frac{x(t)}{r^2\sin\theta}Y_{lm,\varphi}, -\frac{x(t)}{r^2\sin\theta}Y_{lm,\theta}\right],
\end{aligned}$$

or, by lowering indices,

$$\begin{aligned}
\xi_{(0)\alpha} &= [y(t)Y_{lm}, 0, 0, 0], \\
\xi_{(1)\alpha} &= [0, z(t)Y_{lm}, 0, 0], \\
\xi_{(2)\alpha} &= \left[0, 0, w(t)Y_{lm|\theta}, w(t)Y_{lm|\varphi}\right], \\
\xi_{(3)\alpha} &= \left[0, 0, x(t)\epsilon_{\theta\varphi}Y_{lm}{}^{|\varphi}, x(t)\epsilon_{\varphi\theta}Y_{lm}{}^{|\theta}\right].
\end{aligned}$$

where the covariant derivative $|$ is defined with respect to the 2–dimensional metric

$$G_{ab} = d\theta^2 + \sin^2\theta d\varphi^2. \tag{10.73}$$

We impose that, when evaluated at $(t, r, \theta, \varphi) = (\hat{t}, a, \theta_*, \varphi_*)$, the vector ξ^α coincides with $(\delta t, \delta r, \delta\theta, \delta\varphi)$, so that in the new coordinate system Eqs. (10.41) will be valid. Such a transformation leads to the following changes in the metric components:

$$\delta_{(0)}g_{\mu\nu} = \left[\begin{array}{cc|cc} 2\dot{y} & -\frac{f'}{f}y & y\partial_\theta & y\partial_\varphi \\ * & & & \\ \hline * & & & \\ * & & & \end{array}\right] Y_{lm}, \tag{10.74}$$

$$\delta_{(1)}g_{\mu\nu} = \left[\begin{array}{cc|cc} -f'hz & \dot{z} & & \\ * & \frac{h'}{h}z & z\partial_\theta & z\partial_\varphi \\ \hline & * & 2rhz & \\ & * & & 2rhz\sin^2\theta \end{array}\right] Y_{lm}, \tag{10.75}$$

which are purely polar perturbations;

$$\delta_{(2)}g_{\mu\nu} = \left[\begin{array}{cc|cc} & & \dot{w}Y_{lm,\theta} & \dot{w}Y_{lm,\varphi} \\ & & -\frac{2w}{r}Y_{lm,\theta} & -\frac{2w}{r}Y_{lm,\varphi} \\ \hline * & * & 2wY_{lm|\theta\theta} & 2wY_{lm|\theta\varphi} \\ * & * & * & 2wY_{lm|\varphi\varphi} \end{array}\right], \tag{10.76}$$

which are also polar perturbations, and finally

$$\delta_{(3)}g_{\mu\nu} = \left[\begin{array}{cc|cc} & & \dot{x}\epsilon_{\theta\varphi}Y_{lm}{}^{|\varphi} & \dot{x}\epsilon_{\varphi\theta}Y_{lm}{}^{|\theta} \\ & & -\frac{2x}{r}\epsilon_{\theta\varphi}Y_{lm}{}^{|\varphi} & -\frac{2x}{r}\epsilon_{\varphi\theta}Y_{lm}{}^{|\theta} \\ \hline * & * & x\phi_{\theta\theta} & x\phi_{\theta\varphi} \\ * & * & x\phi_{\varphi\theta} & x\phi_{\varphi\varphi} \end{array}\right], \tag{10.77}$$

which are axial perturbations. Here we have defined

$$\phi_{mn} = \epsilon_m{}^a Y_{lm|na} + \epsilon_n{}^a Y_{lm|ma}\,, \tag{10.78}$$

where m, n and a run through θ and φ. Here ϵ_{ab} is again defined with respect to the metric (10.73), so that

$$\epsilon_{\theta\varphi} = -\epsilon_{\varphi\theta} = \sin\theta\,. \tag{10.79}$$

In terms of y and z, the normalization of the 4–velocity would be written as

$$\begin{aligned} 0 &= -f'(a)h(a)z(\hat{t}) + f(a)H(\hat{t},a) - 2f(a)[-f^{-1}(a)\dot{y}(\hat{t})] \\ &= -f'(a)h(a)z(\hat{t}) + f(a)H(\hat{t},a) + 2\dot{y}(\hat{t})\,. \end{aligned}$$

Here we note again that $f_+ = f_-$. In this new coordinate system the metric is given by Eq. (10.42), where

$$\delta g_{\alpha\beta} = \delta_{(1)}g_{\alpha\beta} + \delta_{(2)}g_{\alpha\beta} + \delta_{(3)}g_{\alpha\beta}\,,$$

We are now in a position to match metric components along the shell, which simply sits at $(\hat{t}, a, \theta_*, \varphi_*)$. Of course, all of the matching conditions will be expressed in terms of the Regge-Wheeler metric perturbations, and the motion of the shell in the (internal and external) Regge-Wheeler gauges. In the θ and φ directions, we have

$$x_+(\hat{t}) = x_-(\hat{t}), \tag{10.80}$$

$$w_+(\hat{t}) = w_-(\hat{t})\,, \tag{10.81}$$

$$2h_+(a)z_+(\hat{t}) + aK_+(\hat{t},a) = 2h_-(\hat{t})z_-(\hat{t}) + aK_-(\hat{t},a)\,. \tag{10.82}$$

In the $t\theta$ and $t\varphi$ directions we have, in addition,

$$y_+(\hat{t}) = y_-(\hat{t})\,, \quad h_{0+}(\hat{t},a) = h_{0-}(\hat{t},a)\,. \tag{10.83}$$

while in tt direction the matching condition is automatically satisfied, with

$$\bar{g}_{tt}(\hat{t}, a, \theta_*, \varphi_*) = -f(a)\,, \tag{10.84}$$

accurate up to first order in the perturbations. This is a consistency check, since we have imposed that the four-velocity of mass elements on the shell is

$$u^\alpha = (1/\sqrt{f(a)}, 0, 0, 0)\,, \tag{10.85}$$

which should have a norm of -1. In simplified form, we have

$$[[x]] = [[w]] = [[y]] = [[h_0]] = [[2hz + aK]] = [[2\dot{y} + fH - f'hz]] = 0\,. \tag{10.86}$$

The symbol "[[...]]", as defined by Eq. (10.5), gives the jump of any given quantity across the shell.

The four-velocity of mass elements on the shell is given by Eq. (10.85). The surface stress-energy tensor of the shell is

$$S_{jk} = [\Sigma - \Theta + (\delta\Sigma - \delta\Theta)Y_{lm}]u_j u_k - [\Theta + \delta\Theta\, Y_{lm}]\gamma_{jk}\,, \tag{10.87}$$

where j and k go through t, θ and φ. Now let us try to evaluate the extrinsic curvature of the shell at the location $(\hat{t}, a, \theta_*, \varphi_*)$. First of all, we note that

$$n_\alpha = (0, 1, 0, 0)/\sqrt{\bar{g}^{rr}}\,,$$

and the extrinsic curvature is

$$K_{ij} = -\nabla_i n_j = -n_{j,i} + \Gamma^\mu{}_{ji} n_\mu\,,$$

where i, j run through $t\,, \theta\,, \varphi$. Since n_α only has a nonzero r-component the first term vanishes, and we obtain

$$K_{ij} = \frac{1}{\sqrt{\bar{g}^{rr}}}\Gamma^r{}_{ij}\,.$$

From the static configuration of the star, it is easy to obtain that

$$\begin{aligned}
\|S_{jk}\| &= \begin{bmatrix} \Sigma f(a) & & \\ & -a^2\Theta & \\ & & -a^2\Theta\sin^2\theta \end{bmatrix}, \\
\|\bar{K}_{jk}\| &= a\sqrt{h(a)} \begin{bmatrix} -\frac{2f}{a^2} & & \\ & \left[1 + \frac{af'}{2f}\right] & \\ & & \left[1 + \frac{af'}{2f}\right]\sin^2\theta \end{bmatrix},
\end{aligned}$$

where $j\,, k = t\,, \theta\,, \varphi$. From this we have relations (10.9) for static gravastars.

Now let us focus on first-order quantities. The tensors S_{jk} and K_{jk} can each be decomposed

into six terms: for example,

$$
\begin{aligned}
S_{jk} &= \begin{bmatrix} S^{(1)} & & \\ & S^{(2)} & \\ & & S^{(2)}\sin^2\theta \end{bmatrix} Y_{lm} \\
&+ S^{(3)} \begin{bmatrix} & \partial_\theta & \partial_\varphi \\ \partial_\theta & & \\ \partial_\varphi & & \end{bmatrix} Y_{lm} \\
&+ S^{(4)} \begin{bmatrix} & & \csc\theta\partial_\varphi & -\sin\theta\partial_\theta \\ \csc\theta\partial_\varphi & & & \\ -\sin\theta\partial_\theta & & & \end{bmatrix} Y_{lm} \\
&+ S^{(5)} \begin{bmatrix} 0 & & \\ & Y_{|\theta\theta} & Y_{|\theta\varphi} \\ & Y_{|\varphi\theta} & Y_{|\varphi\varphi} \end{bmatrix} \\
&+ S^{(6)} \begin{bmatrix} 0 & & \\ & \phi_{\theta\theta} & \phi_{\theta\varphi} \\ & \phi_{\varphi\theta} & \phi_{\varphi\varphi} \end{bmatrix} . \qquad (10.88)
\end{aligned}
$$

We have

$$
\begin{aligned}
S^{(1)} &= f\delta\Sigma + [(\Theta - 2\Sigma)(fH - hzf' + 2\dot{y})]\,, && (10.89)\\
S^{(2)} &= -a(aK\Theta + 2hz\Theta + a\delta\Theta)\,, && (10.90)\\
S^{(3)} &= -\Sigma(y + \dot{w})\,, && (10.91)\\
S^{(4)} &= \Sigma(h_0 - \dot{x})\,, && (10.92)\\
S^{(5)} &= -2\Theta w\,, && (10.93)\\
S^{(6)} &= -\Theta x\,, && (10.94)
\end{aligned}
$$

and

$$
\begin{aligned}
\bar{K}^{(1)} &= \frac{f\sqrt{h}}{a}(H - aK') + f\sqrt{h}z\frac{\lambda_L + 2h - ah'}{a^2}, && (10.95)\\
\bar{K}^{(2)} &= \frac{a^2\sqrt{h}}{2}\Bigg\{K' - H' + \frac{2(\dot{H}_1 + \ddot{z})}{f} + \left(1 + \frac{af'}{2f}\right)\frac{2K - H}{a} + \\
&\qquad + \left[\frac{2(h - \lambda_L)}{a^2} + \frac{2f'h + fh'}{af} + \frac{ff'h' - 2(f')^2h + 2hff''}{2f^2}\right]z\Bigg\}, && (10.96)\\
\bar{K}^{(3)} &= \frac{\sqrt{h}}{a}\left[\frac{aH_1}{2} + 2y + a\dot{z} + \left(1 + \frac{af'}{2f}\right)\dot{w}\right], && (10.97)\\
\bar{K}^{(4)} &= \sqrt{h}\left[\frac{\dot{x} - 2h_0}{a}\left(1 + \frac{af'}{2f}\right) + \frac{h_0' - \dot{h}_1}{2}\right], && (10.98)\\
\bar{K}^{(5)} &= \frac{2\sqrt{h}}{a}\left[\frac{az}{2} + w\left(1 + \frac{af'}{2f}\right)\right], && (10.99)\\
\bar{K}^{(6)} &= \sqrt{h}\left[-\frac{h_1}{2} + \frac{x}{a}\left(1 + \frac{af'}{2f}\right)\right], && (10.100)
\end{aligned}
$$

where $\lambda_L = -l(l+1)$. Here $\bar{K}^{(4)}$ and $\bar{K}^{(6)}$ are axial quantities. The junction condition on $\bar{K}^{(6)}$ yield

$$\left[\left[\sqrt{h}h_1\right]\right] = 0, \tag{10.101}$$

which together with $[[h_0]] = 0$ completes the junction conditions for axial perturbations (the junction condition on $\bar{K}^{(4)}$ yields an equation of motion for the variable x). For polar quantities, from $[[\bar{K}^{(5)}]] = 8\pi S^{(5)}$ we have

$$[[\sqrt{h}z]] = 0\,. \tag{10.102}$$

Then matching $[[\bar{K}^{(3)}]] = 8\pi S^{(3)}$ gives us an equation of motion for w, while matching $[[\bar{K}^{(1,2)}]] = 8\pi S^{(1,2)}$ yields

$$\left[\left[\sqrt{h}\left(\frac{H}{a} - K'\right)\right]\right] + \left[\left[\frac{2h}{a^2} - \frac{h'}{a}\right]\right]\sqrt{h}z = 8\pi\delta\Sigma\,, \tag{10.103}$$

$$\left[\left[\sqrt{h}\left(K' - H' + \frac{2\dot{H}_1}{f}\right)\right]\right] - \left[\left[\sqrt{h}\left(1 + \frac{af'}{2f}\right)\frac{H}{a}\right]\right] + \left[\left[\frac{h'}{a} - \frac{2h}{a^2} + \frac{f''h}{f} - \frac{f'h'}{2f}\right]\right]\sqrt{h}z =$$
$$= -16\pi\delta\Theta\,. \tag{10.104}$$

The remaining equations are

$$[[K]] = -2[[\sqrt{h}]]\sqrt{h}z/a = 8\pi\Sigma\sqrt{h}z\,, \tag{10.105}$$

$$[[H]] = \left[\left[\frac{f'\sqrt{h}}{f}\right]\right]\sqrt{h}z = 8\pi(\Sigma - 2\Theta)\sqrt{h}z\,, \tag{10.106}$$

$$\delta\Theta = -v^2\delta\Sigma\,, \tag{10.107}$$

where v is defined as in Eq. (10.47).

The formalism described above is more general than we need for a static thin-shell gravastar. It can easily be adapted to more general horizonless space-times and to static wormholes. For the Mazur-Mottolla gravastar, we have:

$$\Sigma = 0\,, \quad \Theta = -\frac{[[f']]}{16\pi\sqrt{f(a)}}\,,$$
$$[[f]] = 0 = [[f'']]\,, \quad [[f']] = \frac{6M}{a^2}\,, \quad [[f'^2]] = -\frac{12M^2}{a^4}\,.$$

Using the equations of Sec. 10.3.1 above together with these junction conditions we obtain continuity conditions for the shell position, $[[x]] = [[y]] = [[w]] = [[z]] = 0$, and the matching conditions for the axial and polar perturbations functions presented in the main text [Eqs. (10.43), (10.44), (10.45) and (10.46)].

10.9 Appendix: The continued fraction method

Our numerical search for the QNMs of gravastars is based on the continued fraction method, as modified in [301, 304]. The QNMs of an oscillating gravastar are solutions of Eqs. (10.21) and (10.27) satisfying the boundary conditions imposed by physical requirements: Ψ should

be regular at the origin, have the behavior of a purely outgoing wave at infinity and satisfy the junction conditions discussed in Section 10.3.3. The QNM frequencies are the (complex) frequencies $\omega = \omega_R + i\omega_R$ for which these requirements are satisfied.

The numerical determination of the QNM frequencies is nontrivial, especially for modes with large imaginary parts (strongly damped modes). The reason is simple to understand. Solutions of Eq. (10.27) representing outgoing and ingoing waves at infinity have the asymptotic behavior $\Psi^{\rm out} \sim e^{r_*/\tau}$ and $\Psi^{\rm in} \sim e^{-r_*/\tau}$ as $r_* \to \infty$, where $\tau = 1/\omega_I$ is the damping time. Therefore, identifying by numerical integration the purely outgoing solutions (that is, those solutions for which $\Psi^{\rm in}$ is zero) becomes increasingly difficult as the damping of the mode increases. The same problem occurs also in the case of QNMs of BHs, and was solved by Leaver [328]. Leaver found a continued fraction relation that can be regarded as an implicit equation which identifies the quasinormal frequencies, thus circumventing the need to perform an integration out to large values of r_*. This method was subsequently adapted to the polar and axial oscillations of a star [301, 304]. The Regge-Wheeler equation, which describes the perturbed space-time outside the gravastar, becomes

$$\frac{d^2\Psi}{dr_*^2} + \left[\omega^2 - V_{\rm out}\right]\Psi = 0\,, \tag{10.108}$$

with

$$V_{\rm out} = \left(1 - \frac{2M}{r}\right)\left(\frac{l(l+1)}{r^2} - \frac{6M}{r^3}\right) \tag{10.109}$$

and the tortoise coordinate $r_* = r + 2M\ln(r/2M - 1)$. We shall now write the solution of the Regge-Wheeler equation in a power-series form as follows. Defining $z \equiv 1 - R_2/r$, where $r = R_2$ is some point outside the shell of the gravastar, and introducing a function $\phi(z)$, related to $\Psi(r)$ by:

$$\Psi(r) = (r-2M)^{-i2M\omega}e^{-i\omega r}\phi(z) \equiv \chi(r)\phi(z)\,, \tag{10.110}$$

one finds that ϕ satisfies the differential equation:

$$(c_0 + c_1 z + c_2 z^2 + c_3 z^3)\frac{d^2\phi}{dz^2} + (d_0 + d_1 z + d_2 z^2)\frac{d\phi}{dz} + (e_0 + e_1 z)\phi = 0\,. \tag{10.111}$$

The constants depend only on ω, l and R_2 through the relations:

$$\begin{aligned} c_0 = 1 - \frac{2M}{R_2}\,,\ c_1 = \frac{6M}{R_2} - 2\,,\ c_2 = 1 - \frac{6M}{R_2}\,,\ c_3 = \frac{2M}{R_2}\,,\\ d_0 = -2i\omega R_2 + \frac{6M}{R_2} - 2\,,\ d_1 = 2\left(1 - \frac{6M}{R_2}\right)\,,\ d_2 = \frac{6M}{R_2}\,,\\ e_0 = \frac{6M}{R_2} - l(l+1)\,,\ e_1 = -\frac{6M}{R_2}\,. \end{aligned}$$

Let us now perform a power-series expansion of $\phi(z)$:

$$\phi(z) = \sum_{n=0}^{\infty} a_n z^n\,. \tag{10.112}$$

By substituting this expression in Eq. (10.111), the expansion coefficients a_n are found to satisfy a four-term recurrence relation of the form:

$$\begin{aligned} &\alpha_1 a_2 + \beta_1 a_1 + \gamma_1 a_0 = 0\,, \quad n = 1\,, \\ &\alpha_n a_{n+1} + \beta_n a_n + \gamma_n a_{n-1} + \delta_n a_{n-2} = 0\,, \quad n \geq 2\,, \end{aligned} \tag{10.113}$$

where:

$$\begin{aligned}
\alpha_n &= n(n+1)c_0\,, \quad n \geq 1\,, \\
\beta_n &= (n-1)nc_1 + nd_0\,, \quad n \geq 1\,, \\
\gamma_n &= (n-2)(n-1)c_2 + (n-1)d_1 + e_0\,, \quad n \geq 1\,, \\
\delta_n &= (n-3)(n-2)c_3 + (n-2)d_2 + e_1\,, \quad n \geq 2\,.
\end{aligned} \tag{10.114}$$

The coefficient a_0 is a normalization constant, and it is irrelevant from the point of view of imposing outgoing-wave boundary conditions. The ratio a_1/a_0 can simply be determined by imposing the continuity of Ψ and Ψ' at $r = R_2$, since from Eq. (10.110) it follows that:

$$a_0 = \phi|_{z=0} = \frac{\Psi(R_2)}{\chi(R_2)}\,, \tag{10.115}$$

$$\frac{a_1}{a_0} = \frac{R_2}{\Psi(R_2)}\left[\Psi'(R_2) + \frac{i\omega R_2}{R_2 - 2M}\Psi(R_2)\right]\,. \tag{10.116}$$

In the axial case, the values of $\Psi(R_2)$ and $\Psi'(R_2)$ can be obtained by the taking the interior solution (10.22) at $r = a_-$ and applying the junction conditions (10.43) to determine the wavefunction in the exterior, *i.e*, at $r = a_+$. From then onwards, we can numerically integrate the Regge-Wheeler equation (10.27) up to $r = R_2$. The remaining coefficients can then be determined by recursion from Eq. (10.113). In the polar case we proceed in a similar way: we obtain the Zerilli function $Z^{\rm out}$ and its derivative at $r = a_+$ by imposing the matching conditions (10.44)–(10.46). Then we use Eq. (10.38) to obtain the corresponding Regge-Wheeler function at $r = a_+$, integrate forwards to find a_0 and a_1, and finally obtain the remaining coefficients by recursion.

To apply the continued fraction technique, it is easier to consider three-term recurrence relations. Leaver has shown that the four-term recurrence relation (10.113) can be reduced to a three-term recurrence relation by a gaussian elimination step [329]. Define:

$$\hat{\beta}_0 = \frac{a_1}{a_0}\,, \qquad \hat{\alpha}_0 = -1\,, \tag{10.117}$$

where a_1/a_0 is obtained numerically from Eq. (10.116). Now set:

$$\begin{aligned}
&\hat{\alpha}_n = \alpha_n\,, \quad \hat{\beta}_n = \beta_n\,, \quad (n = 0, 1)\,, \\
&\hat{\gamma}_n = \gamma_n\,, \quad (n = 1)\,,
\end{aligned} \tag{10.118}$$

and for $n \geq 2$:

$$\begin{aligned}
&\hat{\alpha}_n = \alpha_n\,, \qquad \hat{\beta}_n = \beta_n - \frac{\hat{\alpha}_{n-1}\delta_n}{\hat{\gamma}_{n-1}}\,, \\
&\hat{\gamma}_n = \gamma_n - \frac{\hat{\beta}_{n-1}\delta_n}{\hat{\gamma}_{n-1}}\,, \qquad \hat{\delta}_n = 0\,.
\end{aligned} \tag{10.119}$$

By this gaussian elimination, Eq. (10.113) reduces to:

$$\hat{\alpha}_n a_{n+1} + \hat{\beta}_n a_n + \hat{\gamma}_n a_{n-1} = 0\,. \tag{10.120}$$

The elimination step is not as trivial as it may seem, because in the process one of the *three* independent solutions to Eq. (10.113) is lost. It can be shown that this solution is not relevant for our purposes [301].

We now turn to investigating the asymptotic behavior of the coefficients a_n in the expansion (10.112). Let us make the ansatz:

$$\lim_{n\to\infty} \frac{a_{n+1}}{a_n} = 1 + \frac{h}{n^{1/2}} + \frac{k}{n} + \dots \tag{10.121}$$

Dividing Eq. (10.113) by $n^2 a_n$, keeping terms up to $\sim n^{-3/2}$ and equating to zero the various terms in the expansion in powers of $n^{-1/2}$ we find the relations:

$$\begin{aligned} &c_0 + c_1 + c_2 + c_3 = 0\,, \\ &2c_0 + c_1 - c_3 = 0\,, \\ &h^2 = 2i\omega R_2\,, \\ &k = -\frac{3}{4} + i\omega(R_2 + 2M)\,. \end{aligned} \tag{10.122}$$

The first two of these equations are identities. Substituting the second pair of equations in Eq. (10.121) we get:

$$\lim_{n\to\infty} a_n = n^{-3/4+i\omega(R_2+2M)} e^{\pm 2\sqrt{2i\omega R_2 n}}\,. \tag{10.123}$$

According to a definition given by Gautschi [330], the solution of Eq. (10.121) corresponding to the plus sign in Eq. (10.123) is said to be *dominant*, whereas that corresponding to the minus sign is said to be *minimal* [330]. If we select the minimal solution the expansion (10.112) is absolutely and uniformly convergent outside the star, provided that we choose R_2 such that $R_2/2 < a < R_2$ and $R_2 > 2$. Furthermore, according to Eq. (10.110), the solution to Eq. (10.108) behaves as a pure outgoing wave at infinity, *i.e* it is the a QNM wavefunction. Thus, the key point is to identify the minimal solutions of Eq. (10.121). According to a theorem due to Pincherle [330], if Eq. (10.121) has a minimal solution then the following continued fraction relation holds:

$$\frac{a_1}{a_0} = \frac{-\hat{\gamma}_1}{\hat{\beta}_1 -}\frac{\hat{\alpha}_1\hat{\gamma}_2}{\hat{\beta}_2 -}\frac{\hat{\alpha}_2\hat{\gamma}_3}{\hat{\beta}_3 -}\dots \tag{10.124}$$

where the continued fraction on the RHS is convergent and completely determined since the coefficients $\hat{\alpha}_n$, $\hat{\beta}_n$ and $\hat{\gamma}_n$, defined in Eqs. (10.118),(10.119) are known functions of ω. Moreover, from Eqs. (10.116) and (10.117) it is apparent that the dependence on the stellar model is all contained in the ratio a_1/a_0. Keeping in mind the definitions (10.117), Eq. (10.124) can be recast in the form:

$$0 = f_0(\omega) = \hat{\beta}_0 - \frac{\hat{\alpha}_0\hat{\gamma}_1}{\hat{\beta}_1 -}\frac{\hat{\alpha}_1\hat{\gamma}_2}{\hat{\beta}_2 -}\frac{\hat{\alpha}_2\hat{\gamma}_3}{\hat{\beta}_3 -}\dots \tag{10.125}$$

Using the inversion properties of continued fractions [331], the latter equation can be inverted n times to yield:

$$0 = f_n(\omega) = \hat{\beta}_n - \frac{\hat{\alpha}_{n-1}\hat{\gamma}_n}{\hat{\beta}_{n-1} -}\frac{\hat{\alpha}_{n-2}\hat{\gamma}_{n-1}}{\hat{\beta}_{n-2} -}\dots\frac{\hat{\alpha}_0\hat{\gamma}_1}{\hat{\beta}_0} - \frac{\hat{\alpha}_n\hat{\gamma}_{n+1}}{\hat{\beta}_{n+1} -}\frac{\hat{\alpha}_{n+1}\hat{\gamma}_{n+2}}{\hat{\beta}_{n+2} -}\frac{\hat{\alpha}_{n+2}\hat{\gamma}_{n+3}}{\hat{\beta}_{n+3} -}\dots \tag{10.126}$$

for $n = 1, 2, ...$ These n conditions are analytically equivalent to Eq. (10.125). However, since the functions $f_n(\omega)$ have different convergence properties, each of them is best suited to find the quasinormal frequencies in a given region of the complex ω plane. This is the main reason for the accuracy and flexibility of the continued fraction technique.

10.10 Appendix: High-compactness limit

To investigate the behavior at the surface of the gravastar in the high-compactness limit, we use the $z \to 1 - z$ transformation law for the hypergeometric function [300],

$$F(a,b,c,z) = (1-z)^{c-a-b}\frac{\Gamma(c)\Gamma(a+b-c)}{\Gamma(a)\Gamma(b)} \times F(c-a,c-b,c-a-b+1,1-z) + \frac{\Gamma(c)\Gamma(c-a-b)}{\Gamma(c-a)\Gamma(c-b)}\,F(a,b,-c+a+b+1,1-z)\,.$$

Using Eq. (10.22) in the limit when $C \to 1$ and $r \to a$ we get

$$\Psi \approx \left[\frac{2(a-r)}{a}\right]^{iM\omega}\frac{\Gamma(l+\frac{3}{2})\Gamma(-i2M\omega)}{\Gamma(\frac{2+l-i2M\omega}{2})\Gamma(\frac{1+l-i2M\omega}{2})} + \left[\frac{2(a-r)}{a}\right]^{-iM\omega}\frac{\Gamma(l+\frac{3}{2})\Gamma(i2M\omega)}{\Gamma(\frac{1+l+i2M\omega}{2})\Gamma(\frac{2+l+i2M\omega}{2})}\,. \tag{10.127}$$

Within our conventions the first term is in-going, while the second term is out-going near the surface. So it is clear that in this regime both in- and out-going modes are present, and QNMs do *not* reduce to the Schwarzschild QNMs (which require only in-going waves). Furthermore, we can clearly see that in-going and out-going waves always have the same magnitude: the gravastar appears like a reflecting object, as suggested by [332]. Because this reflection happens in a polar coordinate system, it can simply be interpreted as due to the fact that waves going into a lossless gravastar will re-emerge without loss. Nevertheless, such a behavior already supports the conclusions of Ref. [291, 292], which showed that (for scalar fields) the ergoregion instability is more effective when the surface of the compact objects behaves like a "perfect mirror" in this sense.

It is easy to show that in the high-compactness limit

$$\Psi'(a_-) = \frac{i\omega\, a}{a-2M}\Psi(a_-)\,. \tag{10.128}$$

Solving for the metric quantities we find, up to dominant terms in $a - 2M$,

$$K(a_-) = \frac{l(l+1)+2ia\omega}{2a}\Psi(a_-)\,, \tag{10.129}$$

$$K'(a_-) = -\omega\frac{-il(l+1)+2\omega a}{2(a-2M)}\Psi(a_-)\,, \tag{10.130}$$

$$H_1(a_-) = -\frac{\omega\, a(\omega\, a-i)}{a-2M}\Psi(a_-)\,, \tag{10.131}$$

$$H_1'(a_-) = -\frac{\omega(\omega\, a-i)(4M+i\omega a^2)}{(a-2M)^2}\Psi(a_-)\,, \tag{10.132}$$

$$H_0(a_-) = -\frac{\omega\, a(\omega\, a-i)}{a-2M}\Psi(a_-)\,, \tag{10.133}$$

$$H_0'(a_-) = -\frac{\omega(\omega\, a-2i)(2M+i\omega a^2)}{(a-2M)^2}\Psi(a_-)\,. \tag{10.134}$$

In the exterior we get

$$K(a_+) = \frac{l(l+1)+2ia\omega}{2a}\Psi(a_-)\,, \tag{10.135}$$

$$K'(a_+) = -\omega\frac{-il(l+1)+4\omega a}{2(a-2M)}\Psi(a_-)\,, \tag{10.136}$$

$$H_1(a_+) = -\frac{\omega\, M(i+4M\omega)}{a-2M}\Psi(a_-)\,, \tag{10.137}$$

$$H_1'(a_+) = -\frac{M\omega(2M\omega+i)(1-4iM\omega)}{(a-2M)^2}\Psi(a_-), \tag{10.138}$$

$$H_0(a_+) = -\frac{M\omega(i+4M\omega)}{a-2M}\Psi(a_-)\,, \tag{10.139}$$

$$H_0'(a_+) = H_1'(a_+)\,. \tag{10.140}$$

Notice that, even though H_1 is not continuous at $r=a$, the Zerilli function is. Indeed, we get

$$Z^{\rm out}(a_+) = \Psi(a_-)\,, \qquad \Psi(a_-) = \Psi(a_+)\,. \tag{10.141}$$

Thus, we conclude that in the high-compactness limit, the master wavefunction for polar perturbations is continuous across the shell. A trivial extension of the known Schwarzschild results then shows that *polar and axial perturbations are isospectral* for large compactness, *i.e*, when $a \to 2M$ and $\mu \to 1/2$.

Chapter 11

Gravitational instability of superspinars

Superspinars are ultracompact objects whose mass M and angular momentum J violate the Kerr bound ($cJ/GM^2 > 1$). Recent studies analyzed the observable consequences of gravitational lensing and accretion around superspinars in astrophysical scenarios. In this chapter we investigate the dynamical stability of superspinars to gravitational perturbations, considering either purely reflecting or perfectly absorbing boundary conditions at the "surface" of the superspinar. We find that these objects are unstable independently of the boundary conditions, and that the instability is strongest for relatively small values of the spin. Also, we give a physical interpretation of the various instabilities that we find. Our results (together with the well-known fact that accretion tends to spin superspinars down) imply that superspinars are very unlikely astrophysical alternatives to black holes.

Contents

11.1 Introduction

Superspinars are vacuum solutions of the gravitational field equations whose mass M and angular momentum $J = aM$ violate the Kerr bound, *i.e.* $a > M$ (here and elsewhere in this chapter we use geometrical units: $G = c = 1$). These geometries could result from high-energy corrections to Einstein's theory of gravity, such as those that would be present in string-inspired models [29]. String-inspired corrections may require a modification of the metric (or some sort of "excision") in a small region surrounding the curvature singularity at the origin, in such a way as to "dress" the singularity. While stable stars with $a > M$ are in

principle allowed in general relativity[a], superspinars have been proposed as an alternative to black holes (BHs), and they are therefore imagined to have a compactness comparable to that of extremal rotating Kerr BHs and to exist in any mass range. Therefore, the observation of rapidly spinning ultracompact objects could potentially reveal or rule out the existence of superspinars.

One argument against the existence of superspinars was put forward in Ref. [292]. There, the authors constructed a toy model for a superspinar by assuming that the external surface of the superspinar can be modeled as a perfect mirror, *i.e.* that the reflection coefficient $\mathcal{R} = 1$ for waves incident on the superspinar. In this case superspinars are destabilized by superradiant effects, *i.e.* by the ergoregion instability first discussed by Friedman, Schutz and Comins [288, 245]. The ergoregion instability occurs on a dynamical timescale, posing a serious challenge to the existence of these objects in nature. However, a perfectly reflecting surface may be an unrealistic assumption. In general we would expect a frequency-dependent reflection coefficient $\mathcal{R}(\omega)$, and correspondingly a frequency-dependent transmission coefficient $\mathcal{T}(\omega) = 1 - \mathcal{R}(\omega)$. The exact form of $\mathcal{R}(\omega)$ depends on the specific model, but unfortunately no exact solutions describing four-dimensional superspinars are known.

A different instability was recently discussed by Dotti *et al.* [338, 339]. These authors studied perturbations of a Kerr solution with $a/M > 1$ (*i.e.*, unlike Ref. [292], they considered an actual naked singularity). They cast the linearized perturbation equations in the form of a self-adjoint operator and analyzed the discrete spectrum of this operator, proving the existence of an infinite number of unstable modes [339].

Here we generalize the stability analyses of Refs. [292] and [339] focusing on a superspinar model obtained by considering the Kerr solution with $a > M$. Besides extending the study of Ref. [292], we also impose an alternative (and perhaps more physical) prescription for the external surface of a four-dimensional superspinar. We assume that a perfectly absorbing surface (a "stringy horizon") is created by high-energy effects at some radius $r = r_0$, and we impose that the reflection coefficient $\mathcal{R}(\omega) \equiv 0$ at that radius. These purely ingoing boundary conditions at $r = r_0$ are designed to make superspinars as stable as possible against the ergoregion instability of Ref. [292]. This instability occurs because, when the boundary at $r = r_0$ is purely reflecting, the negative-energy modes which exist in the ergoregion can only leak to spatial infinity by tunneling through a potential barrier. Modes propagating outside the ergoregion have positive energies. This results in the negative energy of the ergoregion modes to decrease indefinitely, so that their amplitude becomes unbound, triggering an instability. By imposing purely ingoing boundary conditions at $r = r_0$, we basically allow the negative energy trapped in the ergoregion to "fall down a sink"; this could quench the instability to some extent. A similar quenching occurs for Kerr BHs with $a \leq M$, the role of the sink being played by the BH horizon. Clearly, if the reflection coefficient $0 < \mathcal{R}(\omega) < 1$ the quenching would be less efficient. Therefore we conjecture that if superspinars are unstable when $\mathcal{R}(\omega) \equiv 0$, it should be impossible to stabilize them using any other choice of boundary conditions.

In this chapter we analyze the stability of superspinars by imposing either perfectly absorbing ($\mathcal{R}(\omega) \equiv 0$) or perfectly reflecting ($\mathcal{R}(\omega) \equiv 1$) boundary conditions at some arbitrary

[a]Typical equations of state usually lead to stars with $a/M \lesssim 0.7$ [333, 334] that can be treated within a slow-rotation approximation [335]. However, stable, differentially rotating polytropic stars with $a/M \approx 1.1$ can be produced (*e.g.*) with the Whisky code [336, 337]. Also, note that the Kerr bound can be easily violated by *non-compact* objects such as the Earth ($M/R \sim 7 \times 10^{-10}$), which has $J/M^2 \sim 10^3$.

radius $r = r_0$. We find that, quite independently of r_0 and of the chosen boundary conditions, *superspinars are unstable to linearized gravitational perturbations.* For purely ingoing boundary conditions the instability is slightly weaker than in the perfectly reflecting case, but it still occurs on a dynamical timescale $\tau \sim M$, *i.e.* $\tau \sim 5 \times 10^{-6}$ s for an object with $M = M_\odot$ and $\tau \sim 5$ s for a supermassive object with $M \sim 10^6 M_\odot$. We also show that this result is valid for a wide class of theories of gravity. Our findings undermine several claims made in the literature that superspinars might be detected because the shadow they cast due to gravitational lensing [340, 341] or their accretion properties [29, 342, 343, 344, 345, 346] are different from Kerr BHs with $a < M$. While this is true, superspinars are plagued by multiple gravitational instabilities, and therefore they are unlikely to be astrophysically viable BH candidates.

11.2 A simple model of superspinar in four dimensions

Following Gimon and Horava [29], we model a superspinar of mass M and angular momentum $J = aM$ by the Kerr geometry

$$\begin{aligned} ds^2_{\rm Kerr} &= -\left(1 - \frac{2Mr}{\Sigma}\right) dt^2 + \frac{\Sigma}{\Delta} dr^2 - \frac{4Mr}{\Sigma} a \sin^2\theta d\phi dt \\ &+ \Sigma d\theta^2 + \left[(r^2 + a^2)\sin^2\theta + \frac{2Mr}{\Sigma} a^2 \sin^4\theta\right] d\phi^2 \end{aligned} \tag{11.1}$$

where $\Sigma = r^2 + a^2\cos^2\theta$ and $\Delta = r^2 + a^2 - 2Mr$. Unlike Kerr BHs, superspinars have $a/M > 1$ and no horizon. Since the domain of interest is $-\infty < r < +\infty$, the spacetime possesses naked singularities and closed timelike curves in regions where $g_{\phi\phi} < 0$ (see *e.g.* [347]).

We study linear perturbations around the Kerr metric (11.1). Using the Kinnersley tetrad and Boyer-Lindquist coordinates, it is possible to separate the angular and radial variables [348]. Small perturbations of a spin-s field are then reduced to the radial and angular master equations

$$\Delta^{-s} \frac{d}{dr}\left(\Delta^{s+1} \frac{dR_{lm}}{dr}\right) + \left[\frac{K^2 - 2is(r-M)K}{\Delta} + 4is\omega r - \lambda\right] R_{lm} = 0\,, \tag{11.2}$$

$$\left[(1-x^2)_s S_{lm,x}\right]_{,x} + \left[(a\omega x)^2 - 2a\omega s x + s + {}_sA_{lm} - \frac{(m+sx)^2}{1-x^2}\right] {}_sS_{lm} = 0\,, \tag{11.3}$$

where $x \equiv \cos\theta$, $K = (r^2 + a^2)\omega - am$ and the separation constants λ and ${}_sA_{lm}$ are related by

$$\lambda \equiv {}_sA_{lm} + a^2\omega^2 - 2am\omega\,. \tag{11.4}$$

The equations above describe scalar, electromagnetic and gravitational perturbations when $s = 0, \pm 1, \pm 2$ respectively. The oscillation frequencies of the modes can be found from the canonical form of Eq. (11.2). Switching to a "tortoise coordinate" r_* defined by the condition $dr_*/dr = (r^2 + a^2)/\Delta$, we get

$$\frac{d^2Y}{dr_*^2} + VY = 0\,, \tag{11.5}$$

where

$$
\begin{aligned}
Y &= \Delta^{s/2}(r^2+a^2)^{1/2}R\,, \\
V &= \frac{K^2-2is(r-M)K+\Delta(4ir\omega s-\lambda)}{(r^2+a^2)^2}-G^2-\frac{dG}{dr_*}\,,
\end{aligned}
$$

and $G = s(r-M)/(r^2+a^2) + r\Delta(r^2+a^2)^{-2}$. The eigenvalues ${}_sA_{lm}$ in Eq. (11.4) can be expanded in a power series in the parameter $a\omega$ as [349]

$$
{}_sA_{lm} = \sum_{n=0} f^{(n)}_{slm}(a\omega)^n\,. \tag{11.6}
$$

The absence of ingoing waves at infinity implies [350]

$$
Y \sim r^{-s}e^{i\omega r_*}\,, \qquad\qquad r\to\infty\,. \tag{11.7}
$$

The boundary conditions at $r = r_0$ are crucial. Ref. [292] assumed a perfect mirror at $r = r_0$, *i.e.* $Y(r_0) = 0$. If instead we assume the existence of some "stringy horizon" at r_0, we must impose purely ingoing waves as $r \to r_0$. Since for $a > M$ the potential V is regular at any $r = r_0$ (including also $r_0/M = 0$), we can write

$$
V(r) \sim V(r_0) + \mathcal{O}(r-r_0)\,. \tag{11.8}
$$

By expanding Eq. (11.5) in series around $r = r_0$ we find that the general solution is a superposition of ingoing and outgoing waves:

$$
Y \sim Ae^{-ikr_*} + Be^{ikr_*} + O(r_* - r_*(r_0))^3\,, \qquad k^2 = V(r_0)\,, \tag{11.9}
$$

where the sign of k is chosen to recover the well-known boundary condition for a wave-function in an extreme Kerr background ($a \to M$ and $r_0 \to M$): $k = \omega - m\Omega$, where $\Omega = 1/(2M)$ is the angular velocity of an extreme Kerr black hole. Purely ingoing boundary conditions at the stringy horizon imply $B = 0$ in Eq. (11.9) or, equivalently,

$$
\frac{dY}{dr_*} = -ikY\,, \qquad r\to r_0\,. \tag{11.10}
$$

This is the condition we impose in our numerical code.

For each ω, we integrate Eq. (11.5) numerically inward, starting at some large radius (typically $r_\infty = 400M$) where we impose the asymptotic behavior (11.7). Our results are robust to variations of r_∞ in a reasonable range. We stop the numerical integration at $r = r_0$, where the value of the field $Y(\omega, r_0)$ is extracted. Finally, we repeat the integration for different values of ω until the desired boundary condition (either $Y(\omega, r_0) = 0$ or Eq. (11.10)) at $r = r_0$ is satisfied, typically to within an accuracy of 10^{-10}.

In our numerical computations we make use of the series expansion (11.6), truncated at fourth order. When $|a\omega| < 1$, the series expansion is a very good approximation of the exact eigenvalues. However, in some cases (*i.e.* when $|a\omega| \gtrsim 1$), instead of the series expansion we have used exact numerical values of ${}_sA_{lm}$ obtained by solving Eq. (11.3) with the continued fraction method [9].

We focus on the most relevant gravitational perturbations, described by the Teukolsky equation with $s = 2$. To compute unstable modes we also make use of the symmetry [328, 9]

$$m \to -m\,, \quad \omega \to -\omega^*\,, \quad {}_sA_{lm} \to {}_sA^*_{l-m}\,. \tag{11.11}$$

In practice, this symmetry means that modes with azimuthal number $-m$ can be obtained from those with azimuthal number m by changing the sign of the real part of the frequency. Therefore we focus on modes with $\mathrm{Re}[\omega] = \omega_R > 0$ only.

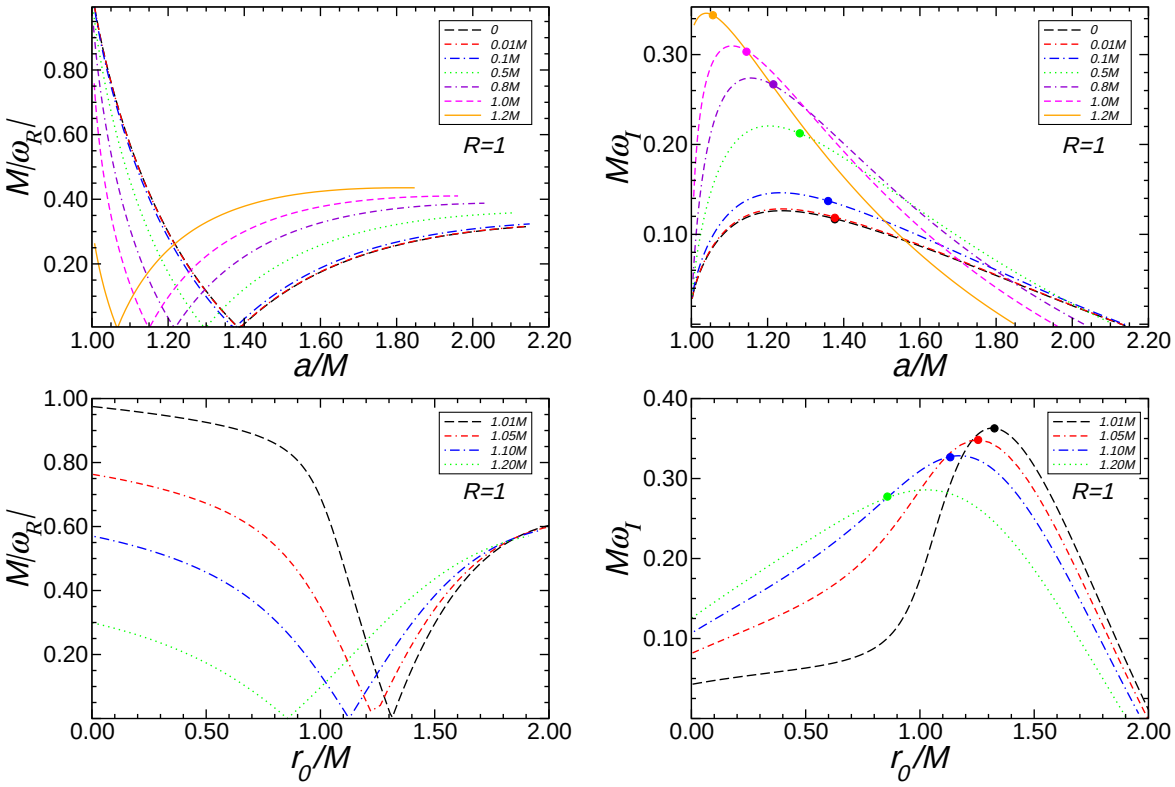

Figure 11.1: Top: Real (left) and imaginary part (right) of unstable gravitational modes of a superspinar as a function of the spin parameter, a/M, for $l = m = 2$ and several fixed values of r_0. Bottom: Real (left) and imaginary part (right) of unstable gravitational modes of a superspinar as a function of the mirror location, r_0/M, for $l = m = 2$ and different fixed values of the spin parameter. Large dots indicate purely imaginary modes.

11.3 Perfect mirror

11.3.1 Unstable modes with $l = m = 2$

Let us start by reviewing and extending the results of Ref. [292], which first found that superspinars with a perfectly reflecting surface are unstable due to the ergoregion instability. In the top panel of Fig. 11.1 we show unstable frequencies for $s = l = m = 2$ as a function of the spin parameter a/M for selected values of r_0/M. We see that the instability (signalled

by a positive imaginary part ω_I for the frequency) is always strong, *i.e.* it always occurs on a short timescale $\tau \equiv 1/\omega_I \sim 10M \sim 5 \times 10^{-5}(M/M_\odot)$ s, at least when $a \lesssim 2.2M$. It is interesting to note that the instability is also effective for $r_0 = M$ and $a = M + \epsilon$, *i.e.* for an object as compact as an extremal Kerr BH with a rotation parameter that only slightly violates the Kerr bound. This is also illustrated in Table 11.1.

Table 11.1: Unstable gravitational ($s = 2$) frequencies with $l = m = 2$ for a superspinar with a perfect reflecting surface ($\mathcal{R} = 1$) and with a "stringy event horizon" ($\mathcal{R} = 0$) at $r = r_0$. All modes in this table have been computed using numerical values of ${}_sA_{lm}$ obtained via the continued fraction method [9].

	$(\omega_R M\,, \omega_I M)$, $\mathcal{R} = 1$			$(\omega_R M\,, \omega_I M)$, $\mathcal{R} = 0$		
r_0/M	$a = 1.1M$	$a = 1.01M$	$a = 1.001M$	$a = 1.1M$	$a = 1.01M$	$a = 1.001M$
0.01	(0.5690 , 0.1085)	(0.9744, , 0.0431)	(0.9810 , 0.0097)	(0.5002 , 0.0173)	(0.9498 , 0.0062)	(1.0286 , 0.0033)
0.1	(0.5548 , 0.1237)	(0.9673 , 0.0475)	(0.9794 , 0.0110)	(0.4878 , 0.0260)	(0.9435 , 0.0093)	(1.0252 , 0.0048)
0.5	(0.4571 , 0.1941)	(0.9256 , 0.0631)	(0.9688 , 0.0155)	(0.3959 , 0.0719)	(0.9016 , 0.0237)	(1.0052. , 0.0091)
0.8	(0.3081 , 0.2617)	(0.8598 , 0.0878)	(0.9507 , 0.0202)	(0.2537 , 0.1053)	(0.8298 , 0.0376)	(0.9793 , 0.0095)
1	(0.1364 , 0.3095)	(0.6910 , 0.1742)	(0.9003 , 0.0640)	(0.0916 , 0.1219)	(0.6530 , 0.0821)	(0.8853 , 0.0313)
1.1	(0.0286 , 0.3248)	(0.4831 , 0.2655)	(0.6071 , 0.2207)	(−0.0078 , 0.1233)	(0.4377 , 0.1230)	(0.5696 , 0.1064)

From Fig. 11.1 and Table 11.1, it is clear that when $r_0 > M$ the imaginary part does not vanish as $a \to M$. This is in agreement with our expectations, since when $r_0 > r_H$ the "BH bomb" instability [351, 292] occurs even when $a < M$.

The dependence of the eigenfrequencies on the mirror location is also shown in the bottom panel of Fig. 11.1 for different values of the spin parameter. The imaginary part of the frequency is positive (*i.e.* the object is unstable) for a wide range of parameters. For any value of a/M in the bottom panel of Fig. 11.1 the instability is strongest when $r_0/M \sim 1$, and is effective also in the limit $r_0/M \ll 1$ (although in this regime high-energy corrections to the background metric could be relevant).

Overall, Fig. 11.1 shows that the strongest instability occurs roughly when $a/M \sim 1.1$. For larger values of the spin the imaginary part decreases and eventually it vanishes (causing the instability to disappear) for a critical value of a/M which depends on r_0. At first sight, this result seems in contrast with the superradiant nature of the instability, as one may naively think that the instability should become stronger for large spins.

In Fig. 11.2 we show that this expectation is not justified by plotting the proper volume of the ergoregion as a function of a/M. The proper volume can be computed via

$$V = 4\pi \int_{\theta_i}^{\pi/2} d\theta \int_{r_i}^{r_f} dr \sqrt{g_{rr} g_{\theta\theta} g_{\varphi\varphi}}\,, \tag{11.12}$$

where we have considered a constant time slice, the metric elements are taken from Eq. (11.1), we have exploited the reflection symmetry of the Kerr metric, and we have already integrated out the φ dependence. For $a < M$ the ergoregion extends between the outer Kerr horizon at $r_H = M + \sqrt{M^2 - a^2}$ and the "outer ergosphere radius" at $r_{e+}(\theta) = M + \sqrt{M^2 - a^2 \cos^2\theta}$. In this case we set $r_i = r_H$, $r_f = r_{e+}$, and $\theta_i = 0$ in the integral above. A straightforward calculation shows that in this case the proper volume increases monotonically with a/M, eventually diverging[a] for $a = M$. However, when $a > M$, the ergoregion extends between the

[a]This is because when $a = M$, $g_{rr} \sim 1/(r - M)^2$ near the horizon $r = M$: this causes the integral (11.12) to diverge logarithmically.

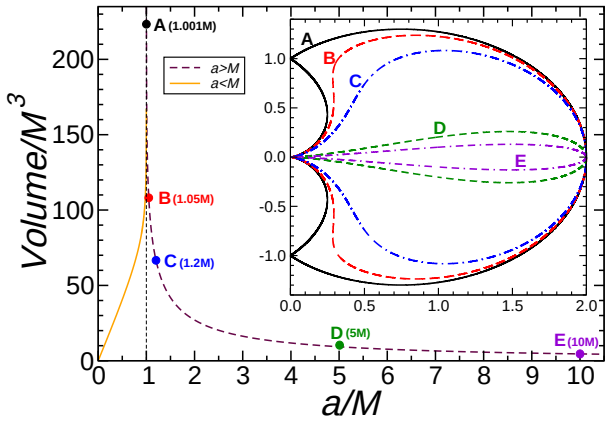

Figure 11.2: Proper volume of the ergoregion as a function of the spin a/M. The volume increases monotonically when $a < M$, is infinite at $a = M$ and decreases monotonically when $a > M$. The proper volumes for $a \sim 2M$ and $a \sim 0.3M$ are roughly the same. In the inset we show the azimuthal section of the ergoregion for selected values of the spin. These spins are marked by filled circles and capital Latin letters in the main plot; their numerical value is indicated in parentheses in the figure. In the limit $a/M \to \infty$ the ergoregion becomes so oblate that its proper volume shrinks to zero.

inner ergosphere at $r_{e-}(\theta) = M - \sqrt{M^2 - a^2 \cos^2\theta}$ and the outer ergosphere $r_{e+}(\theta)$. Therefore we set $r_i = r_{e-}$, $r_f = r_{e+}$, and $\theta_i = \arccos(M/a)$ in the integral (11.12). In this case, the proper volume of the ergosphere monotonically *decreases* with a/M. In the inset of Fig. 11.2 we plot an azimuthal section of the ergoregion for selected values of the spin parameter. The proper volume of the ergoregion vanishes as $a/M \to \infty$ because the ergoregion becomes more and more oblate (in the equatorial direction) as the spin increases. As $a/M \to \infty$ the proper volume shrinks to zero and the ergoregion instability for modes with $l = m = 2$ becomes harmless. In Section 11.5, however, we will see that this suppression of the ergoregion instability is less effective for modes with $l = m \gg 2$, which are more concentrated in the equatorial region and which make superspinars unstable even for larger values of the spin.

11.3.2 Unstable modes with $m = 0$

Superradiance due to an ergoregion is not the only mechanism driving instabilities in superspinars. Unstable modes also exist for $m = 0$, when the condition for superradiance $\omega < m\Omega = 0$ cannot be fulfilled. This is shown in the left panel of Fig. 11.3, where we show different gravitationally unstable modes for $l = 2$ and $m = 0, 1, 2$.

We see that the unstable mode with $m = 2$ exists in the range $0 \leq r_0/M \leq 2$, *i.e.* out to the outer location of the ergoregion in the equatorial plane. Unstable modes with $m = 1$ and $m = 0$ exist only in a more limited range around $r_0 \sim M$. Modes with larger values of $m(\leq l)$ drive stronger instabilities, but the instability for modes with $m = 0$ is also important, because it occurs on a dynamical timescale $\tau = 1/\omega_I \sim M$ for a wide range of parameters. In the right panel of Fig. 11.3 we show some unstable modes with $m = 0$ for different values of the spin parameter.

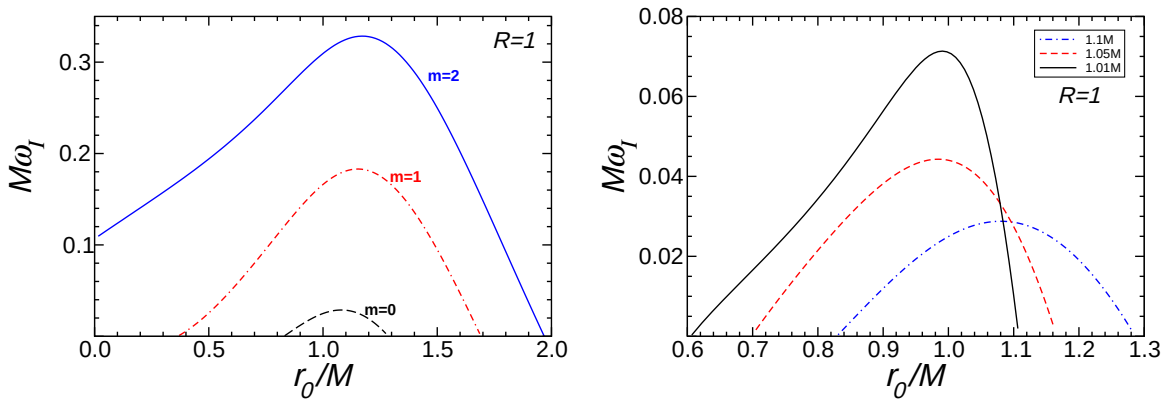

Figure 11.3: Left: Imaginary part of unstable gravitational modes of a superspinar as a function of the mirror location, r_0/M, for $a = 1.1M$, $l = 2$ and $m = 0$, 1, 2. Right: Imaginary part of unstable gravitational modes of a superspinar as a function of the mirror location, r_0/M, for $l = 2$, $m = 0$ and several values of the spin parameter, a.

Unstable modes with $m = 0$ have been recently found by Dotti and Gleiser [338, 339]. By imposing regularity conditions at $r = -\infty$ these authors found (an infinite number of) unstable purely imaginary modes when $a > M$. The superspinar model we are discussing reduces to the spacetime considered in Refs. [338, 339] when $r_0 \to -\infty$ and $\mathcal{R} = 1$. We carried out a search of these purely imaginary unstable modes, and our results agree very well with those of Ref. [339] in this limit. For illustration, in the left panel of Fig. 11.4 we show that the frequency of the $m = 0$ purely imaginary mode for $a = 1.4M$ matches the result of Ref. [339] for $r_0 \to -\infty$. The figure shows that the frequency of these modes settles to its asymptotic value when $r_0 \lesssim -3M$, so it makes sense to fit $M\omega_I$ for these $m = 0$ purely imaginary modes as a function of a, setting $r_0 = -3M$. A comparison between the numerical results and the polynomial fit

$$M\omega_I = 6.375 + 0.177a/M + 0.230(a/M)^2 \tag{11.13}$$

is presented in the right panel of Fig. 11.4. In the range $1.15 \lesssim a/M < 2$ the fit is accurate to within 0.003% and suggests that the imaginary part of the frequency (and therefore the "strength" of the instability) grows approximately as a quadratic function of the spin. We stress that these results have been obtained using the asymptotic expansion of the angular spheroidal eigenvalues [349]

$${}_sA_{lm} \sim (2l - \eta + 1)|a\omega| - s(s+1) + \mathcal{O}(|a\omega|^0)\,, \tag{11.14}$$

where $\eta = 2\max(|m|, |s|)$. Because for these modes $|a\omega| \gtrsim 5$, this expansion is a good approximation of the numerical eigenvalues computed by the continued fraction method [349].

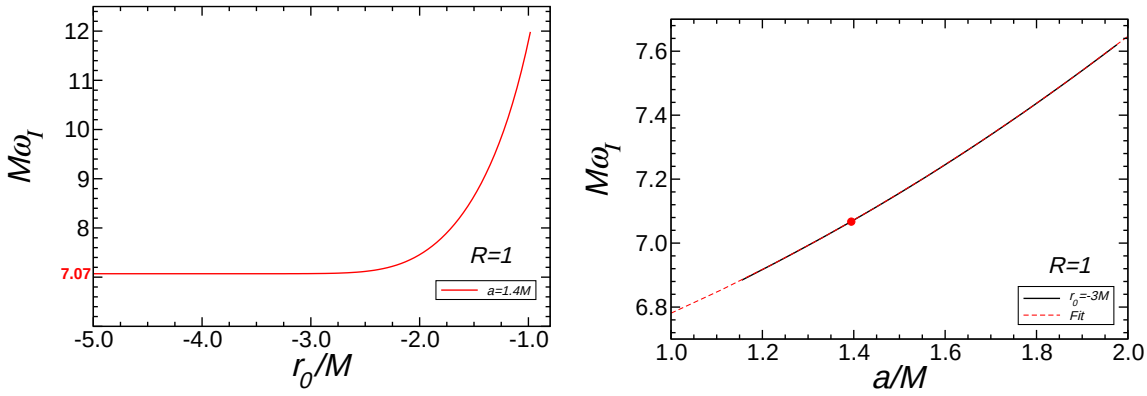

Figure 11.4: Left: Purely imaginary unstable mode as a function of the mirror location, $r_0/M < 0$, for $a = 1.4M$, $s = l = 2$ and $m = 0$. In the limit $r_0 \to -\infty$, $M\omega_I \sim 7.07$, which perfectly agrees with results in Ref. [339]. Right: Purely imaginary unstable mode as a function of the spin, a/M, for $r_0 = -3M$, $s = l = 2$, $m = 0$. Numerical results (black straight line) are consistent with the quadratic fit of Eq. (11.13) (red dashed line). The dot marks the case considered in the left panel.

11.4 Absorbing boundary conditions (horizon-like surface at $r = r_0$)

From the results discussed in the previous section we conclude that a dynamical instability is almost unavoidable in a broad region of the parameter space if the surface of the superspinar is perfectly reflecting. The instability is present even in what would naively seem the most phenomenologically viable case, *i.e.* when $r_0 \sim M$ and $a = M + \epsilon$. One could argue that a perfectly reflecting surface maximizes the efficiency of the ergoregion instability because negative-energy modes, which are potentially dangerous, cannot be absorbed, and that this might not happen for different boundary conditions. In fact, Kerr BHs are stable because (despite superradiant scattering) the negative-energy modes can flow down the horizon. Therefore we expect ingoing boundary conditions ($\mathcal{R} = 0$) at $r = r_0$ to represent the worst possible situation for the ergoregion instability to develop. If we find an instability even in this case, the superspinars described by our simple model are doomed to be unstable. This choice also seems more physically motivated than the perfectly reflecting boundary conditions, because r_0 might be the location of an event horizon formed by string-inspired modifications of gravity at high curvatures. We consider both modes with $l = m = 2$ (which we expect to be affected by the ergoregion instability) as well as modes with $m = 0$, which we found to be unstable in the perfectly reflecting case.

The punchline of this section is that unstable modes exist even when we impose ingoing boundary conditions. Qualitatively, the results are the same as those obtained by imposing perfect reflection at the surface of the superspinar. The instability is slightly weaker than in the previous case, but it is again unavoidable in a wide region of parameter space.

Gravitationally unstable modes with $l = m = 2$ and $\mathcal{R} = 0$ are listed in Table 11.1 and shown in Fig. 11.5 (to be compared with Fig. 11.1). Typically the imaginary part of the unstable modes when $\mathcal{R} = 0$ is only one order of magnitude smaller than that obtained

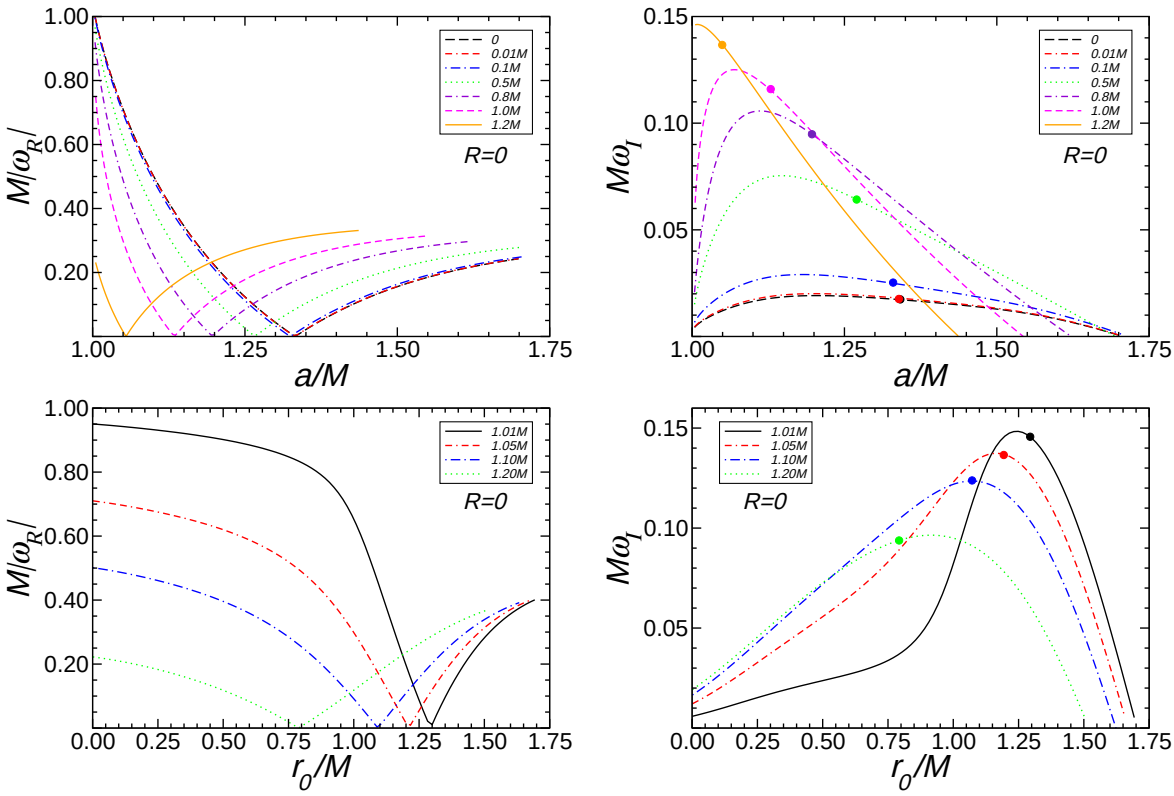

Figure 11.5: Top: Real (left) and imaginary part (right) of unstable gravitational modes of a superspinar as a function of the spin parameter, a/M, for $l = m = 2$ and several fixed values of the horizon location r_0/M. Bottom: Real (left) and imaginary part (right) of unstable gravitational modes of a superspinar as a function of the the horizon location, for $l = m = 2$ and fixed values of the spin parameter. Large dots indicate purely imaginary modes.

imposing $\mathcal{R} = 1$, which causes the instability to disappear at slightly smaller spins, *i.e.* when $a/M \gtrsim 1.75$. However, as already mentioned, in the next section we will present evidence that higher-l modes are unstable for larger values of the spin and show that our results are sufficient to rule out superspinars as astrophysically viable alternatives to Kerr BHs.

Also, we stress that perfectly absorbing "stringy horizons" can only be created by high-energy effects taking place beyond the range of validity of general relativity. From a phenomenological point of view, the region that should be modified by these high-energy corrections is close to the curvature singularity of the Kerr metric ($r_0 \ll M$). Unstable modes generically exists for $a = M + \epsilon$, even in the limit $r_0/M \to 0$. Moreover, results are smooth in the limit $r_0/M \to 0$, which means that in the region spanned by our calculations curvature singularities do not affect our conclusions.

Finally, Fig. 11.6 (to be compared with Fig. 11.3) shows that unstable modes with $m = 0$ are still present when we impose $\mathcal{R} = 0$ at $r = r_0$.

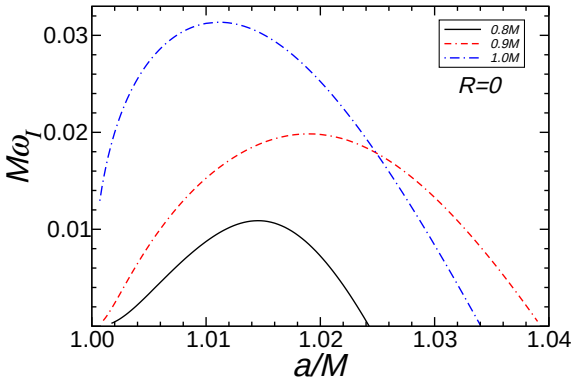

Figure 11.6: Imaginary part of unstable gravitational modes of a superspinar as the spin parameter, a, for $l = 2$, $m = 0$ and several values of the horizon location, r_0.

11.5 Modes with $l = m \gg 1$ and physical origin of the instability

We have seen that when we impose perfectly reflecting boundary conditions ($\mathcal{R} = 1$) superspinars are plagued by several instabilities. Moreover, these instabilities are still present when we impose $\mathcal{R} = 0$, *i.e.* when we consider a "stringy horizon" at $r = r_0$, which would be expected to quench the instabilities. Here we analyze in more detail how these different instabilities arise. We focus first on the case $r_0/M > 0$. For $\mathcal{R} = 1$ from Figs. 11.1 and 11.3 (and analogously for $\mathcal{R} = 0$ from Figs. 11.5 and 11.6) we see that, for both $m = 0$ and $m = 2$, the imaginary part vanishes at some critical radius: $\omega_I(r_{\rm crit}) = 0$. By using a root-finding routine we can solve for the critical radius as a function of the spin parameter a/M. The results are shown in Fig. 11.7. For $m = 2$ and $\mathcal{R} = 1$ the instability occurs in the region below the dot-dashed blue line extending from $a \sim M$ up to $a/M \sim 2.2$. The dashed horizontal line marks the location of the outer ergoregion on the equatorial plane ($r = 2M$). As $a/M \to 1$ the critical radius roughly coincides with the location of the ergoregion, and it decreases monotonically for larger rotation. The situation is similar for $m = 2$ and $\mathcal{R} = 0$ (solid black line extending from $a \sim M$ up to $a/M \sim 1.75$), with the instability disappearing earlier (at $a/M \sim 1.75$) because the ingoing boundary conditions allow negative energy modes to flow down the stringy horizon. This plot confirms our qualitative understanding of the instability: as shown in Fig. 11.2, in the limit $a/M \to \infty$ the proper volume of the ergoregion vanishes and superradiance cannot destabilize the modes at arbitrarily large spins.

It would therefore seem that superspinars with $a > 2.2M$ might be stable, for any value of r_0 and even in the most restrictive case with $\mathcal{R} = 1$. We argue, however, that this is not true if we consider modes with $l = m > 2$. In fact the angular distribution of modes with higher $l = m$ is more concentrated around the equatorial plane. Higher-l modes become more effective at destabilizing the superspinar when the ergoregion is oblate, *i.e.* when $a \gg M$ (see again the inset of Fig. 11.2). This intuitive understanding is confirmed by Fig. 11.8. There we plot the imaginary part of the fundamental unstable modes for $l = m = 2$ and $l = m > 2$ (setting $r_0 = 0$), both for $\mathcal{R} = 1$ and $\mathcal{R} = 0$.

In the case $\mathcal{R} = 1$, unstable modes with higher $l = m$ exist for larger values of the spin.

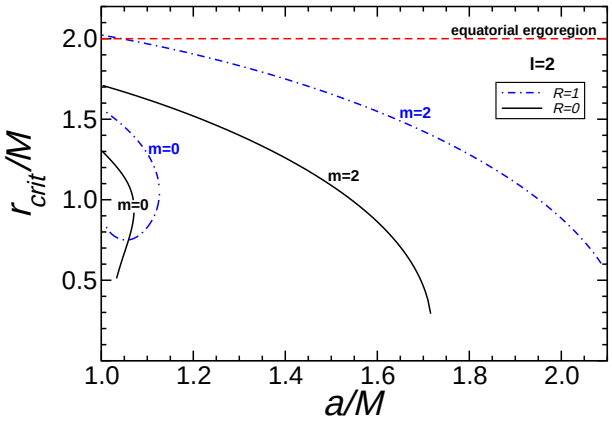

Figure 11.7: Critical radius $r_{\rm crit}/M$ as a function of a/M for $s = l = 2$ and $m = 0, 2$. We impose both $\mathcal{R} = 0$ and $\mathcal{R} = 1$ at $r = r_0$. For $m = 2$ an instability occurs when $r_0 < r_{\rm crit}$. For $m = 0$ an instability occurs in the region delimited by the curves on the left. When $l = m \gg 1$ an instability is expected to occur also when $a \gtrsim 2.2M$ in the $\mathcal{R} = 1$ case, and when $a \gtrsim 1.75M$ in the $\mathcal{R} = 0$ case (cf. Fig. 11.8). Although not shown, the region where $r_0/M < 0$ is expected to be unstable for any value of $a > M$.

For example the $l = m = 5$ mode becomes stable when $a/M \gtrsim 3.6$, while the $l = m = 2$ mode becomes stable when $a/M \gtrsim 2.2$, as previously discussed. Modes with $l = m \gg 1$ are generally difficult to compute with our code. Our results suggest that, for any fixed value of $a/M \gg 1$, there are always unstable modes as long as $l = m$ is sufficiently large. We stress that these results are in contrast with the case of Kerr BHs, where the superradiant amplification is always stronger for $l = m = 2$ [350]. Results are qualitatively similar for $\mathcal{R} = 0$, in which case the $l = m = 3$ instability disappears when $a/M \gtrsim 2$, while the $l = m = 2$ instability disappears when $a/M \gtrsim 1.75$, as previously discussed. However in this case the $l = m = 4$ instability is weaker than the $l = m = 3$ instability, and the $l = m = 5$ instability disappears for smaller values of a/M than in the $l = m = 2$ case. This is because the stringy event horizon quenches the instability of higher-l modes, similarly to the horizon of a Kerr BH.

More in general, the ergoregion instability that we have found here at the linear level can be related to simple kinematical properties of the Kerr spacetime. In fact, as we show in Appendix 11.7, Kerr spacetimes with $a > M$ admit *stable* non-equatorial null circular orbits with *negative* energy. These orbits exist at any radius $r < M$. The very existence of these orbits is enough to prove that the spacetime is plagued by the ergoregion instability, *provided* that purely reflecting boundary conditions ($\mathcal{R} = 1$) are imposed at $r_0 < M$. This is because null orbits are the geometric-optics limit of gravitational perturbations, as can easily be seen by expanding their propagation equation in powers of $1/\lambda$ (λ being the wavelength of the perturbation). Therefore, the existence of stable null circular orbits with negative energies implies the existence of short-wavelength modes with negative energies. Under perfectly reflecting boundary conditions, these modes can only leak to infinity by tunneling through the potential barrier. However, because particles outside the ergoregion must have positive energies, this leak makes the energy of the perturbations inside the ergoregion more and more negative. As a result, their amplitude grows without bound, thus revealing the instability

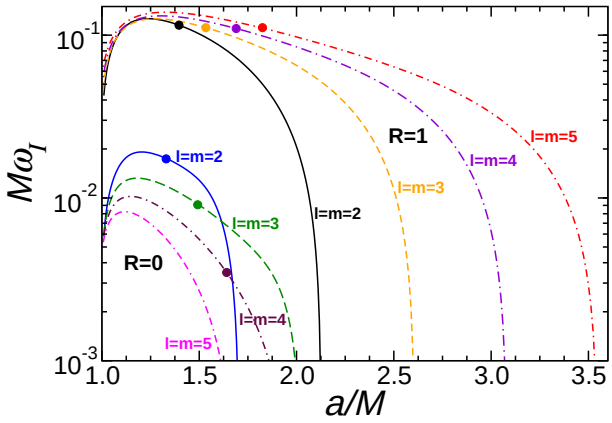

Figure 11.8: Imaginary part of the fundamental unstable mode as a function of the spin a/M for a superspinar with $r_0 = 0$. Upper curves refer to $\mathcal{R} = 1$ with $l = m = 2, 3, 4, 5$. Lower curves refer to $\mathcal{R} = 0$ with $l = m = 2, 3, 4, 5$. Dots indicate purely imaginary modes.

of the spacetime. For these reasons we expect modes with $l = m \gg 1$ to be unstable for arbitrarily large values of a/M, at least for $\mathcal{R} = 1$. This expectation is consistent with the general theorem of Ref. [288], which states that any spacetime possessing an ergoregion, but not an event horizon, is vulnerable to the ergoregion instability. As shown in Fig. 11.8, this expectation is not always justified in the less efficient case with $\mathcal{R} = 0$.

The existence of stable non-equatorial null circular orbits with negative energy clarifies why superspinars are unstable even under perfectly absorbing boundary conditions (*i.e.*, in the presence of a stringy horizon), while for Kerr BHs with $a \leq M$ the presence of the horizon kills the ergoregion instability. For superspinars, the effective potential for gravitational perturbations presents a minimum at small radii (corresponding, in the eikonal limit, to the location of a negative-energy stable non-equatorial null circular orbit), and then rises as $r/M \sim 0$. Therefore, the ergoregion modes need to tunnel through a potential barrier to fall into the "stringy" horizon. The stability of the superspinar depends on a delicate balance between the transmission coefficients through the "inner" and "outer" potential barriers.

A possible objection against instability could be the following. For sufficiently fast rotation (perhaps even for spins as low as $a \sim 6M$, *i.e.* at the higher end of the viable range identified by Ref. [345]), if unstable modes exist in the eikonal limit ($l = m \to \infty$) their imaginary part will be small, even in the case $\mathcal{R} = 1$. The ergoregion instability is due to ergoregion modes leaking to infinity through the potential barrier, but the tunneling becomes less and less effective as the modes behave more and more like particles, because the amplitude transmitted to infinity scales as $\exp(-L/\lambda)$ (where $L \sim M$ is the width of the barrier and λ is the mode's wavelength). It is therefore conceivable that the imaginary part might be so tiny that these modes can be considered stable for all practical purposes.

However, accretion is known to spin superspinars *down* [342]. According to Ref. [352], a BH which is initially nonrotating gets spun up to the extremal limit $a = M$, where it cannot be spun up any more [352, 353], by accreting a mass $\Delta M = (\sqrt{6} - 1)M_{\rm in} = 1.4495 M_{\rm in}$ ($M_{\rm in}$ being the initial BH mass). This corresponds to the accretion of a gas mass $\Delta M_0 = 1.8464 M_{\rm in}$, of which ΔM falls into the BH and $\Delta M_0 - \Delta M$ is dissipated by the disk's viscosity into

electromagnetic radiation. Similarly, a superspinar with $a/M = 7$ gets spun down to $a/M = 1.5M$ (where the ergoregion instability is always effective) by accreting a mass $\Delta M = 1.730 M_{\rm in}$ (corresponding to a gas mass $\Delta M_0 = 2.295 M_{\rm in}$). The two processes (spin-up of a Schwarzschild BH to the extremal Kerr limit, and spin-down of a superspinar from $a/M = 7$ to $a/M = 1.5$) involve amounts of accreted material of the same order of magnitude, hence the corresponding timescales too will be comparable. Supermassive BHs are expected to be spun up to the extremal Kerr limit by coherent accretion[a] on a timescale much smaller than the Hubble time [361], so a superspinar should be spun down to the unstable region on a timescale much smaller than the Hubble time. For this reason, the existence of supermassive superspinars is unlikely in the real Universe.

The situation is slightly different for stellar-mass superspinars. Analytical arguments [362] and population synthesis calculations [363] show that BHs in binaries essentially retain the spin they had at birth, so it is unclear whether accretion would be efficient enough to destabilize a superspinar. On the other hand, as far as we know, no realistic collapse scenario leading to the formation of stellar-mass superspinars has been proposed so far. Typical equations of state lead to compact stars rotating with $a/M \lesssim 0.7$ [333, 334]. Polytropic differentially rotating stars with $a \approx 1.1M$ can in principle exist [336, 337], but they are stable. Even if depleted of 99% of their pressure and induced to collapse, these stars do not form a BH and produce either a supermassive star (which will collapse to a BH with $a < M$ when enough angular momentum has been shed in gravitational waves) or a stable, rapidly rotating star.

For $r_0/M > 0$ there is a second family of unstable modes with $m = 0$ that cannot be superradiant modes. Figs. 11.3 and 11.6 show that, for fixed values of a/M, these modes only exist in a limited range of r_0/M. This range corresponds to the blue dot-dashed line ($\mathcal{R} = 1$ case) and to the solid black line ($\mathcal{R} = 0$ case) on the left of Fig. 11.7, showing that this family of unstable modes only exists for $a/M \lesssim 1.12$.

These unstable modes are related to the existence of *stable* "polar" null circular orbits, *i.e.* circular non-equatorial orbits with vanishing azimuthal component of the orbital angular momentum ($L_z = 0$) [364]. Eq. (11.31) of Appendix 11.7 (see also Fig. 11.9) shows that for the Kerr spacetime such orbits exist when $1 < a/M < \left(-3 + 2\sqrt{3}\right) \approx 1.17996$. For $l = 4$ and $\mathcal{R} = 1$ the instability range for modes with $m = 0$ is $1 < a/M \lesssim 1.14$. However the upper limit of this range is a slowly increasing function of l, and it is plausible that in the eikonal limit it should tend to $\left(-3 + 2\sqrt{3}\right) \sim 1.18$.

In conclusion, let us discuss the case $r_0/M < 0$ (with $\mathcal{R} = 1$), summarized in Fig. 11.4. Now the ring singularity at $r/M = 0$ is naked, and the spacetime also possesses closed timelike curves [365]. Therefore it is not surprising that an infinite number of unstable modes exist also at the linear level [339]. At variance with the ergoregion instability, in the present case the imaginary part of the frequency (and therefore the "strength" of the instability) grows roughly quadratically with a/M (cf. the right panel of Fig. 11.4). The same kind of instability has been found in charged, spherically symmetric BHs with naked singularities [338] and therefore

[a] It has been proposed that supermassive BHs may accrete small lumps of material with essentially random orientations of the orbital angular momentum. This "chaotic accretion" results (on average) in a spin-down of the BH [354], so it is very hard to produce fast spinning BHs at all (whereas spin estimates as large as $a = 0.989^{+0.009}_{-0.002}$ have been reported [355]). Therefore it should be even harder to produce superspinars by chaotic accretion. Binary BH mergers are also known to always produce spins below the Kerr limit [356, 238, 357, 358, 359, 360], so one would be left only with the possibility of postulating that supermassive superspinars are born in the early Universe due to high-energy physics effects beyond the realm of classical general relativity.

it is not related to rotation, but to causality violation (see also the discussion at the end of Ref. [342]). As a matter of fact, we could not find any mode belonging to this family when $r_0/M \geq 0$, *i.e.* when the naked singularity is covered.

In summary: superspinars are plagued by several instabilities for both perfectly reflecting boundary conditions ($\mathcal{R} = 1$ at $r = r_0$) and perfectly absorbing boundary conditions ($\mathcal{R} = 0$ at $r = r_0$). The instability of modes with $l = m$ is related to superradiant scattering. When $r_0 \sim M$, unstable modes with $m = 0$ also exist below some critical rotation parameter: this instability is related to the existence of stable polar null circular orbits in the spacetime (cf. Appendix 11.7). Finally, when $r_0/M < 0$, a third family of $m = 0$ modes exists [339]. This third family of unstable modes is probably related to the existence of naked singularity and closed timelike curves in the spacetime.

11.6 Conclusions

The results reported in this chapter indicate that superspinars are unstable independently of the boundary conditions imposed at the "excision radius" r_0 and in a significant region of the two-dimensional parameter space (a/M, r_0/M), if not in the whole parameter space. The most effective instability at low rotation rates corresponds to the $l = m = 2$ (superradiant) mode, but when $a \sim M$ and $r_0 \sim M$ unstable modes with $m = 0$ also exist. The $l = m = 2$ mode eventually becomes stable at large rotation rates, but unstable modes with $l = m \gg 1$ are expected to exist for any value of a/M, at least for $\mathcal{R} = 1$. While the instability timescale of higher-l modes may turn out to be very long, making them marginally stable for practical purposes, the low-l instability (which affects superspinars with $a/M \lesssim 2$) takes place on a dynamical timescale. Accretion is known to spin superspinars down [342], so our results indicate that superspinars are unlikely astrophysical alternatives to Kerr BHs.

One possible objection is that, in order to assume ingoing boundary conditions at the surface of the superspinar, we must assume that general relativity is modified in that region. Such a modification of general relativity in the excised, high-curvature region surrounding the singularity is implicit in the original superspinar proposal by Gimon and Horava [29], who invoke string theory in order to violate the Kerr bound $a \leq M$. We stress, however, that our results hold for a wide class of theories of gravity. Many proposed alternative theories of gravity admit the Kerr spacetime as an exact solution [366, 367]. Among these theories, we focus on the large class consisting of Brans-Dicke gravity (with or without a potential), and theories that can be reduced to Brans-Dicke theory with a potential via a conformal transformation (*e.g.* $f(R)$ gravity, both in the metric and Palatini formalism [368, 369]). All of these theories admit Kerr-(anti) de Sitter as an exact solution if the scalar field is constant. When perturbed, these solutions satisfy different equations in general relativity and in modified gravity theories [367, 214], due to the presence of an extra scalar degree of freedom (the Brans-Dicke scalar), so one might naively expect the stability properties of the Kerr spacetime to be different. However, one can redefine the tensor modes via a conformal transformation so that the *vacuum* tensor and scalar perturbation equations decouple at linear order [214]. Basically this happens because the Brans-Dicke action reduces to the Einstein-Hilbert action plus a minimally coupled scalar field in the Einstein frame, if no matter fields are present [369]. Therefore, the tensor modes satisfy the same equations in general relativity as in Brans-Dicke theory (or in any other theory that can be recast in Brans-Dicke form via

a conformal transformation.) This means that Eqs. (11.2) and (11.3), which are the starting points of our analysis, retain their validity, and therefore that the instability operates in a wider class of gravity theories.

Our results do not imply that there cannot be stable ultracompact objects with $J/M^2 > 1$. However, they do imply that either (i) Einstein's gravity should be modified in such a way as to retain Kerr as a solution, while at the same time allowing the tensor modes and the "extra" modes to couple at linear order, or (ii) the structure of astrophysical superspinning objects, if they exist at all, is not described by the simple Kerr-based superspinar proposal of Ref. [29].

11.7 Appendix: Geodesics in D-dimensional Kerr spacetimes

The main goal of this appendix is to study the existence of stable null circular orbits (SNCOs) with negative energies in Kerr spacetimes. We are interested in these orbits because the very existence of SNCOs (or more generally, the existence of stable null bound orbits) with *negative* energies is enough to show that a spacetime is subject to the ergoregion instability, *provided that* purely reflecting boundary conditions are imposed at the excision surface $r = r_0$. For completeness we consider D-dimensional Kerr spacetimes with only one nonzero angular momentum parameter, and we specialize to the "ordinary" $D = 4$ case at the end. Our main results for four-dimensional Kerr spacetimes are summarized in Fig. 11.9. The meaning of the different curves on this plot is explained below.

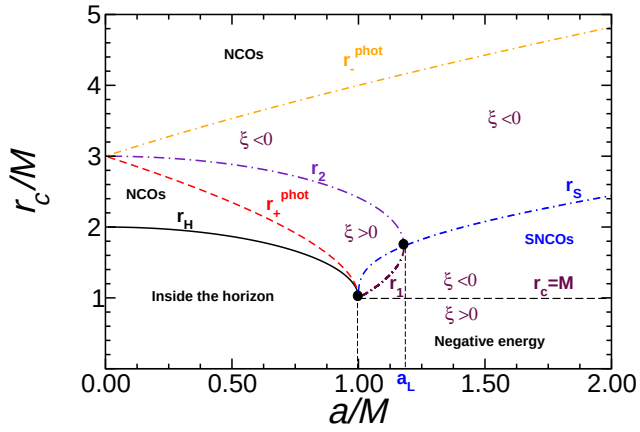

Figure 11.9: The sign of $\xi = L_z/E$ as a function of a/M and the radius r_c/M of null circular orbits. When $a > M$, $\xi \to \infty$ at $r_c = M$. Stable circular null orbits exist when $a > M$ for $r_c < r_S$, and have negative energy when $r_c < M$. Regions marked with NCOs are those where no circular orbits exist. Orbits of constant radius r_1 are *stable* "polar" null circular orbits.

The metric of a D-dimensional Kerr BH with only one nonzero angular momentum parameter is given in Boyer-Lindquist-type coordinates by [370]

$$\begin{aligned} ds^2 &= -\frac{\Delta_D - a^2\sin^2\vartheta}{\Sigma}dt^2 - \frac{2a(r^2+a^2-\Delta_D)\sin^2\vartheta}{\Sigma}dtd\varphi + \\ &+ \frac{(r^2+a^2)^2 - \Delta_D a^2\sin^2\vartheta}{\Sigma}\sin^2\vartheta d\varphi^2 + \frac{\Sigma}{\Delta_D}dr^2 + \Sigma d\vartheta^2 + r^2\cos^2\vartheta d\Omega^2_{D-4}, \end{aligned} \tag{11.15}$$

where $\Sigma = r^2 + a^2\cos^2\vartheta$, $\Delta_D = r^2 + a^2 - M_D r^{5-D}$, $d\Omega^2_{D-4}$ denotes the metric of the unit $(D-4)$-sphere and M_D and a are related to the physical mass M and angular momentum J of the spacetime

$$M_D = \frac{16\pi M}{D-2}A_D\,, \qquad a = \frac{D-2}{2}\frac{J}{M}\,, \tag{11.16}$$

with $A_D = (2\pi)^{(1-D)/2}\Gamma[(D-1)/2]$. The outer horizon is defined as the largest real root of $r_H^2 + a^2 - M_D r_H^{5-D} = 0$.

11.7.1 Equatorial Null Geodesics

For null geodesics in the equatorial plane ($\theta = \pi/2$) of the spacetime (11.15), the radial geodesic equation reads

$$E^{-2}\dot{r}^2 = V_{\rm eff} = R(r)/r^4 = 1 + \frac{M_D}{r^{D-1}}(\xi - a)^2 - \frac{\xi^2 - a^2}{r^2}\,, \tag{11.17}$$

where $\xi = L_z/E$ and where the dot denotes derivatives with respect to the dimensionless affine parameter. Conditions for circular orbits are $V_{\rm eff}(r_c) = V'_{\rm eff}(r_c) = 0$. The condition $V_{\rm eff}(r_c) = 0$ implies

$$\xi = \frac{-aM_D \pm \sqrt{r_c^{2(D-3)}\Delta_D(r_c)}}{r_c^{D-3} - M_D} \tag{11.18}$$

for direct and retrograde orbits, respectively. For $D = 4$ the outer horizon is located at $r = r_H = M + \sqrt{M^2 - a^2}$ and (of course) the Kerr bound implies $a/M \leq 1$. The condition $V'_{\rm eff}(r_c) = 0$ then leads to three different solutions:

$$\begin{aligned} r_\pm^{\rm phot} &= 2M\left\{1 + \cos\left[\frac{2}{3}\cos^{-1}\left(\mp\frac{a}{M}\right)\right]\right\}\,, \\ r_{c-} &= 2M - {\rm Re}[\beta] - \sqrt{3}{\rm Im}[\beta]\,, \end{aligned} \tag{11.19}$$

where

$$\beta = \left[M\left(-M^2 + 2a^2 + 2a\sqrt{a^2 - M^2}\right)\right]^{1/3}\,. \tag{11.20}$$

The three solutions are all real. Orbits with $r_c = r_+^{\rm phot}$ ($r_c = r_-^{\rm phot}$) correspond to unstable direct (retrograde) circular orbits lying outside the horizon, whereas $r_{c-} < r_H$ and therefore this solution does not correspond to physical circular orbits. For $a > M$ there is only one real solution

$$r_-^{\rm phot} = 2M\left\{1 + \cosh\left[\frac{2}{3}\cosh^{-1}\left(\frac{a}{M}\right)\right]\right\}\,, \tag{11.21}$$

corresponding to an unstable null circular orbit. This is shown in Fig. 11.9. It is easy to show that the same qualitative results hold also when $D \geq 5$. Therefore no stable null equatorial circular orbits exist in D-dimensional Kerr spacetimes with a single angular momentum parameter.

11.7.2 Non-equatorial null geodesics

Let us now focus on non-equatorial null geodesics in D-dimensional Kerr spacetimes with a single spin parameter. We shall follow and generalize the approach discussed in Chandrasekhar's book [249].

The separability of the Hamilton-Jacobi equation in Kerr spacetime was proved by Carter, who also discovered an additional constant of motion Q (the "Carter constant") besides the energy, the angular momentum and the norm of the four-velocity [365, 371]. The same procedure can be easily generalized to D-dimensional Kerr spacetimes with a single spin parameter, given by Eq. (11.15). Our basic equations are

$$
\begin{aligned}
&E^{-2}\Sigma^2\dot{r}^2 = R(r) = r^4 + (a^2-\xi^2-\eta)r^2 + M_D[\eta+(\xi-a)^2]r^{5-D} - a^2\eta\,,\\
&E^{-2}\Sigma^2\dot{\theta}^2 = \Theta(\theta) = \eta + a^2\cos^2\theta - \xi^2\cot^2\theta\,,\\
&E^{-1}\Delta_D\Sigma\,\dot{\varphi} = \Phi(r,\theta) = \xi\Delta_D\csc^2\theta - a[a\xi+\Delta_D-(r^2+a^2)]\,,\\
&E^{-1}\Delta_D\Sigma\,\dot{t} = T(r,\theta) = (r^2+a^2)^2 - a^2\Delta_D\sin^2\theta + a\xi[\Delta_D-(r^2+a^2)]\,,
\end{aligned}
$$

where we use a dot to denote derivatives with respect to the dimensionless affine parameter, and where $\xi = L_z/E$, $\eta = Q/E$ are two constants of motion. Notice that the angular equation (11.22) does not depend on D, and that the equations above reduce to Eqs. (190) and (191) of Ref. [249] when $D = 4$.

11.7.2.a Proof of no planar bounded orbits in D dimensional Kerr spacetimes

A relevant question is whether non-equatorial planar orbits exist in these spacetimes. The conditions for a planar orbit ($\theta = \theta_0$ =constant) are $\Theta(\theta_0) = 0 = \Theta'(\theta_0)$. From Eq. (11.22) we see that these conditions are fulfilled on the equatorial plane ($\theta_0 = \pi/2$) only if $\eta = 0$. For $\theta_0 \neq \pi/2$ planar orbits exist if

$$
\eta = -a^2\cos^4\theta_0\,, \qquad \xi = \pm a\sin^2\theta_0\,. \tag{11.22}
$$

For the "plus" branch of the solutions above, the radial equation (11.22) simply becomes $\dot{r} = \pm E$. These geodesics are unbound and describe shear-free null-congruences [249]. The "minus" branch of the solutions describes non-equatorial planar orbits. These solutions only exist when $D = 4$ and $a < M$. Moreover they always lie inside the event horizon, and therefore they do not correspond to physical orbits. For these reasons we do not discuss them further.

11.7.3 Non-equatorial, circular orbits

Since no planar, non-equatorial circular orbits exist in $D-$dimensional Kerr spacetimes, let us focus on non-equatorial, circular orbits, *i.e.* orbits with constant radius but which are not planar (*i.e.* θ is not constant). These orbits are periodic [372, 373, 374] and they are often called "spherical orbits" in the literature, but here we adopt the term "circular orbits" as in Refs. [372, 373, 374].

The conditions for null circular orbits, $R(r_c) = 0$ and $R'(r_c) = 0$, read

$$
r_c^4 + (a^2-\xi^2-\eta)r_c^2 + M_D[\eta+(\xi-a)^2]r_c^{5-D} - a^2\eta = 0\,, \tag{11.23}
$$

$$
4r_c^3 + 2(a^2-\xi^2-\eta)r_c + (5-D)M_D[\eta+(\xi-a)^2]r_c^{4-D} = 0\,, \tag{11.24}
$$

which can be solved for ξ and η as functions of r_c. There are two sets of solutions:

$$\xi = \frac{r_c^2+a^2}{a}\,, \qquad \eta = -\frac{r_c^4}{a^2}\,, \tag{11.25}$$

and

$$\begin{aligned}\xi &= \frac{a^2(D-5)M_D r_c^3 + (D-1)M_D r_c^5 - 2r_c^D(a^2+r_c^2)}{a(D-5)M_D r_c^3 + 2a r_c^D}\,,\\ \eta &= \left[a(D-5)M_D r_c^3 + 2a r_c^D\right]^{-2}\Big\{4M_D r_c^{5+D}(2a^2(D-3)+(D-1)r_c^2) + \\ &- (D-1)^2 M_D^2 r_c^{10} - 4r_c^{2(D+2)}\Big\}\,.\end{aligned} \tag{11.26}$$

The first set of solutions implies $\theta =$ constant and indeed reduces to the "minus" branch of solutions (11.22), which do not correspond to physical orbits.

The second set of solutions, Eqs. (11.26), can describe bound orbits. The condition of stability is simply $R''(r_c) < 0$. By differentiating Eq. (11.22) twice and using Eqs. (11.26) we obtain the following expression for $R''(r_c)$:

$$\begin{aligned}R''(r_c) &= \left[(D-5)M_D r_c^3 + 2r_c^D\right]^{-2}\Big\{-8(D-5)(D-1)M_D^2 r_c^8 + 32 r_c^{2(D+1)} + \\ &+ 16(D-5)M_D r_c^{D+3}\left[a^2(D-3)+(D-1)r_c^2\right]\Big\}\,.\end{aligned}$$

The stability of null circular orbits depends on the sign of the expression above. It is possible to show that stable circular orbits exist for $D=4$ and $a>M$, but not for $D\geq 5$. Therefore in the following we will specialize to $D=4$ spacetime dimensions.

11.7.3.a $D=4$ Kerr spacetime.

When $D=4$, Eqs. (11.26) read

$$\xi = \frac{r_c^2(3M-r_c)-a^2(r_c+M)}{a(r_c-M)}\,, \tag{11.27}$$

$$\eta = \frac{r_c^3\left[4a^2M - r_c(r_c-3M)^2\right]}{a^2(r_c-M)^2}\,. \tag{11.28}$$

These equations correspond to Eqs. (224) and (225) of Ref. [249], and they can be used to define the shadow cast by Kerr BHs or superspinars [341, 340]. When $\eta=0$, from Eq. (11.28) we have $4a^2M - r_c(r_c-3M)^2 = 0$, which defines the equatorial orbits (11.19)-(11.21). In general, however, the constant of motion η can be positive or negative. When $\eta<0$, Eqs. (11.27)-(11.28), together with Eq. (11.22) for the θ-motion, implies that orbits of constant radius are not allowed [249]. When $\eta\geq 0$ circular orbits are allowed, and according to Eq. (11.28) they must satisfy the condition $4a^2M - r_c(r_c-3M)^2 \geq 0$. For $a<M$ this condition reads

$$r_+^{\rm phot} < r_c < r_-^{\rm phot}\,,$$

where $r_-^{\rm phot}$ and $r_+^{\rm phot}$ refer to retrograde and direct unstable photon orbits in the equatorial plane [Eq. (11.19)]. More importantly for the analysis of superspinars, when $a>M$ the condition $\eta>0$ reads

$$r_c < r_-^{\rm phot}\,, \tag{11.29}$$

where $r_-^{\rm phot}$ is given by Eq. (11.21). Notice that the condition above includes also the singular case $r_c = M$ (in fact $\xi, \eta \to \infty$ when $a > M$ and $r_c \to M$).

When $D = 4$, from Eq. (11.27) we see that stable circular orbits exist whenever the orbital radius r_c satisfies the relation $r_c < r_S$, with [340]

$$\frac{r_S}{M} = \begin{cases} 1 + \left[\left(\frac{a}{M}\right)^2 - 1\right]^{1/3} & \text{for } a > M\,, \\ 1 - \left[-\left(\frac{a}{M}\right)^2 + 1\right]^{1/3} & \text{for } a < M\,. \end{cases} \tag{11.30}$$

Null circular orbits with radii smaller than this critical radius are *stable*. When $a > M$, $r_S < r_-^{\rm phot}$, *i.e.* stable circular orbits are allowed. When $a < M$ the critical radius r_S is covered by the horizon, and it becomes "visible" to external observers only when $a > M$. Therefore *stable null circular orbits may exist only for* $a > M$, while orbits with $r < r_S$ around BHs with $a < M$ do not have a physical meaning because they lie inside the horizon.

By substituting Eq. (11.30) into Eqs. (11.27) and (11.28) we can compute the corresponding critical parameters $\eta(r_S) = \eta_S$ and $\xi(r_S) = \xi_S$:

$$\begin{aligned} \frac{\eta_S}{M^2} &= \frac{3M^2}{a^2}\left(1 + \left[\left(\frac{a}{M}\right)^2 - 1\right]^{1/3}\right)^4\,, \\ \frac{\xi_S}{M} &= -\frac{a}{M} + \frac{3M}{a}\left(1 - \left[\left(\frac{a}{M}\right)^2 - 1\right]^{2/3}\right)\,. \end{aligned}$$

For a given value of a/M, when $\eta = \eta_S$ and $\xi = \xi_S$ we have a marginally stable orbit. If instead $\xi \lesssim \xi_S$ we have a stable orbit, while $\eta \lesssim \eta_S$ gives a stable orbit if $a > 3M$ and $\eta \gtrsim \eta_S$ gives a stable orbit if $a < 3M$. However, these are only sufficient conditions, because other stable orbits may exist, far from the critical values η_S and ξ_S. In fact, depending on the value of the spin we can have different situations: (i) for $a < 3M$, if $\eta < \eta_S(a)$ there is only one stable circular orbit (with $r_c < M$), while for $\eta > \eta_S(a)$ we have two stable orbits: one with $r_c < M$ and one with $r_c > M$; (ii) for $a > 3M$, when $\eta < 27M^2$ we have only one stable circular orbit (with $r_c < M$); when $27M^2 < \eta < \eta_S(a)$ we have two stable orbits with $r_c > M$ and one with $r_c < M$; when $\eta > \eta_S(a)$ we have one stable circular orbit with $r_c < M$ and one with $r_c > M$. This can be understood by plotting η as a function of r, with $0 < r < r_S(a)$, for various values of a.

Also, let us consider the sign of the impact parameter $\xi = L_z/E$. A study of Eq. (11.27) shows that there is a critical spin

$$a_L = \sqrt{3\left(-3 + 2\sqrt{3}\right)}M \approx 1.17996M\,, \tag{11.31}$$

such that:

- if $a > a_L$, then $\xi > 0$ for $r_c < M$ and $\xi < 0$ for $r_c > M$. Notice that ξ diverges if $r_c = M$.
- if $M < a < a_L$, then $\xi > 0$ for $r_c < M$ and for $r_1(a) < r_c < r_2(a)$ (with $r_1, r_2 > M$), whereas $\xi < 0$ elsewhere. Notice that ξ diverges if $r_c = M$.

- if $a \leq M$ then $\xi > 0$ for $r_+ < r_c < r_2(a)$, where r_+ is the outer Kerr horizon and $r_2 < 3M$. $\xi < 0$ for $r_c > r_2(a)$.

The situation for a four-dimensional Kerr spacetime is summarized in Fig. 11.9. Orbits of radius r_1 and r_2 carry vanishing angular momentum ($L_z = 0$) and therefore are called "polar" null orbits. Orbits of constant radius r_2 are unstable polar null orbits, while orbits of constant radius r_1 are *stable* polar null orbits, and they exist for $M < a < a_L$.

A relevant question to ask is whether the null circular orbits that we have identified have positive or negative energy. The sign of the energy is determined by imposing that the geodesics be future oriented, *i.e.* that the derivative $\dot{t}$ of the coordinate time with respect to the affine parameter [given by Eq. (11.22)] be positive. (This is because the hypersurfaces $t = \text{const}$ are spacelike for any $r > 0$ if $a > M$, and for any $r > r_H$ if $a \leq M$.) By substituting Eq. (11.27) into Eq. (11.22), we find that for the non-equatorial null circular orbits that we have identified we have

$$\dot{t} = \frac{E}{\Sigma}\left[\frac{r_c^2(r_c+3M)}{r_c - M} + a^2\cos^2\theta\right] . \tag{11.32}$$

Because these orbits cross the equatorial plane (as they have $\eta > 0$), we can evaluate Eq. (11.32) for $\theta = \pi/2$. The energy E is a constant of motion, so it cannot change sign along the trajectory. Then it is clear that all orbits have $E > 0$, with the exception of orbits with $r_c/M < 1$, which, as we have seen, exist only for $a/M > 1$. Indeed, it possible to show explicitly that orbits with $r_c/M < 1$ in Kerr spacetimes with $a/M > 1$ have negative energy at all times. Using Eq. (11.22), one obtains that such orbits have polar angle θ oscillating between $\pi/2 + \theta_c$ and $\pi/2 - \theta_c$, with

$$\cos^2\theta_c = \frac{2r_c\sqrt{M\Delta\left(a^2M + r_c^2(2r_c - 3M)\right)} - \rho}{a^2(r_c - M)^2} , \tag{11.33}$$

where $\rho = r_c^4 - 3M^2r_c^2 + 2a^2Mr_c$. One can show that $\cos^2\theta_c < 1$ for $a/M > 1$ and $r_c/M < 1$. Using this expression in Eq. (11.32) it is then possible to show that the energy must be negative all along trajectories with $a/M > 1$ and $r_c/M < 1$. The region where stable negative-energy orbits exist is shown in Fig. 11.9.

Finally, let us suppose we have a compact object rotating with $a > M$. According to the cosmic censorship conjecture, the singularity at $r/M = 0$ must be excised by some horizon-like one-way membrane or by a reflecting surface. It is then natural to ask the question of what the compactness of the object can be if one wants to excise all SNCOs with negative energies. Because such orbits exist for any $r_c < M$, if $a > M$, the maximum allowed compactness turns out to be $\mu_{\max} = M/r = 1$. Because orbits with $r_c \lesssim M$ lie far away from the singularity at $r/M = 0$, this maximum compactness is not expected to be altered by high-energy corrections.

Conclusion and perspectives

In this dissertation we have explored several aspects of black hole physics, both from a theoretical and from an astrophysical point of view. Although black holes have many faces, some approaches of investigation turn out to be useful in fairly different areas of black hole physics. In particular, the study of black hole perturbations can provide insights on several topics including gauge/gravity duality, astrophysical imprints of strong curvature corrections to GR and possible methods to discriminate between astrophysical black holes and other ultra-compact objects.

A renewed interest in black hole physics comes from their deep connection to quantum gravity. In Part I and Part II we discussed some theoretical and astrophysical aspects of this connection. In Chapters 2 and 3 we studied AdS dilatonic black holes within the gauge/gravity duality. Below a critical temperature, due to string-inspired interactions, the AdS-RN black hole is unstable against scalar perturbations and it undergoes a phase transition toward a new charged dilatonic black hole. From the dual perspective, a neutral scalar operator acquires a non-vanishing expectation value and it drastically affects the transport properties of the boundary theory. In particular, in the new phase we computed the electrical conductivity, which reassembles several properties of electron motion in real materials. The conductivity shows a Drude peak at small frequency and the resistivity has a non-monotonic behavior as a function of the temperature, which is reminiscent of the Kondo effect. We discussed these effects in presence of a magnetic field, both at finite and at vanishing temperature. When the magnetic field equals the charge density, $B = B_c = \rho$, the phase transition is suppressed. The same effect, *i.e.* the expulsion of the condensate by a sufficiently large magnetic field, also exists in holographic models of superconductors. Interestingly, the response of the dual theory to the magnetic field is largely independent from the scalar condensate. In fact, we found the same Hall effect and cyclotron resonances observed in holographic dual to dyonic AdS-RN black branes. Moreover, the magnetic field prevents both the appearance of a Drude peak and the non-monotonic behavior of the resistivity. At zero temperature, the dual theory is reminiscent of a charged strongly coupled plasma. Remarkably, it appears that the model at hand interpolates between a metallic and a charged plasma behavior, depending on the temperature and on the magnetic field. We left this intriguing topic for future investigations.

Furthermore, in Part I we developed a method to compute the long-lived characteristic frequencies of Schwarzschild-AdS black holes, which presumably dominate the thermalization of the dual field theory (Chapter 4). Our numerical method confirms and extends results previously obtained in literature. Finally, in an attempt to gain some analytical insights on black holes with non-trivial scalar hairs, we studied exact vortex black holes in three dimensional AdS gravity (Chapter 5).

The recent Anti de Sitter/Condensed Matter duality is a paradigm within which strongly

coupled field theories can be explored. Further developments are currently pursed vigorously in several directions, including: quark-gluon plasma, holographic superconductors, phase transitions at strong coupling, quantum Hall effects, non-Fermi liquids and strange metals. Within this approach black holes, matter fields and their perturbations play a key role in the understanding of several strong-coupling effects in real condensed matter systems.

Part II was devoted to the investigation of string-inspired aspects of black hole physics, but from an astrophysical point of view. We discussed the gravitational imprint of astrophysical black holes in low-energy effective theories arising from String Theory. We throughly investigated the linear response of Schwarzschild black holes in DCS gravity (Chapter 7) and of slowly-rotating dilatonic black holes in EDGB gravity (Chapter 8). We discussed their stability, and possible astrophysical signatures of string corrections, whose imprint can be detected by future gravitational-wave interferometers. We further confirm that gravitational-wave astronomy can provide evidences for quantum gravity corrections to GR and it could allow for tests of the no-hair theorems. Regardless the specific alternative theory to GR, the general outcome of Part II is that the gravitational spectrum of static and slowly rotating hairy black holes carries a specific signature of strong curvature corrections. Moreover, several astrophysical objects are presumably highly rotating black holes, whose strong-curvature effects near the horizon are expected to be even more effective. Therefore near-extremal black holes in string-inspired theories beyond GR are very promising candidates for astrophysical evidences of String Theory, whose investigation is undoubtedly worth pursuing.

Finally, in Part III we explored some more astrophysical applications of black hole perturbation theory. We discussed the perturbation spectrum, the gravitational-wave emission and the viability of some black hole mimickers. These objects challenge the widely accepted black hole paradigm and some of them are still viable astrophysical alternatives to black holes. In Chapter 10, we discussed the stability issue for static thin-shell gravastars, identifying the parameter space where they are stable. On the other hand, in Chapter 11 we found that superspinars suffer from several strong instabilities and they cannot be viable alternative to astrophysical black holes. This gives a further confirmation of the Cosmic Censorship. Finally, adopting an open-minded approach, we investigated thin-shell gravastars in their stability region, showing that they leave a characteristic signature in realistic astrophysical processes. Similar arguments can be presumably applied to other black hole mimickers, such as boson stars and wormholes, or to some more realistic gravastar models, such as rotating gravastars. These and other developments – including further investigations on the ergoregion instability for rotating black hole mimickers – are left for future works.

Bibliography

[1] J. M. Maldacena, "The large N limit of superconformal field theories and supergravity," *Adv. Theor. Math. Phys.*, vol. 2, pp. 231–252, 1998.

[2] G. T. Horowitz and J. Polchinski, "Gauge / gravity duality," 2006.

[3] S. A. Hartnoll, "Lectures on holographic methods for condensed matter physics," *Class. Quant. Grav.*, vol. 26, p. 224002, 2009.

[4] T. Regge and J. A. Wheeler, "Stability of a Schwarzschild singularity," *Phys. Rev.*, vol. 108, pp. 1063–1069, 1957.

[5] F. J. Zerilli, "Gravitational field of a particle falling in a schwarzschild geometry analyzed in tensor harmonics," *Phys. Rev.*, vol. D2, pp. 2141–2160, 1970.

[6] C. V. Vishveshwara, "Stability of the schwarzschild metric," *Phys. Rev.*, vol. D1, pp. 2870–2879, 1970.

[7] H.-P. Nollert, "Quasinormal modes: the characteristic 'sound' of black holes and neutron stars," *Class. Quant. Grav.*, vol. 16, pp. R159–R216, 1999.

[8] K. D. Kokkotas and B. G. Schmidt, "Quasi-normal modes of stars and black holes," *Living Rev. Rel.*, vol. 2, p. 2, 1999.

[9] E. Berti, V. Cardoso, and A. O. Starinets, "Quasinormal modes of black holes and black branes," *Class. Quant. Grav.*, vol. 26, p. 163001, 2009.

[10] F. Pretorius, "Evolution of Binary Black Hole Spacetimes," *Phys. Rev. Lett.*, vol. 95, p. 121101, 2005.

[11] M. Campanelli, C. O. Lousto, P. Marronetti, and Y. Zlochower, "Accurate Evolutions of Orbiting Black-Hole Binaries Without Excision," *Phys. Rev. Lett.*, vol. 96, p. 111101, 2006.

[12] F. Echeverria, "Gravitational wave measurements of the mass and aangular momentum of a black hole," *Phys. Rev.*, vol. D40, pp. 3194–3203, 1989.

[13] J. D. Bekenstein, "Transcendence of the law of baryon-number conservation in black hole physics," *Phys. Rev. Lett.*, vol. 28, pp. 452–455, 1972.

[14] E. Berti, V. Cardoso, and C. M. Will, "On gravitational-wave spectroscopy of massive black holes with the space interferometer LISA," *Phys. Rev.*, vol. D73, p. 064030, 2006.

[15] P. K. Kovtun and A. O. Starinets, "Quasinormal modes and holography," *Phys. Rev.*, vol. D72, p. 086009, 2005.

[16] D. T. Son and A. O. Starinets, "Viscosity, Black Holes, and Quantum Field Theory," *Ann. Rev. Nucl. Part. Sci.*, vol. 57, pp. 95–118, 2007.

[17] S. K. Blau, "A string-theory calculation of viscosity could have surprising applications," *Physics Today*, vol. 58, no. 5, pp. 23–24, 2005.

[18] C. P. Herzog, "Lectures on Holographic Superfluidity and Superconductivity," *J. Phys.*, vol. A42, p. 343001, 2009.

[19] S. A. Hartnoll, C. P. Herzog, and G. T. Horowitz, "Building a Holographic Superconductor," *Phys. Rev. Lett.*, vol. 101, p. 031601, 2008.

[20] F. Benini, C. P. Herzog, R. Rahman, and A. Yarom, "Gauge gravity duality for d-wave superconductors: prospects and challenges," 2010.

[21] D. T. Son, "Toward an AdS/cold atoms correspondence: a geometric realization of the Schroedinger symmetry," *Phys. Rev.*, vol. D78, p. 046003, 2008.

[22] S. A. Hartnoll, J. Polchinski, E. Silverstein, and D. Tong, "Towards strange metallic holography," 2009.

[23] C. M. Will, "The confrontation between general relativity and experiment," *Living Rev. Rel.*, vol. 9, p. 3, 2005.

[24] A. Abramovici *et al.*, "LIGO: The Laser interferometer gravitational wave observatory," *Science*, vol. 256, pp. 325–333, 1992.

[25] C. B. M. H. Chirenti and L. Rezzolla, "How to tell a gravastar from a black hole," *Class. Quant. Grav.*, vol. 24, pp. 4191–4206, 2007.

[26] S. Alexander and N. Yunes, "Chern-Simons Modified General Relativity," *Phys. Rept.*, vol. 480, pp. 1–55, 2009.

[27] B. Zwiebach, "Curvature Squared Terms and String Theories," *Phys. Lett.*, vol. B156, p. 315, 1985.

[28] M. Visser and D. L. Wiltshire, "Stable gravastars - an alternative to black holes?," *Class. Quant. Grav.*, vol. 21, pp. 1135–1152, 2004.

[29] E. G. Gimon and P. Horava, "Astrophysical Violations of the Kerr Bound as a Possible Signature of String Theory," *Phys. Lett.*, vol. B672, p. 299, 2009.

[30] P. Amaro-Seoane *et al.*, "Astrophysics, detection and science applications of intermediate- and extreme mass-ratio inspirals," *Class. Quant. Grav.*, vol. 24, pp. R113–R169, 2007.

[31] G. 't Hooft, "Dimensional reduction in quantum gravity," 1993.

[32] L. Susskind, "The World as a hologram," *J. Math. Phys.*, vol. 36, pp. 6377–6396, 1995.

[33] J. M. Bardeen, B. Carter, and S. W. Hawking, "The Four laws of black hole mechanics," *Commun. Math. Phys.*, vol. 31, pp. 161–170, 1973.

[34] O. Aharony, S. S. Gubser, J. M. Maldacena, H. Ooguri, and Y. Oz, "Large N field theories, string theory and gravity," *Phys. Rept.*, vol. 323, pp. 183–386, 2000.

[35] J. Polchinski, *String theory. Vol. 2: Superstring theory and beyond.* Cambridge, UK: Univ. Pr. (1998) 531 p.

[36] E. Witten, "Anti-de Sitter space, thermal phase transition, and confinement in gauge theories," *Adv. Theor. Math. Phys.*, vol. 2, pp. 505–532, 1998.

[37] G. t Hooft, "A planar diagram theory for strong interactions," *Nuclear Physics B*, vol. 72, no. 3, pp. 461 – 473, 1974.

[38] S. S. Gubser, I. R. Klebanov, and A. M. Polyakov, "Gauge theory correlators from non-critical string theory," *Phys. Lett.*, vol. B428, pp. 105–114, 1998.

[39] S. A. Hartnoll, "Quantum Critical Dynamics from Black Holes," 2009.

[40] S. W. Hawking and D. N. Page, "Thermodynamics of Black Holes in anti-De Sitter Space," *Commun. Math. Phys.*, vol. 87, p. 577, 1983.

[41] D. T. Son and A. O. Starinets, "Minkowski-space correlators in AdS/CFT correspondence: Recipe and applications," *JHEP*, vol. 09, p. 042, 2002.

[42] G. T. Horowitz, "Introduction to Holographic Superconductors," 2010.

[43] T. Faulkner, H. Liu, J. McGreevy, and D. Vegh, "Emergent quantum criticality, Fermi surfaces, and AdS2," 2009.

[44] K. S. Thorne, (Ed.), R. H. Price, (Ed.), and D. A. Macdonald, (Ed.), "Black holes: the membrane paradigm," New Haven, USA: Yale Univ. Press (1986) 367p.

[45] P. Kovtun, D. T. Son, and A. O. Starinets, "Viscosity in strongly interacting quantum field theories from black hole physics," *Phys. Rev. Lett.*, vol. 94, p. 111601, 2005.

[46] S. S. Gubser, "Breaking an Abelian gauge symmetry near a black hole horizon," *Phys. Rev.*, vol. D78, p. 065034, 2008.

[47] S. A. Hartnoll, C. P. Herzog, and G. T. Horowitz, "Holographic Superconductors," *JHEP*, vol. 12, p. 015, 2008.

[48] D. Mateos, "String Theory and Quantum Chromodynamics," *Class. Quant. Grav.*, vol. 24, pp. S713–S740, 2007.

[49] S. Sachdev and M. Mueller, "Quantum criticality and black holes," 2008.

[50] J. McGreevy, "Holographic duality with a view toward many-body physics," 2009.

[51] W. Israel, "Event horizons in static vacuum space-times," *Phys. Rev.*, vol. 164, pp. 1776–1779, 1967.

[52] S. S. Gubser and S. S. Pufu, "The gravity dual of a p-wave superconductor," *JHEP*, vol. 11, p. 033, 2008.

[53] G. W. Gibbons and K.-i. Maeda, "Black Holes and Membranes in Higher Dimensional Theories with Dilaton Fields," *Nucl. Phys.*, vol. B298, p. 741, 1988.

[54] D. Garfinkle, G. T. Horowitz, and A. Strominger, "Charged black holes in string theory," *Phys. Rev.*, vol. D43, pp. 3140–3143, 1991.

[55] S. Monni and M. Cadoni, "Dilatonic black holes in a S-duality model," *Nucl. Phys.*, vol. B466, pp. 101–111, 1996.

[56] M. J. Duff and J. T. Liu, "Anti-de Sitter black holes in gauged N = 8 supergravity," *Nucl. Phys.*, vol. B554, pp. 237–253, 1999.

[57] S. S. Gubser and F. D. Rocha, "Peculiar properties of a charged dilatonic black hole in AdS5," *Phys. Rev.*, vol. D81, p. 046001, 2010.

[58] S. S. Gubser, "Phase transitions near black hole horizons," *Class. Quant. Grav.*, vol. 22, pp. 5121–5144, 2005.

[59] S. S. Gubser and I. Mitra, "Instability of charged black holes in anti-de Sitter space," 2000.

[60] S. A. Hartnoll and C. P. Herzog, "Impure AdS/CFT," *Phys. Rev.*, vol. D77, p. 106009, 2008.

[61] S. Kachru, X. Liu, and M. Mulligan, "Gravity Duals of Lifshitz-like Fixed Points," *Phys. Rev.*, vol. D78, p. 106005, 2008.

[62] K. Goldstein, S. Kachru, S. Prakash, and S. P. Trivedi, "Holography of Charged Dilaton Black Holes," 2009.

[63] G. T. Horowitz and M. M. Roberts, "Zero Temperature Limit of Holographic Superconductors," *JHEP*, vol. 11, p. 015, 2009.

[64] P. Breitenlohner and D. Z. Freedman, "Positive Energy in anti-De Sitter Backgrounds and Gauged Extended Supergravity," *Phys. Lett.*, vol. B115, p. 197, 1982.

[65] G. Dotti and R. J. Gleiser, "Gravitational instability of Einstein-Gauss-Bonnet black holes under tensor mode perturbations," *Class. Quant. Grav.*, vol. 22, p. L1, 2005.

[66] S. Mignemi, "Exact solutions of dilaton gravity with (anti)-de Sitter asymptotics," 2009.

[67] I. Z. Stefanov, S. S. Yazadjiev, and M. D. Todorov, "Phases of 4D Scalar-tensor black holes coupled to Born- Infeld nonlinear electrodynamics," *Mod. Phys. Lett.*, vol. A23, pp. 2915–2931, 2008.

[68] G. T. Horowitz and M. M. Roberts, "Holographic Superconductors with Various Condensates," *Phys. Rev.*, vol. D78, p. 126008, 2008.

[69] I. R. Klebanov and E. Witten, "AdS/CFT correspondence and symmetry breaking," *Nucl. Phys.*, vol. B556, pp. 89–114, 1999.

[70] T. Hertog and G. T. Horowitz, "Towards a big crunch dual," *JHEP*, vol. 07, p. 073, 2004.

[71] M. Ammon, J. Erdmenger, M. Kaminski, and P. Kerner, "Flavor Superconductivity from Gauge/Gravity Duality," *JHEP*, vol. 10, p. 067, 2009.

[72] R.-G. Cai and Y.-Z. Zhang, "Black plane solutions in four-dimensional spacetimes," *Phys. Rev.*, vol. D54, pp. 4891–4898, 1996.

[73] R.-G. Cai, J.-Y. Ji, and K.-S. Soh, "Topological dilaton black holes," *Phys. Rev.*, vol. D57, pp. 6547–6550, 1998.

[74] C. Charmousis, B. Gouteraux, and J. Soda, "Einstein-Maxwell-Dilaton theories with a Liouville potential," *Phys. Rev.*, vol. D80, p. 024028, 2009.

[75] K. Maeda, M. Natsuume, and T. Okamura, "Universality class of holographic superconductors," *Phys. Rev.*, vol. D79, p. 126004, 2009.

[76] S. S. Gubser and F. D. Rocha, "The gravity dual to a quantum critical point with spontaneous symmetry breaking," *Phys. Rev. Lett.*, vol. 102, p. 061601, 2009.

[77] S.-J. Rey, "String theory on thin semiconductors: Holographic realization of Fermi points and surfaces," *Prog. Theor. Phys. Suppl.*, vol. 177, pp. 128–142, 2009.

[78] S.-S. Lee, "A Non-Fermi Liquid from a Charged Black Hole: A Critical Fermi Ball," *Phys. Rev.*, vol. D79, p. 086006, 2009.

[79] H. Liu, J. McGreevy, and D. Vegh, "Non-Fermi liquids from holography," 2009.

[80] M. Cubrovic, J. Zaanen, and K. Schalm, "String Theory, Quantum Phase Transitions and the Emergent Fermi-Liquid," *Science*, vol. 325, pp. 439–444, 2009.

[81] F. Aprile and J. G. Russo, "Models of Holographic superconductivity," *Phys. Rev.*, vol. D81, p. 026009, 2010.

[82] J. P. Gauntlett, J. Sonner, and T. Wiseman, "Holographic superconductivity in M-Theory," *Phys. Rev. Lett.*, vol. 103, p. 151601, 2009.

[83] S. S. Gubser, S. S. Pufu, and F. D. Rocha, "Quantum critical superconductors in string theory and M- theory," *Phys. Lett.*, vol. B683, pp. 201–204, 2010.

[84] S. S. Gubser, C. P. Herzog, S. S. Pufu, and T. Tesileanu, "Superconductors from Superstrings," *Phys. Rev. Lett.*, vol. 103, p. 141601, 2009.

[85] J. P. Gauntlett, J. Sonner, and T. Wiseman, "Quantum Criticality and Holographic Superconductors in M- theory," *JHEP*, vol. 02, p. 060, 2010.

[86] T. Albash and C. V. Johnson, "A Holographic Superconductor in an External Magnetic Field," *JHEP*, vol. 09, p. 121, 2008.

[87] K. Goldstein *et al.*, "Holography of Dyonic Dilaton Black Branes," 2010.

[88] O. Domenech, M. Montull, A. Pomarol, A. Salvio, and P. J. Silva, "Emergent Gauge Fields in Holographic Superconductors," *JHEP*, vol. 08, p. 033, 2010.

[89] P. P. Fiziev and D. R. Staicova, "Two-dimensional generalization of the Muller root-finding algorithm and its applications," 2010.

[90] S. A. Hartnoll and P. Kovtun, "Hall conductivity from dyonic black holes," *Phys. Rev.*, vol. D76, p. 066001, 2007.

[91] S. A. Hartnoll and C. P. Herzog, "Ohm's Law at strong coupling: S duality and the cyclotron resonance," *Phys. Rev.*, vol. D76, p. 106012, 2007.

[92] G. Festuccia and H. Liu, "A Bohr-Sommerfeld quantization formula for quasinormal frequencies of AdS black holes," 2008.

[93] S. Chandrasekhar and V. Ferrari, "On the non-radial oscillations of a star. IV: An application of the theory of Regge poles," *Proc. Roy. Soc. Lond.*, vol. A434, p. 449, 1992.

[94] S. Chandrasekhar and V. Ferrari *Proc. Roy. Soc. Lond.*, vol. A437, p. 133, 1992.

[95] G. T. Horowitz and V. E. Hubeny, "Quasinormal modes of AdS black holes and the approach to thermal equilibrium," *Phys. Rev.*, vol. D62, p. 024027, 2000.

[96] T. Harmark, J. Natario, and R. Schiappa, "Greybody Factors for d-Dimensional Black Holes," 2007.

[97] J. Grain and A. Barrau, "A WKB approach to scalar fields dynamics in curved space- time," *Nucl. Phys.*, vol. B742, pp. 253–274, 2006.

[98] R. G. Daghigh and M. D. Green, "Highly Real, Highly Damped, and Other Asymptotic Quasinormal Modes of Schwarzschild-Anti De Sitter Black Holes," 2008.

[99] N. Andersson and K. E. Thylwe, "Complex angular momentum approach to black hole scattering," *Class. Quant. Grav.*, vol. 11, pp. 2991–3001, 1994.

[100] N. Andersson, "Complex angular momenta and the black hole glory," *Class. Quant. Grav.*, vol. 11, pp. 3003–3012, 1994.

[101] Y. Decanini, A. Folacci, and B. Jensen, "Complex angular momentum in black hole physics and the quasi-normal modes," *Phys. Rev.*, vol. D67, p. 124017, 2003.

[102] V. Cardoso and J. P. S. Lemos, "Quasi-normal modes of Schwarzschild anti-de Sitter black holes: Electromagnetic and gravitational perturbations," *Phys. Rev.*, vol. D64, p. 084017, 2001.

[103] I. G. Moss and J. P. Norman, "Gravitational quasinormal modes for anti-de Sitter black holes," *Class. Quant. Grav.*, vol. 19, pp. 2323–2332, 2002.

[104] G. Michalogiorgakis and S. S. Pufu, "Low-lying gravitational modes in the scalar sector of the global AdS(4) black hole," *JHEP*, vol. 02, p. 023, 2007.

[105] I. Bakas, "Energy-momentum/Cotton tensor duality for AdS4 black holes," *JHEP*, vol. 01, p. 003, 2009.

[106] J. V. Rocha, "Evaporation of large black holes in AdS: coupling to the evaporon," *JHEP*, vol. 08, p. 075, 2008.

[107] R. A. Konoplya, "On quasinormal modes of small Schwarzschild-anti-de-Sitter black hole," *Phys. Rev.*, vol. D66, p. 044009, 2002.

[108] V. Cardoso and O. J. C. Dias, "Small Kerr-anti-de Sitter black holes are unstable," *Phys. Rev.*, vol. D70, p. 084011, 2004.

[109] E. Berti and K. D. Kokkotas, "Quasinormal modes of Reissner-Nordstroem-anti-de Sitter black holes: Scalar, electromagnetic and gravitational perturbations," *Phys. Rev.*, vol. D67, p. 064020, 2003.

[110] V. Cardoso, O. J. C. Dias, and S. Yoshida, "Classical instability of Kerr-AdS black holes and the issue of final state," *Phys. Rev.*, vol. D74, p. 044008, 2006.

[111] G. Gamow, "Zur Quantentheorie des Atomkernes," *Z. Phys.*, vol. 51, pp. 204–212, 1928.

[112] S. A. Gurvitz, "Novel approach to tunneling problems," *Phys. Rev.*, vol. A38, pp. 1747–1759, 1988.

[113] B. Wang, C.-Y. Lin, and C. Molina, "Quasinormal behavior of massless scalar field perturbation in Reissner-Nordstroem anti-de Sitter spacetimes," *Phys. Rev.*, vol. D70, p. 064025, 2004.

[114] C. Teitelboim, "Nonmeasurability of the quantum numbers of a black hole," *Phys. Rev.*, vol. D5, pp. 2941–2954, 1972.

[115] J. D. Bekenstein, "Novel 'no scalar hair' theorem for black holes," *Phys. Rev.*, vol. D51, pp. 6608–6611, 1995.

[116] T. Hertog, "Towards a Novel no-hair Theorem for Black Holes," *Phys. Rev.*, vol. D74, p. 084008, 2006.

[117] K. Hotta, Y. Hyakutake, T. Kubota, T. Nishinaka, and H. Tanida, "The CFT-interpolating Black Hole in Three Dimensions," *JHEP*, vol. 01, p. 010, 2009.

[118] M. Cadoni and M. R. Setare, "Near-horizon limit of the charged BTZ black hole and AdS2 quantum gravity," 2008.

[119] M. Cadoni, M. Melis, and P. Pani, "Microscopic entropy of black holes and AdS2 quantum gravity," *PoS*, vol. BHS GR AND STRINGS 2008, p. 032, 2008.

[120] C. Martinez, C. Teitelboim, and J. Zanelli, "Charged rotating black hole in three spacetime dimensions," *Phys. Rev.*, vol. D61, p. 104013, 2000.

[121] N. Kim, Y. Kim, and K. Kimm, "Global vortex and black cosmic string," *Phys. Rev.*, vol. D56, pp. 8029–8044, 1997.

[122] D. Maity, S. Sarkar, N. Sircar, B. Sathiapalan, and R. Shankar, "Properties of CFTs dual to Charged BTZ black-hole," 2009.

[123] M. Banados, C. Teitelboim, and J. Zanelli, "The Black hole in three-dimensional space-time," *Phys. Rev. Lett.*, vol. 69, pp. 1849–1851, 1992.

[124] M. Henneaux, C. Martinez, R. Troncoso, and J. Zanelli, "Asymptotically anti-de Sitter spacetimes and scalar fields with a logarithmic branch," *Phys. Rev.*, vol. D70, p. 044034, 2004.

[125] D. Ruelle, *Statistical Mechanics: Rigorous Results*. Addison- Wesley, 1989.

[126] C. Hoyle, D. Kapner, B. Heckel, E. Adelberger, J. Gundlach, U. Schmidt, and H. Swanson, "Sub-millimeter tests of the gravitational inverse-square law," *Phys. Rev. D*, vol. 70, no. 4, p. 042004, 2004.

[127] S. Hawking and R. Penrose, *The nature of space and time: with a new afterword by the authors*. Oxford: Princeton Univ. Press, 2010.

[128] A. G. Riess *et al.*, "Observational Evidence from Supernovae for an Accelerating Universe and a Cosmological Constant," *Astron. J.*, vol. 116, pp. 1009–1038, 1998.

[129] S. Perlmutter *et al.*, "Measurements of Omega and Lambda from 42 High-Redshift Supernovae," *Astrophys. J.*, vol. 517, pp. 565–586, 1999.

[130] D. N. Spergel *et al.*, "Wilkinson Microwave Anisotropy Probe (WMAP) three year results: Implications for cosmology," *Astrophys. J. Suppl.*, vol. 170, p. 377, 2007.

[131] S. M. Carroll, "The cosmological constant," *Living Reviews in Relativity*, vol. 4, no. 1, 2001.

[132] P. J. E. Peebles and B. Ratra, "The cosmological constant and dark energy," *Rev. Mod. Phys.*, vol. 75, pp. 559–606, 2003.

[133] A. Dekel, F. Stoehr, G. A. Mamon, T. J. Cox, and J. R. Primack, "Dark-Matter Haloes in Elliptical Galaxies: Lost and Found," *Nature*, vol. 437, p. 707, 2005.

[134] C. Brans and R. H. Dicke, "Mach's principle and a relativistic theory of gravitation," *Phys. Rev.*, vol. 124, pp. 925–935, 1961.

[135] A. D. F. Shinji Tsujikawa, "f(r) theories," *Living Reviews in Relativity*, vol. 13, no. 3, 2010.

[136] L. Blanchet, "Gravitational radiation from post-newtonian sources and inspiralling compact binaries," *Living Reviews in Relativity*, vol. 5, no. 3, 2002.

[137] D. Psaltis, "Probes and tests of strong-field gravity with observations in the electromagnetic spectrum," *Living Reviews in Relativity*, vol. 11, no. 9, 2008.

[138] B. Caron *et al.*, "The Virgo interferometer," *Class. Quant. Grav.*, vol. 14, pp. 1461–1469, 1997.

[139] E. Berti, A. Buonanno, and C. M. Will, "Estimating spinning binary parameters and testing alternative theories of gravity with LISA," *Phys. Rev.*, vol. D71, p. 084025, 2005.

[140] C. M. Will and N. Yunes, "Testing alternative theories of gravity using LISA," *Class. Quant. Grav.*, vol. 21, p. 4367, 2004.

[141] R. Ruffini and J. Wheeler, *Introducing the Black Hole.* Physics Today 24, 30-41, 1971.

[142] B. Carter, "Axisymmetric Black Hole Has Only Two Degrees of Freedom," *Phys. Rev. Lett.*, vol. 26, pp. 331–333, 1971.

[143] R. M. Wald, "Final states of gravitational collapse," *Phys. Rev. Lett.*, vol. 26, pp. 1653–1655, 1971.

[144] D. C. Robinson, "Uniqueness of the Kerr black hole," *Phys. Rev. Lett.*, vol. 34, pp. 905–906, 1975.

[145] J. D. Bekenstein, "Nonexistence of baryon number for static black holes," *Phys. Rev.*, vol. D5, pp. 1239–1246, 1972.

[146] P. Bizon, "Colored black holes," *Phys. Rev. Lett.*, vol. 64, pp. 2844–2847, 1990.

[147] S. Droz, M. Heusler, and N. Straumann, "New black hole solutions with hair," *Phys. Lett.*, vol. B268, pp. 371–376, 1991.

[148] S. S. Gubser, "Colorful horizons with charge in anti-de Sitter space," *Phys. Rev. Lett.*, vol. 101, p. 191601, 2008.

[149] M. Cavaglia, "Black hole and brane production in TeV gravity: A review," *Int. J. Mod. Phys.*, vol. A18, pp. 1843–1882, 2003.

[150] S. B. Giddings and S. D. Thomas, "High energy colliders as black hole factories: The end of short distance physics," *Phys. Rev.*, vol. D65, p. 056010, 2002.

[151] P. Kanti, "Black holes in theories with large extra dimensions: A Review," *Int. J. Mod. Phys.*, vol. A19, pp. 4899–4951, 2004.

[152] P. Kanti, "Black Holes at the LHC," *Lect. Notes Phys.*, vol. 769, pp. 387–423, 2009.

[153] G. W. Gibbons, "Vacuum Polarization and the Spontaneous Loss of Charge by Black Holes," *Commun. Math. Phys.*, vol. 44, pp. 245–264, 1975.

[154] I. Zlatev, L.-M. Wang, and P. J. Steinhardt, "Quintessence, Cosmic Coincidence, and the Cosmological Constant," *Phys. Rev. Lett.*, vol. 82, pp. 896–899, 1999.

[155] K. Konno, T. Matsuyama, Y. Asano, and S. Tanda, "Flat rotation curves in Chern-Simons modified gravity," *Phys. Rev.*, vol. D78, p. 024037, 2008.

[156] A. D. Linde, "Inflation and string cosmology," *ECONF*, vol. C040802, p. L024, 2004.

[157] J. R. Oppenheimer and H. Snyder, "On Continued gravitational contraction," *Phys. Rev.*, vol. 56, pp. 455–459, 1939.

[158] R. Penrose, "Gravitational collapse and space-time singularities," *Phys. Rev. Lett.*, vol. 14, pp. 57–59, 1965.

[159] R. H. Price, "Nonspherical Perturbations of Relativistic Gravitational Collapse. II. Integer-Spin, Zero-Rest-Mass Fields," *Phys. Rev.*, vol. D5, pp. 2439–2454, 1972.

[160] R. Penrose, "Gravitational collapse: The role of general relativity," *Riv. Nuovo Cim.*, vol. 1, pp. 252–276, 1969.

[161] I. Hauser and F. Ernst, "J. Math. Phys 22, 1051," 1981.

[162] F. D. Ryan, "Gravitational waves from the inspiral of a compact object into a massive, axisymmetric body with arbitrary multipole moments," *Phys. Rev.*, vol. D52, pp. 5707–5718, 1995.

[163] M. Fierz, "On the physical interpretation of P.Jordan's extended theory of gravitation," *Helv. Phys. Acta*, vol. 29, pp. 128–134, 1956.

[164] P. Jordan, "The present state of Dirac's cosmological hypothesis," *Z. Phys.*, vol. 157, pp. 112–121, 1959.

[165] C. M. Will, *Theory and Experiment in Gravitational Physics; rev. version*. Cambridge: Cambridge Univ. Press, 1993.

[166] N. Rosen, "A bi-metric theory of gravitation," *General Relativity and Gravitation*, vol. 4, pp. 435–447, Dec. 1973.

[167] H. van Dam and M. J. G. Veltman, "Massive and massless Yang-Mills and gravitational fields," *Nucl. Phys.*, vol. B22, pp. 397–411, 1970.

[168] R. H. Sanders and S. S. McGaugh, "Modified Newtonian Dynamics as an Alternative to Dark Matter," *Ann. Rev. Astron. Astrophys.*, vol. 40, pp. 263–317, 2002.

[169] J. D. Bekenstein, "Relativistic gravitation theory for the MOND paradigm," *Phys. Rev.*, vol. D70, p. 083509, 2004.

[170] N. Yunes and F. Pretorius, "Dynamical Chern-Simons Modified Gravity I: Spinning Black Holes in the Slow-Rotation Approximation," *Phys. Rev.*, vol. D79, p. 084043, 2009.

[171] C. F. Sopuerta and N. Yunes, "Extreme- and Intermediate-Mass Ratio Inspirals in Dynamical Chern-Simons Modified Gravity," *Phys. Rev.*, vol. D80, p. 064006, 2009.

[172] K. S. Thorne, "Multipole Expansions of Gravitational Radiation," *Rev. Mod. Phys.*, vol. 52, pp. 299–339, 1980.

[173] L. Barack and C. Cutler, "Using LISA EMRI sources to test off-Kerr deviations in the geometry of massive black holes," *Phys. Rev.*, vol. D75, p. 042003, 2007.

[174] F. D. Ryan, "Accuracy of estimating the multipole moments of a massive body from the gravitational waves of a binary inspiral," *Phys. Rev.*, vol. D56, pp. 1845–1855, 1997.

[175] Z.-K. Guo, N. Ohta, and T. Torii, "Black Holes in the Dilatonic Einstein-Gauss-Bonnet Theory in Various Dimensions I – Asymptotically Flat Black Holes –," *Prog. Theor. Phys.*, vol. 120, pp. 581–607, 2008.

[176] K.-i. Maeda, N. Ohta, and Y. Sasagawa, "Black Hole Solutions in String Theory with Gauss-Bonnet Curvature Correction," *Phys. Rev.*, vol. D80, p. 104032, 2009.

[177] P. Kanti, N. E. Mavromatos, J. Rizos, K. Tamvakis, and E. Winstanley, "Dilatonic Black Holes in Higher Curvature String Gravity," *Phys. Rev.*, vol. D54, pp. 5049–5058, 1996.

[178] S. Mignemi and N. R. Stewart, "Charged black holes in effective string theory," *Phys. Rev.*, vol. D47, pp. 5259–5269, 1993.

[179] P. Kanti, N. E. Mavromatos, J. Rizos, K. Tamvakis, and E. Winstanley, "Dilatonic black holes in higher-curvature string gravity. II: Linear stability," *Phys. Rev.*, vol. D57, pp. 6255–6264, 1998.

[180] S. Deser, R. Jackiw, and S. Templeton, "Three-Dimensional Massive Gauge Theories," *Phys. Rev. Lett.*, vol. 48, pp. 975–978, 1982.

[181] A. Lue, L.-M. Wang, and M. Kamionkowski, "Cosmological signature of new parity-violating interactions," *Phys. Rev. Lett.*, vol. 83, pp. 1506–1509, 1999.

[182] R. Jackiw and S. Y. Pi, "Chern-Simons modification of general relativity," *Phys. Rev.*, vol. D68, p. 104012, 2003.

[183] S. Weinberg, "A Tree Theorem for Inflation," *Phys. Rev.*, vol. D78, p. 063534, 2008.

[184] J. Garcia-Bellido, M. Garcia-Perez, and A. Gonzalez-Arroyo, "Chern-Simons production during preheating in hybrid inflation models," *Phys. Rev.*, vol. D69, p. 023504, 2004.

[185] S. H. S. Alexander and S. J. Gates, Jr., "Can the string scale be related to the cosmic baryon asymmetry?," *JCAP*, vol. 0606, p. 018, 2006.

[186] S. H.-S. Alexander, M. E. Peskin, and M. M. Sheikh-Jabbari, "Leptogenesis from gravity waves in models of inflation," *Phys. Rev. Lett.*, vol. 96, p. 081301, 2006.

[187] A. Ashtekar, A. P. Balachandran, and S. Jo, "The CP problem in Quantum Gravity," *Int. J. Mod. Phys.*, vol. A4, p. 1493, 1989.

[188] V. Taveras and N. Yunes, "The Barbero-Immirzi Parameter as a Scalar Field: K- Inflation from Loop Quantum Gravity?," *Phys. Rev.*, vol. D78, p. 064070, 2008.

[189] S. Mercuri and V. Taveras, "Interaction of the Barbero–Immirzi Field with Matter and Pseudo-Scalar Perturbations," *Phys. Rev.*, vol. D80, p. 104007, 2009.

[190] T. L. Smith, A. L. Erickcek, R. R. Caldwell, and M. Kamionkowski, "The effects of Chern-Simons gravity on bodies orbiting the Earth," *Phys. Rev.*, vol. D77, p. 024015, 2008.

[191] M. Adak and T. Dereli, "String-Inspired Chern-Simons Modified Gravity In 4- Dimensions," 2008.

[192] N. Yunes and C. F. Sopuerta, "Perturbations of Schwarzschild Black Holes in Chern-Simons Modified Gravity," *Phys. Rev.*, vol. D77, p. 064007, 2008.

[193] V. Cardoso and L. Gualtieri, "Perturbations of Schwarzschild black holes in Dynamical Chern-Simons modified gravity," *Phys. Rev.*, vol. D80, p. 064008, 2009.

[194] S. Chandrasekhar and S. L. Detweiler, "The quasi-normal modes of the Schwarzschild black hole," *Proc. Roy. Soc. Lond.*, vol. A344, pp. 441–452, 1975.

[195] V. Ferrari and L. Gualtieri, "Quasi-Normal Modes and Gravitational Wave Astronomy," *Gen. Rel. Grav.*, vol. 40, pp. 945–970, 2008.

[196] S. S. Seahra, C. Clarkson, and R. Maartens, "Detecting extra dimensions with gravity wave spectroscopy," *Phys. Rev. Lett.*, vol. 94, p. 121302, 2005.

[197] T. Watanabe *et al. J. Phys. Soc. Jpn. 49, 376*, 1980.

[198] R. H. P. C. T. Cunningham, C. T. and V. Moncrief *Astrophys. J. 224, 643, 643*, 1978.

[199] N. Yunes, D. Psaltis, F. Ozel, and A. Loeb, "Constraining Parity Violation in Gravity with Measurements of Neutron-Star Moments of Inertia," *Phys. Rev.*, vol. D81, p. 064020, 2010.

[200] B. Wang, C. Molina, and E. Abdalla, "Evolving of a massless scalar field in Reissner-Nordstroem Anti-de Sitter spacetimes," *Phys. Rev.*, vol. D63, p. 084001, 2001.

[201] E. S. C. Ching, P. T. Leung, W. M. Suen, and K. Young, "Wave propagation in gravitational systems: Late time behavior," *Phys. Rev.*, vol. D52, pp. 2118–2132, 1995.

[202] A. Arvanitaki, S. Dimopoulos, S. Dubovsky, N. Kaloper, and J. March-Russell, "String Axiverse," 2009.

[203] N. Yunes *private communication*, 2010.

[204] E. Berti, J. Cardoso, V. Cardoso, and M. Cavaglia, "Matched-filtering and parameter estimation of ringdown waveforms," *Phys. Rev.*, vol. D76, p. 104044, 2007.

[205] K. Konno, T. Matsuyama, and S. Tanda, "Rotating black hole in extended Chern-Simons modified gravity," *Prog. Theor. Phys.*, vol. 122, pp. 561–568, 2009.

[206] J. Polchinski, "String theory. Vol. 1: An introduction to the bosonic string," Cambridge, UK: Univ. Pr. (1998) 402 p.

[207] C. G. Callan, Jr., I. R. Klebanov, and M. J. Perry, "String Theory Effective Actions," *Nucl. Phys.*, vol. B278, p. 78, 1986.

[208] D. J. Gross and E. Witten, "Superstring Modifications of Einstein's Equations," *Nucl. Phys.*, vol. B277, p. 1, 1986.

[209] F. Moura and R. Schiappa, "Higher-derivative corrected black holes: Perturbative stability and absorption cross-section in heterotic string theory," *Class. Quant. Grav.*, vol. 24, pp. 361–386, 2007.

[210] S. Alexander, L. S. Finn, and N. Yunes, "A gravitational-wave probe of effective quantum gravity," *Phys. Rev.*, vol. D78, p. 066005, 2008.

[211] S. Alexander and N. Yunes, "A new PPN parameter to test Chern-Simons gravity," *Phys. Rev. Lett.*, vol. 99, p. 241101, 2007.

[212] S. Alexander and N. Yunes, "Parametrized Post-Newtonian Expansion of Chern-Simons Gravity," *Phys. Rev.*, vol. D75, p. 124022, 2007.

[213] G. Esposito-Farese, "Scalar-tensor theories and cosmology and tests of a quintessence-Gauss-Bonnet coupling," 2003.

[214] C. M. Will and H. W. Zaglauer, "Gravitational radiation, close binary systems, and the Brans-Dicke theory of gravity," *Astrophys. J.*, vol. 346, pp. 366–377, Nov. 1989.

[215] G. Esposito-Farese, "Tests of scalar-tensor gravity," *AIP Conf. Proc.*, vol. 736, pp. 35–52, 2004.

[216] T. P. Sotiriou and E. Barausse, "Post-Newtonian expansion for Gauss-Bonnet Gravity," *Phys. Rev.*, vol. D75, p. 084007, 2007.

[217] T. Torii, H. Yajima, and K.-i. Maeda, "Dilatonic black holes with Gauss-Bonnet term," *Phys. Rev.*, vol. D55, pp. 739–753, 1997.

[218] S. O. Alexeev and M. V. Pomazanov, "Black hole solutions with dilatonic hair in higher curvature gravity," *Phys. Rev.*, vol. D55, pp. 2110–2118, 1997.

[219] Z.-K. Guo, N. Ohta, and T. Torii, "Black Holes in the Dilatonic Einstein-Gauss-Bonnet Theory in Various Dimensions II – Asymptotically AdS Topological Black Holes –," *Prog. Theor. Phys.*, vol. 121, pp. 253–273, 2009.

[220] C. M. Will, "Testing the general relativistic "no-hair" theorems using the galactic center black hole SgrA*," 2007.

[221] K. Bamba, Z.-K. Guo, and N. Ohta, "Accelerating Cosmologies in the Einstein-Gauss-Bonnet Theory with Dilaton," *Prog. Theor. Phys.*, vol. 118, pp. 879–892, 2007.

[222] T. Torii and K.-i. Maeda, "Stability of a dilatonic black hole with a Gauss-Bonnet term," *Phys. Rev.*, vol. D58, p. 084004, 1998.

[223] S. W. Hawking, "Black holes in general relativity," *Commun. Math. Phys.*, vol. 25, pp. 152–166, 1972.

[224] R. D. Blandford and R. L. Znajek, "Electromagnetic extractions of energy from Kerr black holes," *Mon. Not. Roy. Astron. Soc.*, vol. 179, pp. 433–456, 1977.

[225] R. Narayan, "Black Holes in Astrophysics," *New J. Phys.*, vol. 7, p. 199, 2005.

[226] F. Eisenhauer *et al.*, "GRAVITY: getting to the event horizon of Sgr A*," 2008.

[227] M. A. Podurets, "Astr. zh.," 1964.

[228] W. L. Ames and K. S. Thorne, "Astrophys. j.," 1968.

[229] V. Cardoso, A. S. Miranda, E. Berti, H. Witek, and V. T. Zanchin, "Geodesic stability, Lyapunov exponents and quasinormal modes," *Phys. Rev.*, vol. D79, p. 064016, 2009.

[230] S. R. Coleman, J. Preskill, and F. Wilczek, "Quantum hair on black holes," *Nucl. Phys.*, vol. B378, pp. 175–246, 1992.

[231] G. Dotti and R. J. Gleiser, "Linear stability of Einstein-gauss-bonnet static spacetimes. part. I: Tensor perturbations," *Phys. Rev.*, vol. D72, p. 044018, 2005.

[232] R. J. Gleiser and G. Dotti, "Linear stability of Einstein-Gauss-Bonnet static spacetimes. II: Vector and scalar perturbations," *Phys. Rev.*, vol. D72, p. 124002, 2005.

[233] J. Mathews, "J. soc. ind. appl. math.," 1962.

[234] C. V. Vishveshwara, "Scattering of Gravitational Radiation by a Schwarzschild Black-hole," *Nature*, vol. 227, pp. 936–938, 1970.

[235] C. F. E. Holzhey and F. Wilczek, "Black holes as elementary particles," *Nucl. Phys.*, vol. B380, pp. 447–477, 1992.

[236] C. F. Gammie, S. L. Shapiro, and J. C. McKinney, "Black Hole Spin Evolution," *Astrophys. J.*, vol. 602, pp. 312–319, 2004.

[237] D. Merritt and M. Milosavljevic, "Massive Black Hole Binary Evolution," *Living Rev. Rel.*, vol. 8, p. 8, 2005.

[238] E. Berti and M. Volonteri, "Cosmological black hole spin evolution by mergers and accretion," *Astrophys. J.*, vol. 684, p. 822, 2008.

[239] M. K. *et al*, "in preparation," 2009.

[240] D. Grumiller and N. Yunes, "How do Black Holes Spin in Chern-Simons Modified Gravity?," *Phys. Rev.*, vol. D77, p. 044015, 2008.

[241] K. Konno, T. Matsuyama, and S. Tanda, "Does a black hole rotate in Chern-Simons modified gravity?," *Phys. Rev.*, vol. D76, p. 024009, 2007.

[242] J. B. Hartle, "Slowly rotating relativistic stars. 1. Equations of structure," *Astrophys. J.*, vol. 150, pp. 1005–1029, 1967.

[243] R. Ruffini and S. Bonazzola, "Systems of selfgravitating particles in general relativity and the concept of an equation of state," *Phys. Rev.*, vol. 187, pp. 1767–1783, 1969.

[244] Y. Kobayashi, M. Kasai, and T. Futamase, "Does a boson star rotate?," *Phys. Rev.*, vol. D50, pp. 7721–7724, 1994.

[245] B. F. Schutz and N. Comins, "On the existence of ergoregions in rotating stars," *Mon. Not. Roy. Astron. Soc.*, vol. 182, pp. 69–76, Jan. 1978.

[246] V. Faraoni and E. Gunzig, "Einstein frame or Jordan frame?," *Int. J. Theor. Phys.*, vol. 38, pp. 217–225, 1999.

[247] J.-P. Bruneton and G. Esposito-Farese, "Field-theoretical formulations of MOND-like gravity," *Phys. Rev.*, vol. D76, p. 124012, 2007.

[248] R. Casadio and B. Harms, "Charged dilatonic black holes: String frame vs. Einstein frame," *Mod. Phys. Lett.*, vol. A14, pp. 1089–1104, 1999.

[249] S. Chandrasekhar, *The Mathematical Theory of Black Holes*. New York: Oxford University Press, 1983.

[250] T. Maki and K. Shiraishi, "Motion of test particles around a charged dilatonic black hole," *Class. Quant. Grav.*, vol. 11, pp. 227–238, 1994.

[251] E. E. Flanagan and S. A. Hughes, "Measuring gravitational waves from binary black hole coalescences. I: Signal to noise for inspiral, merger, and ringdown," *Phys. Rev.*, vol. D57, pp. 4535–4565, 1998.

[252] L. M. Goggin, "Search for black hole ringdown signals in LIGO S4 data," *Class. Quant. Grav.*, vol. 23, pp. S709–S713, 2006.

[253] Y. Tsunesada, D. Tatsumi, N. Kanda, and H. Nakano, "Black-hole ringdown search in TAMA300: Matched filtering and event selections," *Class. Quant. Grav.*, vol. 22, pp. S1129–S1138, 2005.

[254] E. Berti *et al.*, "Inspiral, merger and ringdown of unequal mass black hole binaries: A multipolar analysis," *Phys. Rev.*, vol. D76, p. 064034, 2007.

[255] E. Berti, V. Cardoso, J. A. Gonzalez, and U. Sperhake, "Mining information from binary black hole mergers: a comparison of estimation methods for complex exponentials in noise," *Phys. Rev.*, vol. D75, p. 124017, 2007.

[256] E. Abdalla, R. A. Konoplya, and C. Molina, "Scalar field evolution in Gauss-Bonnet black holes," *Phys. Rev.*, vol. D72, p. 084006, 2005.

[257] R. Konoplya, "Quasinormal modes of the charged black hole in Gauss- Bonnet gravity," *Phys. Rev.*, vol. D71, p. 024038, 2005.

[258] R. A. Konoplya, "Quasinormal modes of the electrically charged dilaton black hole," *Gen. Rel. Grav.*, vol. 34, pp. 329–335, 2002.

[259] B. Kleihaus, J. Kunz, and F. Navarro-Lerida, "Rotating Black Holes in Higher Dimensions," *AIP Conf. Proc.*, vol. 977, pp. 94–115, 2008.

[260] F. Melia, "Supermassive Black Holes," 2007.

[261] A. Mueller, "Experimental evidence of black holes," *PoS*, vol. P2GC, p. 017, 2006.

[262] A. M. Ghez *et al.*, "Measuring Distance and Properties of the Milky Way's Central Supermassive Black Hole with Stellar Orbits," *Astrophys. J.*, vol. 689, pp. 1044–1062, 2008.

[263] S. Doeleman *et al.*, "Event-horizon-scale structure in the supermassive black hole candidate at the Galactic Centre," *Nature*, vol. 455, p. 78, 2008.

[264] R. Schodel *et al.*, "A Star in a 15.2 year orbit around the supermassive black hole at the center of the Milky Way," *Nature*, vol. 419, pp. 694–696, 2002.

[265] E. Maoz, "Dynamical Constraints On Alternatives To Massive Black Holes In Galactic Nuclei," 1997.

[266] M. Coleman Miller, "Constraints on Alternatives to Supermassive Black Holes," *Mon. Not. Roy. Astron. Soc. Lett.*, vol. 367, pp. L32–L36, 2006.

[267] A. E. Broderick, A. Loeb, and R. Narayan, "The Event Horizon of Sagittarius A*," *Astrophys. J.*, vol. 701, pp. 1357–1366, 2009.

[268] D. Psaltis, "Probes and Tests of Strong-Field Gravity with Observations in the Electromagnetic Spectrum," 2008.

[269] M. A. Abramowicz, W. Kluzniak, and J.-P. Lasota, "No observational proof of the black-hole event-horizon," *Astron. Astrophys.*, vol. 396, pp. L31–L34, 2002.

[270] W. Kundt, "Juergen Ehlers - and the Fate of the Black-Hole Spacetimes," *Gen. Rel. Grav.*, vol. 41, pp. 1967–1980, 2009.

[271] M. Visser, "Black holes in general relativity," *PoS*, vol. BHS GR AND STRINGS 2008, p. 001, 2008.

[272] E. Berti and V. Cardoso, "Supermassive black holes or boson stars? Hair counting with gravitational wave detectors," *Int. J. Mod. Phys.*, vol. D15, pp. 2209–2216, 2006.

[273] C. Li and G. Lovelace, "A generalization of Ryan's theorem: Probing tidal coupling with gravitational waves from nearly circular, nearly equatorial, extreme-mass-ratio inspirals," *Phys. Rev.*, vol. D77, p. 064022, 2008.

[274] N. A. Collins and S. A. Hughes, "Towards a formalism for mapping the spacetimes of massive compact objects: Bumpy black holes and their orbits," *Phys. Rev.*, vol. D69, p. 124022, 2004.

[275] K. Glampedakis and S. Babak, "Mapping spacetimes with LISA: inspiral of a test-body in a 'quasi-Kerr' field," *Class. Quant. Grav.*, vol. 23, pp. 4167–4188, 2006.

[276] O. Dreyer *et al.*, "Black hole spectroscopy: Testing general relativity through gravitational wave observations," *Class. Quant. Grav.*, vol. 21, pp. 787–804, 2004.

[277] B. S. Sathyaprakash and B. F. Schutz, "Physics, Astrophysics and Cosmology with Gravitational Waves," *Living Rev. Rel.*, vol. 12, p. 2, 2009.

[278] F. E. Schunck and E. W. Mielke, "General relativistic boson stars," *Class. Quant. Grav.*, vol. 20, pp. R301–R356, 2003.

[279] D. F. Torres, S. Capozziello, and G. Lambiase, "A supermassive scalar star at the galactic center?," *Phys. Rev.*, vol. D62, p. 104012, 2000.

[280] F. S. Guzman, "Accretion disc onto boson stars: A way to supplant black holes candidates," *Phys. Rev.*, vol. D73, p. 021501, 2006.

[281] M. Kesden, J. Gair, and M. Kamionkowski, "Gravitational-wave signature of an inspiral into a supermassive horizonless object," *Phys. Rev.*, vol. D71, p. 044015, 2005.

[282] S. Yoshida, Y. Eriguchi, and T. Futamase, "Quasinormal modes of boson stars," *Phys. Rev.*, vol. D50, pp. 6235–6246, 1994.

[283] J. Balakrishna, R. Bondarescu, G. Daues, F. Siddhartha Guzman, and E. Seidel, "Evolution of 3D boson stars with waveform extraction," *Class. Quant. Grav.*, vol. 23, pp. 2631–2652, 2006.

[284] P. O. Mazur and E. Mottola, "Gravitational condensate stars," 2001.

[285] G. Chapline, E. Hohlfeld, R. B. Laughlin, and D. I. Santiago, "Quantum phase transitions and the breakdown of classical general relativity," *Int. J. Mod. Phys.*, vol. A18, pp. 3587–3590, 2003.

[286] P. O. Mazur and E. Mottola, "Gravitational vacuum condensate stars," *Proc. Nat. Acad. Sci.*, vol. 101, pp. 9545–9550, 2004.

[287] W. Israel, "Singular hypersurfaces and thin shells in general relativity," *Nuovo Cim.*, vol. B44S10, p. 1, 1966.

[288] J. L. Friedman, "Ergosphere instability," *Communications in Mathematical Physics*, vol. 63, pp. 243–255, Oct. 1978.

[289] Y. Zel'dovich, "Zh.eksp.teor.fiz. 14, 270 and zh.eksp.teor.fiz. 62, 2076."

[290] C. Misner, K. Thorne, and J. Wheeler, "Gravitation," 1973.

[291] V. Cardoso, P. Pani, M. Cadoni, and M. Cavaglia, "Ergoregion instability rules out black hole doubles," *Phys. Rev.*, vol. D77, p. 124044, 2008.

[292] V. Cardoso, P. Pani, M. Cadoni, and M. Cavaglia, "Instability of hyper-compact Kerr-like objects," *Class. Quant. Grav.*, vol. 25, p. 195010, 2008.

[293] P. Pani, V. Cardoso, M. Cadoni, and M. Cavaglia, "Ergoregion instability of black hole mimickers," *PoS*, vol. BHS GR AND STRINGS 2008, p. 027, 2008.

[294] C. B. M. H. Chirenti and L. Rezzolla, "On the ergoregion instability in rotating gravastars," *Phys. Rev.*, vol. D78, p. 084011, 2008.

[295] P. P. Fiziev, "Exact Solutions of Regge-Wheeler Equation and Quasi-Normal Modes of Compact Objects," *Class. Quant. Grav.*, vol. 23, pp. 2447–2468, 2006.

[296] L. Lindblom and S. Detweiler, "The quadrupole oscillations of neutron stars," *Astrophys. J. Suppl.*, vol. 53, pp. 73–92, 1983.

[297] S. Detweiler and L. Lindblom, "On the nonradial pulsations of general relativistic stellar models," *Astrophys. J.*, vol. 292, pp. 12–15, 1985.

[298] S. Chandrasekhar and V. Ferrari, "On the non-radial oscillations of a star," *Proc. Roy. Soc. Lond.*, vol. A432, pp. 247–279, 1991.

[299] V. Cardoso and M. Cavaglia, "Stability of naked singularities and algebraically special modes," *Phys. Rev.*, vol. D74, p. 024027, 2006.

[300] M. Abramowitz *et al.*, *Handbook of Mathematical Functions*. New York: New York: Dover, 1970.

[301] M. Leins, H. P. Nollert, and M. H. Soffel, "Nonradial oscillations of neutron stars: A New branch of strongly damped normal modes," *Phys. Rev.*, vol. D48, pp. 3467–3472, 1993.

[302] M. Visser, "Lorentzian wormholes: From Einstein to Hawking," Woodbury, USA: AIP (1995) 412 p.

[303] E. Poisson and M. Visser, "Thin shell wormholes: Linearization stability," *Phys. Rev.*, vol. D52, pp. 7318–7321, 1995.

[304] O. Benhar, E. Berti, and V. Ferrari, "The imprint of the equation of state on the axial w-modes of oscillating neutron stars," *Mon. Not. Roy. Astron. Soc.*, vol. 310, pp. 797–803, 1999.

[305] K. D. Kokkotas, "Axial modes for relativistic stars," *Mon. Not. Roy. Astron. Soc.*, vol. 268, p. 1015, 1994.

[306] W. H. Press, B. P. Flannery, S. A. Teukolsky, and W. T. Vetterling, "Numerical recipes in c++. third edition.."

[307] N. Andersson, Y. Kojima, and K. D. Kokkotas, "On the oscillation spectra of ultracompact stars: An extensive survey of gravitational-wave modes," *Astrophys. J.*, vol. 462, p. 855, 1996.

[308] K. D. Kokkotas and B. F. Schutz, "Normal Modes of a Model Radiating System," *Gen. Rel. Grav.*, vol. 18, p. 913, 1986.

[309] N. Andersson, "Two simple models for gravitational-wave modes of compact stars," *Gen. Rel. Grav.*, vol. 28, pp. 1433–1445, 1996.

[310] E. Berti, "Gravitational waves from perturbed stars," Ph.D. Thesis.

[311] E. Berti, V. Cardoso, and P. Pani, "Breit-Wigner resonances and the quasinormal modes of anti-de Sitter black holes," *Phys. Rev.*, vol. D79, p. 101501, 2009.

[312] Y. Kojima, "Stellar resonant oscillations coupled to gravitational waves," *Prog. Theor. Phys.*, vol. 77, pp. 297–309, 1987.

[313] L. Gualtieri, E. Berti, J. A. Pons, G. Miniutti, and V. Ferrari, "Gravitational signals emitted by a point mass orbiting a neutron star: A perturbative approach," *Phys. Rev.*, vol. D64, p. 104007, 2001.

[314] J. A. Pons, E. Berti, L. Gualtieri, G. Miniutti, and V. Ferrari, "Gravitational signals emitted by a point mass orbiting a neutron star: Effects of stellar structure," *Phys. Rev.*, vol. D65, p. 104021, 2002.

[315] E. Berti, J. A. Pons, G. Miniutti, L. Gualtieri, and V. Ferrari, "Are Post-Newtonian templates faithful and effectual in detecting gravitational signals from neutron star binaries?," *Phys. Rev.*, vol. D66, p. 064013, 2002.

[316] J. M. Bardeen and W. H. Press, "Radiation fields in the schwarzschild background," *J. Math. Phys.*, vol. 14, pp. 7–19, 1973.

[317] S. A. Teukolsky, "Perturbations of a rotating black hole. 1. Fundamental equations for gravitational electromagnetic and neutrino field perturbations," *Astrophys. J.*, vol. 185, pp. 635–647, 1973.

[318] N. Yunes, K. G. Arun, E. Berti, and C. M. Will, "Post-Circular Expansion of Eccentric Binary Inspirals: Fourier-Domain Waveforms in the Stationary Phase Approximation," *Phys. Rev.*, vol. D80, p. 084001, 2009.

[319] E. Poisson, "Gravitational radiation from a particle in circular orbit around a black hole. 6. Accuracy of the postNewtonian expansion," *Phys. Rev.*, vol. D52, pp. 5719–5723, 1995.

[320] Y. Mino, M. Sasaki, M. Shibata, H. Tagoshi, and T. Tanaka, "Black hole perturbation," *Prog. Theor. Phys. Suppl.*, vol. 128, pp. 1–121, 1997.

[321] N. Yunes and E. Berti, "Accuracy of the Post-Newtonian Approximation: Optimal Asymptotic Expansion for Quasi-Circular, Extreme-Mass Ratio Inspirals," *Phys. Rev.*, vol. D77, p. 124006, 2008.

[322] E. Poisson, "Gravitational radiation from a particle in circular orbit around a black hole. 1: Analytical results for the nonrotating case," *Phys. Rev.*, vol. D47, pp. 1497–1510, 1993.

[323] C. Cutler, E. Poisson, G. J. Sussman, and L. S. Finn, "Gravitational radiation from a particle in circular orbit around a black hole. 2: Numerical results for the nonrotating case," *Phys. Rev.*, vol. D47, pp. 1511–1518, 1993.

[324] C. Cutler, D. Kennefick, and E. Poisson, "Gravitational radiation reaction for bound motion around a Schwarzschild black hole," *Phys. Rev.*, vol. D50, pp. 3816–3835, 1994.

[325] E. E. Flanagan and T. Hinderer, "Constraining neutron star tidal Love numbers with gravitational wave detectors," *Phys. Rev.*, vol. D77, p. 021502, 2008.

[326] K. D. Kokkotas, J. Ruoff, and N. Andersson, "The w-mode instability of ultracompact relativistic stars," *Phys. Rev.*, vol. D70, p. 043003, 2004.

[327] T. Damour and S. N. Solodukhin, "Wormholes as Black Hole Foils," *Phys. Rev.*, vol. D76, p. 024016, 2007.

[328] E. W. Leaver, "An Analytic representation for the quasi normal modes of Kerr black holes," *Proc. Roy. Soc. Lond.*, vol. A402, pp. 285–298, 1985.

[329] E. W. Leaver, "Quasinormal modes of Reissner-Nordstrom black holes," *Phys. Rev.*, vol. D41, pp. 2986–2997, 1990.

[330] W. Gautschi, "Computational aspects of three-term recurrence relations," *SIAM Rev.*, vol. 9, pp. 24–82, 1967.

[331] H. Wall, "Analytic theory of continued fractions," *van Nostrand*, 1948.

[332] H. Pfister, "A Spherical mass shell as a 'total reflector' for gravitational waves," *Class. Quant. Grav.*, vol. 13, pp. 2267–2277, 1996.

[333] G. B. Cook, S. L. Shapiro, and S. A. Teukolsky, "Rapidly rotating neutron stars in general relativity: Realistic equations of state," *Astrophys. J.*, vol. 424, p. 823, 1994.

[334] E. Berti and N. Stergioulas, "Approximate Matching of Analytic and Numerical Solutions for Rapidly Rotating Neutron Stars," *Mon. Not. Roy. Astron. Soc.*, vol. 350, p. 1416, 2004.

[335] E. Berti, F. White, A. Maniopoulou, and M. Bruni, "Rotating neutron stars: an invariant comparison of approximate and numerical spacetime models," *Mon. Not. Roy. Astron. Soc.*, vol. 358, pp. 923–938, 2005.

[336] B. Giacomazzo, L. Rezzolla, and N. Stergioulas *in preparation*, 2010.

[337] L. Baiotti, I. Hawke, P. J. Montero, F. Löffler, L. Rezzolla, N. Stergioulas, J. A. Font, and E. Seidel, "Three-dimensional relativistic simulations of rotating neutron-star collapse to a Kerr black hole," *Phys. Rev. D*, vol. 71, pp. 024035–+, Jan. 2005.

[338] G. Dotti, R. Gleiser, and J. Pullin, "Instability of charged and rotating naked singularities," *Phys. Lett.*, vol. B644, pp. 289–293, 2007.

[339] G. Dotti, R. J. Gleiser, I. F. Ranea-Sandoval, and H. Vucetich, "Gravitational instabilities in Kerr space-times," *Class. Quant. Grav.*, vol. 25, p. 245012, 2008.

[340] K. Hioki and K.-i. Maeda, "Measurement of the Kerr Spin Parameter by Observation of a Compact Object's Shadow," *Phys. Rev.*, vol. D80, p. 024042, 2009.

[341] C. Bambi and N. Yoshida, "Shape and position of the shadow in the $\delta = 2$ Tomimatsu-Sato space-time," 2010.

[342] C. Reina and A. Treves, "Some properties and problems of accretion disks about Kerr naked singularities," *Astrophys. J.*, vol. 227, pp. 596–599, Jan. 1979.

[343] C. Bambi, K. Freese, T. Harada, R. Takahashi, and N. Yoshida, "Accretion process onto superspinning objects," *Phys. Rev.*, vol. D80, p. 104023, 2009.

[344] C. Bambi, "Numerical simulations of the accretion process in Kerr space-times with arbitrary value of the Kerr parameter," 2009.

[345] R. Takahashi and T. Harada, "Observational Testability of Kerr bound in X-ray Spectrum of Black-Hole Candidates," *Class. Quant. Grav.*, vol. 27, p. 075003, 2010.

[346] C. Bambi, T. Harada, R. Takahashi, and N. Yoshida, "Outflows from accreting super-spinars," *Phys. Rev.*, vol. D81, p. 104004, 2010.

[347] S. Chandrasekhar, "On algebraically special perturbations of black holes," *Proc. R. Soc. London, Ser. A*, vol. 392, pp. 1–13, 1984.

[348] S. A. Teukolsky, "Rotating black holes - separable wave equations for gravitational and electromagnetic perturbations," *Phys. Rev. Lett.*, vol. 29, pp. 1114–1118, 1972.

[349] E. Berti, V. Cardoso, and M. Casals, "Eigenvalues and eigenfunctions of spin-weighted spheroidal harmonics in four and higher dimensions," *Phys. Rev.*, vol. D73, p. 024013, 2006.

[350] S. A. Teukolsky and W. H. Press, "Perturbations of a rotating black hole. III - Interaction of the hole with gravitational and electromagnet ic radiation," *Astrophys. J.*, vol. 193, pp. 443–461, 1974.

[351] W. H. Press and S. A. Teukolsky, "Floating Orbits, Superradiant Scattering and the Black-hole Bomb," *Nature*, vol. 238, pp. 211–212, July 1972.

[352] J. M. Bardeen, "Kerr Metric Black Holes," *Nature*, vol. 226, pp. 64–65, Apr. 1970.

[353] R. Wald, "Gedanken experiments to destroy a black hole.," *Annals of Physics*, vol. 82, pp. 548–556, 1974.

[354] A. R. King, J. E. Pringle, and J. A. Hofmann, "The evolution of black hole mass and spin in active galactic nuclei," *Mon. Not. Roy. Astron. Soc.*, vol. 385, pp. 1621–1627, Apr. 2008.

[355] L. W. Brenneman and C. S. Reynolds, "Constraining Black Hole Spin Via X-ray Spectroscopy," *Astrophys. J.*, vol. 652, pp. 1028–1043, 2006.

[356] U. Sperhake *et al.*, "Cross section, final spin and zoom-whirl behavior in high- energy black hole collisions," *Phys. Rev. Lett.*, vol. 103, p. 131102, 2009.

[357] L. Rezzolla, E. N. Dorband, C. Reisswig, P. Diener, D. Pollney, E. Schnetter, and B. Szilágyi, "Spin Diagrams for Equal-Mass Black Hole Binaries with Aligned Spins," *Astrophys. J.*, vol. 679, pp. 1422–1426, June 2008.

[358] L. Rezzolla, E. Barausse, E. N. Dorband, D. Pollney, C. Reisswig, J. Seiler, and S. Husa, "Final spin from the coalescence of two black holes," *Phys. Rev. D*, vol. 78, pp. 044002–+, Aug. 2008.

[359] E. Barausse and L. Rezzolla, "Predicting the direction of the final spin from the coalescence of two black holes," *Astrophys. J. Lett.*, vol. 704, pp. L40–L44, 2009.

[360] M. Kesden, G. Lockhart, and E. S. Phinney, "Maximum black-hole spin from quasi-circular binary mergers," *ArXiv e-prints*, May 2010.

[361] M. Volonteri, P. Madau, E. Quataert, and M. J. Rees, "The Distribution and Cosmic Evolution of Massive Black Hole Spins," *Astrophys. J.*, vol. 620, pp. 69–77, Feb. 2005.

[362] A. R. King and U. Kolb, "The evolution of black-hole mass and angular momentum," *Mon. Not. Roy. Astron. Soc.*, vol. 305, pp. 654–660, 1999.

[363] K. Belczynski, R. E. Taam, E. Rantsiou, and M. van der Sluys, "Black Hole Spin Evolution: Implications for Short-Hard Gamma-Ray Bursts and Gravitational Wave Detection," *Astrophys. J.*, vol. 682, pp. 474–486, July 2008.

[364] S. R. Dolan, "The Quasinormal Mode Spectrum of a Kerr Black Hole in the Eikonal Limit," 2010.

[365] B. Carter, "Global structure of the Kerr family of gravitational fields," *Phys. Rev.*, vol. 174, pp. 1559–1571, 1968.

[366] D. Psaltis, D. Perrodin, K. R. Dienes, and I. Mocioiu, "Kerr Black Holes Are Not Unique to General Relativity," *Physical Review Letters*, vol. 100, pp. 091101–+, Mar. 2008.

[367] E. Barausse and T. P. Sotiriou, "Perturbed Kerr Black Holes Can Probe Deviations from General Relativity," *Physical Review Letters*, vol. 101, pp. 099001–+, Aug. 2008.

[368] T. P. Sotiriou and V. Faraoni, "f(R) theories of gravity," *Reviews of Modern Physics*, vol. 82, pp. 451–497, Jan. 2010.

[369] D. Wands, "Extended gravity theories and the Einstein–Hilbert action," *Classical and Quantum Gravity*, vol. 11, pp. 269–279, Jan. 1994.

[370] R. C. Myers and M. J. Perry, "Black Holes in Higher Dimensional Space-Times," *Ann. Phys.*, vol. 172, p. 304, 1986.

[371] B. Carter, "Hamilton-Jacobi and Schrodinger separable solutions of Einstein's equations," *Commun. Math. Phys.*, vol. 10, p. 280, 1968.

[372] S. A. Hughes, "The evolution of circular, non-equatorial orbits of Kerr black holes due to gravitational-wave emission," *Phys. Rev.*, vol. D61, p. 084004, 2000.

[373] S. A. Hughes, "Evolution of circular, non-equatorial orbits of Kerr black holes due to gravitational-wave emission. II: Inspiral trajectories and gravitational waveforms," *Phys. Rev.*, vol. D64, p. 064004, 2001.

[374] E. Barausse, S. A. Hughes, and L. Rezzolla, "Circular and non-circular nearly horizon-skimming orbits in Kerr spacetimes," *Phys. Rev.*, vol. D76, p. 044007, 2007.